



HAL
open science

Approches combinées ab initio et par spectroscopie de luminescence résolue en temps pour l'étude des interactions uranium-ligand

Hanna Oher

► **To cite this version:**

Hanna Oher. Approches combinées ab initio et par spectroscopie de luminescence résolue en temps pour l'étude des interactions uranium-ligand. Chimie de coordination. Université de Lille, 2020. Français. NNT : 2020LILUR032 . tel-03768322

HAL Id: tel-03768322

<https://theses.hal.science/tel-03768322>

Submitted on 3 Sep 2022

HAL is a multi-disciplinary open access archive for the deposit and dissemination of scientific research documents, whether they are published or not. The documents may come from teaching and research institutions in France or abroad, or from public or private research centers.

L'archive ouverte pluridisciplinaire **HAL**, est destinée au dépôt et à la diffusion de documents scientifiques de niveau recherche, publiés ou non, émanant des établissements d'enseignement et de recherche français ou étrangers, des laboratoires publics ou privés.

UNIVERSITÉ LILLE NORD DE FRANCE

Doctoral School ED 104 - Sciences de la Matière, du Rayonnement et de l'Environnement
University Department Laboratoire PhLAM

Thesis defended by **Hanna OHER**

Defended on **November 27, 2020**

In order to become Doctor from Université Lille Nord de France

Academic Field **Physics**

Speciality **Theoretical chemical physics**

**A combined ab initio and
time-resolved laser-induced
fluorescence study of uranium-ligand
interactions**

Thesis supervised by Valérie VALLET Supervisor
Florent RÉAL Co-Supervisor
Thomas VERCOUTER Co-Supervisor

Committee members

<i>Referees</i>	Chantal DANIEL	Senior Researcher at CNRS/Uni. Strasbourg	
	Eric FAULQUES	Senior Researcher at CNRS/Uni. Nantes	
<i>Examiners</i>	Dominique GUILLAUMONT	Senior Researcher at CEA-Marcoule	
	Michel MEYER	Junior Researcher at CNRS/Uni. Bourgogne	
	Jean-François PAUL	Professor at Uni. Lille	Committee President
<i>Supervisors</i>	Valérie VALLET	Senior Researcher at CNRS/Uni. Lille	
	Florent RÉAL	Associate Professor at Uni. Lille	
	Thomas VERCOUTER	Senior Researcher at CEA/Uni. Paris-Saclay	

COLOPHON

Doctoral dissertation entitled “A combined ab initio and time-resolved laser-induced fluorescence study of uranium-ligand interactions”, written by Hanna OHER, completed on January 15, 2021, typeset with the document preparation system \LaTeX and the yathesis class dedicated to theses prepared in France.

UNIVERSITÉ LILLE NORD DE FRANCE

Doctoral School ED 104 - Sciences de la Matière, du Rayonnement et de l'Environnement
University Department Laboratoire PhLAM

Thesis defended by **Hanna OHER**

Defended on **November 27, 2020**

In order to become Doctor from Université Lille Nord de France

Academic Field **Physics**

Speciality **Theoretical chemical physics**

**A combined ab initio and
time-resolved laser-induced
fluorescence study of uranium-ligand
interactions**

Thesis supervised by Valérie VALLET Supervisor
Florent RÉAL Co-Supervisor
Thomas VERCOUTER Co-Supervisor

Committee members

<i>Referees</i>	Chantal DANIEL	Senior Researcher at CNRS/Uni. Strasbourg	
	Eric FAULQUES	Senior Researcher at CNRS/Uni. Nantes	
<i>Examiners</i>	Dominique GUILLAUMONT	Senior Researcher at CEA-Marcoule	
	Michel MEYER	Junior Researcher at CNRS/Uni. Bourgogne	
	Jean-François PAUL	Professor at Uni. Lille	Committee President
<i>Supervisors</i>	Valérie VALLET	Senior Researcher at CNRS/Uni. Lille	
	Florent RÉAL	Associate Professor at Uni. Lille	
	Thomas VERCOUTER	Senior Researcher at CEA/Uni. Paris-Saclay	

UNIVERSITÉ LILLE NORD DE FRANCE

École doctorale ED 104 - Sciences de la Matière, du Rayonnement et de l'Environnement
Unité de recherche Laboratoire PhLAM

Thèse présentée par **Hanna OHER**

Soutenue le 27 novembre 2020

En vue de l'obtention du grade de docteur de l'Université Lille Nord de France

Discipline **Physics**

Spécialité **Chimie physique théorique**

Approches combinées ab initio et par spectroscopie de luminescence résolue en temps pour l'étude des interactions uranium-ligand

Thèse dirigée par Valérie VALLET directeur
Florent RÉAL co-directeur
Thomas VERCOUTER co-directeur

Composition du jury

<i>Rapporteurs</i>	Chantal DANIEL	directeur de recherche au CNRS/Uni. Strasbourg	
	Eric FAULQUES	directeur de recherche au CNRS/Uni. Nantes	
<i>Examineurs</i>	Dominique GUILLAUMONT	directeur de recherche au CEA-Marcoule	
	Michel MEYER	chargé de recherche au CNRS/Uni. Bourgogne	
	Jean-François PAUL	professeur à l'Uni. Lille	président du jury
<i>Directeurs de thèse</i>	Valérie VALLET	directeur de recherche au CNRS/Uni. Lille	
	Florent RÉAL	mcf à l'Uni. Lille	
	Thomas VERCOUTER	directeur de recherche au CEA/Uni. Paris-Saclay	

This thesis has been prepared at the following research units.

Laboratoire PhLAM

Laboratoire PhLAM
CNRS UMR 8523
Université Lille Nord de France
Bâtiment P5
59655 Villeneuve d'Ascq
France

☎ (33)(0)3 20 43 44 84
✉ marc.douay@univ-lille.fr
Web Site <http://phlam.univ-lille.fr>



CEA-Saclay

Laboratoire LANIE
DES/ISAS/DPC/SEARS
Université Paris-Saclay
91191 Gif-sur-Yvette
France

☎ (33)(0)1 69 08 26 59
✉ thomas.vercouter@cea.fr
Web Site <http://cea.fr>



To my beloved family.

À mes trois directeurs bien-aimés.

To myself.

A COMBINED AB INITIO AND TIME-RESOLVED LASER-INDUCED FLUORESCENCE STUDY OF URANIUM-LIGAND INTERACTIONS**Abstract**

Uranyl complexes have been the subject of many research works for fundamental chemistry of actinides, environmental issues, or nuclear fuel cycle processes. The formation of various uranium(VI) complexes, with ligands in solution must be characterized for a better understanding of U(VI) speciation. Uranyl-ligand interactions and symmetry of the complexes both affect the electronic structure of U(VI), and thus its luminescence properties. Time-resolved laser induced fluorescence spectroscopy (TRLFS) is one of the widely used techniques to get insights on the closest chemical environment of the uranyl ion in samples, owing to its high sensitivity and selectivity. However, the luminescence spectra fingerprints hold information within and beyond the first-coordination sphere of uranyl(VI), that needs to be more deeply investigated by supplementary techniques. A promising route for data interpretation consists in creating a synergy between TRLFS and ab initio-based interpretations. Luminescence spectra of uranyl complexes in solution typically show well-spaced vibronic progressions that overlap with the pure electronic transition from the excited state to the ground state. This has driven the theoretical methodology implementation. In the frame of this thesis, time-dependent density functional theory (TD-DFT) with hybrid and range-separated functionals is used to model the electronic structure of uranium(VI) complexes. This represents an effective theoretical approach with a reasonable computational cost and accuracy, compared with computationally expensive wave-function based methods, in a relativistic context. It enabled to characterize the main spectral parameters and the first low-lying excited state of uranyl compounds with different ligands and counterions after the photo-excitation, and to compute with a high accuracy the vibronic progression in order to guide the interpretation of experimental results.

In particular we focused our efforts on characterizing the influence of the organic or inorganic closest chemical environment of the uranium(VI)-based complexes. We studied 1) the influence of the extracting agent such as Aliquate 336 and solvent effect on uranyl tetrahalides; 2) inorganic Ca^{2+} and Mg^{2+} counterions on uranyl triscarbonates; and 3) monoamide ligands (di-2-ethylhexyl-isobutyramide) on uranyl binitrate complexes. Their electronic structures and main spectroscopic properties have been estimated by both TRLFS and ab initio techniques. The theoretical approach enabled to calculate the main luminescence emissions of the complexes with the corresponding assignment of the electronic transitions and vibronic modes involved. For all the studied complexes, a good agreement between theory and experiment was found, allowing to build a full picture about the capabilities of the methods.

Keywords: *ab initio*, photochemistry, uranium, trlfs

Laboratoire PhLAM

Laboratoire PhLAM – CNRS UMR 8523 – Université Lille Nord de France –
Bâtiment P5 – 59655 Villeneuve d’Ascq – France

APPROCHES COMBINÉES AB INITIO ET PAR SPECTROSCOPIE DE LUMINESCENCE RÉVOLUE EN TEMPS POUR L'ÉTUDE DES INTERACTIONS URANIUM-LIGAND**Résumé**

Les complexes d'uranyle ont fait l'objet de nombreux travaux de recherche pour la chimie fondamentale des actinides, les enjeux environnementaux ou les procédés du cycle du combustible nucléaire. La formation de divers complexes d'uranium(VI), avec des ligands en solution doit être caractérisée pour une meilleure compréhension de la spéciation de U(VI). Les interactions uranyl-ligand et la symétrie des complexes modifient la structure électronique de U(VI) et donc ses propriétés de luminescence. La spectrofluorimétrie laser résolue en temps (SLRT) est l'une des techniques largement utilisées pour obtenir des informations sur l'environnement chimique proche de l'ion uranyle dans les échantillons, en raison de sa sensibilité et de sa sélectivité élevées. Cependant, les signatures des spectres de luminescence contiennent des informations liées à la première sphère de coordination de l'uranyle et au-delà, et méritent d'être étudiées de manière plus approfondie par des techniques adaptées.

Une voie prometteuse pour l'interprétation des données consiste à créer une synergie entre SLRT et les interprétations *ab initio*. Les spectres de luminescence des complexes d'uranyle en solution montrent généralement des progressions vibroniques bien espacées qui se chevauchent avec la transition électronique pure provenant de l'état excité à l'état fondamental. Ceci a conduit la mise en œuvre de notre méthodologie théorique. Dans le cadre de cette thèse, la théorie de la fonctionnelle de la densité dépendante du temps (TD-DFT) avec des fonctionnelles hybrides et séparées par une plage est utilisée pour modéliser la structure électronique de complexes d'uranium(VI) dans un contexte relativiste. Cela a permis de caractériser les principaux paramètres spectraux et le premier état excité de plusieurs composés d'uranyle avec différents ligands et contre-ions, et de calculer avec une grande précision la progression vibronique afin de guider l'interprétation des résultats expérimentaux.

En particulier, nous avons concentré nos efforts sur la caractérisation de l'influence de l'environnement chimique le plus proche des complexes à base d'uranium(VI). Nous avons étudié 1) l'influence d'un agent d'extraction tel que l'Aliquate 336 et l'effet du solvant sur les tétrahalogénures d'uranyle; 2) les contre-ions inorganiques Ca^{2+} et Mg^{2+} sur les triscarbonates d'uranyle; et 3) les ligands monoamide (di-2-éthylhexylisobutyramide) sur les complexes de binitrate d'uranyle. Leurs structures électroniques et leurs principales propriétés spectroscopiques ont été estimées par les deux techniques SLRT et *ab initio*. L'approche théorique a permis de calculer les principales émissions de luminescence des complexes avec l'affectation correspondante des transitions électroniques et des modes vibroniques impliqués. Pour tous les complexes étudiés, un bon accord entre la théorie et l'expérience a été obtenu, permettant de construire une image plus complète des capacités des méthodes.

Mots clés : *ab initio*, photochimie, uranium, slrt

Acknowledgments

As this thesis was performed in the collaboration between the laboratory LANIE (CEA-Saclay) and the laboratory PhLAM (University of Lille), I want to express my appreciation to the directors of these units, Thomas Vercouter and Marc Douay, for the given opportunity to pursue my PhD studies.

I would not have written this thesis if three years ago these people had not accepted me as a student. My deepest gratitude to my supervisors Valérie Vallet, Florent Réal and Thomas Vercouter for the three amazing years with you, for your wisdom, patience and scientific experience. Having an opportunity to learn from your experience is an honor, and I did, I am doing and I will proudly do it further in my scientific path.

All the people who found time and made an effort to read this thesis are gratefully acknowledged. I hope you found my dissertation useful and interesting.

Here I cannot forget young researchers Dr. Silvia Diez-Fernandez, Dr. Mouheb Chebi, Dr. Giovanni Manfredi, PhD students Lana Abou Zeid and Bálint Kiss who were supporting me during my work. I must also mention researchers from the PCMT group and the laboratory LANIE for all the interesting discussions we had.

Of course, I would never survive in France without my Russian-speaking community. My closest friends, Sergey Telnov, Dr. Yevhaniia Smortsova, Dr. Volodymir Koverga, Nadya Zhutova, Dr. Olexander Motorny and Anastasiia Halushkina thank you for the wonderful time I have spent with you. My Ukrainian team Andrey Marchenko, Julia Klimova, Anastasiia Koroied and Evhenii Zozulia was never forgetting me despite the distance of 2667 km.

Finally, I acknowledge the most important people of my life. My parents Olga Vasilievna and Alexander Stepanovich, and of course my niece-daughter Elizabeth. Although you hardly understood what I researched on, you were willing to support any decision I made. Your love, patience, understanding and support are everything to me. I love you to the Moon and back.

Contents

Abstract	xi
Acknowledgments	xiii
Contents	xv
General introduction	1
I Methods	11
1 Luminescence of uranyl	13
1.1 Generalities on absorption and emission spectroscopy	13
1.2 Luminescence of uranyl complexes	15
1.3 Time-Resolved Laser-induced Fluorescence Spectroscopy (TRLFS)	21
1.3.1 Advantages and triple selectivity	22
1.3.2 Experimental set-up	25
2 Theoretical methods	33
2.1 Franck-Condon principle in the harmonic approximation	34
2.1.1 Duschinsky rotations	36
2.2 Introduction to Quantum chemistry	38
2.2.1 The Schrödinger equation	38
2.2.2 Born-Oppenheimer approximation	39
2.2.3 Constraints on the Wave function	40
2.3 Density functional theory	41
2.3.1 The Kohn-Sham equation	42
2.3.2 Time-Dependent density functional theory	44
2.3.3 Approximate exchange-correlation functionals	48
2.4 Relativistic effects	52
2.4.1 Dirac equation	53

2.4.2 Relativistic effective core potential	57
2.5 Basis set	58
2.6 Solvent effects	60
2.6.1 Continuum Models	61
2.6.2 Equilibrium and non-equilibrium solvation	64
II Results	73
Outline	75
3 Uranyl tetrahalides	79
3.1 Abstract	79
3.2 Introduction	80
3.3 Experimental details	82
3.3.1 Sample preparation	82
3.3.2 Time-Resolved Laser-Induced Fluorescence Spectroscopy	82
3.3.3 Computational details	83
3.4 Results and discussions	86
3.4.1 Experimental luminescence spectra	86
3.4.2 Ground and excited state structures of the uranyl tetrahalide complexes	88
3.4.3 Theoretical absorption and emission energies	96
3.4.4 Theoretical luminescence spectra	98
3.5 Conclusions	101
4 Uranyl triscarbonates	109
4.1 Abstract	109
4.2 Introduction	110
4.3 Experimental details	114
4.4 Computational details	115
4.5 Results and discussions	118
4.5.1 Experimental luminescence spectra	118
4.5.2 Theoretical ground and excited state structures	122
4.5.3 Experimental and theoretical emission energies	128
4.5.4 Vibronic progressions	132
4.6 Conclusions	136
5 Uranyl binitrates	147
5.1 Introduction	147
5.2 Computational Details	150

5.3 Results	152
5.3.1 Choice of the model systems	152
5.3.2 Theoretical ground and excited-state structures	153
5.3.3 Theoretical emission energies	160
5.3.4 Vibronic progressions	164
5.4 Discussions	167
5.5 Conclusions	173
General conclusions and perspectives	183
A Supplementary information for Chapter 3	189
A.1 Selection of the delay time	189
A.2 Supplemental Tables	191
A.3 Supplemental Figures	199
B Supplementary information for Chapter 4	203
B.1 Extraction of the pure spectra of the (Mg/Ca-) $\text{UO}_2\text{-CO}_3$ species from the raw TRLFS data	203
B.2 Procedure to estimate the spectrum of the $\text{Na}_2\text{MgUO}_2(\text{CO}_3)_3$ com- plex in water	205
B.3 Supplemental Tables	206
B.4 Supplemental Figures	218
Scientific contributions	221
Conferences	221
Publications	221
List of Tables	223
List of Figures	229

General introduction

Actinides are *f*-block elements, like lanthanides, located in the last row of the periodic table (Fig. 1). They are radio-elements in the sense that all their isotopes are radioactive with various radioactive decay times. Only a few actinide isotopes are naturally present on earth due to their very long radioactive decay comparatively to the age of earth (^{235}U , ^{238}U , and ^{232}Th) or due to natural nuclear reactions (^{234}U , ^{230}Th , and ^{231}Pa). The other actinide isotopes have an artificial origin from nuclear bombs and nuclear reactors. Actinides are heavy atoms with a high number of electrons, and most of the actinides can exist at several oxidation states (for instance, plutonium in the aqueous phase may appear as up to four oxidation states at the same time [1, 2]). Thus they exhibit different electronic configurations leading to rich chemical properties. The unique coordination of *f*-elements with ligands [3, 4] and the broad applications related to nuclear chemistry [2] attracted the attention of many experimental and theoretical researchers. Understanding the chemical interactions of actinide elements with other compounds requires to investigate their electronic structures. While the valence electronic structure is often known for light elements, it is sometimes trickier for actinides due to their larger number of electrons, and is still a matter of research.

Actinides are the elements with atomic numbers ranging from 90 to 103 with the corresponding electronic configuration from Ac: $[\text{Rn}]6d^17s^25f^0$ to Lr: $[\text{Rn}]5f^{14}6d^17s^2$. Apart from actinium and thorium, they contain a fully filled *4f*-shell and a partly filled *5f*-shell. The degeneracy of the *f*-shell gives rise to a large number of possible (nearly) degenerate electronic states. Moreover, the *f*-shell might be concomitant with open *6d*- and *7s*-shells, respectively, which can increase the complexity of their valence electronic structure [5, 6]. One

ACTINIDES	Ac	Th	Pa	U	Np	Pu	Am	Cm	Bk	Cf	Es	Fm	Md	No	Lr		

Figure 1: Location of the actinides in the periodic table of elements.

should also take into account that the high nuclear charge leads to appearance of relativistic effects. Despite this, the electronic structures of the early actinides complexes (e.g., U, Np and Pu) have been studied for molecular compounds of actinides by using experimental electronic spectroscopy techniques [7, 8] and theoretical *ab initio* calculations [9, 10]. In the present work, we investigate the electronic structures of uranium complexes in solution because of the high importance of uranium chemistry for environmental issues, for the reprocessing of used nuclear fuels, and for fundamental studies. More precisely, we would like to support luminescence measurements used to characterize uranium speciation with *ab initio* spectral modeling.

Nowadays, a number of uranium-containing complexes, in which the oxidation state of the uranium atom varies from +3 to +6 with coordination numbers from 3 to 8 is known [2, 4, 11]. The most important oxidation states of uranium in natural environment are +4 and +6. Compounds of U(IV) have very low solubility in natural media (from mildly acidic to alkaline), while U(VI) compounds are much more soluble, and may increase the uranium mobility in the environment. In presence of oxygen, the high charge of hexavalent uranium is stabilized

by two oxygen atoms forming the linear uranyl moiety UO_2^{2+} . As a hard Lewis acid, uranyl forms stable complexes with the Lewis bases of inorganic (halides, carbonates, phosphates, etc.) and organic (oxalates, proteins, etc.) nature. Hence, the uranyl ion is a dominant feature of uranium chemistry as it is the base of many complexes of relevance in different fields. One should mention that the chemistry of uranium(VI) compounds in solution is complex. Several species can co-exist under given conditions, causing difficulties for the determination of the uranium speciation. Appropriate techniques have to be used to study uranium(VI) complexes accurately, among which spectroscopic techniques offer many advantages.

There are many spectroscopic techniques used to study electronic structure of uranium-containing complexes and their speciation. Among them the most used are X-Ray [12, 13], absorption [14, 15] and luminescence [16, 17] spectroscopies. In general, spectroscopy deals with the energetic structure and properties of chemical systems. It is based on the observation and analysis of the energy distribution of radiation (e.g., X-Ray, light, etc.) absorbed, emitted or scattered by the object of investigation. The interaction of an energy source with a molecule (in this particular case uranyl complex) results in unique spectral lines, called spectrum. To be able to record the spectrum the molecule must have an ability to response to the energy source.

Each techniques have, of course, advantages and drawbacks. X-Ray absorption at high energy are used to probe the oxidation states of the actinides (XANES - X-ray Absorption Near Edge Structure), or to describe the structure of the first coordination shell (EXAFS - Extended X-Ray Absorption Fine Structure). Though powerful, these absorption spectroscopy techniques may be limited to concentrated or slightly diluted solutions. UV-visible absorption spectroscopy is also a method of choice to determine oxidation states of actinides, but are often insufficiently sensitive to speciation changes, especially at low concentrations. Moreover, using absorption techniques on rather concentrated uranium solutions might introduce a bias if one is aiming at describing a fine interaction between the uranyl cation and its near environment. Indeed, uranium has a propensity at forming polymeric species depending on the pH and concentration.

Luminescence spectroscopy, and more specifically time-resolved laser-

induced fluorescence spectroscopy (TRLFS), has been widely used for uranyl speciation studies, and some other actinides and lanthanides, because of its high sensitivity and selectivity. Uranyl complexes display specific luminescence features, with characteristic band shapes and different luminescence lifetimes [17–22]. The luminescence spectra can then be analyzed to identify the uranyl species, their stoichiometries, complex stabilities and thermodynamic properties. TRLFS allows to measure the luminescence from trace amounts of uranium(VI) which can be easily handled in the laboratory, and are representative of many situations like environmental and biological conditions. The luminescence spectra also contain information about the electronic and vibronic structures of the complexes, which can only be interpreted with an appropriate description of the luminescence transitions.

However, the interpretation of these spectra remains tedious because the spectra may not be the result of a unique chemical species and they may be influenced by several factors, some obvious such as the nature of the first coordination shell, but also from the organic or inorganic counter-cations present in solution, or the polarity of the solvent. The deconvolution of all these effects by the use of solely experimental techniques even proceeded with an extreme care is impossible, as the variation of chemical conditions leads to change of the composition of the sample under investigation. One should also mention the complexity of the decomposition of the species luminescence. It might be performed with the help of mathematical parallel factor analysis (PARAFAC) [22] which requires a large set of experimental data and good theoretical models to get reliable results. The combination of these factors calls for additional theoretical support.

The electronic structure from the luminescence spectra of uranium(VI) complexes, particularly $\text{UO}_2\text{Cl}_x^{2-x}$, has been explained by the magnetic circular dichroism (MCD) spectroscopy [23]. The difficulty is that the MCD spectra should be understood first in order to explain the luminescence observations. Hence, theoretical methods providing direct interpretation of U(VI) luminescence data may offer better support. The *ab initio* quantum modeling appears to be suitable for this aim, and should enable the prediction of the luminescence spectra of uranium(VI)-containing complexes, in relation with the electronic

structure. This implies a rigorous description of electron correlation and relativistic effects in uranium-containing complexes, which remains a challenge for quantum chemistry. The wave-function theory (WFT) based methods were shown to be effective for this task [9, 10, 24, 25], but restricted to small size U(VI) complexes (up to 20 atoms). Thanks to the benchmark studies of Tecmer et al. [26, 27], we can achieve an accurate description of electronic structures for large U(VI) compounds, using density functional theory (DFT) in a relativistic approach by using hybrid and range-separated functionals.

In this thesis we study three important uranium(VI)-based complexes, uranyl tetrachloride, uranyl triscarbonate and uranyl binitrate complexes, by means of time-resolved laser-induced fluorescence spectroscopy and *ab initio* quantum modeling. By providing a dual expertise, we aim to explain ground and excited state uranium(VI) electronic structure and estimate the capabilities of the theoretical modeling techniques. This can be achieved by theoretical model computations of the ground and excited state structures, emission energies and further, reconstruction of theoretical luminescence spectra and their comparison with experimental results. Moreover, by increasing the complexity of the theoretical model, the effects of the first and second coordination spheres of uranium(VI) as well as the influence of solvents of different polarity can be decomposed.

This manuscript consists of two parts. Part I contains two chapters explaining the emission spectroscopy and theoretical methods applied to study uranium(VI) electronic structure. In the Chapter 1 the reader will find a detailed discussion of the luminescent properties of uranium(VI) together with experimental TRFLS technique used to measure luminescence spectra. The Chapter 2 addresses the theoretical background used to develop the *ab initio* based methodology combined with the Franck-Condon principle in the harmonic approximation for the reconstruction of the theoretical spectra. Part II contains three chapters of results. Each chapter is supported by its own introduction and description of theoretical models, and has a shape of a scientific article. Chapter 3 represents a benchmark study on the case of $\text{UO}_2\text{X}_4^{2-}$ ($\text{X}=\text{Cl},\text{Br}$) complexes. There, the step-by-step approach was applied allowing to check the accuracy of the proposed methodology. Chapter 4 is about a performance of both, experimental and

theoretical techniques on $M_n\text{UO}_2(\text{CO}_3)_3^{(4-2n)-}$ ($M=\text{Mg, Ca}$; $n = 1-2$) complexes, and more precisely, about their capabilities to probe the changes in the second coordination sphere. The last Chapter 5 reports a study related to the nuclear fuel reprocessing about the complex $\text{UO}_2(\text{NO}_3)_2(\text{DEHiBA})_2$ and how different might be the spectroscopic properties of its conformers. At the end of this thesis, the reader will find general conclusions that summarize and highlight the achievements, and some perspectives of this PhD work.

Bibliography of the current chapter

- (1) Choppin, G. R. Solution chemistry of the actinides. *Radiochimica Acta* **1983**, *32*, 43–54, DOI: 10.1524/ract.1983.32.13.43.
- (2) Edelstein, N. M.; Fuger, J.; Katz, J. J.; Morss, L. R. In *The chemistry of the Actinide and Transactinide Elements*; Springer: 2010, pp 1753–1835.
- (3) Binnemans, K. Lanthanides and actinides in ionic liquids. *Chemical reviews* **2007**, *107*, 2592–2614, DOI: 10.1021/cr050979c.
- (4) Fortier, S.; Hayton, T. W. Oxo ligand functionalization in the uranyl ion UO_2^{2+} . *Coordination Chemistry Reviews* **2010**, *254*, 197–214, DOI: 10.1016/j.ccr.2009.06.003.
- (5) Denning, R. G. Electronic Structure and Bonding in Actinyl Ions and their Analogs. *Journal of Physical Chemistry A* **2007**, *111*, 4125–4143, DOI: 10.1021/jp071061n.
- (6) Dolg, M. In *Handbook of Relativistic Quantum Chemistry*, Liu, W., Ed.; Springer Berlin Heidelberg: Berlin, Heidelberg, 2017, pp 449–478, DOI: 10.1007/978-3-642-40766-6_5.
- (7) Denning, R.; Snellgrove, T.; Woodwark, D. The electronic structure of the uranyl ion: Part I. The electronic spectrum of $\text{Cs}_2\text{UO}_2\text{Cl}_4$. *Molecular Physics* **1976**, *32*, 419–442, DOI: 10.1080/00268977600103211.
- (8) Flint, C. D.; Tanner, P. A. Electronic and vibrational spectra of $[\text{Me}_4\text{N}]_2\text{UO}_2\text{Cl}_4$. *Journal of the Chemical Society, Faraday Transactions 2: Molecular and Chemical Physics* **1981**, *77*, 1865–1878, DOI: 10.1039/F29817701865.
- (9) Matsika, S.; Zhang, Z.; Brozell, S.; Blaudeau, J.-P.; Wang, Q.; Pitzer, R. Electronic structure and spectra of actinyl ions. *Journal of Physical Chemistry A* **2001**, *105*, 3825–3828, DOI: 10.1021/jp003085z.
- (10) Pierloot, K.; van Besien, E. Electronic structure and spectrum of UO_2^{2+} and $\text{UO}_2\text{Cl}_4^{2-}$. *Journal of Chemical Physics* **2005**, *123*, 204309, DOI: 10.1063/1.2121608.
- (11) Katz, J. J., *The Chemistry of the Actinide and Transactinide Elements*, Fourth Edition; Springer Science & Business Media: 2007; Vol. 5.
- (12) Vitova, T.; Green, J. C.; Denning, R. G.; Löble, M.; Kvashnina, K.; Kas, J. J.; Jorissen, K.; Rehr, J. J.; Malcherek, T.; Denecke, M. A. Polarization dependent high energy resolution X-ray absorption study of dicesium uranyl tetrachloride. *Inorganic Chemistry* **2014**, *54*, 174–182, DOI: 10.1021/ic5020016.

- (13) Teterin, Y. A.; Teterin, A.; Ivanov, K.; Maslakov, K.; Kalmykov, S.; Petrov, V.; Ryzhkov, M.; Suglobov, D. N. Valence XPS structure and chemical bond in $\text{Cs}_2\text{UO}_2\text{Cl}_4$. *Nuclear Technology and Radiation Protection* **2016**, *31*, 37–50, DOI: 10.2298/NTRP1601037T.
- (14) Flint, C. D.; Tanner, P. A. Absorption and luminescence spectra of $[(\text{C}_2\text{H}_5)_3\text{NH}]_2\text{UO}_2\text{Cl}_4$. *Journal of the Chemical Society, Faraday Transactions 2: Molecular and Chemical Physics* **1979**, *75*, 1168–1178, DOI: 10.1039/F29797501168.
- (15) Hill, R. J.; Kemp, T. J.; Allen, D. M.; Cox, A. Absorption spectrum, lifetime and photoreactivity towards alcohols of the excited state of the aqueous uranyl ion (UO_2^{2+}). *Journal of the Chemical Society, Faraday Transactions 1: Physical Chemistry in Condensed Phases* **1974**, *70*, 847–857, DOI: 10.1039/F19747000847.
- (16) Flint, C. D.; Tanner, P. A. Luminescence spectrum of $\text{Cs}_2\text{UO}_2\text{Cl}_4$. *Journal of the Chemical Society, Faraday Transactions 2: Molecular and Chemical Physics* **1978**, *74*, 2210–2217, DOI: 10.1039/F29787402210.
- (17) Wang, Z.; M. Zachara, J.; Liu, C.; Gassman, P.; R. Felmy, A.; B. Clark, S. A cryogenic fluorescence spectroscopic study of uranyl carbonate, phosphate and oxyhydroxide minerals. *Radiochimica Acta* **2008**, *96*, 591–598, DOI: 10.1021/es048448d.
- (18) Moulin, C.; Decambox, P.; Moulin, V.; Decaillon, J. G. Uranium Speciation in Solution by Time-Resolved Laser-Induced Fluorescence. *Analytical Chemistry* **1995**, *67*, 348–353, DOI: 10.1021/ac00098a019.
- (19) Moulin, C.; Decambox, P.; Mauchien, P. State of the art in time-resolved laser-induced fluorescence for actinides analysis: Applications and trends. *Journal of Radioanalytical and Nuclear Chemistry* **1997**, *226*, 135–138, DOI: 10.1007/BF02063637.
- (20) Geipel, G.; Amayri, S.; Bernhard, G. Mixed complexes of alkaline earth uranyl carbonates: A laser-induced time-resolved fluorescence spectroscopic study. *Spectrochimica Acta Part A: Molecular and Biomolecular Spectroscopy* **2008**, *71*, 53–58, DOI: 10.1016/j.saa.2007.11.007.
- (21) Bernhard, G.; Geipel, G.; Reich, T.; Brendler, V.; Amayri, S.; Nitsche, H. Uranyl(VI) carbonate complex formation: Validation of the $\text{Ca}_2\text{UO}_2(\text{CO}_3)_3(\text{aq.})$ species. *Radiochimica Acta* **2001**, *89*, 511–518, DOI: 10.1524/ract.2001.89.8.511.

- (22) Drobot, B.; Steudtner, R.; Raff, J.; Geipel, G.; Brendler, V.; Tsushima, S. Combining luminescence spectroscopy, parallel factor analysis and quantum chemistry to reveal metal speciation—a case study of uranyl (VI) hydrolysis. *Chemical Science* **2015**, *6*, 964–972, DOI: 10.1039/C4SC02022G.
- (23) Görller-Walrand, C.; De Houwer, S.; Fluyt, L.; Binnemans, K. Spectroscopic properties of uranyl chloride complexes in non-aqueous solvents. *Physical Chemistry Chemical Physics* **2004**, *6*, 3292–3298, DOI: 10.1039/B317002K.
- (24) Van Besien, E.; Pierloot, K.; Görller-Walrand, C. Electronic spectra of uranyl chloride complexes in acetone: a CASSCF/CASPT2 investigation. *Physical Chemistry Chemical Physics* **2006**, *8*, 4311–4319, DOI: 10.1039/B607026D.
- (25) Réal, F.; Gomes, A. S. P.; Visscher, L.; Vallet, V.; Eliav, E. Benchmarking Electronic Structure Calculations on the Bare UO_2^{2+} Ion: How Different are Single and Multireference Electron Correlation Methods? *The Journal of Physical Chemistry A* **2009**, *113*, PMID: 19888775, 12504–12511, DOI: 10.1021/jp903758c.
- (26) Tecmer, P.; Gomes, A. S. P.; Ekström, U.; Visscher, L. Electronic spectroscopy of UO_2^{2+} , NUO^+ and NUN : an evaluation of time-dependent density functional theory for actinides. *Physical Chemistry Chemical Physics* **2011**, *13*, 6249–6259, DOI: 10.1039/C0CP02534H.
- (27) Tecmer, P. Towards reliable modeling of excited states of uranium compounds, Ph.D. Thesis, Vrije Universiteit, 2012.

Part I

Methods

Luminescence of uranyl

The experimental technique used along the PhD work is time-resolved laser-induced fluorescence spectroscopy (TRLFS). It is universally applied to detect and probe the speciation, i.e. stoichiometry, species concentrations, coordination, and symmetry of the first coordination sphere of several actinides at specific oxidation states (U(VI), Cm(III), Am(III)), and lanthanides (Ce(III), Eu(III), Gd(III), Sm(III), Tb(III), Dy(III) and Tm(III)). Uranium(VI) has particularly rich spectroscopic features which are sensitive to speciation changes. This is why U(VI) complexes have been widely investigated by TRLFS. In this chapter, the background knowledge about excitation and de-excitation processes will be introduced, as well as their application to uranium(VI) species. The electronic structure of the UO_2^{2+} will be presented to understand the nature of the emission process. The TRLFS main principle and set-up will be described as well.

1.1 Generalities on absorption and emission spectroscopy

When a light source is oriented toward a material, the main processes are reflection, scattering and absorption. Each phenomenon can be exploited as a spectroscopic method for matter investigation. Photon absorption is also a mode of excitation, which brings the absorbing compound into an electronic excited state from which de-excitation naturally occurs. One of the de-excitation pro-

cesses is the emission of photons which is called luminescence. Luminescence or emission spectroscopy provides pieces of information about the chemical speciation of the compound. The energy diagram shown on Figure 1.1 corresponds to a general case, often taken as an example, where for a compound (molecule), the ground state (S_0) and the excited states (S_1 , S_2) have a singlet character ($M=1$), while the excited state T_1 of lower energy has a triplet character ($M=3$).

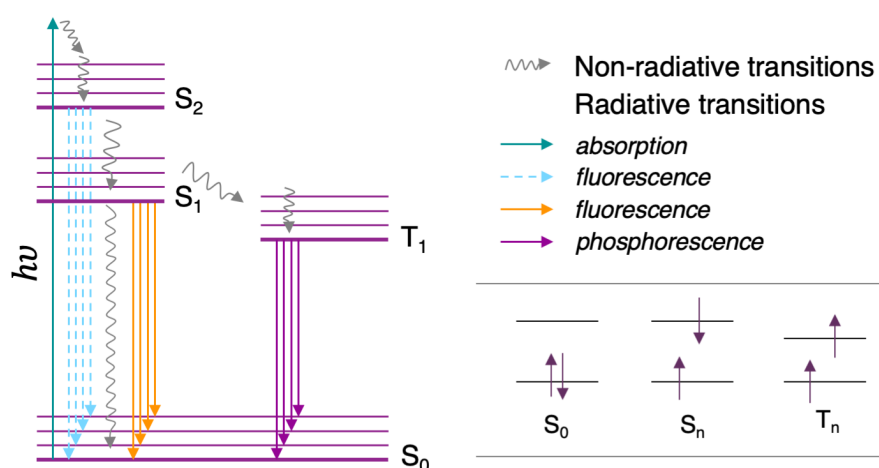


Figure 1.1: General Jablonski diagram representing the electronic transitions in a diatomic molecule.

The absorption step is characterized by passing a molecule from the ground state S_0 to an excited state S_n with the energy difference

$$\Delta E = h\nu \quad (1.1)$$

where h is the Planck constant and ν is the frequency of the incident photon. The absorption process is very fast with respect to other processes ($\approx 10^{-15}$ s) [28]. After, the absorbed energy is dissipated in a non-radiative manner by either vibrational relaxation ($\approx 10^{-13} - 10^{-12}$ s) or internal conversion ($\approx 10^{-12} - 10^{-16}$ s) in order to reach the lowest energy vibronic states of the first excited electronic state S_1 . The de-excitation of the molecule occurs either by a radiative process with emission of light of frequency determined by the

difference in energy between the initial level and target vibronic levels of S_0 (fluorescence, $\approx 10^{-9} - 10^{-7}$ s), or by a non-radiative process. Radiative de-excitation from higher excited states S_n is also possible, but the corresponding emissions are generally in the high energy range and have a very short lifetime; thus these are almost not detectable. This type of excitation/de-excitation is mostly applied to organic molecules, but one can consider another way of de-excitation process. Usually it is slow because it is supported by the inter-system crossing ($\approx 10^{-9} - 10^1$ s): a compound from its excited state S_1 (singlet) goes into another excited state of different spin multiplicity T_1 (triplet) as shown on Fig. 1.1. In this case, the return of an electron to the ground state may or may not occur radiatively (phosphorescence, $\approx 10^{-6} - 10^1$ s). The phosphorescence is in fact delayed relative to excitation, and less intense compared to the de-excitation without a change of a spin (i.e., fluorescence). Due to the spin-selection rules the singlet-triplet transitions are forbidden, but they can be observed because of other effects (for instance, spin-orbit coupling in case the case of heavy elements, such as f -elements) [28]. In parallel with the phosphorescence process, the numerous collisions with solvent molecules favor intersystem crossing and/or vibrational relaxation in S_0 .

In some cases, the radiative emission of a compound can be inhibited by energy exchange with another molecule. These processes fall into two categories: the transfer of energy to an acceptor molecule, and exchange by vibrational movements leading to static (interaction with the ground state) or dynamic (interaction with the excited state) quenching.

1.2 Luminescence of uranyl complexes

The luminescence of uranium compounds was a subject of spectroscopic studies of several generations in Becquerel family and dates back to over more than 100 years ago. Starting from the early 1800s and until the 1870s, they investigated the fluorescence and phosphorescence to be able for the first time to record fluorescence spectra of several uranyl salts [29]. Within the next 50 years, many researchers have been studying the spectroscopy of uranium. In the first book on the fluorescence of uranyl compounds, Nichols and Howers [30]

inferred that the fluorescence is observed in the energy range from 20 000–15 000 cm^{-1} , but no assignment for the lines was provided at that time. Later, in a second book by Dieke and Duncan [31], the contributions of the symmetrical, anti-symmetrical and bending vibrational frequencies of the uranyl unit to the fluorescence spectrum was deduced, along with an understanding that these parameters may vary with the composition of close chemical environment of the UO_2^{2+} moiety. In 1949, Kasha [32] noted that the transitions are electric dipole forbidden (Laporte selection rule), as confirmed by the low absorption extinction coefficient values.

Since these times, many groups have worked on the fluorescence spectra interpretation on the basis of the electronic structure. It was difficult to study, but still several hypotheses about the electronic structure of the uranyl ion have been proposed. The third book on the uranyl spectroscopy by Rabinowitch and Belford [33] summarizes some of the electronic structure knowledge. But the most detailed studies were performed by the group of R.G. Denning starting from the 1970s [7]. Until now, this information is gathering since new experimental and theoretical techniques have been developed.

Electronic structure of UO_2^{2+}

The U^{6+} with the noble gas electronic configuration $[\text{Rn}]5f^06d^07s^0$ has a highly positive charge and is reduced in solution. Thus, U^{6+} is stabilized by two O atoms through the formation of two bonds resulting in a new linear ion called uranyl UO_2^{2+} ($D_{\infty h}$) (Fig. 1.2). The electronic structure of this molecular ion has been determined. U(VI) is a 5*f* metal. In comparison with the 5*d* metal series [34, 35] for which the ligand-field effects are predominant and can modify energy levels, the effect of spin-orbit coupling is predominant for uranium, and more generally for actinides (Fig. 1.3).



Figure 1.2: The uranyl(VI) di-cation structure.

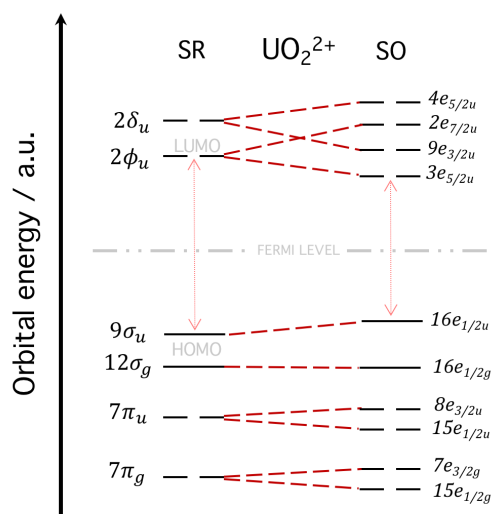


Figure 1.3: The effect of the spin-orbit coupling on the bare UO_2^{2+} . The schematic diagram is obtained at the spin free at spin-orbit CAM-B3LYP/DFT level of theory.

The schematic energies of uranyl valence orbitals as well as their Kohn-Sham representations are shown on Fig. 1.4. The highest occupied molecular orbitals (HOMOs) are $3\sigma_g$, $3\sigma_u$, $1\pi_g$ and $2\pi_u$ (the notation is taken from Denning energy level diagram [5]). They form by the mixing of the $5f$ and $6d$ atomic orbitals of uranium with the $2p$ atomic orbitals of oxygen. These orbitals are mostly located on the oxygen atoms, showing that the electronic density is associated with the oxygen atoms mainly. On the energy levels scheme, the σ_u bonding orbital has higher energy compared to others. The position on the scale depends on the overlapping of the $5f$ and $6d$ U orbitals with the $2p$ O orbitals. In more general studies on the uranyl electronic structure, the contribution of the $6s$ and $6p$ U electrons was also considered to the build the MOs. The $6s$ uranium orbital is comparable with the $5f$ orbitals and $6p$ because their XPS (X-Ray Photoelectron Spectroscopy allowing to measure the core electrons binding energy) ionizations show large axial field splittings that correlate inversely with the $\text{U}-\text{O}_{\text{yl}}$ bond distance [36]. Finally, the $2s$ O atomic orbitals also participate because of their near degeneracy, and σ -interaction with $6s$ and $6p$ U electrons. Usually, these orbitals are not important while studying low-lying excited states. The lowest

unoccupied molecular orbitals $1\delta_u$ and $1\phi_u$ (LUMOs) are uranium-based orbitals $5f_\delta$ and $5f_\phi$, which do not participate in the bonding with the oxygen atoms as a result of symmetry constraints.

The uranyl di-cation is often associated with ligands in the equatorial plane (Fig. 1.5). Since UO_2^{2+} is a hard Lewis acid, the interactions with ligands which are hard Lewis bases are favored. The chemical interactions are often mostly of ionic character, rather than covalent, although covalent compounds may form with ligands of high electronegativity [37, 38]. The uranyl electronic structure mainly change as a result of covalent ligands interaction with U through the d - and f -type orbitals [7, 9, 16, 39]. When interactions with ligands are mostly ionic, the induced charge transfer in the $\text{U}-\text{O}_{\text{yl}}$ bond also affects the electronic structure. This is the reason why luminescence spectroscopy can probe chemical interaction as will be discussed in the next section.

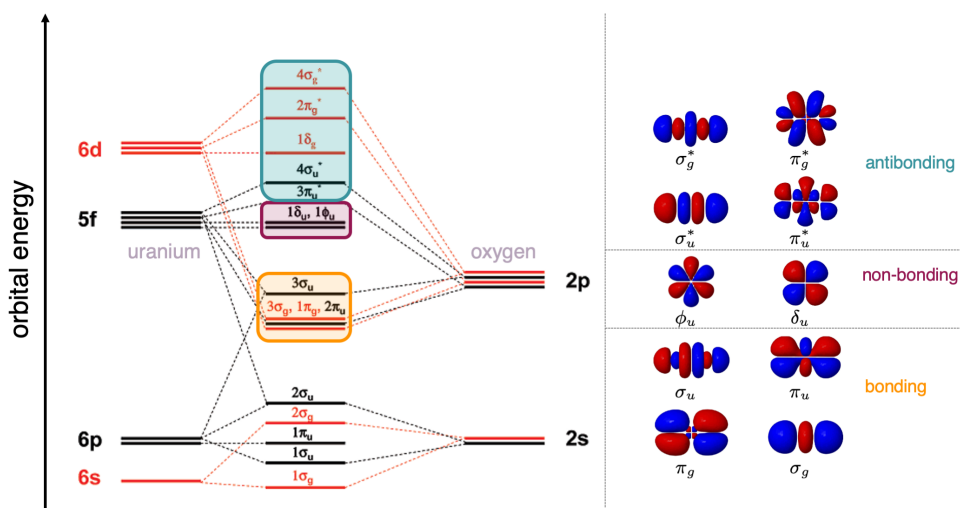


Figure 1.4: Energy levels [5] and characteristic Kohn-Sham molecular orbitals of uranyl.

Luminescence spectra

The fluorescence spectra of the uranyl-based complexes have the characteristic shape of five equally distant bands (right panel of Fig. 1.6) and locate in the range

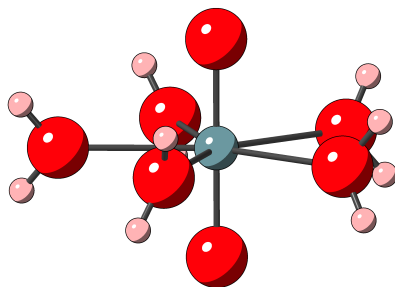


Figure 1.5: Penta-aqua-uranyl $\text{UO}_2(\text{H}_2\text{O})_5^{2+}$ structure.

from $21\,000\text{--}15\,000\text{ cm}^{-1}$ on average. The typical fluorescence decay time of uranyl in aqueous acidic solution is observed to be by about 2 microseconds [18, 40] and may change depending on the pH. However, the term fluorescence applied to actinide's emission is misleading, the majority of the experimental spectra refer to phosphorescence [11] because of their long decay times. Despite experimental efforts there is no detailed information about the primary deactivation process; thus it is better to use the term luminescence to describe the emission of uranyl complexes.

The luminescence spectrum of uranyl-based complexes typically shows vibronic progressions that overlap with the pure electronic transition from the luminescent states to the ground state. The electronic transitions result in a change in both electronic and vibrational energies (vibronic transition). This process is much faster than the nuclear movements (i.e., internuclear separation is not changing). The probability of a transition and the observed intensity is determined by the overlap of the vibrational wave functions, which change as a function of the internuclear separation (known as the Franck-Condon principle, see Chapter 2). Dieke and Duncan [31] suggested that the vibronic progressions of uranyl are built as a sum of its symmetric stretching, antisymmetric stretching and bending vibrations. Several authors established experimentally that this can be simplified as the symmetrical stretching $\text{U}-\text{O}_{\text{yl}}$ vibration predominantly coupled to the electronic transition of uranyl [33]. Thus, in the case of uranyl-based complexes the vibronic progression means that there is a coupling to the symmetrical stretching mode of the uranyl unit. Figure 1.6 represents a simpli-

fied Franck-Condon diagram and the corresponding spectrum of uranyl(VI). In this diagram, the absorption occurs from the S_0 ground state to higher singlet states S_n (states with predominantly singlet character with spin-orbit coupling; here state number 1). The energy then goes down to the triplet state T_1 (or state with predominantly triplet character in the intermediate coupling scheme) from where it starts to relax back to the fundamental state. One should note that in addition to the electronic transition, the vibronic relaxation occurs from the ν'_0 vibronic level of T_1 to ν_0, ν_1, ν_2 etc. vibronic levels of S_0 state.

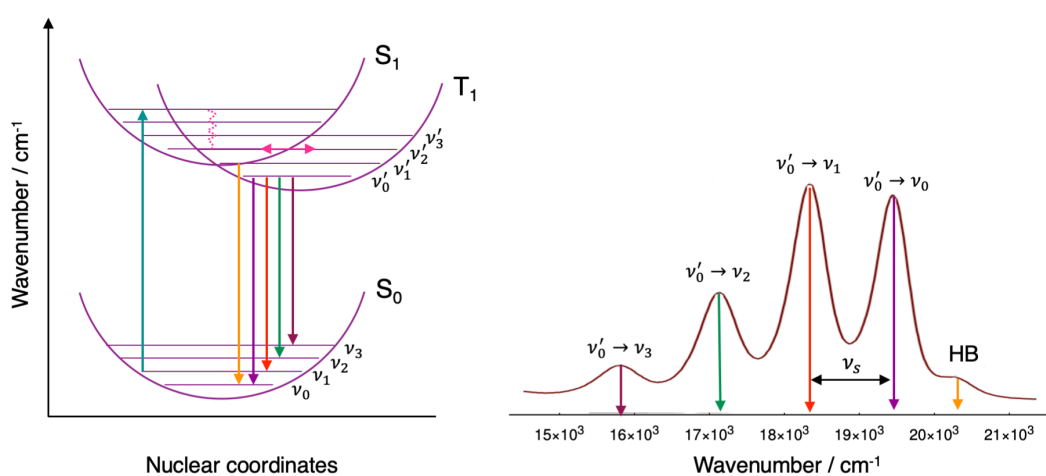


Figure 1.6: A simplified Franck-Condon principle diagram applied to U(VI) luminescence [41](left) and the time-resolved luminescence spectrum of uranyl in aqueous acidic media (pH = 1) with corresponding transition lines (right).

The scheme on Figure 1.6 is built on the base of theoretical and experimental studies. The calculations of the electronic spectra of the UO_2^{2+} and $\text{UO}_2\text{Cl}_4^{2-}$ were performed at different levels of theory by Zhang et al. [29], Matsika et al. [42], Pierloot et al. [10, 43], Réal et al. [25, 44] and others [24, 26, 45]. Their results were supported mostly by the experimental electronic spectra obtained by Denning's group [7]. All these studies confirm that the luminescence of uranyl-based complexes arises from the non-bonding $5f_\delta$ or $5f_\phi$ orbitals of U mainly to the bonding σ_u orbital of ligands (Fig. 1.4) meaning that the transition is partly a metal-to-ligand charge transfer mixed with a local transition of energy on uranium. The first low-lying state is located around

$19\,000\text{ cm}^{-1}$ on the energy scale and found to have a dominant triplet character with the $3\sigma_u 1\delta_u$ configuration. Because the energy of the singlet state of the same configuration is out of the luminescence spectra region it cannot be detected by fluorescent spectroscopy (by about $28\,000\text{ cm}^{-1}$ for UO_2^{2+} [10, 43, 44]). By the spin selection rule the triplet-singlet transitions are strictly forbidden, but this rule is overpassed in the intermediate coupling scheme, and these transitions are observable experimentally.

According to the uranyl(VI) electronic structure changes, the luminescence spectra usually provide three key pieces of information about both the axial and equatorial bonding to the uranium atom. The first is the position the electronic transition energy. The second is the vibrational spacing, which provides the energy of the total symmetric stretching mode ν_s of the uranyl moiety. The third is the band intensity ratio, which is, together with the ν_s value, able to estimate the U–O_{yl} bond strength [46]. These three parameters are very sensitive to the closed chemical environment of uranyl and allow to estimate the electronic structure changes in a combination with experimental magnetic circular dichroism (MCD) spectroscopy or theoretical *ab initio* calculations, for instance. The luminescence spectra of uranyl can be recorded by time-resolved laser-induced fluorescence spectroscopy (TRLFS) technique known for its sensitivity and selectivity to uranium(VI) complexes. The key principle, as well as the advantages and use of TRLFS is discussed in the last section of this chapter.

1.3 Time-Resolved Laser-induced Fluorescence Spectroscopy (TRLFS)

TRLFS is a technique which analyzes the light emission after an excitation of a compound by a pulsed laser. Initially it was developed at CEA in the 1980s for the analysis of small concentrations of actinides (particularly U(VI) and Cm(III)) samples [47]. Despite the low molar extinction coefficient of *f*-elements, the use of a laser as excitation source compensates with its high number of photons for excitation. It has been shown that the detection of traces of actinides is possible

in aqueous solutions [19, 48, 49], non-aqueous solvents [50] and minerals [17]. Nowadays, TRLFS is mainly used to determine the closest chemical environment of the UO_2^{2+} , Cm^{3+} and Am^{3+} luminescent species, i.e., to study their speciation and kinetics [51–56]. Moreover, the determination of thermodynamic properties such as formation constants, enthalpy and entropy of reactions, and activation energies also become accessible when the laser technique is combined with temperature control [40, 41, 57–59].

In the specific case of U(VI), by probing the electronic structures dependent on the interaction of uranyl UO_2^{2+} with ligands, the TRLFS technique will give access to some structural properties as well as the uranyl ground state symmetrical stretching mode and uranyl elongation from the ground to the excited state by comparing different luminescence spectra [23, 60].

1.3.1 Advantages and triple selectivity

The TRLFS is a non-intrusive technique which maintains the molecular information and has a number of advantages for the study of actinides. It is highly sensitive allowing to detect the U(VI) luminescence from its trace amounts, for instance in solutions containing down to 10^{-13} M of uranium (VI) [19]. Moreover, the specific characterization of a uranium(VI) complex is made possible by the three general features of the TRLFS technique (triple selectivity): *i*) the possibility to set the excitation wavelength, *ii*) the recording of the fluorescence spectra and decay time, and *iii*) the use of the temporal resolution for species discrimination.

Excitation wavelength The luminescence of a compound is induced by the laser beam at a given wavelength. The laser may be tuned to match the maximum absorption band of the compound. With pulsed lasers (nitrogen gas laser, Nd:YAG, etc.), the excitation wavelength is generally fixed in the ultraviolet (UV) region, and adapted to one or more chemical species. Selection by laser excitation is generally insufficient to observe a particular species of one element, but the use of tunable Optical Parametric Oscillator (OPO) allows to set an excitation wavelength in a range where a better signal from one kind of luminescent

species can be acquired.

Luminescence spectrum and decay time The luminescence spectra of actinides complexes are made up of bands that are more or less sensitive to their speciation. The decay time τ also varies depending on their chemical environment due to vibrational couplings with ligands which affect the rate of the de-excitation, more precisely the ratio between the radiative and non-radiative processes.

A change in the number of particles N , in the emitting state can be defined by using the first-order rate law for all processes which may occur after excitation:

$$\frac{dN}{dt} = -kN = -(k_r + k_{nr})N, \quad (1.2)$$

where k_r and k_{nr} correspond to the rate constants of the radiative and non-radiative processes, respectively. Since k determines the rate of all the processes in the system, the total decay time τ of the excited state is:

$$\tau = \frac{1}{k}. \quad (1.3)$$

In case when we have only radiative processes, $k = k_r$, thus $\tau = \tau_r$. Hence, the ratio of τ over τ_r will determine the quantum yield of radiative processes $\phi = \tau/\tau_r$. The decay time also allows to assess the number of luminescent species present in a sample, when admitting that each mono-exponential component of the luminescence decay reflects the luminescence of one single species.

Temporal resolution When the decay times are sufficiently distinct for different compounds, the discrimination of the species in solution is allowed by the choice of temporal parameters without any chemical separation. TRLFS is based on a pulsed laser excitation followed by temporal resolution of the luminescent signal that leads to the elimination of unwanted short decay time fluorescence.

The excitation source generates energy pulses at a given frequency. Each laser shot defines an initial time t_0 from which the total emitting signal is measurable in a time window Δt (Fig. 1.7).

When several species i are present, the curves obtained for a given wavelength λ are described using the relation:

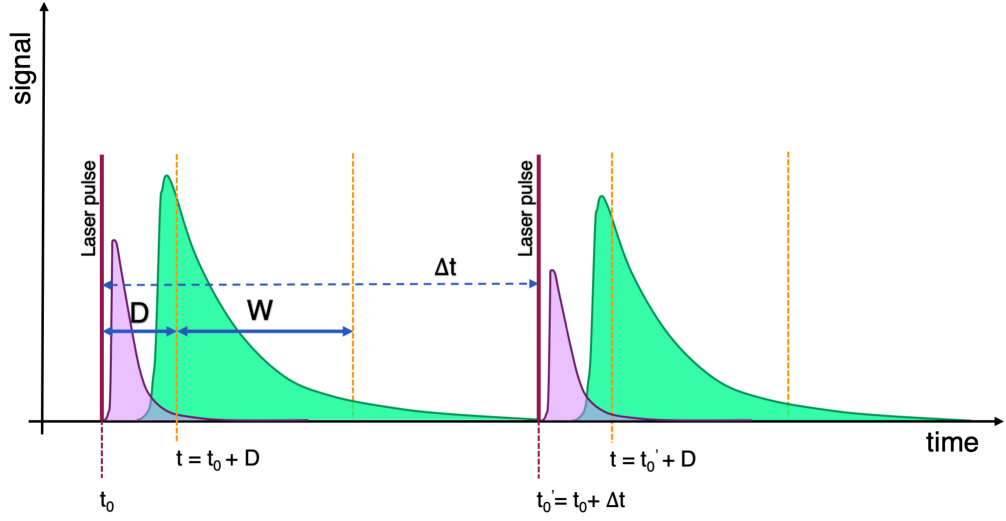


Figure 1.7: A temporal resolution principle used for the time-resolved laser-induced fluorescence spectroscopy measurements.

$$F_{\lambda}(t) = \sum_i F_{0,\lambda,i} \exp\left(-\frac{t}{\tau_i}\right), \quad (1.4)$$

where parameters $F_{0,\lambda,i}$ and τ_i are determined by fitting exponential functions on the luminescence decay curves. $F_{0,\lambda,i}$ is defined by the following expression:

$$F_{0,\lambda,i} = \kappa \times I^{\circ} t_{int} \times l \times \varepsilon_{\lambda_{exc},i} \times \phi_{\lambda,i} \times [i], \quad (1.5)$$

where κ is an apparatus constant, I° is the intensity of the incident light, t_{int} is the counting time, l is the optical path length, $\varepsilon_{\lambda_{exc},i}$ is the absorption extinction coefficient at a given excitation wavelength λ_{exc} , $\phi_{\lambda,i}$ is the quantum yield of species i at the wavelength λ and $[i]$ is the species concentration.

The detector is synchronized with the laser pulses so that the measuring gate, defined by a delay D , with respect to t_0 , and a width W (Fig. 1.7), can be chosen.

$$F(\lambda, D, W) = \sum_i F_{0,\lambda,i} \int_D^{D+W} \exp\left(-\frac{t}{\tau_i}\right) dt. \quad (1.6)$$

When two emitting species with the decay times τ_1 and τ_2 co-exist in one sample, with the conditions that τ_1 is lower compared to τ_2 , their signals can be

separated. While setting $D \approx 3\tau_1$, the emission from the species 1 is decreasing so to become negligible giving the possibility to measure only the luminescence from species 2. Accordingly, the luminescence intensity $F(\lambda, D, W)$ measured at the wavelength λ and for given W and D values, should be treated by the following equation[61]:

$$F(\lambda, D, W) = \kappa \times \sum_{s=0}^N \left[[S] \times f_s^0(\lambda) \times \exp\left(-\frac{D}{\tau_s}\right) \times \left(1 - \exp\left(-\frac{D}{\tau_s}\right)\right) \right], \quad (1.7)$$

where κ is the apparatus factor, N is a number of emitting species, τ_s is the decay time of the emitting species S , and $f_s^0(\lambda)$ is the molar fluorescence intensity of the species S at $D=0$.

1.3.2 Experimental set-up

The experimental studies were performed on 1–2 ml samples with a small amount of uranium ($10^{-5} - 10^{-6}$ M). The uranyl chloride and carbonate samples preparations are described in the corresponding Chapters 3 and 4. TRLFS requires a pulsed source for excitation, a mono- or polychromator, and a detection device that is synchronized with the laser pulses. The scheme of the used TRLFS technique is shown on Figure 1.8.

As the excitation source, a 355 nm tripled Nd:YAG laser (Surelite, Continuum, USA) delivering 170 mJ of energy is used with a 5–10 ns pulse at 10 Hz. After, an optical parametric oscillation (OPO) system (Horizon, Continuum, USA) was set to the visible light region to be able to excite uranium(VI) samples in the 400–450 nm range, where specific U(VI) absorption bands exist. The value of the excitation wavelength (λ_{ex}) is chosen to optimize the luminescence signal and corresponds to the maximum absorption of the U(VI) complexes. A sample is placed at the 1 cm quartz cell (QS101, Suprasil, Hellma Analytics). The sample holder is equipped with a controlled-temperature thermostat (Peter Huber Kältemaschinenbau AG, Germany) with circulating water in order to minimize the influence of the temperature on uranium(VI) luminescence. The luminescence signal is collected 90° from the axis of the incident beam and

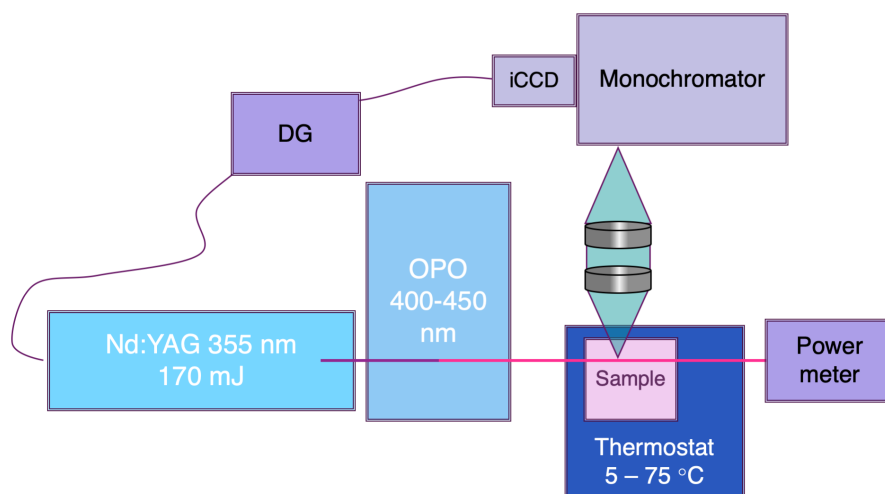


Figure 1.8: The scheme of the used TRLFS technique.

focused on the monochromator spectrometer (Acton SP-2358i, Roper Scientific) which can be set at 300, 600 or 1800 lines/mm grating depending on the desired wavelength envelope or resolution. To detect the time-resolved luminescence signal, an intensified CCD camera (iStar DH734-25F-03, Andor Technology, UK) cooled is used. The iCCD is cooled by the Peltier effect ($-10\text{ }^{\circ}\text{C}$) and synchronized to the laser pulses by the delay generator (DG). Since the settings of the gate width and delay time, the same as the number of acquisitions have an impact on the luminescence signal and are different for all uranyl complexes studied in this work. The used parameters are specified in the chapters discussing the results corresponding to each type of the studied uranyl(VI) complexes.

Bibliography of the current chapter

- (5) Denning, R. G. Electronic Structure and Bonding in Actinyl Ions and their Analogs. *Journal of Physical Chemistry A* **2007**, *111*, 4125–4143, DOI: 10.1021/jp071061n.
- (7) Denning, R.; Snellgrove, T.; Woodwark, D. The electronic structure of the uranyl ion: Part I. The electronic spectrum of Cs₂UO₂Cl₄. *Molecular Physics* **1976**, *32*, 419–442, DOI: 10.1080/00268977600103211.
- (9) Matsika, S.; Zhang, Z.; Brozell, S.; Blaudeau, J.-P.; Wang, Q.; Pitzer, R. Electronic structure and spectra of actinyl ions. *Journal of Physical Chemistry A* **2001**, *105*, 3825–3828, DOI: 10.1021/jp003085z.
- (10) Pierloot, K.; van Besien, E. Electronic structure and spectrum of UO₂²⁺ and UO₂Cl₄²⁻. *Journal of Chemical Physics* **2005**, *123*, 204309, DOI: 10.1063/1.2121608.
- (11) Katz, J. J., *The Chemistry of the Actinide and Transactinide Elements*, Fourth Edition; Springer Science & Business Media: 2007; Vol. 5.
- (16) Flint, C. D.; Tanner, P. A. Luminescence spectrum of Cs₂UO₂Cl₄. *Journal of the Chemical Society, Faraday Transactions 2: Molecular and Chemical Physics* **1978**, *74*, 2210–2217, DOI: 10.1039/F29787402210.
- (17) Wang, Z.; M. Zachara, J.; Liu, C.; Gassman, P.; R. Felmy, A.; B. Clark, S. A cryogenic fluorescence spectroscopic study of uranyl carbonate, phosphate and oxyhydroxide minerals. *Radiochimica Acta* **2008**, *96*, 591–598, DOI: 10.1021/es048448d.
- (18) Moulin, C.; Decambox, P.; Moulin, V.; Decaillon, J. G. Uranium Speciation in Solution by Time-Resolved Laser-Induced Fluorescence. *Analytical Chemistry* **1995**, *67*, 348–353, DOI: 10.1021/ac00098a019.
- (19) Moulin, C.; Decambox, P.; Mauchien, P. State of the art in time-resolved laser-induced fluorescence for actinides analysis: Applications and trends. *Journal of Radioanalytical and Nuclear Chemistry* **1997**, *226*, 135–138, DOI: 10.1007/BF02063637.
- (23) Görller-Walrand, C.; De Houwer, S.; Fluyt, L.; Binnemans, K. Spectroscopic properties of uranyl chloride complexes in non-aqueous solvents. *Physical Chemistry Chemical Physics* **2004**, *6*, 3292–3298, DOI: 10.1039/B317002K.
- (24) Van Besien, E.; Pierloot, K.; Görller-Walrand, C. Electronic spectra of uranyl chloride complexes in acetone: a CASSCF/CASPT2 investigation. *Physical Chemistry Chemical Physics* **2006**, *8*, 4311–4319, DOI: 10.1039/B607026D.

- (25) Réal, F.; Gomes, A. S. P.; Visscher, L.; Vallet, V.; Eliav, E. Benchmarking Electronic Structure Calculations on the Bare UO_2^{2+} Ion: How Different are Single and Multireference Electron Correlation Methods? *The Journal of Physical Chemistry A* **2009**, *113*, PMID: 19888775, 12504–12511, DOI: 10.1021/jp903758c.
- (26) Tecmer, P.; Gomes, A. S. P.; Ekström, U.; Visscher, L. Electronic spectroscopy of UO_2^{2+} , NUO^+ and NUN : an evaluation of time-dependent density functional theory for actinides. *Physical Chemistry Chemical Physics* **2011**, *13*, 6249–6259, DOI: 10.1039/C0CP02534H.
- (28) Valeur, B., *Molecular Fluorescence: Principles and Applications*, Publisher; Wiley: 2001, DOI: 10.1002/3527600248.
- (29) Zhang, Z.; Pitzer, R. M. Application of relativistic quantum chemistry to the electronic energy levels of the uranyl ion. *The Journal of Physical Chemistry A* **1999**, *103*, 6880–6886, DOI: 10.1021/jp991867q.
- (30) Nichols, E. L.; Howes, H. L.; Merritt, E.; Wilber, D. T.; Wick, F. G., *Fluorescence of the uranyl salts*; 298; Carnegie institution of Washington: 1919.
- (31) Dieke, G. H.; Duncan, A. B. F., *Spectroscopic properties of uranium compounds*; McGraw-Hill: 1949.
- (32) Kasha, M. Vibrational Fine Structure in the Absorption Spectra of Uranyl and Plutonyl Ions in Aqueous Solution. *The Journal of Chemical Physics* **1949**, *17*, 349–349, DOI: 10.1063/1.1747257.
- (33) Rabinowitch, E.; Belford, R. L., *Spectroscopy and photochemistry of uranyl compounds*; Pergamon Press: 1964; Vol. 1, DOI: 10.1002/ange.19650772125.
- (34) Irkhin, Y. P. Electron structure of the $4f$ shells and magnetism of rare-earth metals. *Soviet Physics Uspekhi* **1988**, *31*, 163–170, DOI: 10.1070/PU1988v031n02ABEH005700.
- (35) Mizokawa, T. Electronic structure of $5d$ transition-metal compounds. *Journal of Electron Spectroscopy and Related Phenomena* **2016**, *208*, 78–82, DOI: 10.1016/j.eispec.2015.12.005.
- (36) Veal, B.; Lam, D.; Carnall, W.; Hoekstra, H. X-ray photoemission spectroscopy study of hexavalent uranium compounds. *Physical Review B* **1975**, *12*, 5651–5663, DOI: doi.org/10.1103/PhysRevB.12.5651.

- (37) Vallet, V.; Wahlgren, U.; Grenthe, I. Probing the nature of chemical bonding in uranyl (VI) complexes with quantum chemical methods. *The Journal of Physical Chemistry A* **2012**, *116*, 12373–12380, DOI: 10.1021/jp3091123.
- (38) Di Pietro, P.; Kerridge, A. U–Oyl Stretching Vibrations as a Quantitative Measure of the Equatorial Bond Covalency in Uranyl Complexes: A Quantum-Chemical Investigation. *Inorganic Chemistry* **2016**, *55*, 573–583, DOI: 10.1021/acs.inorgchem.5b01219.
- (39) Hennig, C.; Servaes, K.; Nockemann, P.; Van Hecke, K.; Van Meervelt, L.; Wouters, J.; Fluyt, L.; Görrler-Walrand, C.; Van Deun, R. Species Distribution and Coordination of Uranyl Chloro Complexes in Acetonitrile. *Inorganic Chemistry* **2008**, *47*, 2987–2993, DOI: 10.1021/ic7014435.
- (40) Eliet, V.; Grenthe, I.; Bidoglio, G. Time-resolved laser-induced fluorescence of uranium(VI) hydroxo-complexes at different temperatures. *Applied spectroscopy* **2000**, *54*, 99–105, DOI: 10.1366/0003702001948178.
- (41) Demnitz, M.; Hilpmann, S.; Lösch, H.; Bok, F.; Steudtner, R.; Patzschke, M.; Stumpf, T.; Huittinen, N. Temperature-dependent luminescence spectroscopic investigations of uranyl(VI) complexation with the halides F^- and Cl^- . *Dalton Transactions* **2020**, *49*, 7109–7122, DOI: 10.1039/D0DT00646G.
- (42) Matsika, S.; Pitzer, R. M. Actinyl Ions in $Cs_2UO_2Cl_4$. *Journal of Physical Chemistry A* **2001**, *105*, 637–645, DOI: 10.1021/jp003032h.
- (43) Pierloot, K.; van Besien, E.; van Lenthe, E.; Baerends, E. J. Electronic spectrum of UO_2^{2+} and $[UO_2Cl_4]^{2-}$ calculated with time-dependent density functional theory. *Journal of Chemical Physics* **2007**, *126*, 194311, DOI: 10.1063/1.2735297.
- (44) Réal, F.; Vallet, V.; Marian, C.; Wahlgren, U. Theoretical investigation of the energies and geometries of photoexcited uranyl(VI) ion: A comparison between wave-function theory and density functional theory. *The Journal of Chemical Physics* **2007**, *127*, 214302, DOI: 10.1063/1.2814157.
- (45) Gomes, A. S. P.; Jacob, C. R.; Réal, F.; Visscher, L.; Vallet, V. Towards systematically improvable models for actinides in condensed phase: the electronic spectrum of uranyl in $Cs_2UO_2Cl_4$ as a test case. *Physical Chemistry Chemical Physics* **2013**, *15*, 15153–15162, DOI: 10.1039/C3CP52090K.
- (46) Bartlett, J. R.; Cooney, R. P. On the determination of uranium-oxygen bond lengths in dioxouranium (VI) compounds by Raman spectroscopy. *Journal of Molecular Spectroscopy* **1989**, *193*, 295–300, DOI: 10.1016/0022-2860(89)80140-1.

- (47) Mauchien, P. *Dosage de l'uranium par spectrofluorimétrie à source d'excitation laser*; tech. rep.; CEA-R-5300, 1983.
- (48) Berthoud, T.; Decambox, P.; Kirsch, B.; Mauchien, P.; Moulin, C. Direct determination of traces of lanthanide ions in aqueous solutions by laser-induced time-resolved spectrofluorimetry. *Analytica Chimica Acta* **1989**, *220*, 235–241, DOI: 10.1016/S0003-2670(00)80266-4.
- (49) Decambox, P.; Mauchien, P.; Moulin, C. Direct trace determination of curium by laser-induced time-resolved spectrofluorometry. *Radiochimica Acta* **1989**, *48*, 23–28, DOI: 10.1524/ract.1989.48.12.23.
- (50) Kimura, T.; Nagaishi, R.; Kato, Y.; Yoshida, Z. Luminescence study on solvation of americium (III), curium (III) and several lanthanide (III) ions in nonaqueous and binary mixed solvents. *Radiochimica Acta* **2001**, *89*, 125–130, DOI: 10.1524/ract.2001.89.3.125.
- (51) Eliet, V.; Bidoglio, G.; Omenetto, N.; Parma, L.; Grenthe, I. Characterisation of hydroxide complexes of uranium(VI) by time-resolved fluorescence spectroscopy. *Journal of the Chemical Society, Faraday Transactions* **1995**, *91*, 2275–2285, DOI: 10.1039/FT9959102275.
- (52) Fanghänel, T.; Kim, J.; Paviet, P.; Klenze, R.; Hauser, W. Thermodynamics of radioactive trace elements in concentrated electrolyte solutions: hydrolysis of Cm^{3+} in NaCl-solutions. *Radiochimica Acta* **1994**, *66*, 81–88, DOI: 10.1524/ract.1994.6667.special-issue.81.
- (53) Geipel, G. Some aspects of actinide speciation by laser-induced spectroscopy. *Coordination Chemistry Reviews* **2006**, *250*, 844–854, DOI: 10.1016/j.ccr.2005.11.007.
- (54) Moulin, C.; Amekraz, B.; Doizi, D.; Plancque, G.; Steiner, V. Speciation of lanthanides and actinides by time-resolved laser-induced fluorescence (TRLIF) and electrospray mass spectrometry (ES-MS) from the geosphere to the biosphere. *Journal of Inorganic Biochemistry* **2001**, *86*, 347–347.
- (55) Stumpf, T.; Fanghänel, T.; Grenthe, I. Complexation of trivalent actinide and lanthanide ions by glycolic acid: a TRLFS study. *Journal of the Chemical Society, Dalton Transactions* **2002**, 3799–3804, DOI: 10.1039/B204679B.
- (56) Vercouter, T.; Vitorge, P.; Amekraz, B.; Giffaut, E.; Hubert, S.; Moulin, C. Stabilities of the Aqueous Complexes $\text{Cm}(\text{CO}_3)_3^{3-}$ and $\text{Am}(\text{CO}_3)_3^{3-}$ in the Temperature Range 10–70 °C. *Inorganic Chemistry* **2005**, *44*, 5833–5843, DOI: 10.1021/ic050214n.

- (57) Moll, H.; Geipel, G.; Brendler, V.; Bernhard, G.; Nitsche, H. Interaction of uranium(VI) with silicic acid in aqueous solutions studied by time-resolved laser-induced fluorescence spectroscopy (TRLFS). *Journal of Alloys and Compounds* **1998**, *271*, 765–768, DOI: 10.1016/S0925-8388(98)00203-5.
- (58) Kirishima, A.; Kimura, T.; Tochiyama, O.; Yoshida, Z. Speciation study on complex formation of uranium(VI) with phosphate and fluoride at high temperatures and pressures by time-resolved laser-induced fluorescence spectroscopy. *Radiochimica Acta* **2004**, *92*, 889–896, DOI: 10.1524/ract.92.12.889.55111.
- (59) Kirishima, A.; Kimura, T.; Tochiyama, O.; Yoshida, Z. Speciation study on uranium (VI) hydrolysis at high temperatures and pressures. *Journal of Alloys and Compounds* **2004**, *374*, 277–282, DOI: 10.1016/j.jallcom.2003.11.105.
- (60) Geipel, G.; Bernhard, G.; Rutsch, M.; Brendler, V.; Nitsche, H. Spectroscopic properties of uranium(VI) minerals studied by time-resolved laser-induced fluorescence spectroscopy (TRLFS). *Radiochimica Acta* **2000**, *88*, 757–762, DOI: 10.1524/ract.2000.88.9-11.757.
- (61) In *Laser Spectroscopy for Sensing*, Baudelet, M., Ed.; Woodhead Publishing: 2014, pp xv–xix, DOI: 10.1016/B978-0-85709-273-1.50022-2.

Theoretical methods

The modelling of the luminescence of uranyl compounds requires the precise determination of electronic transitions between low-lying excited states and the ground state, accounting for the vibronic progression. As explained in Chapter 1, uranyl luminescence is characterized by the emission bands related to the vibronic spectrum. A well-established way for such calculations is to use Franck-Condon principle in the harmonic approximation, that will be presented in the beginning of this chapter. This requires to compute equilibrium geometries, harmonic frequencies, and normal mode vectors for both the ground and luminescent states. The emission energies are also necessary to predict for the determination of the “hot band” position, i.e. the vertical emission from the vibronically-excited luminescent state, as well as the spectral origin on the energy scale. These data can be obtained by using quantum chemical methods. When dealing with actinides that contain a high number of electrons to consider, the inclusion of relativistic effects is crucial. In this chapter, the quantum chemical methods as well as density functional theory in a non-relativistic framework will be presented. Then, the relativistic Dirac equation will be introduced along with relativistic approximations, such as the two component zero-order regular approximation, and the definition of relativistic effective core potentials. The concepts of basis sets and solvation models will be presented at the end of this chapter.

2.1 Franck-Condon principle in the harmonic approximation

The excitation and deexcitation of an electron out of an occupied orbital is a very fast process compared to the time of molecular vibrations. According to the Born-Oppenheimer approximation [62], the motions of electrons are indeed much more rapid than those of the nuclei (see Section 2.2.2). Transitions occur when the nuclear distances are equal to the equilibrium bond lengths of the molecule in its electronic ground state. Thus during the electronic excitation, the positions of the nuclei are unchanged and they do not accelerate until the moment of the intersection of the vertical transition line with the potential energy curve of another electronic state. At this stage, the transition is considered complete and the molecule begins to vibrate at an energy of the line-curve intersection producing a vibronic spectrum (Fig. 2.1). The same applies for deexcitation by luminescence towards the different vibronic levels of the electronic ground state. In these cases, the Franck-Condon principle [63] applies: an electronic transition is most likely to occur without changes in the position of the nuclei in the molecular entity and its environment.

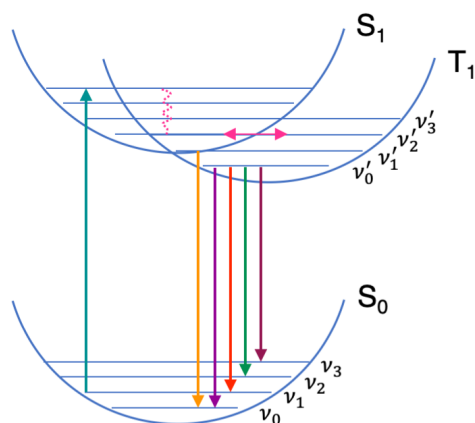


Figure 2.1: Franck-Condon principle energy diagram. The S_0 corresponds to the ground state potential energy curve, while S_1 and T_1 represent first singlet and triplet states, respectively.

In the quantum mechanical description, the wave function is described by the product of an electronic ψ and a vibrational χ wave function. The probability of an electronic transition between two states equals to:

$$|\langle \psi' \chi' | M | \psi'' \chi'' \rangle|^2 \quad (2.1)$$

where $\psi'' \chi''$ and $\psi' \chi'$ correspond to initial and final states, respectively. Since the transition operator M only depends on the electronic component, the nuclear part can be separated and the previous expression can be rewritten as the product of two terms:

$$|\langle \psi' | M | \psi'' \rangle|^2 |\langle \chi' | \chi'' \rangle|^2 \quad (2.2)$$

where the second term is called the Franck-Condon factor (FCF) and corresponds to the intensity of a vibronic transition.

In the harmonic approximation, the vibrational wave functions are products of one-dimensional harmonic oscillator wave functions. In the case where the normal coordinates of the initial and final states are assumed to be the same, the multidimensional Franck-Condon factors are simply the products of one-dimensional FCFs and can be evaluated analytically. But in the other cases, where the normal modes of both states are significantly different (non-parallel), and the coordinates of the vibrational wave functions of the two electronic states are different, the full FCFs cannot be represented by the products of one-dimensional integrals. This is supposedly the case for our systems of interest with a large number of normal modes N ($N = 3K - 6$, for non-linear molecules with K atoms). In the Chapters 3 and 5 we will be dealing with large uranyl complexes where the probability to have non-parallel normal modes in the ground and luminescence state is high. Hence, the multidimensional Franck-Condon factors will be necessarily evaluated taking into account Duschinsky rotations [64, 65] as described in the following section.

2.1.1 Duschinsky rotations

In a molecule, the normal modes of the initial and final states, noted \vec{Q}'' and \vec{Q}' , respectively, are linked through the Duschinsky transformation (Fig. 2.2) [66]:

$$\vec{Q}' = S \cdot \vec{Q}'' + \vec{d} \quad (2.3)$$

with the normal mode rotation matrix $S[N \times N]$ and the vector of displacements $\vec{d}[N]$ along the normal coordinates equal to:

$$S = L'^T L'' \quad (2.4)$$

$$\vec{d} = L'^T \sqrt{T} (\vec{x}'' - \vec{x}') \quad (2.5)$$

where $L''[N \times 3K]$ and $L'[N \times 3K]$ are rectangular matrices composed of N mass-weighted normal vectors of the initial and final states respectively; $\vec{x}''[3K]$ and $\vec{x}'[3K]$ are the Cartesian geometries vectors; and $T[3K \times 3K]$ is a diagonal matrix composed of the atomic masses.

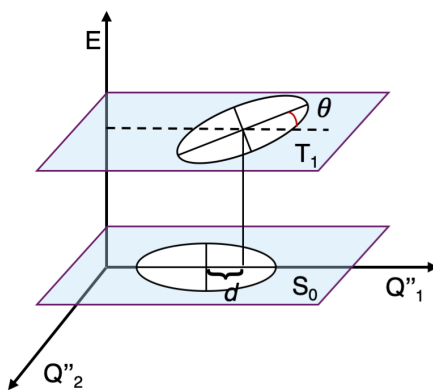


Figure 2.2: Schematic two-dimensional description of Duschinsky rotation potential energy surface.

The overlap integral (FCF) between the ground vibrational states of the initial and final electronic states is given by [64]:

$$\langle \chi' | \chi'' \rangle = \frac{2^{N/2}}{\sqrt{\det(S)}} \left[\prod_{\eta=1}^N \left(\frac{\omega'_\eta}{\omega''_\eta} \right)^{1/4} \sqrt{\det(Q)} \left[e^{-1/2 \vec{\delta}^T (1-P) \vec{\delta}} \right] \right] \quad (2.6)$$

where ω''_η and ω'_η are the frequencies of the η -th normal mode of the initial and final states, respectively. The matrices P and Q are equal to:

$$P = JQJ^T \quad (2.7)$$

$$Q = (1 - J^T J)^{-1} \quad (2.8)$$

with

$$J = \lambda' S \lambda''^{-1} \quad (2.9)$$

$\vec{\delta}$ is a vector $[N]$ equal to the displacement vector \vec{d} corrected by the diagonal matrix λ of a corresponding state:

$$\vec{\delta} = \lambda' \vec{d} \quad (2.10)$$

$$\lambda' = \text{diag}\{\sqrt{\omega'_1}, \sqrt{\omega'_2}, \dots, \sqrt{\omega'_N}\} \quad (2.11)$$

$$\lambda'' = \text{diag}\{\sqrt{\omega''_1}, \sqrt{\omega''_2}, \dots, \sqrt{\omega''_N}\} \quad (2.12)$$

The Franck-Condon factors for the transitions from the ground vibrational state of the initial electronic state are calculated recursively from the $\langle \chi' | \chi'' \rangle$ integral by the differentiation of Eq. 2.6 with respect to the coherent initial and final states $\langle \gamma | \alpha \rangle$. The coherent states are defined as the eigenstates of all the annihilation operators ¹, and realize the basis of the dynamical group representation space along with the vibrational states. The final form of these equations depends on the molecule's properties such as symmetry, type of transition, vibrational modes and also on the vibrational quantum number. The derivation can be found in the work of Doktorov et al. [67, 68].

The “hot band,” which is basically the transition between the two vibrationally excited electronic states, i.e. neither is the overall ground state (orange

¹an operator which lowers the number of particles in a given electronic state by one

line on Fig. 2.1) [69], also can be predicted from the FCF integrals. However, the experimental “hot band” intensity depends on many side factors (mainly quenching effects) that cannot be included in this theoretical model. Since the used methodology for FCFs calculations only relies on static but not on dynamic parameters, the “hot band” intensity will not be correct, in our specific case of the uranyl complexes. For those who are interested in the methodology of “hot band” computations, we refer to the work of Berger et al. [64].

2.2 Introduction to Quantum chemistry

2.2.1 The Schrödinger equation

The time-dependent Schrödinger equation [70], describes the evolution of the electronic wave function with time and represents the fundamental quantum mechanical equation of physics and chemistry:

$$\hat{H}\psi = i\hbar\frac{\partial\psi}{\partial t} \quad (2.13)$$

where $\psi(t)$ is the wave function of the state under consideration (ground or excited state), \hat{H} is the Hamiltonian operator, i is the imaginary number and \hbar is the Planck constant divided by 2π . When the system is considered to be stationary at a moment t [71], the equation becomes as an eigenvalue equation which is independent of time:

$$\hat{H}(\mathbf{r}, \mathbf{R})\psi(\mathbf{r}, \mathbf{R}) = E\psi(\mathbf{r}, \mathbf{R}) \quad (2.14)$$

where $\psi(\mathbf{r}, \mathbf{R})$ is the wave function of the system, in our case of electrons at the positions $\{\mathbf{r} = \mathbf{r}_1, \dots, \mathbf{r}_n\}$ and nuclei at the positions $\{\mathbf{R} = \mathbf{R}_1, \dots, \mathbf{R}_N\}$ and E being the total energy. The \hat{H} Hamiltonian for a molecule is written as:

$$\hat{H} = -\sum_i \frac{1}{2} \nabla_i^2 - \sum_A \frac{1}{2M_A} \nabla_A^2 - \sum_{i,A} \frac{Z_A}{r_{iA}} + \frac{1}{2} \sum_{i \neq j} \frac{1}{r_{ij}} + \frac{1}{2} \sum_{A \neq B} \frac{Z_A Z_B}{R_{AB}} \quad (2.15)$$

where i and j are indices running over the electrons, while A and B are related to the nuclei; r_{ij} is the distance between the i and j electrons, r_{iA} is the distance between electron i and the corresponding nucleus A , and R_{AB} corresponds to the distance between two nuclei. The atomic number and atomic mass of a nucleus A are denoted as Z_A and M_A , respectively. In equation 2.15, the first two terms represent the kinetic energy operators of the electrons and nuclei, respectively, while the last three terms are the standard Coulomb interaction potential operators for electron-nucleus, electron-electron and nucleus-nucleus interactions, respectively.

2.2.2 Born-Oppenheimer approximation

As the difference in mass and velocity between the electrons and a nucleus is large, it is possible to decouple the Hamiltonian as a sum of the electronic \hat{H}^{el} and the nuclear \hat{H}^{nuc} Hamiltonians:

$$\hat{H} = \hat{H}^{el} + \hat{H}^{nuc} \quad (2.16)$$

In the Born-Oppenheimer approximation [62], the exact wave function then can be approximated as a product of an electron and a nuclear part:

$$\psi(\mathbf{r}, \mathbf{R}) = \psi_{\mathbf{R}}^{el}(\mathbf{r})\psi^{nuc}(\mathbf{R}) \quad (2.17)$$

The term describing the nuclear kinetic energy in equation 2.15 can be neglected; thus the electronic Hamiltonian can be defined as:

$$\hat{H}^{el} = \hat{T} + \hat{W} + \hat{V} \quad (2.18)$$

where \hat{T} is a electronic kinetic energy operator:

$$\hat{T} = \sum_{i=1}^N \left(-\frac{1}{2} \nabla_i^2 \right) \quad (2.19)$$

and \hat{W} is the two-electron operator:

$$\hat{W} = \sum_i^N \sum_{j<i}^N \left(\frac{1}{|r_i - r_j|} \right) \quad (2.20)$$

which is describing the Coulomb interaction between electrons i and j . \hat{V} represents some external potential:

$$\hat{V} = \sum_{i=1}^N v(\mathbf{r}_i) \quad (2.21)$$

In the Born-Oppenheimer approximation, the nuclear interaction term is found to be constant in the total energy calculation. Therefore the problem can be reduced to the search of the electronic wave function which depends on the position of the electrons, and parametrically on the positions of the nuclei. The electrons evolve on a potential energy surface (PES), which energy at every nuclei positions, $E_{\mathbf{R}}^{el}$, can be obtained by solving the following equation:

$$\hat{H}^{el} \psi_{\mathbf{R}}^{el} = E_{\mathbf{R}}^{el} \psi_{\mathbf{R}}^{el} \quad (2.22)$$

Despite this simplification, the solution of the Schrödinger equation is still complex, due to the electrostatic interaction term which involves the coordinates of two electrons. Thus, the methods presented further down, referred to as electronic structure methods, have a purpose of solving this eigenvalue problem.

2.2.3 Constraints on the Wave function

The first hypothesis to solve Eqn. 2.22 is to simplify the complex interactions of a many-electron system by considering the electrons as independent particles. Hence the n-particle wave function can be written as the product of N-particle orbitals ϕ (more details in Section 2.5):

$$\psi(\mathbf{r}_1, \dots, \mathbf{r}_N) = \phi_1(\mathbf{r}_1) \dots \phi_N(\mathbf{r}_N) \quad (2.23)$$

As a fermion with spin 1/2, the electron obeys the Pauli exclusion princi-

ple [72], stating that two identical fermions cannot occupy the same quantum state simultaneously, and therefore the wave function describing the system must be antisymmetric with respect to the exchange of two electrons because of their indistinguishability (*i.e.* they differ by a quantum number):

$$\psi(i, j) = -\psi(j, i) \quad (2.24)$$

A trial wave function that satisfies this requirement is the Slater determinant [73] composed of orthonormal spin orbitals:

$$\psi(\mathbf{r}_1, \mathbf{r}_2, \dots, \mathbf{r}_N) = \frac{1}{\sqrt{N!}} \begin{vmatrix} \phi_1(\mathbf{r}_1) & \phi_1(\mathbf{r}_2) & \cdots & \phi_1(\mathbf{r}_N) \\ \phi_2(\mathbf{r}_1) & \phi_2(\mathbf{r}_2) & \cdots & \phi_2(\mathbf{r}_N) \\ \vdots & \vdots & \vdots & \vdots \\ \phi_n(\mathbf{r}_1) & \phi_n(\mathbf{r}_2) & \cdots & \phi_n(\mathbf{r}_N) \end{vmatrix} \quad (2.25)$$

with the spin orbitals in a row and the electron coordinates in a column. $\frac{1}{\sqrt{N!}}$ is a normalization constant. The limitation of the single determinant model is that it does not adequately describe the global electronic structure and the effect on this structure from instantaneous repulsion between the electrons. The energy that is not recovered, is called correlation energy. Different approaches have been developed to extend the independent particle model, and account for the correlation energy. Methods based on the Wave Function Theory (WFT) will not be detailed here since they are much too expensive for the modeling of the actinides complexes of a big size. We rather focus on Density Functional Theory (DFT), which appeared more appropriate for our calculations.

2.3 Density functional theory

The electronic wave function $\psi(\mathbf{r})$ is a function of $3N$ coordinates (where N is a number of electrons in a system), thus the solution of the Eq. 2.22 can require a high computational cost for large systems and especially for molecules containing heavy elements. The Density Functional Theory (DFT) can be used to obtain an energy of the molecule's ground state. The total electron density $\rho(\mathbf{r})$ [74] can describe the electronic structure of a molecule instead of its wave function.

By using the Thomas-Fermi theorem [75, 76], Hohenberg and Kohn [77] have shown that the exact energy of the ground state in an external potential is a function of the density $F[\rho(\mathbf{r})]$:

$$E[\rho(\mathbf{r})] = F[\rho(\mathbf{r})] + \int \rho(\mathbf{r})v(\mathbf{r})d\mathbf{r} \quad (2.26)$$

where v is the Coulomb attraction between the nuclei and the electrons. ρ , the total electron density of N electrons is defined as:

$$\rho(\mathbf{r}_1) = N \int d\mathbf{r}_2 \dots d\mathbf{r}_N d\sigma_1 \dots d\sigma_N |\psi(\mathbf{r}_1\sigma_1 \mathbf{r}_2\sigma_2, \dots, \mathbf{r}_N\sigma_N)|^2 \quad (2.27)$$

where the integration is carried out over all spin and spatial coordinates apart from one set of spatial coordinates, which was taken to be that of electron 1.

$F[\rho(\mathbf{r})]$ is a universal functional of the total electron density that corresponds to the sum of the kinetic energy term $T[\rho(\mathbf{r})]$ and the electron energy functional $E_{ee}[\rho(\mathbf{r})]$:

$$F[\rho(\mathbf{r})] = T[\rho(\mathbf{r})] + E_{ee}[\rho(\mathbf{r})] \quad (2.28)$$

2.3.1 The Kohn-Sham equation

The Hohenberg-Kohn theorem has proven the existence of the functional of a density, but not its solution. Within a year, the solution has been proposed by Kohn and Sham (KS) [78]. It is based on the assumption of a reference system of non-interacting electrons with an external potential v_s chosen in a way that its electron density equals the electron density of the fully interacting system. The Hamiltonian of the non-interacting reference system is then written as:

$$\hat{H} = - \sum_{i=1}^N \frac{1}{2} \nabla_i^2 + \sum_{i=1}^N v_s(\mathbf{r}_i) \quad (2.29)$$

The KS ground-state solution can be expressed as a single Slater determinant constructed from the so-called KS orbitals $\{\phi_i\}$, which are solutions of the following

eigenvalue problem:

$$\left(-\frac{1}{2}\nabla_i^2 + v_s(\mathbf{r})\right)\phi_i(\mathbf{r}) = \epsilon_i\phi_i(\mathbf{r}) \quad (2.30)$$

where ϕ_i is a single-particle function of the non-interacting reference system. The KS potential $v_s(\mathbf{r})$ is defined as:

$$v_s(\mathbf{r}) = v_{ext}(\mathbf{r}) + v_H(\mathbf{r}) + v_{xc}(\mathbf{r}) \quad (2.31)$$

where the $v_{ext}(\mathbf{r})$ is the external potential resulting from the electron-nucleus interaction [79], but might also include contributions from other external potentials. $v_H(\mathbf{r})$ and $v_{xc}(\mathbf{r})$ are the Hartree and exchange-correlation potentials respectively,

$$v_H(\mathbf{r}) = \frac{\delta J[\rho(\mathbf{r})]}{\delta\rho(\mathbf{r})} \quad (2.32)$$

$$v_{xc}(\mathbf{r}) = \frac{\delta E_{xc}}{\delta\rho(\mathbf{r})} \quad (2.33)$$

As the KS potential (Eq. 2.31) depends on the KS orbitals, Eq. 2.30 needs to be solved by a self-consistent procedure until convergence is reached.

According to the KS formalism, the total energy functional $E[\rho(\mathbf{r})]$ is written as:

$$E[\rho(\mathbf{r})] = v^{nuc}(\mathbf{R}) + \int d\mathbf{r}\rho(\mathbf{r})v(\mathbf{r}) + T_s[\rho(\mathbf{r})] + J[\rho(\mathbf{r})] + E_{xc}[\rho(\mathbf{r})] \quad (2.34)$$

where $v^{nuc}(\mathbf{R})$ is the nuclear repulsion energy, with \mathbf{R} the electron-nucleus distance. $T_s[\rho(\mathbf{r})]$ represents the kinetic energy of the reference non-interacting system, with density $\rho(\mathbf{r})$:

$$T_s[\rho(\mathbf{r})] = \sum_{i=1}^N \langle \phi_i | -\frac{1}{2}\nabla_i^2 | \phi_i \rangle \quad (2.35)$$

$J[\rho(\mathbf{r})]$ is the classical Coulomb repulsion energy:

$$J[\rho(\mathbf{r})] = \frac{1}{2} \int \int d\mathbf{r}_1 d\mathbf{r}_2 \frac{\rho(\mathbf{r}_1)\rho(\mathbf{r}_2)}{|\mathbf{r}_1 - \mathbf{r}_2|} \quad (2.36)$$

The last term in Eq. 2.34 is the exchange-correlation energy $E_{xc}[\rho(\mathbf{r})]$, that includes both the difference of kinetic energy between a system of interacting electrons and non-interacting KS electrons, and the difference between the electron-electron interaction in quantum mechanics and the classical Coulomb interaction (exchange and correlation):

$$E_{xc}[\rho(\mathbf{r})] = T[\rho(\mathbf{r})] - T_s[\rho(\mathbf{r})] + E_{ee}[\rho(\mathbf{r})] + J[\rho(\mathbf{r})] \quad (2.37)$$

Making use of the last equation, the density dependent functional $F[\rho(\mathbf{r})]$ can be rewritten as:

$$F[\rho(\mathbf{r})] = T_s[\rho(\mathbf{r})] + E_{xc}[\rho(\mathbf{r})] \quad (2.38)$$

The Kohn-Sham formalism has key advantages allowing to solve the time-independent Schrödinger equation for heavy elements and large molecules with less computational cost because 1) the density of the non-interacting system equals the density of the interacting one, and 2) the evaluation of the kinetic energy of a single-particle can occur through the set of orbitals which contain the largest part of the kinetic energy of the fully interacting system. However, DFT calculations directly depend on the exchange-correlation energy, $E_{xc}[\rho(\mathbf{r})]$, which has no exact mathematical expression. A number of approximations have been proposed, and adapted for different quantum chemical systems or certain set of properties [74]. The approximations and functionals applied for our spectroscopic study of uranyl complexes will be discussed in Section 2.3.3.

2.3.2 Time-Dependent density functional theory

To describe the physical and chemical properties that involve electronic excitation the standard KS-DFT is limited, as it describes only a static picture of the system. The ground-state DFT formalism has been extended to its time-dependent variant—time-dependent density functional theory (TD-DFT). As for DFT, this method has some advantages with respect to the size of the studied system, but one should be careful while applying it for the computation of excited-state properties. TD-DFT basically allows one to access single excitations, but may not be reliable to describe doubly and highly excited states,

multiconfigurational and charge transfer states. All these are mainly related to the shortcomings of the exchange-correlation functional approximations and to date, no functional is able to solve them simultaneously. As discussed in Chapter 1, the excited states of uranyl complexes arise from single excitations, where one electron is promoted from a doubly occupied orbital into the low-lying unoccupied ones. These transitions have a local character partly mixed with a charge transfer from the bonding orbitals of the ligands to the non-bonding orbitals of U(VI). Knowing this background information, one can conclude that in this particular case, the TD-DFT in combination with a proper exchange-correlation functional, shall be able to predict the excited states with a sufficient accuracy.

The TD-DFT is applied to the situations where the system in its ground state is exposed to a time-dependent perturbation modifying its external potential. An overview of the fundamental TD-DFT is well discussed in Ref. [80]. In the time-dependent Schrödinger equation 2.13, the external potential in the electronic Hamiltonian is substituted by the time-dependent potential:

$$\hat{H}^{el}(t) = \hat{T} + \hat{W} + \hat{V}(t) \quad (2.39)$$

where the first two operators are identical to Eqs. 2.19 and 2.20, while the time-dependent potential reads

$$\hat{V}(t) = \sum_{i=1}^N v(\mathbf{r}_i, t) \quad (2.40)$$

Using a similar proof to the Hohenberg and Kohn theorem for the ground state, Runge and Gross have demonstrated the existence of a correlation between the time-dependent electron density $\rho(\mathbf{r}, t)$ and the time-dependent external potential $v(\mathbf{r}, t)$ [81]. As a result the total time-dependent wave function is unique to within a phase factor:

$$\tilde{\psi}(\mathbf{r}, t) = e^{-i\beta(t)} \psi[\rho, \psi_0](t) \approx e^{-i\beta(t)} \psi[\rho](t) \quad (2.41)$$

where ψ_0 is a stationary ground state completely determined by the ground-state density. The elimination of ψ_0 from Eq. 2.41 and the inclusion of vector

potentials lead to an extension of DFT to TD-DFT [82].

Since the TD-DFT is not following the self-consistent field procedure, the second Hohenberg-Kohn theorem cannot be applied directly, and the energy functional has been replaced by the action functional written there in its alternative form [83]:

$$A[\rho(\mathbf{r}, t)] = B[\rho(\mathbf{r}, t)] - \int_{t_0}^{t_1} dt \int d\mathbf{r} v(\mathbf{r}, t) \rho(\mathbf{r}, t) \quad (2.42)$$

where t_0 and t_1 are the beginning and the end of the time step and $B[\rho(\mathbf{r}, t)]$ is a functional independent of the external potential:

$$B[\rho(\mathbf{r}, t)] = \int_{t_0}^{t_1} dt \langle \psi[\rho](t) | i \frac{\partial}{\partial t} - \hat{T} - \hat{W} | \psi[\rho](t) \rangle \quad (2.43)$$

where used $\psi[\rho](t)$ comes from Eq. 2.41.

The minimization of the action functional defined in Eq. 2.42 leads to the time-dependent Kohn-Sham equation (KS-TD):

$$\left[-\frac{1}{2} \nabla^2 + v_s(\mathbf{r}, t) \right] \phi_i(\mathbf{r}, t) = i \frac{\partial}{\partial t} \phi_i(\mathbf{r}, t) \quad (2.44)$$

where the first term is the kinetic energy operator and the $v_s(\mathbf{r}, t)$ is the time-dependent effective potential of non-interacting particles:

$$v_s(\mathbf{r}, t) = v_{ext}(\mathbf{r}, t) + v_{SCF}(\mathbf{r}, t) \quad (2.45)$$

$v_{ext}(\mathbf{r}, t)$ corresponds to the external potential which is composed of a stationary and time-dependent part, the latter being usually treated in a perturbative manner. The second term $v_{SCF}(\mathbf{r}, t)$ is the self-consistent field potential:

$$v_{SCF}(\mathbf{r}, t) = \int d\mathbf{r}' \frac{\rho(\mathbf{r}', t)}{|\mathbf{r} - \mathbf{r}'|} + v_{xc}(\mathbf{r}, t) \quad (2.46)$$

where the first term is the Coulomb potential and $v_{xc}(\mathbf{r}, t)$ is the time-dependent

exchange-correlation kernel evaluated for the ground-state density [80]:

$$v_{xc}(\mathbf{r}, t) = \left. \frac{\delta A_{xc}}{\delta \rho(\mathbf{r}', t)} \right|_{\rho(\mathbf{r}, t)} \quad (2.47)$$

As the functional A_{xc} is unknown, it needs to be approximated. In the limit of an external potential which varies slowly in time, it reduced to:

$$A_{xc} = \int_{t_0}^{t_1} E_{xc}[\rho_t] dt \quad (2.48)$$

where E_{xc} is the exchange-correlation functional of stationary DFT and ρ_t denotes density evaluated at time t . It is called the adiabatic approximation and is a local approximation in time used to determine the response of the charge density through the exchange-correlation potential.

In this thesis, to study the vertical excitation and emission energies in the TD-DFT formalism, the use of the linear response (LR) regime is required. If we split the time-dependent external potential into a static term and time-dependent perturbation term, then the theory can be split into an ordinary static DFT and a LR theory to the limit of small time-dependent perturbations. Basically, we compute first the KS energies, wave functions and the ground-state electronic density and then we do a LR-TDDFT calculation of the density variation $\delta\rho(\mathbf{r}, t)$ corresponding to the external time-dependent perturbation $\delta v(\mathbf{r}, t)$. From $\delta\rho(\mathbf{r}, t)$ we can calculate the polarizability χ of the system defined as the LR coefficient $\delta\rho = \chi\delta v$ of the density with respect to the external potential. The polarizability is a fundamental quantity and contains the excitation energies of the system.

To study excitation it is convenient to switch from the time space to the frequency ω -space. After a Fourier transformation, all the convolution products in time space become direct products in frequency space. In the notation proposed by Casida *et al.* [81], the excitation or emission energies are the solutions of the generalized eigenvalue problem:

$$\begin{pmatrix} A & B \\ B^* & A^* \end{pmatrix} \begin{pmatrix} X \\ Y \end{pmatrix} = \omega \begin{pmatrix} 1 & 0 \\ 0 & -1 \end{pmatrix} \begin{pmatrix} X \\ Y \end{pmatrix} \quad (2.49)$$

with

$$A_{ia,jb} = \delta_{ij}\delta_{ab} + \langle ij|ab\rangle + \eta\langle ij|ab\rangle + (1 - \eta)\langle ij|f_{xc}|ab\rangle \quad (2.50)$$

and

$$B_{ia,jb} = \langle ij|ab\rangle - \eta\langle ij|ab\rangle + (1 - \eta)\langle ij|f_{xc}|ab\rangle \quad (2.51)$$

where a, b and i, j are occupied and virtual orbitals respectively, and $\langle ij|f_{xc}|ab\rangle$ is the exchange-correlation kernel. The admixture of exact Hartree-Fock exchange is quantified by the η parameter:

$$\langle ij|f_{xc}|ab\rangle = \int dr dr' \phi_i(\mathbf{r})\phi_j(\mathbf{r}') \frac{\delta^2 E_{xc}}{\delta\rho(\mathbf{r})\rho(\mathbf{r}')} \phi_a(\mathbf{r}')\phi_b(\mathbf{r}) \quad (2.52)$$

The exchange-correlation kernel is a fundamental quantity in LR-TDDFT and is a big unknown of the theory. So, once we have an expression for the kernel, it is relatively easy to calculate the full polarizability of the molecule and derive excitation energies. Eq. 2.49 is known as the Casida's equation. This equation allows to compute excitation and emission energies of a molecule through the ω eigenvalue. Further details on the linear response function can be found in Ref. [81] and [84].

Within the LR-TDDFT the oscillator strengths associated with the excitations can be calculated from the ($\mathbf{X}\mathbf{Y}$) eigenvectors. The oscillator strength can be interpreted as the probability for the system to make the transition to the excited state. Since in uranyl(VI) complexes, the triplet-singlet transitions are forbidden by the spin selection rule in the spin-orbit free picture, the oscillator strengths are strictly equal to zero. Despite the fact that this rule is relaxed in the intermediate coupling scheme when spin-orbit coupling is accounted for, the oscillator strength values are too low to be an object of discussion.

2.3.3 Approximate exchange-correlation functionals

Based on the benchmark studies of Tecmer et al. [27], the M06 [85], PBE0 [86] and CAM-B3LYP [87] were found to be the most accurate functionals for quantitative studies of actinide spectroscopy. In this PhD work, the PBE0 functional was used to obtain the structural parameters of the ground and excited states of actinide

complexes, while the CAM-B3LYP was used to compute the excitation and emission energies. Here we would like to describe the functionals elaboration to give an idea about their nature and their key features.

To find the universal functional adapted to different types of systems, it is reasonable to separate the exchange-correlation energy $E_{xc}[\rho(\mathbf{r})]$ into exchange and correlation terms:

$$E_{xc}[\rho] = E_x[\rho] + E_c[\rho] \quad (2.53)$$

Then the exchange and correlation energies can be expressed in terms of corresponding energies per particle:

$$E_x[\rho] = \int \rho(\mathbf{r}) \epsilon_x(\rho(\mathbf{r})) d\mathbf{r} \quad (2.54)$$

$$E_c[\rho] = \int \rho(\mathbf{r}) \epsilon_c(\rho(\mathbf{r})) d\mathbf{r} \quad (2.55)$$

By definition, the exchange energy only involves electrons with identical spins, while the correlation of the electrons with the same spin differs and is therefore separable from the correlation of the electrons with opposite spins:

$$E_x[\rho] = E_x^\alpha[\rho_\alpha] + E_x^\beta[\rho_\beta] \quad (2.56)$$

$$E_c[\rho] = E_c^{\alpha\alpha}[\rho_\alpha] + E_c^{\beta\beta}[\rho_\beta] + E_c^{\alpha\beta}[\rho_\alpha, \rho_\beta] \quad (2.57)$$

with $\rho = \rho_\alpha + \rho_\beta$ and $\rho_\alpha = \rho_\beta$ for a closed-shell singlet state.

Local density approximation (LDA)

The first approximation proposed for the exchange-correlation energy was the local density approximation (LDA) method [78, 88], in which the energy is a local function of the energy density. In LDA, the exchange energy is given by the Dirac formula:

$$E_x^{LDA}[\rho] = -C_x \int \rho(\mathbf{r})^{\frac{4}{3}} d^3r \quad (2.58)$$

where C_x is a fitting constant for an exchange part. The correlation part corresponds to that of a free-electron gas and has been fitted numerically to val-

ues obtained with quantum Monte-Carlo simulations [89]. This lead to the parametrization of Vosko, Wilk and Nusair (VWN) [89] and or the PW92 functional developed by Perdew and Wang [88].

The binding energies of molecules obtained at the LDA level are often overestimated while the bond lengths are underestimated. LDA might be suitable for solid-state systems where the electron density can be considered as slowly varying in space but for most chemical systems this approximation is not sufficiently accurate.

Generalized gradient approximation (GGA)

Another approximation of the exchange-correlation energy is the generalized gradient approximation (GGA) which corrects the homogeneous or *local* character of LDA by including the electron density and its derivative:

$$E_{xc}^{GGA}[\rho] = \int \rho \epsilon_{xc}^{GGA}(\rho, \nabla \rho) dr \quad \epsilon_{xc}^{GGA} = \epsilon_x^{GGA} + \epsilon_c^{GGA} \quad (2.59)$$

Several GGA functionals have been proposed for the exchange and correlation parts. Lee, Yang and Parr (LYP) [90] suggested a correction of the correlation energy, with four adjusted parameters. Perdew, Burke and Ernzerhof (PBE) [91] constructed a functional where the exchange part takes the form:

$$\epsilon_x^{PBE} = \epsilon_x^{LDA} \left(1 + a - \frac{a}{1 + bx^2} \right) \quad (2.60)$$

and the correlation part reads

$$\begin{aligned} \epsilon_c^{PBE} &= \epsilon_c^{LDA} + cf_3^3 \ln \left(1 + dt^2 \left(\frac{1 + At^2}{1 + At^2 + A^2 t^4} \right) \right) \\ A &= d \left[\exp \left(-\frac{\epsilon_c^{LDA}}{cf_3^3} \right) - 1 \right] \\ f_3(\zeta) &= \frac{1}{2} [(1 + \zeta)^{\frac{2}{3}} + (1 - \zeta)^{\frac{2}{3}}] \\ t &= [2(3\pi^3)^{\frac{1}{3}} f_3]^{-1} x \end{aligned} \quad (2.61)$$

where a , b and c are determined in a non-empirical way, x is depending on a

density of spin component and ζ is the relative spin polarization.

The inclusion of the first-order gradient correction to LDA leads to a better description of atomic bonding and thus gives more accurate binding energies and molecular geometries. GGAs can be expanded to include information about the electron density and gradient in terms of the Laplacian and non-interacting kinetic energy (so-called second-order corrections), leading to meta-GGA functionals [92–94]. The PBE functional has a simple form compared to other GGA-based functionals, but still the exchange part should be improved to better describe systems with large number of electrons.

Hybrid-GGA functionals

Hybrid functionals are built-up from the combination of a GGA part and an exact Hartree-Fock exchange contribution which tends to fit accurately experimental data. In this work the PBE0 [86, 95] functional has been used to describe structural parameters of the actinides complexes as validated by several studies [96–101]. This functional consists of 25 % of the HF exchange energy added to the PBE exchange functional described above:

$$E_{xc}^{PBE0} = \frac{1}{4}E_x^{HF} + \frac{3}{4}E_x^{PBE} + E_c^{PBE} \quad (2.62)$$

Hybrid approximations are today commonly used for molecular DFT calculations, because the exact HF exchange potential improves the chemical systems descriptions, namely atomistic energies, bond lengths, reaction barriers [74]. Moreover, the advantage is that the exchange part can be adjusted to improve the treatment of specific cases. The fraction of explicit HF exchange also adds a $-\frac{\eta}{r}$ dependence to local and semi-local exchange-correlation functionals. This improves the description of diffuse electronic states (Rydberg), and charge-transfer transitions, though it is neither physically, nor mathematically correct.

Long-range corrected functionals

The idea to go beyond hybrid functionals appeared when the standard DFT exchange functionals showed a tendency to underestimate $4s$ - $3d$ interaction

energies of the first-row transition metals. A new type of functionals appeared called the long-range corrected (LC) exchange functionals. Tsuneda and co-workers [102, 103] proposed that the exact exchange should be present not only globally at both short- and long inter-electronic distances, but also at the long-range orbital-orbital interaction. The electron repulsion operator is thus partitioned into short- and long-range contributions:

$$\frac{1}{r_{12}} = \frac{1 - \text{erf}(\mu r_{12})}{r_{12}} + \frac{\text{erf}(\mu r_{12})}{r_{12}} \quad (2.63)$$

where μ determines the balance between short- and long-range exchanges at intermediate r_{12} values. The key point is that the DFT exchange interaction is included at short range, E_x^{sr} , and that the long-range exchange interaction is described with the HF exchange E_x^{lr} [87]:

$$E_x^{LC} = E_x^{sr} + E_x^{lr} \quad (2.64)$$

Hereinafter, the Coulomb attenuation procedure was combined to the B3LYP exchange-correlation functional using two additional parameters:

$$\frac{1}{r_{12}} = \frac{1 - [\alpha + \beta \text{erf}(\mu r_{12})]}{r_{12}} + \frac{\alpha + \beta \text{erf}(\mu r_{12})}{r_{12}} \quad (2.65)$$

where the separation parameter $\mu = 0.33$, and $\alpha = 0.19$ and $\beta = 0.46$ correspond to a fraction of HF exchange at short- and long inter-electronic distances, respectively. This approximation was named Coulomb attenuating method-B3LYP (CAM-B3LYP) [87]. It allows to compute with an accuracy of about 0.1 eV charge-transfer excitation energies using TD-DFT [27].

2.4 Relativistic effects

When dealing with actinide complexes, relativistic effects have to be considered. Due to the number of electrons of the uranium atom ($Z=92$), all the non-relativistic approaches are not appropriate because the high atomic number implies for the electrons close to the nuclei to have a velocity close to that of the

speed of light [104], changing the atomic electronic structure. There are two types of relativistic effects: scalar (independent of the electron spin) and spin-orbit (dependent on the electron spin). In the first case, the electrons located close to the nuclei are moving with a very high speed and moving closer to the center causing the contraction and stabilization of s and p orbitals. This contributes to simultaneously destabilizing the d and f electrons in the outer shells. In the case of spin-orbit relativistic contribution, the interaction of the electron magnetic moment and the magnetic induction created by the kinetic motion of the orbital results in the splitting of orbitals with angular momenta greater than 0 (p , d , f , etc.). Thus, the basic concepts of relativistic quantum chemistry need to be introduced to be able to treat actinides in a proper way. In this section we will introduce the Dirac equation and one of its two-component approximations, the zero-order regular approximation. The key aspects of relativistic effective core potentials will be discussed as well.

2.4.1 Dirac equation

The relativistic energy of a free particle is

$$E = c\sqrt{p^2 + m_e^2 c^2} \quad (2.66)$$

where m_e is the mass of the electron and p is its momentum. If one replaces the variables of this equation by the corresponding quantum mechanical operators, one shall be able to derive the expression of a relativistic quantum Hamiltonian. Dirac [105] realized that the only way to derive a relativistic Hamiltonian, which is a linear operator with respect to the momentum like for the non-relativistic Hamiltonian, was to introduce the algebra quantities α and β . The Dirac equation, in an external electromagnetic potential describes the relativistic motion of an electron as:

$$\left(\beta m_0 c^2 + e\phi + \alpha \cdot \pi - i\hbar \frac{\partial}{\partial t} \right) \psi = 0 \quad (2.67)$$

where

$$\boldsymbol{\pi} = \mathbf{p} + e\mathbf{A} \quad (2.68)$$

$$\mathbf{p} \rightarrow \mathbf{p} - q\mathbf{A}; E \rightarrow -q\phi \quad (2.69)$$

where ϕ is a scalar potential and \mathbf{A} is the vector potential describing the magnetic field. $q = -e$ goes for an electron, $q = +e$ for a positron. $\boldsymbol{\alpha}$ is a quantity which has to be determined as soon as it contains information about the spin of the particle. $\boldsymbol{\alpha}$ and $\boldsymbol{\beta}$ are the 4×4 matrices that are defined as:

$$\alpha_x = \begin{pmatrix} 0 & 0 & 0 & 1 \\ 0 & 0 & 1 & 0 \\ 0 & 1 & 0 & 0 \\ 1 & 0 & 0 & 0 \end{pmatrix}, \alpha_y = \begin{pmatrix} 0 & 0 & 0 & -i \\ 0 & 0 & i & 0 \\ 0 & -i & 0 & 0 \\ i & 0 & 0 & 0 \end{pmatrix}, \alpha_z = \begin{pmatrix} 0 & 0 & 1 & 0 \\ 0 & 0 & 0 & -1 \\ 1 & 0 & 0 & 0 \\ 0 & -1 & 0 & 0 \end{pmatrix}, \quad (2.70)$$

$$\beta = \begin{pmatrix} 1 & 0 & 0 & 0 \\ 0 & 1 & 0 & 0 \\ 0 & 0 & -1 & 0 \\ 0 & 0 & 0 & -1 \end{pmatrix} \quad (2.71)$$

These can be expressed in terms of the Pauli matrices σ_i , the zero 2×2 matrix 0_2 and the 2×2 identity matrix 1_2 :

$$\alpha_x = \begin{pmatrix} 0_2 & \sigma_x \\ \sigma_x & 0_2 \end{pmatrix}, \alpha_y = \begin{pmatrix} 0_2 & \sigma_y \\ \sigma_y & 0_2 \end{pmatrix}, \alpha_z = \begin{pmatrix} 0_2 & \sigma_z \\ \sigma_z & 0_2 \end{pmatrix} \quad (2.72)$$

$$\beta = \begin{pmatrix} 1_2 & 0_2 \\ 0_2 & -1_2 \end{pmatrix} \quad (2.73)$$

where the Pauli matrices are:

$$\sigma_x = \begin{pmatrix} 0 & 1 \\ 1 & 0 \end{pmatrix}, \sigma_y = \begin{pmatrix} 0 & -i \\ i & 0 \end{pmatrix}, \sigma_z = \begin{pmatrix} 1 & 0 \\ 0 & -1 \end{pmatrix} \quad (2.74)$$

The four-dimensional form of $\boldsymbol{\alpha}$ and $\boldsymbol{\beta}$ requires the wave function to be a four-component vector. There are two spectra of energy solutions of this equation,

separated by $2m_e c^2$:

$$E_{\pm} = \pm c \sqrt{p^2 + m_e^2 c^2} \quad (2.75)$$

showing that an electron can occupy a positive or negative state. Due to the Pauli principle, Dirac supposed all the negative states to be fully occupied [106], so the electrons would not be able to occupy them.

One can rewrite the Dirac equation by shifting the energy spectrum by $-m_e c^2$, so that the lower bound of the high-energy spectrum matches that of electrons in the non-relativistic Schrödinger equation:

$$\begin{pmatrix} (V - E)1_2 & c(\boldsymbol{\sigma} \cdot \mathbf{p}) \\ c(\boldsymbol{\sigma} \cdot \mathbf{p}) & (V - 2m_e c^2 - E)1_2 \end{pmatrix} \begin{pmatrix} \psi^L(\mathbf{r}) \\ \psi^S(\mathbf{r}) \end{pmatrix} = 0 \quad (2.76)$$

This leads us to introduce $\psi^L(\mathbf{r})$ and $\psi^S(\mathbf{r})$ the so-called large (L) and small (S) components, holding each of them the two α and β spin degrees of freedom:

$$\psi(\mathbf{r}) = \begin{pmatrix} \psi^L(\mathbf{r}) \\ \psi^S(\mathbf{r}) \end{pmatrix} = \begin{pmatrix} \psi_{\alpha}^L(\mathbf{r}) \\ \psi_{\beta}^L(\mathbf{r}) \\ \psi_{\alpha}^S(\mathbf{r}) \\ \psi_{\beta}^S(\mathbf{r}) \end{pmatrix} \quad (2.77)$$

The solutions of the Dirac equation for a free electron ($V = 0$) can be obtained by solving the following matrix equation:

$$\begin{pmatrix} -E1_2 & c(\boldsymbol{\sigma} \cdot \mathbf{p}) \\ c(\boldsymbol{\sigma} \cdot \mathbf{p}) & (-2m_e c^2 - E)1_2 \end{pmatrix} \begin{pmatrix} \psi^L(\mathbf{r}) \\ \psi^S(\mathbf{r}) \end{pmatrix} = 0 \quad (2.78)$$

Since the four-component Dirac equation integrates both electronic and positronic states, it appears desirable to simplify the problem to treat only the electronic degrees of freedom. While it is straightforward to do so for the one-electron Dirac equation [107] (See the Foldy–Wouthuysen transformation), it is more complicated for many-electron systems.

Zero-Order Regular Approximation

In the past two decades, a number of two-component Hamiltonians have been derived. Among them are the Douglas-Kroll-Hess (DKH) Method [108, 109], the Pauli Hamiltonian [110], and the Zero-Order Regular Approximation (ZORA) [111]. The advantage of all of these Hamiltonians is that one can separate a scalar part that can be used with or without the spin-orbit part.

From Eq. 2.76, we can write the relationship between $\psi^L(\mathbf{r})$ and $\psi^S(\mathbf{r})$ as

$$\psi^S(\mathbf{r}) = K(E, \mathbf{r}) \frac{\boldsymbol{\sigma} \cdot \mathbf{p}}{2m_e c} \psi^L(\mathbf{r}) \quad (2.79)$$

with the operator $K(E, \mathbf{r})$ defined as:

$$K(E, \mathbf{r}) = \left[1 + \frac{E - V}{2m_e c^2} \right]^{-1} = \left[1 - \frac{V}{2m_e c^2} \right]^{-1} \left[1 + \frac{E}{2m_e c^2 - V} \right]^{-1} \quad (2.80)$$

If one keeps only the first term of the right-hand side of Eq. 2.80, one obtains the ZORA (zeroth-order regular approximation) Hamiltonian:

$$\hat{H}^{ZORA} = \hat{V} + (\boldsymbol{\sigma} \cdot \mathbf{p}) \frac{c^2}{2m_e c^2 - V} (\boldsymbol{\sigma} \cdot \mathbf{p}) \quad (2.81)$$

This formulation includes the spin-orbit coupling in $(\boldsymbol{\sigma} \cdot \mathbf{p})$ which can be easily separated to obtain the scalar relativistic (SR) ZORA Hamiltonian. Later, van Wüllen [112] pointed out that the scalar relativistic effects could be fully included in a kinetic operator \hat{T}_{SR}^{ZORA} :

$$\hat{T}_{SR}^{ZORA} = \mathbf{p} \frac{c^2}{2m_e c^2 - V} \mathbf{p} \quad (2.82)$$

This property is very useful when the effect of the spin-orbit component is negligible, for example during the calculations of the structural properties of actinides [10]. Such separation allows to decrease the time and computational cost.

2.4.2 Relativistic effective core potential

The electrons of an atom can be approximately divided into two groups depending on their location relatively to the core: namely the core and valence electrons. The core electrons, located close to the nucleus, are usually not involved in chemical bonds, while the valence electrons, located further away from the nucleus, actively participate in chemical bonding. As discussed earlier, in the frame of relativistic quantum chemistry, a proper treatment of such large number of electrons can be very expensive; thus the core and valence electrons can be treated in two different ways. For the core electrons, the relativistic effective core potential (R-ECP) [113] can be used to replace them by an effective core potential. As the number of electrons explicitly treated decreases, the number of atomic basis functions can be reduced. The calculation of the electron correlation energy then becomes less expensive. Thus the Hamiltonian can be reduced to the sum of the interaction between the valence electrons and the interaction of the former with the nucleus/core electrons. It is called the valence Hamiltonian:

$$\hat{H}_v = \sum_i^{N_v} \hat{H}_i + \sum_{i<j}^{N_v} \frac{1}{r_{ij}} + V_{ECP} \quad (2.83)$$

where N_v is a number of valence electrons and V_{ECP} is the effective core potential, which can take the following analytical form:

$$V_{ECP} = -\frac{Z_{eff}}{r} + \sum_{l_j} \left(\sum_k a_{l_j,k} r^{n_{l_j,k}-2} \exp\{-\alpha_{l_j,k} r^2\} \right) P_{l_j} \quad (2.84)$$

$$P_{l_j} = \sum_{m_j=-j}^j |l_j m_j\rangle \langle l_j m_j| \quad (2.85)$$

where Z_{eff} corresponds to the core charge, i.e., the nucleus charge decreased by the number of core electrons, a , n and α are the parameters that depend on the total angular momenta j and are determined by a fitting procedure of a n -term polynomial. These parameters are carefully adjusted to reproduce the best all-electron relativistic reference calculations [6, 114].

The number of core electrons replaced (and thus frozen) by the ECP has an impact on the accuracy of the calculations. For actinides, two types of RECP have been developed: small-core and large-core ECP including 60 and 78 (or more) electrons, respectively. Depending on the strength of the interaction of the actinide's valence electrons with the associated ligands, the choice of the core size should be made. For our study we assumed that uranyl-ligand interactions are strong, since they significantly modify the electronic structure of uranium(VI). It has been shown that large-core RECP would bias the results [115] while small-core RECP are as accurate as all-electron results for geometries and valence transition energies [116, 117].

2.5 Basis set

It has been mentioned in Section 2.2 that the wave function is described by a Slater determinant expressed in terms of orthonormal spin orbitals. A spin orbital represents a molecular orbital (MO) in case of a molecule. Since a molecule is composed of atoms, the molecular orbital can be represented by a Linear Combination of Atomic Orbitals (LCAO) [118]:

$$\phi_i = \sum_j^{N_{AO}} c_{ij} \psi_j = \sum_j^{N_{AO}} c_{ij} \sum_k^{N_b} d_{jk} \chi_k \quad (2.86)$$

where d_{jk} is the expansion coefficient, χ_k is the atomic basis set function, and N_b is the number of basis functions used. A minimal basis set has one basis function for each occupied orbital. Additional orbitals are often added to account for polarization, and correlation, for example. In quantum chemical calculations, the atomic orbitals can take two mathematical forms: the Slater Type Orbitals (STO) [119] and the Gaussian Type Orbitals (GTO) [120] which are both products of a radial part $R_l(\mathbf{r})$ and a spherical harmonic function $Y_l^m(\theta, \phi)$.

STOs have the following radial part:

$$R_l(r) = N r^l e^{-\zeta r} \quad (2.87)$$

where l is the principal quantum number, N is a normalizing constant, r is the electron-nucleus distance and ζ is a constant related to the effective charge of the nucleus. STO basis sets are well suited for atomic calculations due to their good behavior at very short and long distances from the nucleus. However they are less suited for molecular systems because the two-electron integrals involving several centers cannot be computed analytically.

To bypass the integration issue, the GTOs were introduced with their radial part:

$$R_l(r) = N r^l e^{-\alpha r^2} \quad (2.88)$$

However, the GTOs have two major flaws: they decrease very quickly when moving away from the nucleus and, on the other hand, they have a zero derivative near the nucleus. One of the methods to best approximate atomic orbitals is to replace each Slater orbital with a linear combination of several Gaussian-like orbitals thus defining a contracted Gaussian basis function as illustrated by Figure 2.3.

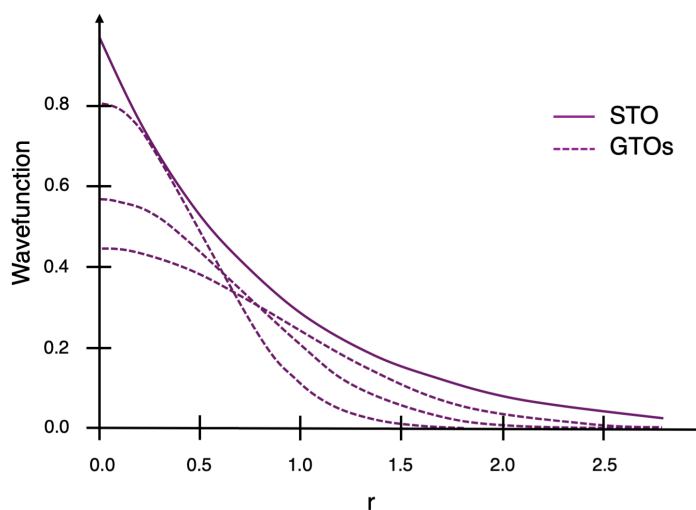


Figure 2.3: Construction of the Slater type function by n GTO ($n=1-3$).

The minimal LCAOs to build-up molecular orbitals are usually not enough to obtain a chemically sound description of the electronic density of the molecule.

To improve the description one can double the number of basis functions. This results in the so-called double- ζ quality (DZ) basis sets. The basis set can be extended to triple (TZ), quadruple (QZ) and so on. As for actinides, we are mostly interested in valence properties the use of TZ or QZ basis set is required. So it can be less expensive to use more functions for the valence electrons than for the core electrons. The resulting basis sets are split-valence basis sets (SV). Further improvements of the basis set come from the addition of polarization (P) functions with higher angular momenta than the occupied functions. These functions are essential to describe chemical bonds and the valence electron correlation in actinide complexes.

While choosing a basis set, the electronic structure method should also be taken into account. For DFT calculations, the use of TZ basis sets with polarization functions is usually enough [121]. So, for our calculations, polarized valence triple- ζ (TZVP) basis sets were chosen. More precisely, for the computations of the structural and vibrational properties, the second generation Ahlrichs basis sets, def2-TZVP [122], have been used for all light elements, while for the uranium atom, the first generation def-TZVP [123] basis set was chosen together with the small-core R-ECP [124]. To compute excitation and emission energies with the two-component ZORA Hamiltonian, the ADF software [125] has been used together with the all-electron relativistic TZ2P Slater-type basis sets [126] (triple- ζ with two polarization functions quality), as validated by Tecmer et al. [26, 27].

2.6 Solvent effects

When we are considering the environmental effects in solution chemistry, the solvent effect is usually the first topic. The effects of a solvent on the luminescence properties are usually complex, and are mostly related to the solvent polarity. It is thus essential to take them into account. There are two ways to treat solvent effects within computational chemistry, using either explicit or implicit solvent models. Explicit solvation is not realistic in the case of actinides because of the tremendous computational growth as explicit solvent molecules need to be modeled, and the large number of local minima that need to be considered as the

solvent molecules orient with respect to the solute. Within this thesis implicit solvation models were used to treat both short- and long-range solvent effects.

2.6.1 Continuum Models

A standard approach for implicitly describing the solvent is to represent it as a dielectric polarizable continuum, and to place the solute in a cavity of approximately molecular shape. The charge distribution ρ of the solute inside the cavity will polarize the dielectric continuum with a given solvent permittivity ϵ_r , that in turn polarizes the solute charge distribution. The solvent reaction field is described by polarization charges distributed on the surface of the cavity. The interaction with the solvent (s) can be taken into account through a reaction potential $\hat{V}(S,s)$ that acts as a perturbation on the solute (S). This interaction operator calculates the system's response as a result of going from a gaseous infinitely separated system to the one in a continuum solution. The Hamiltonian in a continuum solvent model can be written as:

$$\hat{H}_{eff}(S,s) = \hat{H}(S) + \hat{V}(S,s) \quad (2.89)$$

where $\hat{H}(S)$ is the Hamiltonian of the solute in the gas phase. The solvent reaction potential $\hat{V}(S,s)$ can be expressed in terms of a charge density spread on the cavity surface, the *apparent surface charge*, and its interaction with the polarizable dielectric continuum surrounding the cavity. This is achieved by expanding the apparent surface charge that builds up at the solute-solvent interface in terms of spherical Gaussian functions located at each surface element in which the cavity surface is discretized. The usual SCF procedure can describe this interaction and also yields the wave function and energy for the solvated molecule. Because of the polarization of the cavity walls, these methods are called polarized continuum methods (PCM), and since the final interaction energy has to be computed iteratively, the SCF procedure is called a self-consistent reaction field (SCRF) calculation.

The conductor-like polarizable continuum model (C-PCM)

A further variation of PCM is the conductor-like polarizable continuum model (C-PCM), which is often considered as one of the most successful solvation model [127]. In the C-PCM approach the solute is placed in a cavity formed by the envelope of spheres centered on the atoms or molecule (see Figure 2.4). Inside the cavity the dielectric constant is the same as in vacuum, outside it takes the value of the desired solvent.

The cavity surface is built by a set of finite elements called tesserae. Each tessera is characterized by the position of its center r_i , area a_i , and the vector normal to the surface passing through its center n_i . The conductor-like reaction field is the result of an apparent polarization charge distribution on the cavity surface. Basically, the polarization charges are expressed in terms of finite point charges placed in each tessera. The solvation charge can be obtained by solving a system of N coupled linear equations (N being the number of tesserae):

$$\mathbf{D}\mathbf{q} = -\mathbf{b} \quad (2.90)$$

where \mathbf{D} is a matrix which depends on the dielectric constant of a solvent and tesserae, \mathbf{q} and \mathbf{b} are the vectors that collect the solvation charges and the total electrostatic potential generated by solute nuclei and electrons on tesserae, respectively. For C-PCM, the matrix \mathbf{D} and the vectors \mathbf{q} and \mathbf{b} are defined as:

$$\begin{cases} D_{ii} = \frac{\epsilon_r}{\epsilon_r - 1} 1.07 \sqrt{\frac{4\pi}{a_i}} \\ D_{ij} = \frac{\epsilon_r}{\epsilon_r - 1} \frac{1}{|r_i - r_j|} \end{cases} \quad (2.91)$$

$$q_i = a_i \sigma(\vec{r}_i) \quad (2.92)$$

$$b_i = V(\vec{r}_i) \quad (2.93)$$

where $\sigma(\vec{r}_i)$ is the charge density of the tessera i and $V(\vec{r}_i)$ is an electrostatic potential generated by the solute in the tessera i .

The interaction energy between the solute and solvent can be written as

$$E_{int} = \sum_i^N b_i q_i = \sum_i^N V(\vec{r}_i) q_i \quad (2.94)$$

The interaction potential (conductor-like reaction field) between the solute and solvent charges, in equation 2.89, can then be written as a finite sum over the tesserae:

$$\hat{V}_\sigma = \sum_i^N \frac{\sigma(\vec{r}_i)}{|r - r_i|} = \sum_i^N \frac{q_i}{|r - r_i|} \quad (2.95)$$

More details about the conductor-like polarizable continuum model and illus-

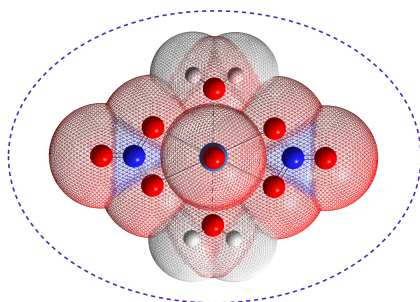


Figure 2.4: C-PCM solute cavity for uranyl binitrate complex.

trative applications can be found in the references [127–130].

The conductor-like screening model (COSMO)

The conductor-like screening model (COSMO) is another continuum solvation model, in which the polarization charges of the continuum, caused by the polarity of the solute are derived from a scaled-conductor approximation. The charges q of Eq. 2.95 are lowered by a factor $f(\epsilon_r)$:

$$q' = f(\epsilon_r)q \quad (2.96)$$

the scaling factor being

$$f(\epsilon_r) = \frac{\epsilon_r - 1}{\epsilon_r + x} \quad (2.97)$$

where the value x depends on the molecular charge (0.5 for neutral molecules, 0.0 for ions). Further details about COSMO can be found in the publications by Klamt et al. [131–133].

2.6.2 Equilibrium and non-equilibrium solvation

A common limitation of the continuum models is their inability to account for the dynamic effects of solvation. Indeed, the solvent responds in two different ways to changes in the electronic state of the solute: it polarizes its electron distribution, which is a very rapid process, and the solvent molecules reorient themselves, the latter being a much slower process.

An equilibrium calculation describes a situation where the solvent has the time to fully respond to the solute, for instance, during a geometry optimization that is a process which takes place on the same time scale as the molecular motions within the solvent. A non-equilibrium calculation is appropriate for processes which are too rapid for the solvent to have time to fully respond, for example, a vertical electronic excitation or emission.

The solute-solvent interaction is described in terms of a set of apparent solvation charges distributed over the surface of the cavity which contains the solute. To treat the effects of non-equilibrium linked to the relaxation time of the solvent molecules, the solvation charges, which represent the solvent, are divided into two components (for each tessera i):

$$q_i = q_{i,f} + q_{i,s} \quad (2.98)$$

where $q_{i,f}$ is the fast component able to follow the changes in the solute and $q_{i,s}$ is the slow component.

In the form of a vector, we have

$$\mathbf{q}_f = \frac{\varepsilon_f - 1}{\varepsilon_r - 1} \mathbf{q} \text{ and } \mathbf{q}_s = \frac{\varepsilon_r - \varepsilon_f}{\varepsilon_r - 1} \mathbf{q} \quad (2.99)$$

where ε_f is a new dielectric constant describing the fast polarization and ε_r is the static dielectric constant used previously.

All the solvation charges $q_{i,f}$ will be in equilibrium at all times t with the

solute: they will adapt to the change undergone by it. The rest of the solvation charges $q_{i,s}$ will remain in the initial state, that before the perturbation, *i.e.*, respectively the ground state in the case of an absorption spectrum and the excited state in the case of an emission spectrum. Thus to calculate a vertical transition between two states, it is necessary to carry out a calculation on a first state, where the two components are optimized for this state, and then a separate calculations on the other electronic states where only the fast component is optimized, the slow components being taken from the initial state. Hence during all the calculations, the reaction field is in equilibrium with the starting state and only with this state.

More examples of equilibrium and non-equilibrium solvation application can be found in Ref. [134, 135].

Bibliography of the current chapter

- (6) Dolg, M. In *Handbook of Relativistic Quantum Chemistry*, Liu, W., Ed.; Springer Berlin Heidelberg: Berlin, Heidelberg, 2017, pp 449–478, DOI: 10.1007/978-3-642-40766-6_5.
- (10) Pierloot, K.; van Besien, E. Electronic structure and spectrum of UO_2^{2+} and $\text{UO}_2\text{Cl}_4^{2-}$. *Journal of Chemical Physics* **2005**, *123*, 204309, DOI: 10.1063/1.2121608.
- (26) Tecmer, P.; Gomes, A. S. P.; Ekström, U.; Visscher, L. Electronic spectroscopy of UO_2^{2+} , NUO^+ and NUN : an evaluation of time-dependent density functional theory for actinides. *Physical Chemistry Chemical Physics* **2011**, *13*, 6249–6259, DOI: 10.1039/C0CP02534H.
- (27) Tecmer, P. Towards reliable modeling of excited states of uranium compounds, Ph.D. Thesis, Vrije Universiteit, 2012.
- (62) Born, M.; Oppenheimer, R. Zur Quantentheorie der Molekeln. *Annalen der Physik* **1927**, *389*, 457–484, DOI: 10.1002/andp.19273892002.
- (63) Atkins, P. W.; Friedman, R. S., *Molecular quantum mechanics*; Oxford university press: 2011.
- (64) Berger, R.; Fischer, C.; Klessinger, M. Calculation of the vibronic fine structure in electronic spectra at higher temperatures. 1. Benzene and pyrazine. *The Journal of Physical Chemistry A* **1998**, *102*, 7157–7167, DOI: 10.1021/jp981597w.
- (65) Kupka, H.; Cribb, P. Multidimensional Franck–Condon integrals and Duschinsky mixing effects. *The Journal of Chemical Physics* **1986**, *85*, 1303–1315, DOI: 10.1063/1.451216.
- (66) Duschinsky, F. The importance of the electron spectrum in multi atomic molecules. Concerning the Franck-Condon principle. *Acta Physicochim. URSS* **1937**, *7*, 551–566.
- (67) Doktorov, E.; Malkin, I.; Man'Ko, V. Dynamical symmetry of vibronic transitions in polyatomic molecules and the Franck-Condon principle. *Journal of Molecular Spectroscopy* **1975**, *56*, 1–20, DOI: 10.1016/0022-2852(75)90199-X.
- (68) Doktorov, E.; Malkin, I.; Man'ko, V. Dynamical symmetry of vibronic transitions in polyatomic molecules and the Franck-Condon principle. *Journal of Molecular Spectroscopy* **1977**, *64*, 302–326, DOI: 10.1016/0022-2852(77)90269-7.
- (69) Califano, S., *Vibrational states*; Wiley: 1976.

- (70) Schrödinger, E. Quantisierung als Eigenwertproblem. *Annalen der Physik* **1926**, 384, 361–376, DOI: 10.1002/andp.19263840404.
- (71) Szabo, A.; Ostlund, N. S., *Modern Quantum Chemistry: Introduction to Advanced Electronic Structure Theory*; Courier Corporation: 1996.
- (72) Pauli, W. Über den Zusammenhang des Abschlusses der Elektronengruppen im Atom mit der Komplexstruktur der Spektren. *Zeitschrift für Physik* **1925**, 31, 765–783, DOI: 10.1007/BF02980631.
- (73) Slater, J. C. The theory of complex spectra. *Physical Review* **1929**, 34, 1293–1322, DOI: 10.1103/PhysRev.34.1293.
- (74) Koch, W.; Holthausen, M. C., *A Chemist's Guide to Density Functional Theory*, 1st ed.; Wiley: 2001, DOI: 10.1002/3527600043.
- (75) Thomas, H. L. On the capture of electrons by moving electrified particles. *Proceedings of the Royal Society of London. Series A, Containing papers of a mathematical and physical character* **1927**, 114, 561–576, DOI: 10.1098/rspa.1927.0058.
- (76) Fermi, E. Eine statistische Methode zur Bestimmung einiger Eigenschaften des Atoms und ihre Anwendung auf die Theorie des periodischen Systems der Elemente. *Zeitschrift für Physik* **1928**, 48, 73–79, DOI: 10.1007/BF01351576.
- (77) Hohenberg, P.; W, K. Inhomogeneous electron gas. *Physical Review* **1964**, 136, 864–871, DOI: 10.1103/PhysRev.136.B864.
- (78) Kohn, W.; Sham, L. Self-consistent equations including exchange and correlation effects. *Physical Review* **1965**, 140, 1133–1138, DOI: 10.1103/PhysRev.140.A1133.
- (79) Piela, L., *The ideas of quantum chemistry*; Elsevier: 2013.
- (80) Marques, M. A.; Maitra, N. T.; Nogueira, F. M.; Gross, E. K.; Rubio, A., *Fundamentals of time-dependent density functional theory*; Springer Science & Business Media: 2012; Vol. 837.
- (81) Casida, M. E. In *Recent Advances In Density Functional Methods: (Part I)*; World Scientific: 1995, pp 155–192, DOI: 10.1142/9789812830586_0005.
- (82) Mahan, G. D.; Subbaswamy, K., *Local density theory of polarizability*; Springer Science & Business Media: 2013.
- (83) Van Leeuwen, R. Causality and symmetry in time-dependent density-functional theory. *Physical Review Letters* **1998**, 80, 1280–1283, DOI: 10.1103/PhysRevLett.80.1280.

- (84) Olevano, V. In *Structures on different time scales*, Woike, T., Schaniel, D., Eds.; De Gruyter: Berlin, 2018, pp 101–142, DOI: 10.1515/9783110433920-004.
- (85) Zhao, Y.; Truhlar, D. G. A new local density functional for main-group thermochemistry, transition metal bonding, thermochemical kinetics, and noncovalent interactions. *The Journal of Chemical Physics* **2006**, *125*, 194101–18, DOI: 10.1063/1.2370993.
- (86) Ernzerhof, M.; Scuseria, G. E. Assessment of the Perdew–Burke–Ernzerhof exchange–correlation functional. *Journal of Chemical Physics* **1999**, *110*, 5029–5036, DOI: 10.1063/1.478401.
- (87) Yanai, T.; Tew, D. P.; Handy, N. C. A new hybrid exchange–correlation functional using the Coulomb-attenuating method (CAM-B3LYP). *Chemical Physics Letters* **2004**, *393*, 51–57, DOI: 10.1016/j.cpllett.2004.06.011.
- (88) Perdew, J. P.; Wang, Y. Accurate and simple analytic representation of the electron-gas correlation energy. *Physical Review B* **1992**, *45*, 13244–13249, DOI: 10.1103/PhysRevB.45.13244.
- (89) Vosko, S. H.; Wilk, L.; Nusair, M. Accurate spin-dependent electron liquid correlation energies for local spin density calculations: a critical analysis. *Canadian Journal of Physics* **1980**, *58*, 1200–1211, DOI: 10.1139/p80-159.
- (90) Lee, C.; Yang, W.; Parr, R. G. Development of the Colle-Salvetti correlation-energy formula into a functional of the electron density. *Physical Review B* **1988**, *37*, 785–789, DOI: 10.1103/PhysRevB.37.785.
- (91) Perdew, J. P.; Burke, K.; Ernzerhof, M. Generalized Gradient Approximation Made Simple. *Physical Review Letters* **1996**, *77*, 3865–3868, DOI: 10.1103/PhysRevLett.77.3865.
- (92) Zhao, Y.; Schultz, N. E.; Truhlar, D. G. Exchange-correlation functional with broad accuracy for metallic and nonmetallic compounds, kinetics, and noncovalent interactions. *Journal of Chemical Physics* **2005**, *123*, 161103–4, DOI: 10.1063/1.2126975.
- (93) Zhao, Y.; Truhlar, D. G. Density functionals with broad applicability in chemistry. *Accounts of Chemical Research* **2008**, *41*, 157–167, DOI: 10.1021/ar700111a.
- (94) Jacquemin, D.; Perpète, E. A.; Ciofini, I.; Adamo, C.; Valero, R.; Zhao, Y.; Truhlar, D. G. On the performances of the M06 family of density functionals for electronic excitation energies. *Journal of Chemical Theory and Computation* **2010**, *6*, 2071–2085, DOI: 10.1021/ct100119e.

- (95) Grimme, S. Accurate description of van der Waals complexes by density functional theory including empirical corrections. *Journal of Computational Chemistry* **2004**, *25*, 1463–1473, DOI: 10.1002/jcc.20078.
- (96) Šulka, M.; Cantrel, L.; Vallet, V. Theoretical Study of Plutonium(IV) Complexes Formed within the PUREX Process: A Proposal of a Plutonium Surrogate in Fire Conditions. *Journal of Physical Chemistry A* **2014**, *118*, 10073–10080, DOI: 10.1021/jp507684f.
- (97) Behrle, A. C.; Kerridge, A.; Walensky, J. R. Dithio- and diselenophosphinate thorium (IV) and uranium (IV) complexes: molecular and electronic structures, spectroscopy, and transmetalation reactivity. *Inorganic Chemistry* **2015**, *54*, 11625–11636, DOI: 10.1021/acs.inorgchem.5b01342.
- (98) Tanti, J.; Lincoln, M.; Kerridge, A. Decomposition of *d*- and *f*-shell contributions to uranium bonding from the quantum theory of atoms in molecules: Application to uranium and uranyl halides. *Inorganics* **2018**, *6*, 88–19, DOI: 10.3390/INORGANICS6030088.
- (99) Behrle, A. C.; Barnes, C. L.; Kaltsoyannis, N.; Walensky, J. R. Systematic Investigation of Thorium (IV)– and Uranium (IV)–Ligand Bonding in Dithiophosphonate, Thioselenophosphinate, and Diselenophosphonate Complexes. *Inorganic Chemistry* **2013**, *52*, 10623–10631, DOI: 10.1021/ic401642a.
- (100) Schnaars, D. D.; Gaunt, A. J.; Hayton, T. W.; Jones, M. B.; Kirker, I.; Kaltsoyannis, N.; May, I.; Reilly, S. D.; Scott, B. L.; Wu, G. Bonding Trends Traversing the Tetravalent Actinide Series: Synthesis, Structural, and Computational Analysis of $An^{IV}(Aracnac)_4$ Complexes ($An = Th, U, Np, Pu$; $Aracnac = ArNC(Ph)CHC(Ph)O$; $Ar = 3,5-tBu_2C_6H_3$). *Inorganic Chemistry* **2012**, *51*, 8557–8566, DOI: 10.1021/ic301109f.
- (101) Kirker, I.; Kaltsoyannis, N. Does covalency *really* increase across the 5f series? A comparison of molecular orbital, natural population, spin and electron density analyses of $AnCp_3$ ($An = Th-Cm$; $Cp = \eta^5-C_5H_5$). *Dalton Transactions* **2011**, *40*, 124–131, DOI: 10.1039/C0DT01018A.
- (102) Tawada, Y.; Tsuneda, T.; Yanagisawa, S.; Yanai, T.; Hirao, K. A long-range-corrected time-dependent density functional theory. *The Journal of Chemical Physics* **2004**, *120*, 8425–8433, DOI: 10.1063/1.1688752.
- (103) Iikura, H.; Tsuneda, T.; Yanai, T.; Hirao, K. A long-range correction scheme for generalized-gradient-approximation exchange functionals. *The Journal of Chemical Physics* **2001**, *115*, 3540–3544, DOI: doi.org/10.1063/1.1383587.

- (104) Pyykkö, P. Relativistic effects in structural chemistry. *Chemical Reviews* **1988**, *88*, 563–594, DOI: 10.1021/cr00085a006.
- (105) Dirac, P. A. M. The quantum theory of the electron. *Proceedings of the Royal Society of London. Series A, Containing Papers of a Mathematical and Physical Character* **1928**, *117*, 610–624, DOI: 10.1098/rspa.1928.0023.
- (106) Dirac, P. A. M. A theory of electrons and protons. *Proceedings of the Royal Society of London. Series A, Containing papers of a mathematical and physical character* **1930**, *126*, 360–365, DOI: 10.1098/rspa.1930.0013.
- (107) Foldy, L. L.; Wouthuysen, S. A. On the Dirac theory of spin 1/2 particles and its non-relativistic limit. *Physical Review* **1950**, *78*, 29–36, DOI: 10.1103/PhysRev.78.29.
- (108) Douglas, M.; Kroll, N. M. Quantum electrodynamical corrections to the fine structure of helium. *Annals of Physics* **1974**, *82*, 89–155, DOI: 10.1016/0003-4916(74)90333-9.
- (109) Hess, B. A. Relativistic electronic-structure calculations employing a two-component no-pair formalism with external-field projection operators. *Physical Review A* **1986**, *33*, 3742–3748, DOI: 10.1103/PhysRevA.33.3742.
- (110) Dyall, K. G.; Fægri Jr, K., *Introduction to relativistic quantum chemistry*; Oxford University Press: 2007.
- (111) Van Lenthe, E.; Baerends, E.-J.; Snijders, J. G. Relativistic regular two-component Hamiltonians. *Journal of Chemical Physics* **1993**, *99*, 4597–4610, DOI: 10.1063/1.466059.
- (112) Van Wüllen, C. Molecular density functional calculations in the regular relativistic approximation: Method, application to coinage metal diatomics, hydrides, fluorides and chlorides, and comparison with first-order relativistic calculations. *The Journal of Chemical Physics* **1998**, *109*, 392–399, DOI: 10.1063/1.476576.
- (113) Krauss, M.; Stevens, W. J. Effective potentials in molecular quantum chemistry. *Annual Review of Physical Chemistry* **1984**, *35*, 357–385, DOI: 10.1146/annurev.pc.35.100184.002041.
- (114) Dolg, M.; Cao, X. Relativistic Pseudopotentials: Their Development and Scope of Applications. *Chemical Reviews* **2012**, *112*, 403–480, DOI: 10.1021/cr2001383.

- (115) Batista, E. R.; Martin, R. L.; Hay, P. J.; Peralta, J. E.; Scuseria, G. E. Density functional investigations of the properties and thermochemistry of UF_6 and UF_5 using valence-electron and all-electron approaches. *Journal of Chemical Physics* **2004**, *121*, 2144–2150, DOI: 10.1063/1.1768518.
- (116) Vallet, V.; Schimmelpfennig, B.; Maron, L.; Teichteil, C.; Leininger, T.; Gropen, O.; Grenthe, I.; Wahlgren, U. Reduction of uranyl by hydrogen: an *ab initio* study. *Chemical Physics* **1999**, *244*, 185–193, DOI: 10.1016/S0301-0104(99)00112-3.
- (117) Réal, F.; Vallet, V.; Marian, C.; Wahlgren, U. Theoretical investigation of the energies and geometries of photo-excited uranyl(VI) ion: a comparison between wave-function theory and density functional theory. *Journal of Chemical Physics* **2007**, *127*, 214302, DOI: 10.1063/1.2814157.
- (118) Eschrig, H., *Optimized LCAO method and the electronic structure of extended systems*; Springer: 1989.
- (119) Slater, J. C. Atomic shielding constants. *Physical Review* **1930**, *36*, 57–64, DOI: 10.1103/PhysRev.36.57.
- (120) Boys, S. F. Electronic wave functions-I. A general method of calculation for the stationary states of any molecular system. *Proceedings of the Royal Society of London. Series A. Mathematical and Physical Sciences* **1950**, *200*, 542–554, DOI: 10.1098/rspa.1950.0036.
- (121) Patzschke, M. Studies of new inorganic species using relativistic quantum chemistry, Ph.D. Thesis, University of Helsinki, 2006.
- (122) Weigend, F.; Ahlrichs, R. Balanced basis sets of split valence, triple zeta valence and quadruple zeta valence quality for H to Rn: Design and assessment of accuracy. *Physical Chemistry Chemical Physics* **2005**, *7*, 3297–3305, DOI: 10.1039/B508541A.
- (123) Weigend, F.; Häser, M.; Patzelt, H.; Ahlrichs, R. RI-MP2: optimized auxiliary basis sets and demonstration of efficiency. *Chemical Physics Letters* **1998**, *294*, 143–152, DOI: 10.1016/S0009-2614(98)00862-8.
- (124) Küchle, W.; Dolg, M.; Stoll, H.; Preuss, H. Energy-adjusted pseudopotentials for the actinides. Parameter sets and test calculations for thorium and thorium monoxide. *Journal of Chemical Physics* **1994**, *100*, 7535–7542, DOI: 10.1063/1.466847.
- (125) Baerends, E. J. et al. ADF2018, SCM, Theoretical Chemistry, Vrije Universiteit, Amsterdam, The Netherlands, <https://www.scm.com>.

- (126) Van Lenthe, E.; Baerends, E. J. Optimized Slater-type basis sets for the elements 1–118. *Journal of Computational Chemistry* **2003**, *24*, 1142–1156, DOI: 10.1002/jcc.10255.
- (127) Tomasi, J.; Mennucci, B.; Cammi, R. Quantum mechanical continuum solvation models. *Chemical Reviews* **2005**, *105*, 2999–3094, DOI: 10.1021/cr9904009.
- (128) Barone, V.; Cossi, M. Quantum Calculation of Molecular Energies and Energy Gradients in Solution by a Conductor Solvent Model. *Journal of Physical Chemistry A* **1998**, *102*, 1995–2001, DOI: 10.1021/jp9716997.
- (129) Takano, Y.; Houk, K. Benchmarking the conductor-like polarizable continuum model (CPCM) for aqueous solvation free energies of neutral and ionic organic molecules. *Journal of Chemical Theory and Computation* **2005**, *1*, 70–77, DOI: 10.1021/ct049977a.
- (130) Cossi, M.; Rega, N.; Scalmani, G.; Barone, V. Energies, structures, and electronic properties of molecules in solution with the C-PCM solvation model. *Journal of Computational Chemistry* **2003**, *24*, 669–681, DOI: 10.1002/jcc.10189.
- (131) Klamt, A.; Schüürmann, G. COSMO: a new approach to dielectric screening in solvents with explicit expressions for the screening energy and its gradient. *Journal of Chemical Society, Perkin Transactions 2* **1993**, *5*, 799–805, DOI: 10.1039/P29930000799.
- (132) Klamt, A. Conductor-like Screening Model for Real Solvents: A New Approach to the Quantitative Calculation of Solvation Phenomena. *Journal of Physical Chemistry* **1995**, *99*, 2224–2235, DOI: 10.1021/j100007a062.
- (133) Klamt, A.; Jonas, V. Treatment of the outlying charge in continuum solvation models. *Journal of Chemical Physics* **1996**, *105*, 9972–9981, DOI: 10.1063/1.472829.
- (134) Fukuda, R.; Ehara, M.; Nakatsuji, H.; Cammi, R. Nonequilibrium solvation for vertical photoemission and photoabsorption processes using the symmetry-adapted cluster–configuration interaction method in the polarizable continuum model. *The Journal of Chemical Physics* **2011**, *134*, 104109, DOI: 10.1063/1.3562211.
- (135) Kim, H. J.; Hynes, J. T. Equilibrium and nonequilibrium solvation and solute electronic structure. I. Formulation. *The Journal of Chemical Physics* **1990**, *93*, 5194–5210, DOI: 10.1063/1.459665.

Part II

Results

Outline

Luminescence spectroscopy is particularly interesting to investigate U(VI) compounds regarding both their chemical and electronic structures. The experimental luminescence spectrum, composed of several emission bands, is usually analyzed by determining the band shape, the band positions, particularly "hot band" position, and the band spacing. Interpretation and assignment of transitions is however a difficult task from the only experimental measurements. Different contributions to the recorded spectrum may occur from each luminescing U(VI) compounds. Indeed the spectra may be influenced by both short-range and long-range effects, such as the nature of the first-shell ligands, the effects of the counter-ions, and solvent effects. While adding complexity in the data interpretation, a better understanding and characterization of these effects on the U(VI) luminescence will improve the spectroscopic techniques like TRLFS as powerful speciation tools. Complementary to these experimental data, *ab initio* calculations performed on selected model systems could help rationalize these different effects and attribute the various bands of the observed spectra. Thus, by using different complexes of uranium(VI) and by decomposing the impact of ligands, symmetry and counter-ions on the luminescence spectra, as well as the solvent effects (organic versus aqueous media), we were aiming not just to study the effect of different parameters described above, but also to check the universality of the chosen theoretical methodology. This objective has been targeted considering also the importance of using an effective approach that balances accuracy and computational expenses in the calculation of the luminescence spectra of uranium(VI) complexes.

To do so, three model uranyl(VI)-complex systems were selected as depicted in Fig 2.5. The three complexes contain the ligands , Cl^- , CO_3^{2-} and NO_3^- .

Their associated properties will be discussed in three following chapters. For each of them, the proposed pathway consists of several methodological steps: analysis of computed structural parameters (optimized geometries and associated harmonic frequencies) of the ground and luminescent states, followed by the estimation of emission energies coming out from the excited state. These steps were benchmarked with data from literature or from specific measurements. The last and the most interesting and original part of the methodology in this study is the experimental spectrum assignment which is provided by vibronic progression calculation.

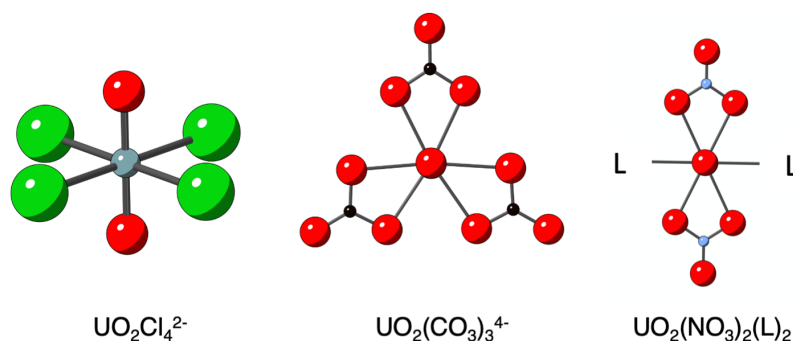


Figure 2.5: The structures of the studied model systems.

The $\text{UO}_2\text{Cl}_4^{2-}$ complex has been thoroughly studied. Experimental and theoretical data are available in the literature mainly from crystal structures. These data allow to validate the structural and energetic data calculated for complexes, which are of high importance for the vibronic progression calculation. Moreover, the luminescence spectrum assignment is available for this complex thanks to the magnetic circular dichroism data. In Chapter 3, the theoretical methodology has been probed on the case of $\text{UO}_2\text{X}_4^{2-}$ ($\text{X}=\text{Cl}, \text{Br}$) complexes to decompose the effect of the first coordination sphere of uranyl in the D_{4h} symmetry. However, the speciation of uranyl in presence of chloride anions in aqueous media often result in a mixture of stoichiometries. Thus the recorded spectra usually contain several contributions to the luminescence corresponding to the different species with different symmetry and coordination. Luckily, the

uranyl tetrachloride anionic complex can be stabilized in non-aqueous media, in which luminescence can be directly measured. In our study, the tetraalkylammonium salt Aliquate 336 was used to extract the $\text{UO}_2\text{Cl}_4^{2-}$ anion from aqueous to organic phase (*n*-dodecane) by an ion pairing mechanism forming the compound $[\text{A336}]_2[\text{UO}_2\text{Cl}_4]$. We modeled the luminescence spectra of the uranyl tetrahalide complex with two A336 as counteranions. The comparison of the results with bare $\text{UO}_2\text{Cl}_4^{2-}$ anion allowed to decompose the effect of a solvent of low polarity, as well as the influence of the organic counteranion placed in the second coordination sphere.

The next part of this PhD study is dedicated to the case of the $\text{UO}_2(\text{CO}_3)_3^{4-}$ complexes of the D_{3h} symmetry. The triscarbonatouranyl with inorganic Ca^{2+} and Mg^{2+} as counteranions in aqueous media has been extensively studied to mine the speciation and thermodynamic data. From the TRLFS data, it has been observed, that the nature of counteranion and its amount change the luminescence intensity. Since the Franck-Condon principle implicates a link between the structure and the luminescence intensity, the structural data are necessary to explain changes in the luminescence intensity. Unfortunately, the data obtained by EXAFS technique do not show any measurable difference in the $\text{M}_n\text{UO}_2(\text{CO}_3)_3^{(4-2n)-}$ ($\text{M} = \text{Mg}, \text{Ca}; n = 0-2$) complexes structures, that could be used to explain the luminescence. In Chapter 4, to explain experimental observations, we have applied the theoretical methodology on the model systems $\text{Na}_m\text{M}_n\text{UO}_2(\text{CO}_3)_3^{(4-m-2n)-}$ ($\text{M} = \text{Mg}, \text{Ca}; m, n = 0-2$) including the long-range water solvation. An extensive analysis of the structures and harmonic frequencies has been performed. The nature of the "hot band" on experimental spectra could be defined. The effect of the first coordination sphere on the luminescence has been decomposed, as it is reflected more in emission energies than in structural parameters, allowing also to understand the "famous" blue shift of the luminescence of the triscarbonatouranyl complexes. The correlation of the luminescence intensity with the nature and amount of the inorganic counteranion has also been deduced, thanks to computed vibronic progressions.

The last Chapter 5 is devoted to uranyl binitrate compounds. These complexes have a particular interest in the nuclear industry, especially in the reprocessing of used nuclear fuel. The modified PUREX extraction process is designed

to extract U(VI) in a form of $\text{UO}_2(\text{NO}_3)_2(\text{L})_2$ as it has been confirmed by EXAFS, XRD and TRLS measurements. In our study, the L ligands are two molecules of N,N-di-(ethyl-2-hexyl)isobutyramide (DEHiBA) monoamide used to bind to the first coordination sphere of uranyl. The position of DEHiBA molecules can be in *trans* or *cis* with respect to the nitrate ligands and they can co-exist in solution. In order to use luminescence spectroscopy for speciation issue, it is important to determine whether or not these conformers could be discriminated by their spectroscopic properties. To answer this question, the spectra of *trans*- and *cis*- $\text{UO}_2(\text{NO}_3)_2(\text{DEHiBA})_2$ conformers were modeled and compared to the available experimental time-resolved luminescence spectra. Moreover, to quantify the effect of DEHiBA on $\text{UO}_2(\text{NO}_3)_2$, the hydrated uranyl binitrate $\text{UO}_2(\text{NO}_3)_2(\text{H}_2\text{O})_2$ complexes in the same *trans* and *cis* configurations were modeled to show the impact of organic DEHiBA to the luminescence spectra.

Investigation of the luminescence of $[\text{UO}_2\text{X}_4]^{2-}$ ($\text{X}=\text{Cl}, \text{Br}$) complexes in organic phase using time-resolved laser-induced fluorescence spectroscopy and quantum chemical simulations

The material presented in this chapter forms the publication [136].

3.1 Abstract

The luminescence properties of the $[\text{UO}_2\text{Cl}_4]^{2-}$ complex in an organic phase, especially the influence of large organic counter cations, have been studied by time-resolved laser-induced fluorescence spectroscopy (TRLFS) and ab initio modeling. The experimental spectrum was assigned by vibronic Franck-Condon calculations on quantum chemical methods based on a combination of relativistic density functional approaches. The shape of the luminescence spectrum of the uranyl tetrachloride complex is determined by symmetrical vibrations and

geometrical change upon emission. The possible change of the luminescence properties depending on the first and second uranyl coordination sphere was predicted theoretically for $[\text{UO}_2\text{Br}_4]^{2-}$ and $[\text{R}_4\text{N}]_2[\text{UO}_2\text{Cl}_4]$ ($[\text{R}_4\text{N}] = [\text{Bu}_4\text{N}]$, [A336]) systems. The computations reveal that for U(VI), the second coordination sphere has little influence on the spectrum shape, making speciation of uranyl complexes with identical first coordination-sphere ligands tedious to discriminate. The computed structural changes agreed well with experimental trends; theoretical spectra and peaks attribution are in a good accordance with TRLFS and magnetic circular dichroism (MCD) data respectively.

3.2 Introduction

The knowledge of the stoichiometries and stabilities of the chemical species of uranium is of key importance for the understanding of the chemical reactivity of uranium in environmental or industrial situations. The speciation of uranium in solution has thus been a major topic of investigations by both experimental and theoretical methods. Among the powerful spectroscopic techniques, time-resolved laser-induced luminescence spectroscopy (TRLFS) has been widely used for the characterization of uranyl species in solutions and in solid phases, because of its high sensitivity to changes of the first coordination sphere of UO_2^{2+} . The luminescence spectra of uranyl complexes in solution show in general a narrow energetic range of about 6000 cm^{-1} . In this region only a single electronic transition between the initial and final states can be identified and it is vibrationally resolved with the bands corresponding to different vibrational quantum numbers [137]. In the case of mixtures of uranyl species, the interpretation of TRLFS data can be difficult as one needs to deconvolute overlapping emission spectra in similar time frame. Therefore spectroscopic considerations are often insufficient to unambiguously determine the nature of the complexes. This is why a theoretical support based on quantum chemical modeling appears as a way to better validate TRLFS data interpretations by decomposing the different effects that might induce changes in the emission spectra of uranyl complexes.

Several research teams have tried to simulate emission spectra of uranyl complexes with quantum chemical methods [138–140], based on either wave-

function theory (WFT) or density functional theory (DFT), and taking into account relativistic effects [104, 141–143] (scalar relativistic effects and spin-orbit coupling) as they are important for actinide complexes. While WFT methods are well-suited for accurate calculations, the high computing costs limit the simulations to small clusters of heavy elements like uranium. DFT approaches are more appropriate for cost-effective calculations applied to actinides, but can be challenged regarding their accuracy for the description of the electronic ground and excited states, and their ability to reproduce low-lying electronic transitions and their vibronic resolutions. Tecmer et al. [26] have evaluated the accuracy of pure and hybrid exchange-correlation functionals for the bare uranyl cation isoelectronic uranium triatomics, arguing that hybrid functionals can be used for quantitative prediction of the low-lying excited states of uranyl. Uranyl tetrachloride complexes have been thoroughly studied as a reference system because direct comparisons with luminescence data from crystals are possible [144]. Moreover, this complex can also be stabilized in non-aqueous solvents [23, 145, 146], and is of interest in some solvent extraction protocols [147, 148]. The structure of the uranyl tetrachloride is well-established with four chloride ions in the equatorial plane of the UO_2^{2+} moiety, resulting in a D_{4h} symmetry. The effects of second-sphere counter cations, solvent molecules or solvating agents also have to be considered, as to quantify their influence on the structures, the electronic states energies, and the vibronic progressions.

In this work we compare the results of *ab initio* calculations to experimental data obtained from a *n*-dodecane solution in which the uranyl tetrachloride complex was extracted by a tetra-alkyl ammonium molecule (Aliquate[®] 336). The methodology is a step-by-step approach in order to validate the hypotheses and approximations we made. The computations of the ground and the excited state structural and vibrational parameters are necessary for the understanding of theoretical and experimental spectra. Because the main effect on the luminescence data is commonly accepted to originate from the first coordination sphere, the chloride ligands were substituted by bromides to discuss the trends, validate our method, and evaluate its applicability to other types of uranyl complexes. We will also quantify the effects of outer-sphere counter ions and long-range solvation effects on the computed spectra.

3.3 Experimental details

3.3.1 Sample preparation

[A336]₂[UO₂Cl₄] in *n*-dodecane The sample preparation method has been adapted from Hellé et al. [148, 149]. Aliquate[®] 336 (98 %) was purchased from Alfa Aesar. HCl (32 %), 1-decanol (99 %) and *n*-dodecane were purchased from Sigma-Aldrich. HClO₄ was purchased from Merck. All reagents were used as received without further purification. A stock solution of uranium(VI) was prepared by dissolution of U₃O₈ in a hot perchloric acid solution. The U(VI) concentration was checked by inductively coupled plasma mass spectrometry (ICP-MS). The aqueous solution was prepared by dilution of this stock solution into a 5 M hydrochloric acid solution to get a uranium (VI) concentration of 10⁻⁵ M. Deionized water (Alpha-Q, Millipore, 18.2 MΩ cm) was used for the preparation of all aqueous solutions.

The organic solution was prepared by dissolving weighed amounts of Aliquate[®] 336 and 1-decanol in sufficient amount of *n*-dodecane to reach a concentration of 10⁻² M of Aliquate[®] 336 with 1 % of 1-decanol. It was then pre-equilibrated by contact with a uranium-free 5 M hydrochloric acid solution during 2 h of shaking and separated.

For uranium extraction, 2 mL of the aqueous solution was contacted with an equal volume of the pre-equilibrated organic solution. The mixture was shaken in a thermomixer at 20 °C during 1 h, and about 2 mL of the organic phase was sampled after 2 h of decantation for the spectroscopic measurements.

3.3.2 Time-Resolved Laser-Induced Fluorescence Spectroscopy

The sample was put in a 1 cm-path-length quartz cuvette that was placed in a TRFLS set-up as described afterwards. The excitation wavelength was provided by a tunable OPO system (PantherEx OPO, Excel Technology) pumped by a Nd/YAG laser at 355 nm (Surelite-I, Excel Technology). The excitation was tuned to $\lambda_{ex} = 427$ nm which corresponds to a maximum of absorption by uranium(VI) in our samples. The 5 ns laser pulses were generated at 10 Hz for an energy of

about 3.15 mJ]. The detection set-up has already been described elsewhere [150]. The luminescence signal was collected during a gate width of 200 μ s, with a gate delay of 100 ns after the excitation by the laser pulse, the delay value being carefully chosen as discussed in the Annex A. The luminescence spectrum of the sample was recorded at room temperature (22 ± 1 °C) from the accumulation of 1000 scans. The background noise was subtracted by the software from the recorded spectrum of a $[A336]_2[UO_2Cl_4]$ in *n*-dodecane sample.

3.3.3 Computational details

Since our aim is to use quantum chemical methods to elucidate the luminescence band shapes of the complexes, several data need to be calculated. The ground-state and first excited state geometries, their associated harmonic frequency spectra and Hessian matrices have to be computed in order to derive the overlap integrals between the vibrational wave-functions associated to the ground and excited states - Frank-Condon factors (FCFs). The FCFs were computed using ezSpectrum 3.0 [151] program by taking all necessary data generated by the ab initio packages described below. The Duschinsky rotations were used as implemented in the program. The numbers of vibrational quanta in excited and ground state were selected to be one and five, respectively. All the spectra were computed at 300 K. For the larger systems, all normal modes with vibrational frequencies larger than 1000 cm^{-1} were excluded from the FCFs calculations, to keep the computational costs affordable.

Model systems The interactions between uranyl and its first and second coordination spheres might affect the electronic structure of the uranyl unit. As the influence of the chloride ligands in $UO_2Cl_4^{2-}$ complex was excellently reviewed by different experimental [5, 23, 145, 152, 153] and theoretical methods [10, 42, 43, 45, 154], this system was selected as a benchmark to quantify the effect of ligands in the first coordination sphere by substituting chlorides by bromides, and the effect of the counter-ions in the second coordination sphere, *i.e.* the quaternary ammonium cations. Furthermore, to discuss the importance of long-range solvent effects, the model systems were computed in gas phase and

with inclusion of solvent effects (*n*-dodecane and acetone). The structures are represented in Fig. 3.1

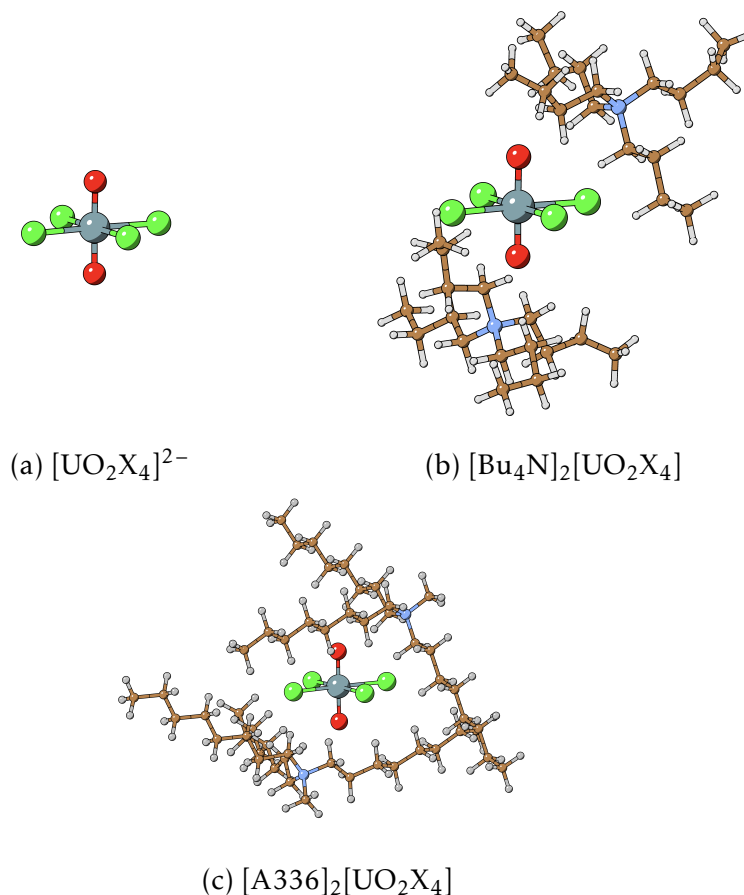


Figure 3.1: The complexes structures of $[\text{R}_4\text{N}]_2[\text{UO}_2\text{X}_4]$ ($[\text{R}_4\text{N}] = [\text{Bu}_4\text{N}]$, $[\text{A336}]$ and $\text{X}=\text{Cl}$, Br) in gas phase optimized at the DFT/PBE0 level of theory.

Structures of the ground and excited states, and harmonic frequencies In the sake of keeping the computational costs within week scale and of simplifying the data analysis, the structures of the uranyl tetrahalides complexes were enforced to D_{4h} symmetry, whereas no symmetry constrains were applied to the complexes with a second coordination sphere. All the ground-state molecular geometries were optimized including the relativistic effects at the spin-free level in the gas phase and with solvent effect using Density functional Theory (DFT). The Kohn-

Sham equation was solved using the hybrid PBE0 functional [86]. The structure of the first low-lying excited state was optimized using the time-dependent (TD)-DFT/PBE0 method as implemented in Turbomole V7.3 2018 [155] and Gaussian 16 [156] codes. The vibrational harmonic frequencies were computed using either an analytic Hessian matrix or numerical finite differences of the gradient. All geometries considered for the vibronic spectra calculations represent true minima as they have no imaginary frequencies.

In these calculations, def2-TZVP (second generation of triple- ζ polarization quality) Karlsruhe basis sets [122, 123] have been used for all light elements (H, C, N, O, Cl). For the heaviest atoms, small-core Relativistic Effective Core Pseudopotentials (RECP) were used, namely the 60-core electron one for uranium [124, 157] along with the def-TZVP (first generation of triple- ζ polarization quality) basis set [158], and the 28-core electrons ECP for bromine with the associated aug-cc-pVTZ-PP basis set [159]. To speed up the calculations, the resolution of the identity approximation to compute the Coulomb Integrals (RI-J) [160, 161] with appropriate auxiliary basis sets [158, 162] was employed.

Vertical absorption and emission energies Based on the benchmark calculations carried out by Tecmer et al. [26, 163, 164] on a series of uranium(VI)-based compounds, the CAM-B3LYP [87] exchange-correlation functional was found to be more accurate than PBE0 for uranyl valence transition energies. Thus, to accurately position the “hot bands”, the vertical excitation and emission energies with and without accounting for solvent effects were obtained from the ground and excited-state structures, respectively, with TD-DFT single-point calculations with the latter functional and the Amsterdam Density Functional package (ADF2018.01) [125]. All atoms were described by TZ2P Slater-type basis sets [126] (triple- ζ with two polarization functions quality), without frozen core approximation. The scalar relativistic (SR) and spin-orbit coupling (SOC) effects were accounted for by the ZORA Hamiltonian [111].

Continuum solvent models Long-range solvent effects were modeled by polarized continuum medium models, with two similar flavors, the Continuum Polarizable Conductor Model (CPCM) [128, 130] one implemented in Gaussian

16 program, and the conductor-like screening model (COSMO) model [131–133] implemented in the ADF package. The used relative permittivity values (ϵ_r) for *n*-dodecane and acetone are 2.006 and 20.493, respectively.

3.4 Results and discussions

3.4.1 Experimental luminescence spectra

The time-resolved luminescence spectrum of the uranyl sample in the presence of chloride ions and Aliquate[®] 336 in *n*-dodecane with 1 % of 1-decanol is shown on Figure 3.2 (black line). It is superimposed with the spectrum (red line) acquired by Görller-Walrand et al. [23] in similar conditions and in acetone. The spectrum also compares well to those obtained earlier in chloroaluminate [153], tetraalkylammonium [146] and pyrrolidinium [145] ionic liquids. The spectrum of $[A336]_2[UO_2Cl_4]$ in *n*-dodecane in Figure 3.2 show an electronic transition ("hot band") at low energy about $21\,000\text{ cm}^{-1}$ followed by a series of vibronic peaks in the $20\,300\text{--}16\,000\text{ cm}^{-1}$ range, which is typical of the $[UO_2Cl_4]^{2-}$ species with a D_{4h} coordination symmetry [7]. A mono-exponential decay with a fluorescence lifetime of $0.3\text{ }\mu\text{s}$ was measured for the uranium(VI) sample in a presence of chloride ions, Aliquate[®] 336 and *n*-dodecane. It confirms the formation of a unique complex, which was assumed to be $[A336]_2[UO_2Cl_4]$ with four chloride ions coordinated to uranyl in its equatorial plane, in line with the extracted complex stoichiometry [147].

The decomposition of the $[A336]_2[UO_2Cl_4]$ luminescence spectra has been performed by Reiller et al. [147]. The resolution of the presently used apparatus did not allow to resolve well some of the transitions, and revealed only the wide components which cover several vibronic progressions in one peak. Moreover, a difference of the relative intensities is observed around $20\,295\text{ cm}^{-1}$ in *n*-dodecane due to the long gate width selected to collect more luminescence signal in our measurements. The spectrum in *n*-dodecane is shifted to the blue side by 30 cm^{-1} , compared to the one in acetone, and only by 5 cm^{-1} with respect to the one in $[Bu_3MeN][Tf_2N]$ ionic liquid [146]. Thus, from the measurements, one can conclude that neither the counter-ion nor the type of solvent have any

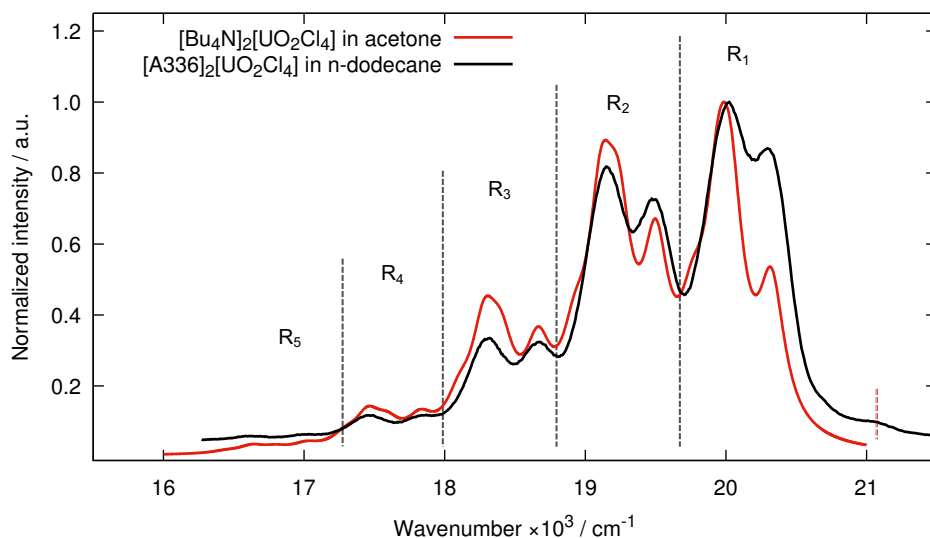


Figure 3.2: Recorded time-resolved luminescence spectra of $[\text{Bu}_4\text{N}]_2[\text{UO}_2\text{Cl}_4]$ in acetone (the maxima taken from Görller-Walrand et al. [[23]], the Lorentzian shape computed) and $[\text{A336}]_2[\text{UO}_2\text{Cl}_4]$ in *n*-dodecane (this work). Vertical dashed red line shows the “hot band” position and R_n , ($n = 1 - 5$) corresponds to vibronic progression region. Details on the spectral data are available in Table A.1 of the Annex A.

significant influence on the position of maxima of the luminescence bands. The change in the relative intensities of the transitions along the vibronic progression has been attributed by Sornein et al. [146] to the formation of C–H...Cl hydrogen bonding between the chloride of the $[\text{UO}_2\text{Cl}_4]^{2-}$ moiety and a hydrogen atom of a cation present in the ionic liquid. As we are using an aprotic solvent (*n*-dodecane), this effect may also be present in our uranyl tetrachloride sample.

The spacing between the vibronic progressions of the luminescence spectrum corresponds to the ground-state uranyl stretching frequency value ν_s . One can extract ν_s value by only taking into account the spacing between the vibrational maxima of the same nature for $[\text{A336}]_2[\text{UO}_2\text{Cl}_4]$ in *n*-dodecane. The resulting ν_s value amounts to $836 \pm 18 \text{ cm}^{-1}$, which is in good agreement with the values, $823 \pm 14 \text{ cm}^{-1}$, 825 cm^{-1} , and $850 \pm 25 \text{ cm}^{-1}$ observed in acetone [23], $[\text{C}_4\text{mim}][\text{Tf}_2\text{N}]$ [145], and in $[\text{Bu}_3\text{MeN}][\text{Tf}_2\text{N}]$ [146], respectively. This vibra-

tion corresponds to a Raman active vibration of the uranyl unit and can be correlated to the U–O_{yl} bond length. Using the empiric relation of Bartlett and Cooney [46]:

$$R_{U-O_{yl}} = 106.5 \times \nu_s^{-2/3} + 0.575 \quad (3.1)$$

we calculated the U–O_{yl} bond length to be equal to 1.77 ± 0.01 Å (using $\nu_s = 836 \pm 18$ cm⁻¹) for our uranyl sample. This value agrees with all experimental data listed in Table 3.1, and can therefore serve as reference data to assess the accuracy of the *ab initio* calculations we will now discuss.

3.4.2 Ground and excited state structures of the uranyl tetrahalide complexes

Uranyl tetrahalide dianions The structure of uranyl tetrachloride dianion has been well-studied by the variety of theoretical and experimental techniques [5, 10, 144, 163, 165–168]. The inclusion of all effects to mimic the experimental conditions is challenging for *ab initio* calculations, namely because of the difficulties in building chemically relevant chemical models and the fast growing of the computational costs as the system size grows. The present quantum chemical study was performed on models with increasing chemical complexity to approach the solution sample.

The spin-free optimized ground and the first excited state distances between uranium and the coordinated atoms of the $[\text{UO}_2\text{Cl}_4]^{2-}$ and $[\text{UO}_2\text{Br}_4]^{2-}$ together with experimental data are shown in Table 3.1.

In the $[\text{UO}_2\text{Cl}_4]^{2-}$ gas-phase PBE0 calculations, the ground state U–O_{yl} bond length 1.758 Å value is in a good agreement with 1.766 Å obtained with the CCSD(T) wave-function method, while U–Cl bond length 2.714 Å comes out shorter than 2.735 Å. Moreover, the PBE0 geometries are in good accordance with the all-electron CAM-B3LYP results reported by Tecmer et al. [163]. This gives us confidence in the ability of PBE0 to provide fairly accurate geometries of the uranium(VI) containing complexes. The inclusion of solvent effects on $[\text{UO}_2\text{Cl}_4]^{2-}$ does not significantly change the U–O_{yl} bond distance

as compared to the gas-phase calculations, but it shortens U–Cl bond length as the solvent polarity increases. Keeping in mind that we do not have strictly the same conditions as in the experiment, it is worth examining trends in both theoretical and experimental data. The comparison of the experimental crystal structure of $\text{Cs}_2\text{UO}_2\text{Cl}_4$ [144] with the structure of uranyl tetrachloride dianion in acetonitrile [166] shows that the U–O_{yl} bond length is almost the same in both conditions, while U–Cl values are found to be longer in solution by about 0.01 Å.

To quantify the influence of the ligand nature in the first coordination sphere, the chloride ligands were replaced by bromide ligands which have the same type of bonding with uranium, but larger ionic radii. The uranyl ion coordinated by four bromide ligands has been prepared in crystal form [167], while it is hardly stabilized in solution. The experimental structure of $\text{Cs}_2\text{UO}_2\text{Br}_4$ crystal shows that U–O_{yl} bond distance (1.777 Å) is almost equal to the one found in the chloride homologue, $\text{Cs}_2\text{UO}_2\text{Cl}_4$ ($R_{\text{U-O}_{yl}} = 1.774$ Å), whereas the U–Br distance is longer by 0.149 Å than U–Cl bond length. The gas-phase geometries of $[\text{UO}_2\text{Cl}_4]^{2-}$ and $[\text{UO}_2\text{Br}_4]^{2-}$ follow this trend; the substitution of chloride by bromide ligands leads to the insignificant stabilization of U–O_{yl} bond, and the U–Br bond distance is longer by 0.169 Å than the U–Cl, as the U–Br bond is weaker than the U–Cl one.

The lowest triplet excited state in $[\text{UO}_2\text{X}_4]^{2-}$ complexes corresponds to an excitation of an electron out of an orbital that is a mixture of the bonding σ_u orbital of the uranyl unit and the halide valence p orbitals, into the non-bonding δ_u uranium orbital. When the transition occurs the U–O_{yl} bond weakens and the excited state potential curve shifts along the symmetric U–O_{yl} mode to larger U–O_{yl} distances and becomes flatter [43]. Looking at the excited state geometries of the uranyl tetrahalide dianions, one can note a lengthening of the U–O_{yl} bond by 0.031 Å and 0.028 Å, in $[\text{UO}_2\text{Cl}_4]^{2-}$ and $[\text{UO}_2\text{Br}_4]^{2-}$, respectively, since the excitation depopulates the U–O_{yl} bonding orbital. The differences of the U–X, (X=Cl, Br) bonds are small, about 0.010 Å on average. From highly resolved low-temperature two-photon absorption spectra of $\text{Cs}_2\text{UO}_2\text{Cl}_4$, Denning et al. [5, 7] determined that the U–O_{yl} and U–Cl bonds elongate by 0.070 Å and 0.014 Å, respectively. Inclusion of long-range solvent effects affect the excited state

Table 3.1: Ground and excited state geometries of the $[\text{UO}_2\text{X}_4]^{2-}$, $\text{X} = \text{Cl}, \text{Br}$ compared to selected previous results.

	$R_{\text{U}-\text{O}_i}, \text{\AA}$	$R_{\text{U}-\text{X}}, \text{\AA}$	Compound/media	Method	Ref.
Ground state					
$[\text{UO}_2\text{Cl}_4]^{2-}$	1.758	2.714	gas-phase	R-ECP/PBE0	this work
	1.766	2.735	gas-phase	CCSD(T)	[165]
	1.764	2.712	gas-phase	all-electron/CAM-B3LYP	[163]
	1.774	2.671	$\text{Cs}_2\text{UO}_2\text{Cl}_4$	X-ray	[144]
	1.759	2.699	CPCM n-dodecane	R-ECP/PBE0	this work
	1.761	2.683	CPCM acetone	R-ECP/PBE0	this work
	1.770	2.680	acetonitrile	EXAFS	[166]
$[\text{UO}_2\text{Br}_4]^{2-}$	1.750	2.883	gas-phase	R-ECP/PBE0	this work
	1.749	2.905	gas-phase	R-ECP/CAM-B3LYP	this work
	1.777	2.820	$\text{Cs}_2\text{UO}_2\text{Br}_4$	X-ray	[167]
Excited state					
$[\text{UO}_2\text{Cl}_4]^{2-}$	1.789	2.721	gas-phase	R-ECP/PBE0	this work
	1.844	2.685	$\text{Cs}_2\text{UO}_2\text{Cl}_4$	Two-photon absorption	[5]
	1.790	2.706	CPCM n-dodecane	R-ECP/PBE0	this work
	1.791	2.692	CPCM acetone	R-ECP/PBE0	this work
$[\text{UO}_2\text{Br}_4]^{2-}$	1.778	2.895	gas-phase	R-ECP/PBE0	this work
	1.780	2.918	gas-phase	R-ECP/CAM-B3LYP	this work

structure in the same way as for the ground state.

The analysis of the vibrational frequencies is very important for the characterization of the theoretical luminescence spectra, as specific vibrations appear in the vibronic progression. Some of the ground-state vibrational frequencies are responsible for the band spacing in the experimental luminescence spectrum, while the atomic displacement between the ground and excited-state geometries is responsible for the intensities ratio. The U–X (ν_{U-X}), U–O_{yl} (ν_s) symmetrical stretching modes and O_{yl}–U–O_{yl} bending mode (ν_b) contribute to the luminescence spectra shape to a large extent, and their values for the [UO₂Cl₄]²⁻ and [UO₂Br₄]²⁻ complexes are listed in Table 3.2. The U–O_{yl} asymmetrical stretching mode (ν_a), which is vibronically silent, is also shown to discuss trends. Using the vibrational perturbation theory [169, 170] as implemented in Gaussian 16 [156], we have computed the anharmonic corrections, which turned out to be small, of the order of 5 and 3 cm⁻¹ for the ground and excited states respectively (See Table A.2 in the Annex A).

For the gas-phase [UO₂Cl₄]²⁻ model, the computed ν_{U-Cl} , ν_b , ν_s and ν_a frequencies are smaller in the excited state than in the ground state by 4, 4, 80 and 115 cm⁻¹, respectively. The PBE0 calculations reproduce with an impressive accuracy the measured red shift of the stretching mode, ν_s , 82 cm⁻¹, in Cs₂UO₂Cl₄, and underestimates that for the bending mode, 20 cm⁻¹. The latter discrepancy has negligible impact as the ν_s dominates the vibronic progressions visible in the luminescence spectra.

Turning now to the vibrational frequencies obtained with solvent effects, we observed opposite behavior of the U–Cl and U–O_{yl} frequencies. With increasing of polarity the ν_{U-Cl} stretching frequencies insignificantly increase (4 and 7 cm⁻¹) for the ground and excited states, respectively, while the uranyl ν_b , ν_s and ν_a decrease by 5 up to 25 cm⁻¹ in both states. This shift of the ground-state frequencies should be observable in the computed luminescence spectra, namely in the spacing between the vibrationally resolved peaks, while the change of the excited state frequencies should only affect the vibronic intensities.

The substitution of chlorides by bromides in the uranyl equatorial plane lead to the following changes in the vibrational spectra. Compared to uranyl tetrachloride, the ν_b value decreased by less than 10 cm⁻¹ in both ground and excited

Table 3.2: Ground and excited state vibrational frequencies (in cm^{-1}) of the $[\text{R}_4\text{N}]_2[\text{UO}_2\text{X}_4]$, ($[\text{R}_4\text{N}] = [\text{Bu}_4\text{N}]$, $[\text{A336}]$) compounds.

System	ν_{U-X}	ν_b	ν_s	ν_a	Method	Ref.
Ground state						
$[\text{UO}_2\text{Cl}_4]^{2-}$	237	275	894	974	R-ECP/PBE0 gas-phase	this work
	235	269	889	960	R-ECP/PBE0 n-dodecane	this work
	241	265	889	949	R-ECP/PBE0 acetone	this work
	264 [5]	250	832	915	Raman and IR in solid	[7]
$\text{Cs}_2\text{UO}_2\text{Cl}_4$						
$[\text{Me}_4\text{N}]_2[\text{UO}_2\text{Cl}_4]$			831	909	Raman and IR in solid	[171]
	240	263	869		Raman in solid	[172]
	270	286	869	945	R-ECP/PBE0 gas-phase	this work
	258	262	833	919	Raman and IR in CH_2Cl_2 solution	[173]
$[\text{A336}]_2[\text{UO}_2\text{Cl}_4]$	266	288	876	957	R-ECP/PBE0 gas-phase	this work
$[\text{UO}_2\text{Br}_4]^{2-}$	144	262	907	988	R-ECP/PBE0 gas-phase	this work
$[\text{C}_7\text{H}_{16}\text{NO}_2][\text{UO}_2\text{Br}_4]$	173	252	826	904	Raman and IR in solid	[174]
Excited state						
$[\text{UO}_2\text{Cl}_4]^{2-}$	233	271	814	859	R-ECP/PBE0 gas-phase	this work
	236	268	811	854	R-ECP/PBE0 n-dodecane	this work
	240	263	808	848	R-ECP/PBE0 acetone	this work
$\text{Cs}_2\text{UO}_2\text{Cl}_4$		230	750	830	N.A.	[23]
$[\text{Bu}_4\text{N}]_2[\text{UO}_2\text{Cl}_4]$	266	281	799	845	R-ECP/PBE0 gas-phase	this work
$[\text{A336}]_2[\text{UO}_2\text{Cl}_4]$	261	284	802	854	R-ECP/PBE0 gas-phase	this work
$[\text{UO}_2\text{Br}_4]^{2-}$	151	264	876	935	R-ECP/PBE0 gas-phase	this work

states. The ν_s increased by 13 and 62 cm^{-1} in the ground and excited states, respectively. Similarly, the ν_a increased by 14 cm^{-1} for the ground and 76 cm^{-1} for the first excited state. The U–Br stretching mode is 83 cm^{-1} lower in both ground and excited states than the U–Cl symmetric stretching vibration. This is in line with the ground-state experimental trends measured for $\text{Cs}_2\text{UO}_2\text{Cl}_4$ and $[\text{C}_7\text{H}_{16}\text{NO}_2][\text{UO}_2\text{Br}_4]$ (91, 2, 6 and 9 cm^{-1} for $\nu_{\text{U-Br}}$, ν_b , ν_s and ν_a , respectively). These changes indicate that the bromide ligand has a smaller effect on the electronic structure of uranium than chloride, since the U–Br interaction has less impact on the U–O_{yl} bonding. Consistently, the ν_s frequency is larger than in $[\text{UO}_2\text{Cl}_4]^{2-}$ and close to the bare uranyl value. For $[\text{UO}_2\text{Br}_4]^{2-}$ the shifts of vibrational frequencies between the ground and excited state are listed in Table A.10 of the Annex A.

Organic cation - uranyl tetrachloride: $[\text{A336}]_2[\text{UO}_2\text{Cl}_4]$ The $[\text{UO}_2\text{Cl}_4]^{2-}$ dianion in interaction with the organic ligand has been prepared in the conditions described in the experimental section. The final compound is predicted to be the uranyl tetrachloride associated with two extractant cations of methyltrioctylammonium $[\text{A336}]_2[\text{UO}_2\text{Cl}_4]$ as a result of an ion-exchange mechanism [147]. Interestingly, Görrler-Warland et al. [23] stabilized the $[\text{UO}_2\text{Cl}_4]^{2-}$ dianion in solution with tetrabutylammonium chloride (Bu_4NCl), a ligand belonging to the group of tetraalkylammonium salts as the Aliquate[®] 336. For our purpose, the geometries of the ground and luminescent states of both complexes were optimized placing the two counter-cations in the second coordination sphere in a *trans* position. The bond distances are shown in Table 3.3, while the vibrational frequencies are shown in Table 3.2.

If one compares the computed geometrical parameters to that of the models without an explicit second-coordination sphere (Table 3.1), the counter-cations induce a weakening of uranyl bond and the loss of the D_{4h} symmetry. These changes are due to the presence of weak hydrogen bonds between the hydrogen atoms of the alkyl chains of cation with the oxygen and chloride atoms of uranyl tetrachloride unit [146] (see Annex A Figure A.3 and Table A.3). The ground-state geometries of uranyl tetrachloride in $[\text{Bu}_4\text{N}]_2[\text{UO}_2\text{Cl}_4]$ and $[\text{A336}]_2[\text{UO}_2\text{Cl}_4]$ have been found to be nearly the same; the U–O_{yl} bond lengths

are longer by about 0.010 Å than in the bare $[\text{UO}_2\text{Cl}_4]^{2-}$ complex. Moreover, because of the symmetry distortion and interaction of chloride ligands with the counter ion, the U–Cl distances differ by 0.026 up to 0.118 Å as compared to the bare $[\text{UO}_2\text{Cl}_4]^{2-}$. Even though our theoretical model does not account for the long-range effects induced by the presence of other species beyond the second coordination sphere, these gas-phase structures are in a good accordance with the experimental crystal structures measured for parent compounds with a shorter alkyl chain, such as $[\text{Me}_4\text{N}]_2[\text{UO}_2\text{Cl}_4]$ and $[\text{Et}_4\text{N}]_2[\text{UO}_2\text{Cl}_4]$ [171]. This observation makes us conclude that the chain length of a tetraalkylammonium cation has merely no influence on the U–O_{yl} and U–Cl bond-length values and that both organic counter-cations (R_4N) interact with the uranyl tetrachloride dianion in a similar way. Since the influence of long-range solvent effects on the $[\text{UO}_2\text{Cl}_4]^{2-}$ bare complexes is negligible, we rely in the following on the gas-phase structures for the $[\text{R}_4\text{N}]_2[\text{UO}_2\text{Cl}_4]$ complexes.

The addition of two counter-cations in our chemical model does not change the nature of the first excited state. As a result, the luminescent-state geometry is not significantly impacted by the counter-cations: as compared to the bare $[\text{UO}_2\text{Cl}_4]^{2-}$ complexes, the U–O_{yl} bond length stretches by 0.028 Å for $[\text{R}_4\text{N}]_2[\text{UO}_2\text{Cl}_4]$ and the U–Cl distances are from 0.003 up to 0.027 Å longer for both types of complexes.

The calculated frequencies have been compared with data from experimental Raman and IR measurements of different crystals or liquid samples of $[\text{R}_4\text{N}]_2[\text{UO}_2\text{Cl}_4]$ [171–173]. The computed symmetrical stretching frequency ν_s for $[\text{Bu}_4\text{N}]_2[\text{UO}_2\text{Cl}_4]$ matches the value measured for the $[\text{Et}_4\text{N}]_2[\text{UO}_2\text{Cl}_4]$ crystal [172]. For $[\text{Bu}_4\text{N}]_2[\text{UO}_2\text{Cl}_4]$, the gas-phase computed frequencies ν_{U-Cl} , ν_b , ν_s and ν_a are overestimated by 12, 24, 36 and 26 cm^{-1} , respectively, with respect to the values measured in dichloromethane solution [173]. From emission spectroscopy measurements, symmetric-stretching vibrational frequency (ν_s) for $[\text{Bu}_4\text{N}]_2[\text{UO}_2\text{Cl}_4]$ in acetone and for $[\text{A336}]_2[\text{UO}_2\text{Cl}_4]$ in *n*-dodecane, were estimated at 823 [23] and 836 cm^{-1} , respectively. Our gas-phase calculations for these exact complexes yield slightly blue-shifted values, 869 and 876 cm^{-1} .

The differences in computed harmonic frequencies of $[\text{UO}_2\text{Cl}_4]^{2-}$ in the two $[\text{R}_4\text{N}]_2[\text{UO}_2\text{Cl}_4]$ complexes are found to be small. The counter-ions in the

Table 3.3: Ground and excited state geometries of the $[R_4N]_2[UO_2Cl_4]$ compounds compared to selected experimental results.

	$R_{U-O_{ij}}, \text{ \AA}$	$R_{U-Cl}, \text{ \AA}$	Compound	Method	Ref.
Ground state					
	1.766(6)	2.648(1)-2.677(1)	$[Me_4N]_2[UO_2Cl_4]$	X-ray	[171]
	1.76(2)-1.77(3)	2.65(1)-2.68(1)	$[Et_4N]_2[UO_2Cl_4]$	X-ray	[171]
	1.769	2.596-2.753	$[Bu_4N]_2[UO_2Cl_4]$	R-ECP/PBE0	this work
	1.767	2.609-2.740	$[A336]_2[UO_2Cl_4]$	R-ECP/PBE0	this work
Excited state					
	1.796	2.599-2.780	$[Bu_4N]_2[UO_2Cl_4]$	R-ECP/PBE0	this work
	1.795	2.614-2.761	$[A336]_2[UO_2Cl_4]$	R-ECP/PBE0	this work

second-coordination sphere only slightly affect the calculated frequencies with respect to the $[\text{UO}_2\text{Cl}_4]^{2-}$ bare ion; the ν_{U-Cl} is 29 cm^{-1} higher, the ν_b has increased by 13 cm^{-1} , while the ν_s and ν_a modes were found to be lower by 18 and 14 cm^{-1} , respectively. This is a result of the loss of symmetry together with the interplay of some motions of hydrogen and carbon atoms in alkyl chain in the vibrational motions. Based on the Franck-Condon principle, one can note that it should improve the band spacing between the vibronic progressions of theoretical luminescence spectrum that will be discussed further down.

The shifts of theoretical frequencies between the ground and excited state of $[\text{A336}]_2[\text{UO}_2\text{Cl}_4]$ are found to be similar to what was experimentally obtained for $\text{Cs}_2\text{UO}_2\text{Cl}_4$. The computed uranyl symmetrical stretching mode shifted by 74 cm^{-1} , very close to the experimental value of 82 cm^{-1} . However, the ν_{U-Cl} and ν_b do not vary during the excitation.

3.4.3 Theoretical absorption and emission energies

As the luminescence spectrum of uranium (VI) complexes arises from the electronic transition from the lowest excited state to the ground state, coupled to progression of vibronic bands, the examination of the whole electronic spectrum is pointless. In this step, we aim at foreseeing the sensitivity to the quantum chemical method of the first triplet excited state absorption and emission energies of the uranyl tetrachloride complex, and on the spectral features of uranium (VI) complexes.

The $[\text{UO}_2\text{Cl}_4]^{2-}$ dianion electronic spectrum has been computed previously with the different levels of theory and detailed discussions of the electronic structure can be found in the literature [10, 42, 43, 163]. From the previous studies it is known that for uranyl dication coordinated by ligands the lowest excited state arises from the σ_u highest molecular orbital (HOMO) to the δ_u lowest unoccupied orbital (LUMO). The HOMO corresponds to the bonding combination of uranium $5f$ and $6p$ and oxygen $2p$ atomic orbitals, and $3p$ orbital of first-shell ligands, while the LUMO is a nonbonding uranium $5f$ orbital (Figure 3.3). The detailed analysis of the atomic orbitals contributions performed with multi-reference CASSCF (complete active space self-consistent

field) calculations by Pierloot and van Beisen [10] suggests that the lowest-lying excitation corresponds to a metal-centered transition from the bonding to nonbonding orbital of uranium, with a marginal ligand-to-metal charge transfer character. Hence, we can use in our discussion the UO_2^{2+} spin-free notations ($D_{\infty h}$), thus labeling the ground state as $^1\Sigma_g^+$ and the luminescent state as $^3\Delta_g$.

The vertical absorption E_{VA} and emission E_{VE} energies, were obtained at all-electron SOC CAM-B3LYP level of theory and are reported here together with experimental values (Table 3.4). They were computed with the summation of the fully relativistic electronic vertical energies associated with the spin-free zero-point energies correction. It should be noted that the experimental data correspond to the band-origin values obtained from polarized absorption or luminescence spectra and emission energies taken from UV-Visible spectroscopic measurements. Thus the direct comparison with theoretical results is not relevant, but we rather discuss whether the theoretical data reproduce the experimental trends.

Table 3.4: Experimental and computed vertical absorption (E_{VA}) and vertical emission (E_{VE}) energies of uranyl tetrahalide complexes (in cm^{-1}). The computed values are obtained at the all-electron SOC CAM-B3LYP level of theory, and corrected with the spin-free Zero-Point Energy correction of the ground and luminescent states.

	Theor.		Exp.	
	E_{VA}	E_{VE}	Band-origin	Emission
$[\text{UO}_2\text{Cl}_4]^{2-}$ gas-phase	20737	19924	20096 ^a	
$[\text{UO}_2\text{Cl}_4]^{2-}$ acetone	20822	20116		
$[\text{UO}_2\text{Br}_4]^{2-}$ gas-phase	20746	20041	19968 ^b	
$[\text{Bu}_4\text{N}]_2[\text{UO}_2\text{Cl}_4]$ acetone		20009	20097 ^c	21000 ^c
$[\text{A336}]_2[\text{UO}_2\text{Cl}_4]$ <i>n</i> -dodecane		20041		21025

^a Ref. [7], ^b Ref. [175], ^c Ref. [23]

As seen in Table 3.4, the vertical absorption energy of $[\text{UO}_2\text{Cl}_4]^{2-}$ increases by 85 cm^{-1} with the addition of acetone due to its small polarity. In the vertical emission energies, a blue shift of 117 cm^{-1} is observed when chlorides are replaced by bromide ligands. On the contrary, the band origins seem red shifted by 128 cm^{-1} , from chloride to bromide complexes according to experimental data [7,

175]. The presence of multiple non-equivalent uranyl sites in $[\text{UO}_2\text{Br}_4]^{2-}$ crystal studied by Flint et al. [175] may cause a reverse shift of the whole spectrum and hampers a direct comparison between theoretical and experimental results.

The luminescent state is known to be more sensitive to the solvent polarity [176]. We indeed observed a larger shift of about 192 cm^{-1} with the inclusion of acetone solvent than for absorption energies. With addition of Bu_4N in the second coordination sphere, the E_{VE} increased by 85 cm^{-1} , as expected since the displacements between the ground and excited state $[\text{UO}_2\text{Cl}_4]^{2-}$ geometries are larger with than without counter cations. Both theoretical E_{VE} and experimental emission energies of $[\text{UO}_2\text{Cl}_4]^{2-}$ are blue shifted by 32 or 25 cm^{-1} when immersed in *n*-dodecane or acetone, respectively.

It is worth noting that in the experimental spectra, the band-origin value of $[\text{UO}_2\text{Cl}_4]^{2-}$ is the same within 1 cm^{-1} in the $\text{Cs}_2\text{UO}_2\text{Cl}_4$ crystal and in $[\text{Bu}_4\text{N}]_2[\text{UO}_2\text{Cl}_4]$ in acetone. This is fully consistent with the fact that the singly occupied molecular orbitals in the luminescent state do not show any contribution from the second-sphere counter-ions (See Figure 3.3).

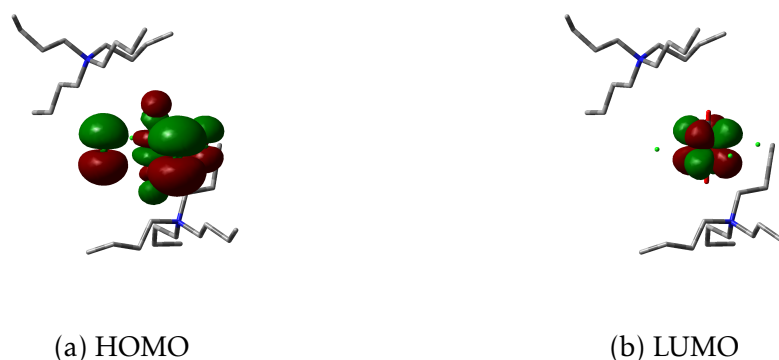


Figure 3.3: The highest occupied (HOMO) and lowest unoccupied molecular orbitals (LUMO) of $[\text{Bu}_4\text{N}]_2[\text{UO}_2\text{Cl}_4]$ in gas phase obtained at RECP DFT/PBE0 level of theory.

3.4.4 Theoretical luminescence spectra

To simplify the comparison within all spectra, let them be obtained from our quantum chemical calculations or from experiment, they are all normalized so

that the first peak in the low energy region matches the experimental amplitude. Neither homogeneous nor heterogeneous line broadening effects are included in our computed spectra because of their complicated prediction [138]. We will thus restrict ourselves to discussing the stick spectra.

The most relevant parameters influencing the spectral intensity distribution are the vibrational wavefunctions of both initial and excited states. The spectral shape is significantly linked to the bond-length changes between the two electronic states, as identified by Su et al. [140] thanks to a semi-classical vibronic approach. In that study, they solely considered the progression of one vibrational mode - ν_s . They concluded that the computed bond-length of the excited state is estimated without a sufficient accuracy to properly simulate the intensities. In our study, the theoretical luminescence spectra of $[\text{UO}_2\text{Cl}_4]^{2-}$ and $[\text{UO}_2\text{Br}_4]^{2-}$ in gas phase were obtained by including all vibrational modes to be able to assign all the finer details of the measured vibrational progressions. The theoretical spectra are displayed on Figure 3.4. The first band appearing in the progression corresponds to the 0-0 vibrational transition. In all uranium(VI) compounds at room temperature (300 K), luminescence arises from a low oscillator strength electronic transition followed by the vibrational progression in the ν_s mode of the electronic ground state equal to 894 cm^{-1} . Because the ν_s is totally symmetric it preserves the symmetry of the vibronic (electronic+vibrational) wave function. In $[\text{UO}_2\text{Cl}_4]^{2-}$, the totally symmetric ν_{U-Cl} mode is also excited vibronically, therefore contributing to a line in the vibronic progression which is distant from the 0-0 line by 235 cm^{-1} . However, as we already commented upon the fact that the U-X lengthening from the ground and excited states is underestimated by our quantum approach, we cannot expect the computed relative intensities to match the experimental ones. Still, our predicted spectra place the peaks distribution and band spacing in great agreement with the experimental results. As other vibronic transitions might not be easily visible on Figure 3.4, we provide a detailed assignment in Annex A.

Setting the $[\text{UO}_2\text{Cl}_4]^{2-}$ spectra computed in gas phase side-by-side with those computed in *n*-dodecane and acetone solvents (See Fig. A.4 of the Annex A) reveals that long-range solvent interactions have a minor influence on the spectral profiles, mostly on the intensities of ν_{U-X} vibrational mode contribu-

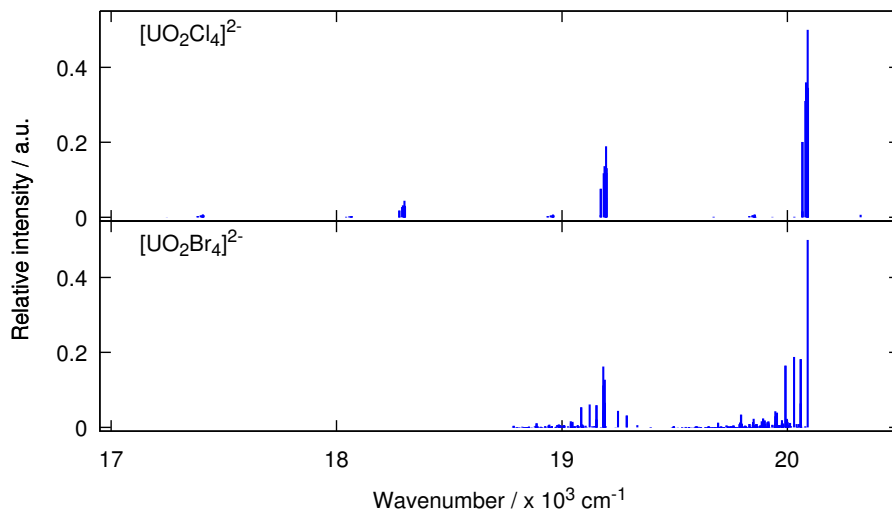


Figure 3.4: Theoretical luminescence spectra of $[\text{UO}_2\text{Cl}_4]^{2-}$ and $[\text{UO}_2\text{Br}_4]^{2-}$ in gas phase computed at 300 K.

tions. Nevertheless, the $[\text{UO}_2\text{Br}_4]^{2-}$ luminescence spectrum displays some more intense contributions and longer vibronic progressions than $[\text{UO}_2\text{Cl}_4]^{2-}$ (see the bottom panel on Fig. 3.4). This is due to a larger geometrical displacements between the ground and excited state structures (see Table A.10 in Annex A), which leads to the appearance of U–Br in-plane bending mode progression, distant by 96 cm^{-1} from the 0-0 line.

The computed luminescence spectrum of $[\text{A336}]_2[\text{UO}_2\text{Cl}_4]$ in gas phase is overlaid with the experimental one on Figure 3.5. This figure highlights the fact that both the energy positions and the band spacings of the computed vibronic transitions match nicely the experimental envelope, though with the reserve that the band spacing is somewhat red shifted as the ground state symmetrical stretching is slightly overestimated by the R-ECP DFT/PBE0 level of theory and anharmonicity corrections are not accounted for. The vibronic progressions do not change significantly as compared to bare $[\text{UO}_2\text{Cl}_4]^{2-}$. In agreement with Görrler-Walrand et al. [23] results, our theoretical approach embeds four vibronic progressions (See Table A.8 in the Annex A), the first one from ν_s , which is in our calculation just 40 cm^{-1} shifted compared to experiment, the second from

the rocking vibrational modes. While Görller-Walrand et al. attributed the other progressions to the out-of-plane bending of the chloride anions, our analysis assigns them to the symmetrical and anti-symmetrical Cl–U–Cl stretchings.

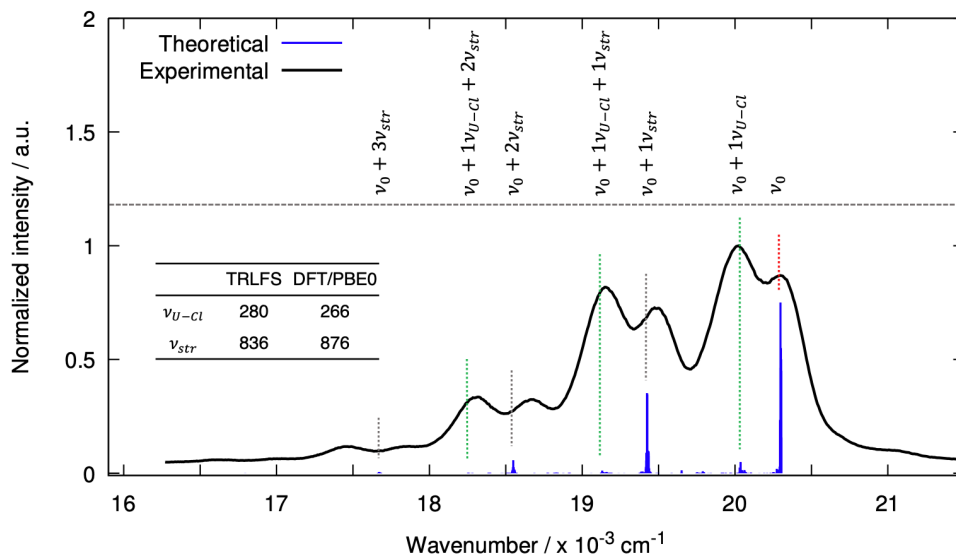


Figure 3.5: Experimental and theoretical luminescence spectra of $[A336]_2[UO_2Cl_4]$ in *n*-dodecane and a gas-phase respectively at 300 K.

3.5 Conclusions

Probing and quantifying the long-range effects of large organic counter-cations on $[UO_2Cl_4]^{2-}$ complex luminescence spectra was realized by two approaches, one experimental using TRLFs, and the second using *ab initio*-based approaches. For the latter, relativistic DFT quantum chemical methods were found to be quantitative and effective tools to rationalize and predict uranium(VI)-based complex luminescence properties. Thanks to a benchmark with respect to previous studies on $[UO_2Cl_4]^{2-}$ in crystal and solvent phases, we have been able to assess the degree of reliability of such an approach by comparison of ground and luminescence states structures and frequencies. However, this theoretical protocol reaches some limitations, since we were not able to compute the exact geometrical displacements of the complexes upon excitation from the

ground to first excited state, as compared to experimental data. As a result, the computed intensities of the vibronic bands do not coincide with the experimental ones. Conversely, the peak positions of the luminescence spectra are correctly reproduced, and the band spacings and theoretical assignments are in a good accordance with our experimental data.

In this work, we have used step-wise growing chemical models to quantify the influence of i) the first coordination sphere by substituting chloride anions by bromides; ii) the influence of second-sphere counter cations; iii) and long-range solvent effects with a polarizable continuum model, with the aim of approaching the experimental conditions. We have found that both long-range solvent effect and second coordination sphere have a little influence on vibronic intensities, while their effect is more significant for the prediction of other spectroscopic parameters, such as emission energies and vibronic band spacings of the $[\text{UO}_2\text{Cl}_4]^{2-}$ complex. This also confirms that the TRLFS spectroscopy may not be sensitive enough to discriminate long-range interactions induced by the counter-cations present in the vicinity of the luminescent center.

Bibliography of the current chapter

- (5) Denning, R. G. Electronic Structure and Bonding in Actinyl Ions and their Analogs. *Journal of Physical Chemistry A* **2007**, *111*, 4125–4143, DOI: 10.1021/jp071061n.
- (7) Denning, R.; Snellgrove, T.; Woodwark, D. The electronic structure of the uranyl ion: Part I. The electronic spectrum of $\text{Cs}_2\text{UO}_2\text{Cl}_4$. *Molecular Physics* **1976**, *32*, 419–442, DOI: 10.1080/00268977600103211.
- (10) Pierloot, K.; van Besien, E. Electronic structure and spectrum of UO_2^{2+} and $\text{UO}_2\text{Cl}_4^{2-}$. *Journal of Chemical Physics* **2005**, *123*, 204309, DOI: 10.1063/1.2121608.
- (23) Görrler-Walrand, C.; De Houwer, S.; Fluyt, L.; Binnemans, K. Spectroscopic properties of uranyl chloride complexes in non-aqueous solvents. *Physical Chemistry Chemical Physics* **2004**, *6*, 3292–3298, DOI: 10.1039/B317002K.
- (26) Tecmer, P.; Gomes, A. S. P.; Ekström, U.; Visscher, L. Electronic spectroscopy of UO_2^{2+} , NUO^+ and NUN : an evaluation of time-dependent density functional theory for actinides. *Physical Chemistry Chemical Physics* **2011**, *13*, 6249–6259, DOI: 10.1039/C0CP02534H.
- (42) Matsika, S.; Pitzer, R. M. Actinyl Ions in $\text{Cs}_2\text{UO}_2\text{Cl}_4$. *Journal of Physical Chemistry A* **2001**, *105*, 637–645, DOI: 10.1021/jp003032h.
- (43) Pierloot, K.; van Besien, E.; van Lenthe, E.; Baerends, E. J. Electronic spectrum of UO_2^{2+} and $[\text{UO}_2\text{Cl}_4]^{2-}$ calculated with time-dependent density functional theory. *Journal of Chemical Physics* **2007**, *126*, 194311, DOI: 10.1063/1.2735297.
- (45) Gomes, A. S. P.; Jacob, C. R.; Réal, F.; Visscher, L.; Vallet, V. Towards systematically improvable models for actinides in condensed phase: the electronic spectrum of uranyl in $\text{Cs}_2\text{UO}_2\text{Cl}_4$ as a test case. *Physical Chemistry Chemical Physics* **2013**, *15*, 15153–15162, DOI: 10.1039/C3CP52090K.
- (46) Bartlett, J. R.; Cooney, R. P. On the determination of uranium-oxygen bond lengths in dioxouranium (VI) compounds by Raman spectroscopy. *Journal of Molecular Spectroscopy* **1989**, *193*, 295–300, DOI: 10.1016/0022-2860(89)80140-1.
- (86) Ernzerhof, M.; Scuseria, G. E. Assessment of the Perdew–Burke–Ernzerhof exchange–correlation functional. *Journal of Chemical Physics* **1999**, *110*, 5029–5036, DOI: 10.1063/1.478401.

- (87) Yanai, T.; Tew, D. P.; Handy, N. C. A new hybrid exchange–correlation functional using the Coulomb-attenuating method (CAM-B3LYP). *Chemical Physics Letters* **2004**, *393*, 51–57, DOI: 10.1016/j.cpllett.2004.06.011.
- (104) Pyykkö, P. Relativistic effects in structural chemistry. *Chemical Reviews* **1988**, *88*, 563–594, DOI: 10.1021/cr00085a006.
- (111) Van Lenthe, E.; Baerends, E.-J.; Snijders, J. G. Relativistic regular two-component Hamiltonians. *Journal of Chemical Physics* **1993**, *99*, 4597–4610, DOI: 10.1063/1.466059.
- (122) Weigend, F.; Ahlrichs, R. Balanced basis sets of split valence, triple zeta valence and quadruple zeta valence quality for H to Rn: Design and assessment of accuracy. *Physical Chemistry Chemical Physics* **2005**, *7*, 3297–3305, DOI: 10.1039/B508541A.
- (123) Weigend, F.; Häser, M.; Patzelt, H.; Ahlrichs, R. RI-MP2: optimized auxiliary basis sets and demonstration of efficiency. *Chemical Physics Letters* **1998**, *294*, 143–152, DOI: 10.1016/S0009-2614(98)00862-8.
- (124) Küchle, W.; Dolg, M.; Stoll, H.; Preuss, H. Energy-adjusted pseudopotentials for the actinides. Parameter sets and test calculations for thorium and thorium monoxide. *Journal of Chemical Physics* **1994**, *100*, 7535–7542, DOI: 10.1063/1.466847.
- (125) Baerends, E. J. et al. ADF2018, SCM, Theoretical Chemistry, Vrije Universiteit, Amsterdam, The Netherlands, <https://www.scm.com>.
- (126) Van Lenthe, E.; Baerends, E. J. Optimized Slater-type basis sets for the elements 1–118. *Journal of Computational Chemistry* **2003**, *24*, 1142–1156, DOI: 10.1002/jcc.10255.
- (128) Barone, V.; Cossi, M. Quantum Calculation of Molecular Energies and Energy Gradients in Solution by a Conductor Solvent Model. *Journal of Physical Chemistry A* **1998**, *102*, 1995–2001, DOI: 10.1021/jp9716997.
- (130) Cossi, M.; Rega, N.; Scalmani, G.; Barone, V. Energies, structures, and electronic properties of molecules in solution with the C-PCM solvation model. *Journal of Computational Chemistry* **2003**, *24*, 669–681, DOI: 10.1002/jcc.10189.
- (131) Klamt, A.; Schüürmann, G. COSMO: a new approach to dielectric screening in solvents with explicit expressions for the screening energy and its gradient. *Journal of Chemical Society, Perkin Transactions 2* **1993**, *5*, 799–805, DOI: 10.1039/P29930000799.

- (132) Klamt, A. Conductor-like Screening Model for Real Solvents: A New Approach to the Quantitative Calculation of Solvation Phenomena. *Journal of Physical Chemistry* **1995**, *99*, 2224–2235, DOI: 10.1021/j100007a062.
- (133) Klamt, A.; Jonas, V. Treatment of the outlying charge in continuum solvation models. *Journal of Chemical Physics* **1996**, *105*, 9972–9981, DOI: 10.1063/1.472829.
- (136) Oher, H.; Réal, F.; Vercoeur, T.; Vallet, V. Investigation of the Luminescence of $[\text{UO}_2\text{X}_4]^{2-}$ (X = Cl, Br) Complexes in the Organic Phase Using Time-Resolved Laser-Induced Fluorescence Spectroscopy and Quantum Chemical Simulations. *Inorganic Chemistry* **2020**, *59*, 5896–5906, DOI: 10.1021/acs.inorgchem.9b03614.
- (137) Visnak, Jakub; Sobek, Lukás Quantum chemical calculations and spectroscopic measurements of spectroscopic and thermodynamic properties of given uranyl complexes in aqueous solutions with possible environmental and industrial applications. *EPJ Web Conf.* **2016**, *128*, 02002, DOI: 10.1051/epjconf/201612802002.
- (138) Su, J.; Wang, Y.-L.; Wei, F.; Schwarz, W.; Li, J. Theoretical Study of the Luminescent States and Electronic Spectra of UO_2Cl_2 in an Argon Matrix. *Journal of Chemical Theory and Computation* **2011**, *7*, 3293–3303, DOI: 10.1021/ct200419x.
- (139) Su, J.; Wang, Z.; Pan, D.; Li, J. Excited States and Luminescent Properties of UO_2F_2 and Its Solvated Complexes in Aqueous Solution. *Inorganic Chemistry* **2014**, *53*, 7340–7350, DOI: 10.1021/ic5006852.
- (140) Su, J.; Zhang, K.; Schwarz, W. E.; Li, J. Uranyl-glycine-water complexes in solution: Comprehensive computational modeling of coordination geometries, stabilization energies, and luminescence properties. *Inorganic Chemistry* **2011**, *50*, 2082–2093, DOI: 10.1021/ic200204p.
- (141) Dylla, K. G.; Fægri, K., *Introduction to relativistic quantum chemistry*; Oxford University Press: New York, 2007.
- (142) Autschbach, J. Perspective: Relativistic effects. *Journal of Chemical Physics* **2012**, *136*, 150902, DOI: 10.1063/1.3702628.
- (143) Reiher, M.; Wolf, A., *Relativistic Quantum Chemistry: The Fundamental Theory of Molecular Science, 2nd Edition*; WILEY-VCH Verlag: 2014.
- (144) Watkin, D. J.; Denning, R. G.; Prout, K. Structure of dicaesium tetrachlorodioxouranium (VI). *Acta Crystallographica C* **1991**, *47*, 2517–2519, DOI: 10.1107/S0108270191006777.

- (145) Nockemann, P.; Servaes, K.; Van Deun, R.; Van Hecke, K.; Van Meervelt, L.; Binnemans, K.; Görrler-Walrand, C. Speciation of Uranyl Complexes in Ionic Liquids by Optical Spectroscopy. *Inorganic Chemistry* **2007**, *46*, 11335–11344, DOI: 10.1021/ic701752j.
- (146) Sornein, M.-O.; Cannes, C.; Le Naour, C.; Lagarde, G.; Simoni, E.; Berthet, J.-C. Uranyl complexation by chloride ions. Formation of a tetrachlorouranium (VI) complex in room temperature ionic liquids [Bmim][Tf₂N] and [MeBu₃N][Tf₂N]. *Inorganic Chemistry* **2006**, *45*, 10419–10421, DOI: 10.1021/ic061751q.
- (147) Reiller, P. E.; Mariet, C. Luminescence of uranium(VI) after liquid-liquid extraction from HCl in n-dodecane/1-dodecanol by Aliquat® 336 by time-resolved laser-induced luminescence spectroscopy. *Radiochimica Acta* **2019**, in press, DOI: 10.1515/ract-2019-3177.
- (148) Hellé, G.; Mariet, C.; Cote, G. Liquid-liquid extraction of uranium (VI) with Aliquat® 336 from HCl media in microfluidic devices: Combination of micro-unit operations and online ICP-MS determination. *Talanta* **2015**, *139*, 123–131, DOI: 10.1016/j.talanta.2015.02.046.
- (149) Hellé, G.; Mariet, C.; Cote, G. Liquid-liquid microflow patterns and mass transfer of radionuclides in the systems Eu (III)/HNO₃/DMDBTDMMA and U (VI)/HCl/Aliquat® 336. *Microfluid. Nanofluid.* **2014**, *17*, 1113–1128, DOI: 10.1007/s10404-014-1403-1.
- (150) Vercouter, T.; Vitorge, P.; Amekraz, B.; Moulin, C. Stoichiometries and Thermodynamic Stabilities for Aqueous Sulfate Complexes of U(VI). *Inorganic Chemistry* **2008**, *47*, 2180–2189, DOI: 10.1021/ic701379q.
- (151) Mozhayskiy, V.; Krylov, A. ezSpectrum, <http://iopenshell.usc.edu/downloads>.
- (152) Denning, R.; Ironside, C.; Thorne, J.; Woodwark, D. Electronic energy transfer in actinyl crystals. *Molecular Physics* **1981**, *44*, 209–224, DOI: 10.1080/00268978100102391.
- (153) Hopkins, T. A.; Berg, J. M.; Costa, D. A.; Smith, W. H.; Dewey, H. J. Spectroscopy of UO₂Cl₄²⁻ in Basic Aluminum Chloride- 1-Ethyl-3-methylimidazolium Chloride. *Inorganic Chemistry* **2001**, *40*, 1820–1825, DOI: 10.1021/ic001027m.
- (154) Ruipérez, F.; Wahlgren, U. Charge Transfer in Uranyl(VI) Halides [UO₂X₄]²⁻ (X = F, Cl, Br, and I). A Quantum Chemical Study of the Absorption Spectra. *Journal of Physical Chemistry A* **2010**, *114*, 3615–3621, DOI: 10.1021/jp911271q.

- (155) TURBOMOLE V7.3 2018, a development of University of Karlsruhe and Forschungszentrum Karlsruhe GmbH, TURBOMOLE GmbH, since 2007; available from <http://www.turbomole.com>. 1989-2007.
- (156) Frisch, M. J. et al. Gaussian 16 Revision B.01, Gaussian Inc. Wallingford CT, 2016.
- (157) Cao, X.; Dolg, M.; Stoll, H. Valence basis sets for relativistic energy-consistent small-core actinide pseudopotentials. *Journal of Chemical Physics* **2003**, *118*, 487–496, DOI: 10.1063/1.1521431.
- (158) Eichkorn, K.; Weigend, F.; Treutler, O.; Ahlrichs, R. Auxiliary basis sets for main row atoms and transition metals and their use to approximate Coulomb potentials. *Theoretical Chemistry Accounts* **1997**, *97*, 119–124, DOI: 10.1007/s002140050244.
- (159) Peterson, K. A.; Figgen, D.; Goll, E.; Stoll, H.; Dolg, M. Systematically convergent basis sets with relativistic pseudopotentials. II. Small-core pseudopotentials and correlation consistent basis sets for the post-d group 16–18 elements. *Journal of Chemical Physics* **2003**, *119*, 11113–11123, DOI: 10.1063/1.1622924.
- (160) Deglmann, P.; May, K.; Furche, F.; Ahlrichs, R. Nuclear second analytical derivative calculations using auxiliary basis set expansions. *Chemical Physics Letters* **2004**, *384*, 103–107, DOI: 10.1016/j.cpllett.2003.11.080.
- (161) Bauernschmitt, R.; Häser, M.; Treutler, O.; Ahlrichs, R. Calculation of excitation energies within time-dependent density functional theory using auxiliary basis set expansions. *Chemical Physics Letters* **1997**, *264*, 573–578, DOI: 10.1016/S0009-2614(96)01343-7.
- (162) Weigend, F. Accurate Coulomb-fitting basis sets for H to Rn. *Physical Chemistry Chemical Physics* **2006**, *8*, 1057–1065, DOI: 10.1039/B515623H.
- (163) Tecmer, P.; Bast, R.; Ruud, K.; Visscher, L. Charge-Transfer Excitations in Uranyl Tetrachloride ($[\text{UO}_2\text{Cl}_4]^{2-}$): How Reliable are Electronic Spectra from Relativistic Time-Dependent Density Functional Theory? *Journal of Physical Chemistry A* **2012**, *116*, 7397–7404, DOI: 10.1021/jp3011266.
- (164) Tecmer, P.; Govind, N.; Kowalski, K.; De Jong, W. A.; Visscher, L. Reliable modeling of the electronic spectra of realistic uranium complexes. *Journal of Chemical Physics* **2013**, *139*, 034301, DOI: 10.1063/1.4812360.
- (165) Dau, P.; Su, J.; Liu, H.-T.; Huang, D.-L.; Li, J.; Wang, L.-S. Photoelectron spectroscopy and the electronic structure of the uranyl tetrachloride dianion: $\text{UO}_2\text{Cl}_4^{2-}$. *Journal of Chemical Physics* **2012**, *137*, 064315, DOI: 10.1063/1.4742062.

- (166) Servaes, K.; Hennig, C.; Deun, V. R.; Görller-Walrand, C. Structure of $[\text{UO}_2\text{Cl}_4]^{2-}$ in Acetonitrile. *Inorg. Chem.* **2005**, *44*, 7705–7707, DOI: 10.1021/ic051098r.
- (167) Wilson, R. E.; Skanthakumar, S.; Cahill, C.; Soderholm, L. Structural studies coupling X-ray diffraction and high-energy X-ray scattering in the $\text{UO}_2^{2+} - \text{HBr}_{\text{aq}}$ system. *Inorganic Chemistry* **2011**, *50*, 10748–10754, DOI: 10.1021/ic201265s.
- (168) Deifel, N. P.; Cahill, C. L. Supramolecular chemistry with uranyl tetrahalide ($[\text{UO}_2\text{X}_4]^{2-}$) anions. *Comptes Rendus Chimie* **2010**, *13*, 747–754, DOI: 10.1016/j.crci.2010.01.009.
- (169) Barone, V. Vibrational zero-point energies and thermodynamic functions beyond the harmonic approximation. *Journal of Chemical Physics* **2004**, *120*, 3059, DOI: 10.1063/1.1637580.
- (170) Barone, V. Anharmonic vibrational properties by a fully automated second-order perturbative approach. *Journal of Chemical Physics* **2005**, *122*, 014108, DOI: 10.1063/1.1824881.
- (171) Schnaars, D. D.; Wilson, R. E. Structural and Vibrational Properties of $\text{U(VI)O}_2\text{Cl}_4^{2-}$ and $\text{Pu(VI)O}_2\text{Cl}_4^{2-}$ Complexes. *Inorganic Chemistry* **2013**, *52*, 14138–14147, DOI: 10.1021/ic401991n.
- (172) Newbery, J. Vibrational spectra of the $[\text{UO}_2\text{Cl}_4]^{2-}$ and the $[\text{UO}_2\text{Br}_4]^{2-}$ ions. *Spectrochimica Acta A* **1969**, *25*, 1699–1702, DOI: 10.1016/0584-8539(69)80158-3.
- (173) Gal, M.; Goggin, P.; Mink, J. Mid-, far-infrared and raman spectra of uranyl complexes in aqueous solutions. *Journal of Molecular Spectroscopy* **1984**, *114*, 459–462, DOI: 10.1016/0022-2860(84)87186-0.
- (174) Marzotto, A.; Graziani, R.; Bombieri, G.; Forsellini, E. Preparation, properties, and crystal structure of bis (acetylcholine) tetrabromodioxouranium (VI). *Journal of Crystal and Molecular Structure* **1974**, *4*, 253–262, DOI: 10.1007/BF01198181.
- (175) Flint, C. D.; Tanner, P. A. Electronic and vibrational spectra of $[\text{Me}_4\text{N}]_2\text{UO}_2\text{Br}_4$. *Journal of Chemical Society, Perkin Transactions 2* **1982**, *78*, 103–112, DOI: 10.1039/F29827800103.
- (176) In *Principles of Fluorescence Spectroscopy*, Lakowicz, J. R., Ed.; Springer US: Boston, MA, 2006, pp 205–235, DOI: 10.1007/978-0-387-46312-4_6.

Influence of alkaline earth metal ions on structures and luminescent properties of $\text{Na}_m\text{M}_n\text{UO}_2(\text{CO}_3)_3^{(4-m-2n)-}$ (M = Mg, Ca; m, n = 0-2): time-resolved fluorescence spectroscopy and *ab initio* studies

The material presented in this chapter forms the publication [177].

4.1 Abstract

The luminescence spectra of triscarbonatouranyl complexes were determined by experimental and theoretical methods. Time-resolved laser-induced fluorescence spectroscopy (TRLFS) was used to monitor spectra of uranyl and bicarbonate solutions at 0.1 mol/kg_{H₂O} ionic strength and pH ca. 8. The concentrations of Mg²⁺ and Ca²⁺ in the samples were chosen in order to vary the proportions of the

alkaline earth ternary uranyl complexes $\text{MgUO}_2(\text{CO}_3)_3^{2-}$, $\text{CaUO}_2(\text{CO}_3)_3^{2-}$, and $\text{Ca}_2\text{UO}_2(\text{CO}_3)_3$. The luminescence spectrum of each complex was determined by decomposition in order to compare with the simulated spectra of model structures $\text{Na}_m\text{M}_n\text{UO}_2(\text{CO}_3)_3^{(4-m-2n)-}$ ($\text{M} = \text{Mg, Ca}$; $m, n = 0-2$) obtained by quantum chemical methods. The Density Functional Theory (DFT) and time-dependent (TD)-DFT methods were used with the PBE0 functional to optimize the structures in the ground and excited states, respectively, including relativistic effects at the spin-free level, and water solvent effects using a continuum polarizable conductor model (CPCM). The changes in the structural parameters were quantified with respect to the nature and the amount of alkali earth counterions to explain the luminescence spectra behavior. The first low-lying excited state was successfully computed, together with the vibrational harmonic frequencies. The DFT calculations confirmed that uranyl luminescence originates from electronic transitions from one of the four non-bonding 5f orbitals of uranium to an orbital that has a uranyl- σ (5f, 6d) character mixed with the 2p atomic orbitals of the carbonate oxygens. Additional single-point calculations using the more accurate TD-DFT/CAM-B3LYP allow to determine the position of the luminescence “hot band” for each structure in the range 467-476 nm, and compared fairly well with experimental reports at around 465 nm. The complete luminescence spectra were built from theoretical results with the corresponding assignment of the electronic transitions and vibronic modes involved, mainly the U–O_{ax} stretching mode. The resulting calculated spectra showed a very good agreement with experimental band positions and band spacing attributed to $\text{MgUO}_2(\text{CO}_3)_3^{2-}$, $\text{CaUO}_2(\text{CO}_3)_3^{2-}$, and $\text{Ca}_2\text{UO}_2(\text{CO}_3)_3$. The evolution of luminescence intensities with the number of alkaline earth metal ions in the structure was also correctly reproduced.

4.2 Introduction

After light excitation in the UV or visible range, most uranium(VI) compounds produce luminescence in the energy range 15 000 – 22 000 cm^{-1} (650-450 nm), which has been extensively studied since the spectra are fingerprints of the coordination of the uranyl ion UO_2^{2+} . The positions of the luminescence bands,

band spacings, bandwidths, and intensities are features that can be interpreted to determine the nature and number of ligands in the first coordination layer of UO_2^{2+} , and the local symmetry of the complex. This information is looked for by chemists in order to give the best description of uranium speciation both in solutions and in solids. Time-resolved laser-induced fluorescence spectroscopy (TRLFS) has been widely used for the identification and characterization of U(VI) compounds since it is a non-intrusive, sensitive, and selective technique to detect the luminescence of U(VI) species, even with traces of uranium [18, 178]. The main spectroscopic features are usually reported in the literature and spectral attributions have been proposed for many aqueous inorganic complexes [57, 150, 179–183] and minerals [184–192].

The case of the carbonate species is particularly interesting [21, 183, 187, 190, 193, 194]. Both anionic complexes $\text{UO}_2(\text{CO}_3)_2^{2-}$ and $\text{UO}_2(\text{CO}_3)_3^{4-}$ are characterized by an absorption spectrum shifted to longer wavelengths as compared with UO_2^{2+} aqua ion and its hydrolyzed species [195, 196]. Meinrath et al. reported 20 years ago that the luminescence of $\text{UO}_2(\text{CO}_3)_2^{2-}$ seemed to be too weak to be easily observed [180]. Conversely, recent works have shown that the use of modern TRLFS set-up allows measuring $\text{UO}_2(\text{CO}_3)_2^{4-}$ at ambient temperature [194, 197]. It has been shown that the U(VI) luminescence is increasing when alkaline earth metal ions are added into a solution that contains $\text{UO}_2(\text{CO}_3)_2^{4-}$, *i.e.*, in the presence of dissolved bicarbonate. The repartition of these species (and solids) can be described in e.g. a $\log_{10}(a(\text{HCO}_3^-)/a(\text{H}^+))$ vs. $\log_{10}(a(\text{Ca}^{2+})/a(\text{H}^+)^2)$ plan for Ca. There was a direct evidence of the formation of ternary complexes $\text{CaUO}_2(\text{CO}_3)_3^{2-}$ and $\text{Ca}_2\text{UO}_2(\text{CO}_3)_3$ where the calcium ions enter the second coordination layer of the uranyl and interact with the carbonate ligands, as first reported by Bernhard et al., [198] and investigated later on by several groups [20, 183, 193, 194, 199–202].

The luminescence of such complexes exhibits a hypsochromic shift of the whole spectrum by about 300 cm^{-1} compared with the free ion, when most other U(VI) compounds, like phosphates, silicates, hydroxides, or organic complexes, are showing a bathochromic shift. The blue-shifted luminescence of the triscarbonatouranyl(VI) entities results from the strong interaction of UO_2^{2+} with the carbonate ligands that bind the uranium atom with two out of their three oxy-

gens in the equatorial plane of the uranyl ion, leading to a six-fold-coordinated uranyl structure. Thanks to this unusual feature, TRLFS has enabled the direct identification of alkaline earth triscarbonatouranyl complexes in many different types of waters like *e.g.*, seepage water of mine tailing pile [198], granitic groundwater [203], seawater [204], natural drinking water from wells [193], and in sediment pore waters of the Hanford contaminated sites [205].

The reason of the increase of the triscarbonatouranyl species luminescence intensity in presence of calcium is still unclear and may originate from either favorable vibronic coupling or diminution of quenching effects from the carbonate ion. Similar observations have been made with the less stable ternary $\text{MgUO}_2(\text{CO}_3)_3^{2-}$ and $\text{SrUO}_2(\text{CO}_3)_3^{2-}$ complexes [206, 207], while the confirmation of the existence of the ternary $\text{Mg}_2\text{UO}_2(\text{CO}_3)_3$ complex is still discussed [20, 199, 206].

Quantum chemical modeling is an appropriate theoretical support for a better understanding of the luminescence of these ternary triscarbonatouranyl complexes with alkaline earth metal cations. The luminescence of solid triscarbonatouranyl has been successfully described and analyzed using periodic density functional theory (DFT), particularly in the case of liebigite $\text{Ca}_2\text{UO}_2(\text{CO}_3)_3 \cdot 11\text{H}_2\text{O}$ and the dehydrated $\text{Ca}_2\text{UO}_2(\text{CO}_3)_3$ crystal [208]. While it is established that the luminescence of uranyl compounds is related to transitions from $5f_\delta$ and $5f_\phi$ excited levels, the nature of the ground state orbitals still needs to be more precisely defined for the aqueous uranyl carbonate complexes. For this reason, the quantum chemical systems of triscarbonatouranyl complex were supplemented with sodium counterions (from 1 to 3 Na^+ depending on the amount of alkaline earth metal present) to maintain the highest symmetry and reduce total molecular charge. This constitutes a first objective of the present work with support of quantum chemistry modeling.

Investigating luminescence properties from a uranyl complex requires a step-by-step methodology. The geometry of the complexes first needs to be correctly built both in the ground and excited states, which can be checked by comparison with structural studies on triscarbonatouranyl complexes, with and without calcium that were deeply investigated. On the one hand, structures and atomic distances were determined by X-Ray Diffraction (XRD) [209], and

Extended X-ray Absorption Fine Structure (EXAFS) [21, 190, 206, 210, 211] both in crystal form and in solution, respectively. Vibration frequencies are also available from measurements by Raman and Infrared spectroscopy [212–215]. On the other hand, theoretical methods were applied to triscarbonatouranyl complex by DFT[216] or hybrid DFT [217], Quantum Mechanical Charge Field Molecular Dynamics (QMCF-MD) [218], or classical molecular dynamics (MD) simulations [216, 219]. Then one needs to calculate and identify the excited states that may be involved in the electronic transitions. TD-DFT has demonstrated its ability to reproduce electronic transitions in uranyl compounds from low-lying excited states, including relativistic effects, electron correlation, and spin-orbit coupling [26, 136]. The calculation of the coupling factors between the different vibrational states of the ground and excited states can be achieved using the Franck-Condon approach for dipole-allowed transitions, to finally describe luminescence spectra.

Quantum chemical methods have already been applied to simulate the luminescence properties of uranyl chloride crystals [144] and complexes [138, 220], uranyl fluoride [139], and uranyl glycine complex [140]. We recently applied a methodology developed by Tecmer et al. [26], and tested on the tetra-halogen compounds $\text{UO}_2\text{Cl}_4^{2-}$ that resulted in simulated luminescence spectra in good accordance with experimental data [136]. Our approach based on DFT and time-dependent DFT, offers a good compromise between the accuracy of the calculations and a rather low computational cost, which enables the application of the method to larger molecular assemblies, especially with actinides.

In the present work, we optimized the geometries of the $\text{Na}_m\text{M}_n\text{UO}_2(\text{CO}_3)_3^{(4-m-2n)-}$ (M=Mg, Ca; m,n = 0-2) complexes by DFT, and compared with literature data to evaluate the reliability of the uranyl distances and harmonic frequencies and their change between the ground and luminescent states to capture the evolution of intensities. The luminescence properties calculated by TD-DFT methods were compared to experimental data acquired with our TRLFS set-up, and from the literature. Finally, the present results from quantum chemical modeling are discussed and provide a better understanding of the luminescence bands and intensities of the ternary alkaline earth metal triscarbonatouranyl complexes.

4.3 Experimental details

Reagents and solution Five samples of varying $[Mg]/([Ca] + [Mg])$ ratios from 100% to about 50% were prepared for further acquisition of resulting luminescence signals of $M_nUO_2(CO_3)_3^{(4-2n)-}$ ($M = Mg^{2+}, Ca^{2+}; n = 1,2$). The ionic strength was fixed at 0.1 mol/kg_{H₂O} by dissolving appropriate quantity of anhydrous NaCl (Sigma-Aldrich, ACS reagent, $\geq 99\%$) in Millipore deionized water (Alpha-Q, 18.2 M Ω cm). The uranium concentration was of 50 μ mol/kg_{H₂O} after successive dilutions of concentrated stock solution of natural U(VI) prepared with U₃O₈ solid and 37% hydrochloric acid (Sigma-Aldrich, ACS reagent). Using a hydrogen ion-sensitive glass electrode (Mettler Toledo, USA), the aqueous pH value was maintained ca. 8 for all the sample solutions. In order to maintain the performance accuracy, the four-point calibration with commercial solutions of fixed pH at 1.68, 4.01, 6.87, and 10.01 was daily required. The adjustment of pH 8 was done through the addition of freshly prepared NaOH (Analytical Grade, Fisher) and diluted HCl solutions. The sodium bicarbonate solution (Analytical Grade, Fisher) was freshly prepared, the introduced quantity of which was calculated based on the chemical equilibrium between the aqueous solution in the absence of alkaline earth metal ions and atmospheric CO₂(g). Calcium chloride (Sigma-Aldrich, ACS reagent, $\geq 99\%$) and magnesium chloride (Sigma-Aldrich, ACS reagent, $\geq 99\%$) solutions of various concentrations were used to control the concentration of Ca²⁺ and Mg²⁺. Reagent preparations in experiments were performed by weighing and measurements of pH values were done in triplicate at 22 °C. The aqueous pH values were regularly checked during the preparation and the last check was conducted just before the luminescence measurement.

Luminescence measurements A 2 mL U(VI) solution aliquot was taken from the prepared test sample and placed in a 1 cm quartz fluorescence cuvette (QS101, Suprasil, Hellma Analytics). A preliminary equilibration, period of 10 min at 22 °C for the used cuvette has been reached prior to data acquisition using a thermostated sample holder connected to a thermostat with circulating water (Peter Huber Kältemaschinenbau AG, Germany). As described fully elsewhere[194], the excitation laser beam was generated by a 355 nm tripled

Nd:YAG laser (Surelite, Continuum, USA) coupled to an optical parametric oscillator system (Horizon, Continuum, USA), delivering 5 ns pulses at 10 Hz. The excitation wavelength was set at 450 nm, allowing an optimal luminescence signal – proper balance between quantum yield of U(VI) species and laser energy – after a preliminary test. The excitation energy at 450 nm was monitored using a RJP-734 Joule-meter (Laser Probe, Inc, and was about 23 mJ.

A spectrometer (Acton SP-2358i, Roper Scientific) equipped with an intensified CCD camera (iStar DH734-25F-03, Andor Technology) was used to collect the luminescence signal with either a 300 or a 1800 lines /mm . The 300 lines /mm grating capable of recording the convolution of various fluorescing components was first selected to measure the full uranyl emission spectra covering the wavelength range of 425 nm to 615 nm with a resolution estimated at 0.2 nm for each sample solution. The 1800 lines /mm grating providing a resolution estimated at 0.025 nm was then used to focus on specific characteristic peaks with the aim of detecting their possible modifications as a function of Mg/(Ca + Mg) ratios, as well as aqueous compositions in terms of $M_n\text{UO}_2(\text{CO}_3)_3^{(4-2n)-}$ species. The time-resolved measurements were carried out at a delay time of $D = 25$ ns after the laser pulse and during a measurement gate width of $W = 1$ μs . Each spectrum was the result of signal accumulated over more than 4000 laser shots depending on the grating used.

4.4 Computational details

The simulation of the luminescence spectra of uranyl complexes were done using the ezSpectrum 3.0 [151] program to compute the Franck-Condon factors, corresponding to the overlaps between the luminescent and the ground vibrational wavefunctions. As in our previous work, Duschinsky rotations of the normal modes were included [136]. The numbers of vibrational quanta in excited and ground state were selected to be one and five, respectively to match the number of transitions on experimental spectra. All the stick spectra were computed at 300 K. In order to be able to make a comparison of theoretical results with experimental curves, the calculated peaks were broadened homogeneously using Lorentzian functions with a width corresponding to the experimental values

of the full width at half-maximum. For the spectra simulations all data were generated by the ab initio packages as described below.

The interactions between uranyl and its first and second coordination spheres might affect the electronic structure of the uranyl unit. In order to keep reasonable computational costs, the ab initio calculations were performed on model molecular systems built to represent the triscarbonatouranyl negatively charged complex charge-compensated by counter cations in its close environment (Fig. 4.1). In the present study, the triscarbonatouranyl complex was built with three bidentate carbonate ligands in the equatorial plane of the uranyl ion, matching a D_{3h} symmetry (Fig. 4.1, (a)), as evidenced by EXAFS solution data [211, 221]. Then Na^+ counter ions were positioned in between the carbonate ligands. The $\text{Na}_3\text{UO}_2(\text{CO}_3)_3^-$ model complex was first created to reduce the complex total charge to minus one while keeping the D_{3h} symmetry, and taken as a reference structure (Fig. 4.1,(b)), instead of the bare $\text{UO}_2(\text{CO}_3)_3^{4-}$ complex, as such a highly charged anion is necessarily stabilized in solution with charge-balancing cations. Then structures in which one or two Na^+ cations are substituted by Ca^{2+} or Mg^{2+} were investigated (Fig. 4.1 (c) and (d), respectively), leading to neutral and mono-charged cationic complex, respectively. The geometries of these model systems were computed with inclusion of solvent effect to imitate experimental conditions.

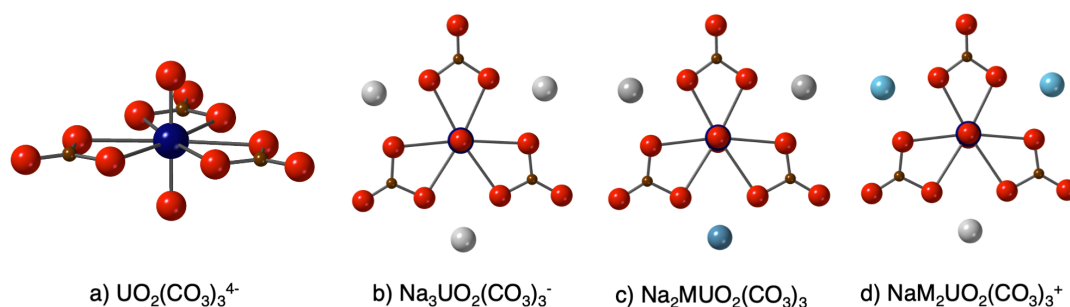


Figure 4.1: The structures of uranyl bidentate tri-carbonate complexes $\text{Na}_m\text{M}_n\text{UO}_2(\text{CO}_3)_3^{(4-m-2n)-}$ ($\text{M} = \text{Mg}, \text{Ca}$; $m, n = 0-2$) in water with different composition of the second coordination sphere optimized at the DFT/PBE0 level of theory. In red - O, brown - C, dark blue - U, gray - Na, light blue - Ca, Mg.

The QM methods were used as described and justified in our previous study [136]. All the ground-state and excited-state molecular geometries were optimized including the relativistic effects at the spin-free level using the PBE0 functional of the density [86], and accounting for water solvent effects via the CPCM [156] (the permittivity of water $\epsilon_r = 78.35$). Note that spin-orbit coupling effects (SOC) are not expected to affect uranyl ground and excited state geometries as discussed by Pierloot et al. [10]. The structure of the first low-lying excited state was optimized using the time-dependent (TD)-DFT/PBE0 method as implemented in Gaussian 16 code [156], with equilibrium CPCM solvation. The vibrational harmonic frequencies were computed using an analytic Hessian matrix, and all relaxed geometries considered for the vibronic spectra calculations represent real minima as they have no imaginary frequencies. In these calculations, the def2-TZVP (second generation of triple- ζ polarization quality) basis sets [122, 123] have been used for all light elements i.e., C, O, Na, Mg, and Ca. The uranium atom is described by a small-core Relativistic Effective Core Pseudopotentials (RECP), which accounts for scalar relativistic of the uranium 60 core-electrons [124, 157], and the valence electrons are described by the def-TZVP (first generation of triple-zeta polarization quality) basis set [158]. In the TD-DFT calculations, the Gaussian program defaults for frozen core orbitals were overridden to freeze the U (5s, 5p, 5d), C (1s), O (1s), Na (1s), Mg (1s), and Ca (1s, 2s, and 2p) orbitals.

According to benchmark calculations carried out by Tecmer et al. [26, 163, 164] on a series of uranium(VI)-based compounds, the CAM-B3LYP [87] exchange-correlation functional was found to be more accurate than PBE0 for uranyl valence transition energies, for similar optimized structures. Thus, to accurately position the “hot bands”, CAM-B3LYP TD-DFT single-point calculations including spin-orbit coupling (SOC) effects with the ZORA Hamiltonian [111], and modeling the water solvent with the conductor-like screening model (COSMO) model [131–133] were performed at the spin-free ground and excited-state structures, with the Amsterdam Density Functional package (ADF2018.01) [125]. All atoms were described by TZ2P Slater-type basis sets (triple ζ with two polarization functions quality) [126], without the frozen core approximation.

There are controversies in the literature regarding the nature of the “hot band”

in the luminescence spectra of uranyl-based complexes [140]. We considered that it corresponds to an average of the lowest-lying electronic transitions, which is a hypothesis difficult to confirm experimentally, but appears reasonable in the case of uranyl compounds. Indeed, at the SOC level, four excited states in the luminescent energy range are very close in energy (within a 900 cm^{-1} range). They correspond to excitations of an electron out from the σ highest occupied molecular orbital (HOMO) into the four non-bonding orbitals noted $f_{-\delta,+ \delta}$, $f_{-\phi,+ \phi}$ – we refer to orbitals, to ease the chemical discussion, while we should formally refer to spinors – that are nearly degenerate. In the present work the “hot band” is defined after averaging the two pairs among the first four excited states including the Zero-Point-Energy (ZPE) corrections estimated for the ground state and the lowest spin-free triplet excited state, assuming the ZPE being almost identical for all the excited states considered here. The latter assumption is reasonable since the excited states are of similar nature and the previously published theoretical results proved, at least for the symmetric stretches [10, 44], that the excited-state frequencies only vary by few wave numbers ($< 10\text{ /cm}$).

4.5 Results and discussions

4.5.1 Experimental luminescence spectra

Figure 4.2 shows the fluorescence spectra acquired with respectively 300 lines/mm grating for the global emission spectra (a), and 1800 lines/mm grating for the five specific characteristic peaks (b)-(f) at $D = 25\text{ ns}$. Table 4.1 lists the aqueous concentrations of alkaline earth metal ions and the speciation calculations results in terms of ternary complexes for each sample solution with published thermodynamic data using PhreeqC [222], with which the use of SIT (Specific ion Interaction Theory) [223] for modelling the influence of ionic strength is possible. The sum of $[\text{Mg}]$ and $[\text{Ca}]$ is maintained at around $0.04\text{ mol/kg}_{\text{H}_2\text{O}}$ for this series with varying ratios of $[\text{Mg}^{2+}]/([\text{Mg}^{2+}] + [\text{Ca}^{2+}])$ from 1 to 0.5.

As shown in Figure 4.2(a), the M-U(VI)-CO_3 ($\text{M} = \text{Mg, Ca}$) spectra confirm the existence of desirable species. Successive substitution of magnesium by

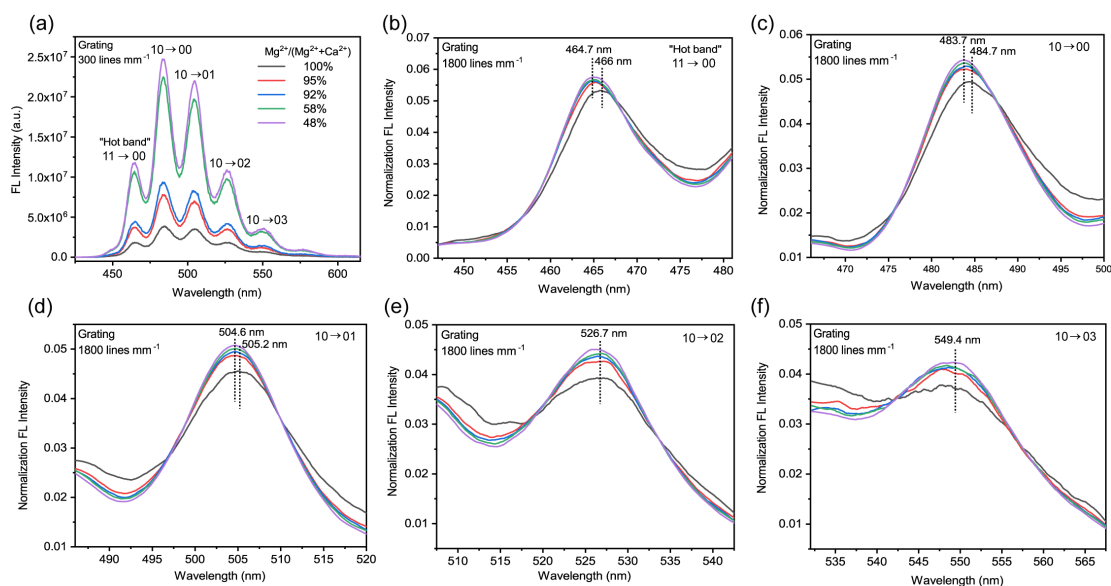


Figure 4.2: Measured luminescence spectra of U(VI) at various concentration ratios $[Mg^{2+}]/([Mg^{2+}] + [Ca^{2+}])$ using (a) the 300 lines /mm grating, and (b)-(f) using the 1800 lines /mm grating for each characteristic peak, normalized to the area of the spectrum in the working wavelength range.

calcium in the ternary triscarbonatouranyl moiety results in markedly enhanced luminescence intensity as the test solutions evolve from the condition where $Mg_n UO_2(CO_3)_3^{(4-2n)-}$ predominate to where $Ca_n UO_2(CO_3)_3^{(4-2n)-}$ are in high proportion (Table 4.1). The formation constants of Ca complexes are slightly larger than those of Mg complexes. Using reported data [201], one can express the following equilibrium and complexation constant.



This explains that a low quantity of calcium compared to that of magnesium in sample No.2 leads steadily to a relatively large fraction of Ca-UO₂-CO₃ species (49%). On addition of Ca, the increasing luminescence intensity suggests that $Ca_n UO_2(CO_3)_3^{(4-2n)-}$ exhibits higher capacity to fluoresce than $Mg_n UO_2(CO_3)_3^{(4-2n)-}$. Nevertheless, the use of the 300 lines /mm grating does not allow discriminating the spectral differences since the characteristic peak positions, determined by a Gaussian-based decomposition, differ within the uncertainties among samples. Therefore, the use of the 1800 lines /mm grating was required to probe the possible differences recorded at ambient temperature.

Table 4.1: The aqueous compositions of prepared sample solutions calculated with published thermodynamic data from Shang et al. [194], Lee et al. [206] and Dong et al. [201]

No.	$[\text{Ca}^{2+}]$ (m)	$\text{CaUO}_2(\text{CO}_3)_3^{2-}$ (m)	$\text{Ca}_2\text{UO}_2(\text{CO}_3)_3(\text{aq})$ (m)	$\text{Ca-UO}_2\text{-CO}_3$
1	0	0	0	0%
2	2.06 10 ⁻³	1.80 10 ⁻⁵	6.26 10 ⁻⁶	49%
3	3.16 10 ⁻³	2.09 10 ⁻⁵	1.15 10 ⁻⁵	65%
4	1.81 10 ⁻²	1.20 10 ⁻⁵	3.66 10 ⁻⁵	97%
5	2.29 10 ⁻²	1.02 10 ⁻⁵	3.90 10 ⁻⁵	98%
No.	$[\text{Mg}^{2+}]$ (m)	$\text{MgUO}_2(\text{CO}_3)_3^{2-}$ (m)	$\text{Mg}_2\text{UO}_2(\text{CO}_3)_3(\text{aq})$ (m)	$\text{Mg-UO}_2\text{-CO}_3$
1	4.30 10 ⁻²	3.72 10 ⁻⁵	2.07 10 ⁻⁶	79%
2	3.98 10 ⁻²	1.91 10 ⁻⁵	9.90 10 ⁻⁷	40%
3	3.56 10 ⁻²	1.29 10 ⁻⁵	6.15 10 ⁻⁷	27%
4	2.52 10 ⁻²	9.09 10 ⁻⁷	2.95 10 ⁻⁸	2%
5	2.11 10 ⁻²	5.08 10 ⁻⁷	1.38 10 ⁻⁸	1%

A closer inspection of Figure 4.2 (b)-(d) shows very small hypsochromic shifts of the first three peaks in the whole spectra when the observed signal evolves from the spectral components from $\text{Mg}_n\text{UO}_2(\text{CO}_3)_3^{(4-2n)-}$ to those of $\text{Ca}_n\text{UO}_2(\text{CO}_3)_3^{(4-2n)-}$. This could only be detected with the 1800 lines /mm gratings. The observed emission bands at longer wavelengths respond even less sensitively to this evolution of signal. More precisely, the center wavelength of the first peak, i.e., the “hot band”, representing the electronic transitions $11 \rightarrow 00$ undergoes a small shift from 466 nm ($\nu = 21\,459\text{ cm}^{-1}$) down to 464.7 nm ($\nu = 21\,519\text{ cm}^{-1}$). The second and the third peaks, corresponding to $10 \rightarrow 00$ and $10 \rightarrow 01$, are respectively shifted from 484.7 nm ($\nu = 20\,631\text{ cm}^{-1}$) down to 483.7 nm ($\nu = 20\,674\text{ cm}^{-1}$), and from 505.2 nm ($\nu = 19\,794\text{ cm}^{-1}$) to 504.6 nm ($\nu = 19\,818\text{ cm}^{-1}$). For the last two peaks — $10 \rightarrow 02$ and $10 \rightarrow 03$ (Figure 4.2 (e),(f)) — the center wavelengths remain nearly invariable. What stands out also in the emission spectra is that the influence of $\text{Mg}_n\text{UO}_2(\text{CO}_3)_3^{(4-2n)-}$ complexes on the center wavelength shift is rather limited once the fraction of Ca complexes is over 50%. As observed in experiments, the hypsochromic shift wavelengths is no longer significant when the fraction of Ca complexes increases from 49% (No.2) to 98% (No.5).

These experimental results first reveal that the interaction of alkaline earth metal ions with triscarbonatouranyl group does not seem to alter the inner-sphere coordination mode of the central uranyl ion in terms of conformational changes, supported by the fact that the emission spectra of $\text{M}-\text{U}(\text{VI})-\text{CO}_3$ complexes generally display the typical spectral profiles of $\text{UO}_2(\text{CO}_3)_3^{4-}$ species. Second, only minor modifications in characteristic emission bands have been detected using the 1800 lines/mm grating when Mg^{2+} is replaced by Ca^{2+} in the ternary species. The most intense peaks of vibronic transitions $10 \rightarrow 0\nu$ ($\nu = 0, 1$), as well as the “hot band” are more sensitive to the change of counter ions in the second coordination sphere. The slight bathochromic shifts in the case of Mg (compared to Ca) indirectly give indications that $\text{M}^{2+}/\text{UO}_2(\text{CO}_3)_3^{4-}$ interactions can generate very subtle differences in U(VI) fluorescence behavior where a detailed quantitative description of the $\text{M}^{2+}/\text{UO}_2^{2+}/\text{CO}_3^{2-}$ system with quantum chemical modeling provides a useful account of the experimental results.

4.5.2 Theoretical ground and excited state structures

All the key distances for the $\text{Na}_m\text{M}_n\text{UO}_2(\text{CO}_3)_3^{(4-m-2n)-}$ are reported in Table 4.2 along with the experimental data available in literature. To discuss the effect of the second-sphere counter cations on the first coordination shell bond lengths, we take the $\text{Na}_3\text{UO}_2(\text{CO}_3)_3^-$ complex as reference. In its ground-state structure, the following atomic distances were computed: the axial $\text{U}-\text{O}_{\text{ax}}$ bond length at 1.791 Å, the equatorial $\text{U}-\text{O}_{\text{eq}}$ at 2.433 Å, the U-C at 2.902 Å, and the $\text{U}-\text{O}_{\text{dist}}$ (O_{dist} being the most distant oxygen) at 4.141 Å. The U-Na bond distance was equal to 3.823 Å. Our calculated values are in good agreement with EXAFS data obtained in solution [190, 206]. One can point out that the use of another functional of the density, namely B3LYP, and slightly different basis sets [211], has a small impact on the computed distances, as we observe variations not larger than 0.03 Å for the distances within the uranyl first-coordination shell, and 0.14 Å within the second-coordination sphere.

Let us start with general observations on the structural changes induced by the replacement of one Na^+ ion by magnesium or calcium in the second coordination sphere, using the notations of Figure 4.2. The uranyl subunit, initially linear, was found to be slightly bent, with an $\text{O}_{\text{ax}}-\text{U}-\text{O}_{\text{ax}}$ angle of about 176°, and all the U-C bond lengths are no longer equivalent because of the different electrostatic interactions (Figure 4.3). In general, the $\text{U}-\text{O}_{\text{eq}}$ bond lengths with the oxygen atoms closer to the sodium ion (r_1) shortened, whereas the ones with the oxygen atoms closer to the alkaline earth metal (r_3) lengthened; the $\text{U}-\text{O}_{\text{eq}}$ bond lengths (r_2) located between a sodium ion and an alkaline earth ion remained almost unchanged. A similar behavior was obtained for U-C and $\text{U}-\text{O}_{\text{dist}}$ bond lengths: they got shorter close to sodium environment (r_A) and longer if magnesium or calcium is near (r_B).

The substitution of one sodium in the reference $\text{Na}_3\text{UO}_2(\text{CO}_3)_3^-$ by one magnesium decreased the $\text{U}-\text{O}_{\text{ax}}$ bond length by 0.009 Å. The U-C bond lengths vary depending on the counterion present in the vicinity as described previously. In the $\text{Na}_2\text{MgUO}_2(\text{CO}_3)_3$ complex, the computed U-Mg distance is underestimated by our method (about 0.31 Å) as compared to experimental data [223]. The replacement of a second Na^+ by magnesium-induced identical shortening of

the U–O_{ax} bond length as compared to the complex with one magnesium. The U–Mg bond remained the same for both Na₂MgUO₂(CO₃)₃ and NaMg₂UO₂(CO₃)₃⁺ complexes. To the best of our knowledge, the structure of the Mg₂UO₂(CO₃)₃ in solution has never been determined experimentally.

By looking at the series of calcium complexes, a similar tendency in the ground state geometries was observed. Like in case of the complex with one calcium, a slightly shorter decrease of axial U–O_{ax} bond length about 0.006 Å was observed, while the U–C bonds remained essentially unchanged. Unlike the Na₂MgUO₂(CO₃)₃ complex, for which U–Na was longer than U–Mg, the U–Ca, and U–Na bonds are found to be almost identical *i.e.* ~ 3.8 Å in the Na₂CaUO₂(CO₃)₃ complex, which is in a good agreement with EXAFS analysis [190]. This elongation of 0.286 Å of the distance to the alkaline earth metal dication is in line with the fact that Mg²⁺ has a smaller ionic radius (0.72 Å) than Ca²⁺ (1.00 Å) [224]. The NaCa₂UO₂(CO₃)₃⁺ complex formed by the addition of a second Ca²⁺ in the outer shell showed that the uranyl unit and first coordination sphere took a similar geometry to that of the NaMg₂UO₂(CO₃)₃⁺ complex. The difference in U–Mg bond lengths in the complexes with one and two Ca²⁺ ions was found to be 0.061 Å, while the difference in the U–Ca bond lengths was 0.022 Å between the complexes with one and two Ca²⁺ ions.

Looking at the available experimental structures including either Na⁺, Ca²⁺ or Mg²⁺, one can conclude that the U–O_{ax}, U–O_{carbonate} and U–C are rather insensitive with respect to the nature of the cation, and the observed variations when changing the counter cations are of similar magnitude as the ones reported theoretically. Our calculations sometimes underestimate by approximately 0.1 Å at most the distances between the uranium atom and the carbonates ligands and the counter cations. We suspect that this minor structural discrepancy might be imputable to the choice of the functional or to the fact that our chemical model is too limited, as explicit solvent (water molecules) are not included. However, we may assume that our calculated geometries are reliable enough to reproduce trends for the luminescence properties.

The bond lengths of the excited-state structures are reported in Table 4.3, and are compared to the bond lengths found in the ground-state geometries. For the reference Na₃UO₂(CO₃)₃[–] complex and both series of magnesium and

Table 4.2: Ground state geometries (in Å) of $\text{Na}_m\text{M}_n\text{UO}_2(\text{CO}_3)_3^{(4-m-2n)-}$ ($\text{M}=\text{Mg}, \text{Ca}$; $m, n = 0-2$) complexes computed with the PBE0 functional in the CPCM water solvent, and compared to selected literature data. The experimental uncertainties are given in parentheses.

Ground state	U-O _{ax}	U-O _{eq}	U-C	U-O _{dist}	U-M	U-Na	Method
	$r_1/r_2/r_3$	$r_1/r_2/r_3$	r_A/r_B	r_A/r_B			
$\text{Na}_3\text{UO}_2(\text{CO}_3)_3^-$	1.791	2.433	2.902	4.141		3.823	PBE0/CPCM
	1.806	2.457	2.930	4.188		3.961	B3LYP/PCM [211]
$\text{Na}_2\text{MgUO}_2(\text{CO}_3)_3^-$	1.782	2.387/2.439/ 2.477	2.857/2.948	4.089/4.172	3.515	3.801	PBE0/CPCM
	1.774	2.390/2.429/ 2.470	2.900/2.980	4.119/4.193	3.511	3.740	PBE0/CPCM
$\text{Na}_2\text{CaUO}_2(\text{CO}_3)_3$	1.785	2.404/2.433/ 2.469	2.874/2.931	4.108/4.162	3.865	3.818	PBE0/CPCM
	1.779	2.406/2.437/ 2.462	2.902/2.953	4.129/4.176	3.864	3.796	PBE0/CPCM
$\text{UO}_2(\text{CO}_3)_3^{4-}$	1.81(1)	2.44(1)	2.92(1)	4.17(1)			EXAFS [211]
	1.80(2)	2.44(2)	2.89(2)	4.20(2)			EXAFS [21]
$\text{MgUO}_2(\text{CO}_3)_3^{2-}$	1.80(1)	2.46(1)	2.91(2)	4.20(2)	3.82(6)		EXAFS [206]
	1.79(2)	2.43(2)	2.88(2)	4.15(2)	3.95(2)	3.80(2)	EXAFS [188]
$\text{Ca}_2\text{UO}_2(\text{CO}_3)_3$	1.80(2)	2.43(2)	2.88(2)	4.15(2)	4.05(2)		EXAFS [188]
	1.81(2)	2.44(2)	2.90(2)	4.22(2)	3.94(2)		EXAFS [21]

Table 4.3: Excited state geometries (in Å) of $\text{Na}_m\text{M}_n\text{UO}_2(\text{CO}_3)_3^{(4-m-2n)-}$ ($\text{M}=\text{Mg}, \text{Ca}; m, n = 0-2$) complexes computed with the PBE0 functional in the CPCM water solvent.

	U-O _{ax}	U-O _{eq} $r_1, r'_1 /$ $r_2, r'_2 /$ r_3, r'_3	U-C	U-O _{dist}	U-M	U-Na	Method
$\text{Na}_3\text{UO}_2(\text{CO}_3)_3^-$	1.826	2.442	2.908	4.147		3.822	TD-PBE0
$\text{Na}_2\text{MgUO}_2(\text{CO}_3)_3$	1.817	2.374/2.410/ 2.436/2.447/ 2.482/2.505	2.857/ 2.952/ 2.958	4.090/4.180/ 4.183	3.521	3.783/ 3.809	TD-PBE0
$\text{NaMg}_2\text{UO}_2(\text{CO}_3)_3^+$	1.810	2.379/2.380/ 2.454/2.455/ 2.479/2.480	2.903(x2)/ 2.988	4.123/4.124/ 4.202	3.518/ 3.519	3.717	TD-PBE0
$\text{Na}_2\text{CaUO}_2(\text{CO}_3)_3$	1.820	2.406/2.422/ 2.425/2.428/ 2.482/2.497	2.882/2.933/ 2.927	4.118/4.164/ 4.168	3.875	3.817/ 3.806	TD-PBE0
$\text{NaCa}_2\text{UO}_2(\text{CO}_3)_3^+$	1.815	2.398(x2)/ 2.462(x2)/ 2.467(x2)	2.908(x2)/ 2.956	4.135(x2)/ 4.180	3.871(x2)	3.778	TD-PBE0

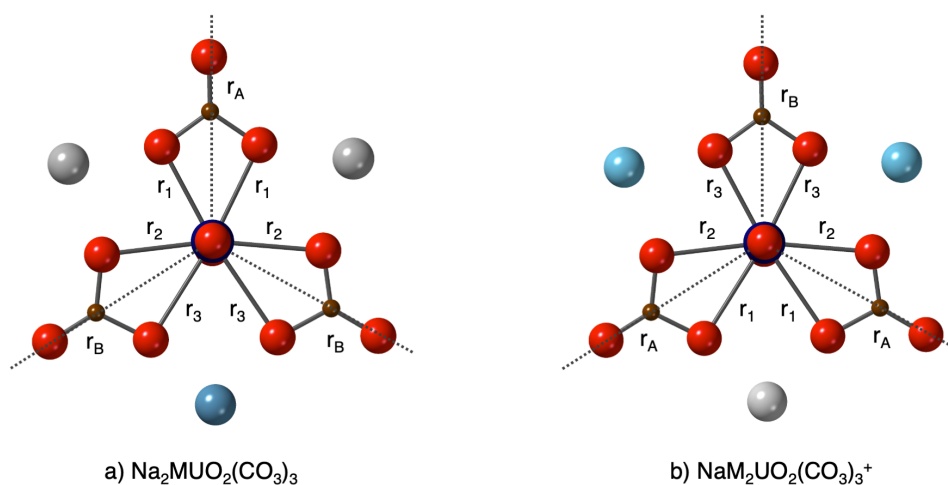


Figure 4.3: Schematic notation of U–CO₃ bonds in a) $\text{Na}_2\text{MUO}_2(\text{CO}_3)_3$ and b) $\text{NaM}_2\text{UO}_2(\text{CO}_3)_3^+$ (M = Mg, Ca) complexes depending on the position of the alkaline earth metals in the second coordination sphere. Notation r_1 , r_2 and r_3 correspond to different U–O_{eq} bonds, while the dashed lines r_A and r_B correspond to different U–C and U–O_{dist} bonds. In red - O, brown - C, dark blue - U, gray - Na, light blue - Ca, Mg.

calcium complexes, the U–O_{ax} bond elongates by 0.035-0.036 Å upon excitation. One can see that for the Mg/Ca systems, the bond lengths of the U–O_{eq} are not degenerate any longer. An increase of the U–O_{eq}, U–C and U–O_{dist} bonds between the ground and excited states was found to be in the range from 0 to 0.01 Å. The positions of Na⁺ and alkaline earth cations in the excited state were found to be rather similar after excitation of an electron. The U–Na bond lengths shortened by up to 0.023 Å along the series, while the excitation process resulted in a small elongation of the U–M bond by at most 0.01 Å. Additional analysis of the structural changes are presented in a table form in the Annex B. As there is no literature data available for the excited state structures of triscarbonatouranyl complexes, it is difficult to quantitatively estimate the accuracy of the TD-DFT relaxed calculations. Nevertheless, small elongations of atomic bonds were observed as could be expected as a result of the transition from bonding to non-bonding orbital of the uranium, as observed for the uranyl tetrahalide complexes [136]. As the main objective here is to describe the evolution

of the luminescence properties in the series, the methodology appears to be trustworthy.

The intensity distributions observed in the luminescence spectra of U(VI)-based complexes are closely related to the uranyl vibrational modes, mostly the uranyl symmetrical stretching ν_s . Thus, we have reported in Table 4.4 the computed frequency values of the ground and excited state uranyl bending ν_b , symmetrical ν_s and anti-symmetrical ν_a stretching modes.

The values for ν_s and ν_a in the $K_4UO_2(CO_3)_3$ crystal were measured by Raman and IR spectroscopies at 300 K [225]. The experimental solid-state symmetrical and anti-symmetrical stretching frequencies amounted to 806 and 882 cm^{-1} , and agreed well with ours, 837 and 877 cm^{-1} , computed for the $Na_3UO_2(CO_3)_3^-$ complex with inclusion of long-range hydration effects. The ν_b for this complex was computed at 286 cm^{-1} but it could not be compared to any experimental data. It is noteworthy that with the addition of counterions, the uranyl bending motion is coupled with the vibration and deformation motions of the carbonate ligands. It is thus inappropriate to discuss this vibrational frequency as pure bending mode of the uranyl unit. The same observation was made by Kalashnyk et al. for the andersonite mineral $Na_2CaUO_2(CO_3)_3 \cdot xH_2O$ ($x=5.3 - 5.6$) [213] for which they reported ν_b in the 225-285 cm^{-1} range. We calculated 255-282 cm^{-1} for the $Na_2CaUO_2(CO_3)_3$ complex, which appears to be consistent. Moreover, as the charge of the complex increases with the addition of Mg^{2+} or Ca^{2+} in the second coordination sphere, gradual shifts to larger vibrational energies of the uranyl stretching modes ν_s and ν_a were observed when sodium was replaced by alkaline earth metal, with a shift of about +17-21 cm^{-1} for the magnesium complexes, and +13-14 cm^{-1} for the calcium complexes.

In the first excited state, the uranyl vibrational stretching frequencies are smaller than in the ground state whereas the bending ones are nearly identical. For the reference $Na_3UO_2(CO_3)_3^-$ complex, symmetrical and anti-symmetrical stretching modes decreased by 125 and 100 cm^{-1} , respectively. A similar tendency, within 10 cm^{-1} , was observed for the other $Na_mM_nUO_2(CO_3)_3^{(4-m-2n)-}$ ($M = Mg, Ca; m, n = 0-2$) compounds. A complete analysis of vibrational frequencies behavior is available in the Annex B.

Table 4.4: Ground and excited-state vibrational frequencies (in cm^{-1}) of $\text{Na}_m\text{M}_n\text{UO}_2(\text{CO}_3)_3^{(4-m-2n)-}$ ($\text{M} = \text{Mg}, \text{Ca}$; $m, n = 0-2$) complexes computed with the PBE0 functional in the CPCM water solvent.

	ν_b	ν_s	ν_a	Method
Ground state				
$\text{Na}_3\text{UO}_2(\text{CO}_3)_3^-$	286	837	877	PBE0/CPCM
$\text{Na}_2\text{MgUO}_2(\text{CO}_3)_3$	230-285	857	898	PBE0/CPCM
$\text{NaMg}_2\text{UO}_2(\text{CO}_3)_3^+$	250-305	874	918	PBE0/CPCM
$\text{Na}_2\text{CaUO}_2(\text{CO}_3)_3$	255-282	850	891	PBE0/CPCM
$\text{NaCa}_2\text{UO}_2(\text{CO}_3)_3^+$	242-288	862	905	PBE0/CPCM
$\text{K}_4\text{UO}_2(\text{CO}_3)_3$		806	882	IR/Raman [225]
$\text{Na}_2\text{CaUO}_2(\text{CO}_3)_3 \cdot x\text{H}_2\text{O} (x=5.3 - 5.6)$	225-285	833	931	Raman [213]
Excited state				
$\text{Na}_3\text{UO}_2(\text{CO}_3)_3^-$	276	712	777	TD-PBE0/CPCM
$\text{Na}_2\text{MgUO}_2(\text{CO}_3)_3^-$	238-278	722	796	TD-PBE0/CPCM
$\text{NaMg}_2\text{UO}_2(\text{CO}_3)_3^+$	224-307	739	812	TD-PBE0/CPCM
$\text{Na}_2\text{CaUO}_2(\text{CO}_3)_3$	228-275	720	791	TD-PBE0/CPCM
$\text{NaCa}_2\text{UO}_2(\text{CO}_3)_3^+$	233-278	728	801	TD-PBE0/CPCM

4.5.3 Experimental and theoretical emission energies

In experimental luminescence spectra the first observed electronic transition, usually called the “hot band” is located near 465 nm, and can be detected at room temperature [17]. The study of the electronic structure of uranyl-based complexes shows that the luminescent state usually corresponds to the first low-lying triplet states that are nearly degenerate. Even though the triplet-singlet transitions are forbidden by the spin selection rule in the spin-orbit free picture, this rule is relaxed in the intermediate coupling scheme when spin-orbit coupling is accounted for and can be observed experimentally. The analysis of the molecular orbitals involved in excitations to the first four triplet states (1a-4a) confirmed that uranyl luminescence originates from transitions involving an electron placed in one of the four non-bonding $5f$ orbitals of uranium(VI) to an orbital that has a uranyl σ ($5f, 6d$) character mixed with the $2p$ atomic orbitals of the carbonate oxygens (Figure 4.4). Thus, the emission process in the triscarbonatouranyl bidentate complexes corresponds to a local transition from

one of the non-bonding to bonding uranyl orbitals, with a moderate metal-to-ligand charge transfer character.

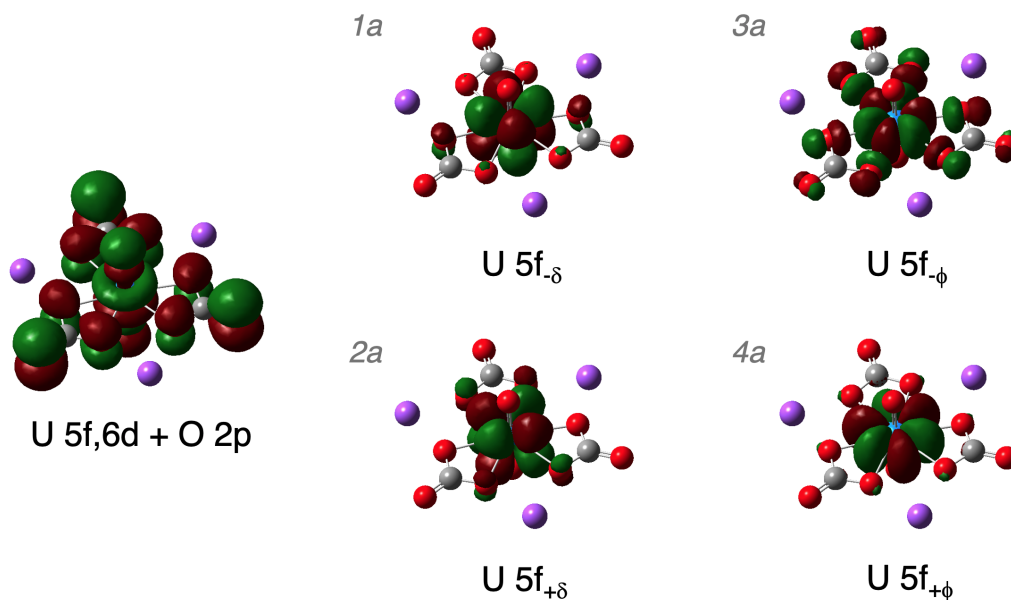


Figure 4.4: The highest occupied and lowest unoccupied molecular orbitals of $\text{Na}_3\text{UO}_2(\text{CO}_3)_3^-$ involved in the triplet-singlet electronic transitions, responsible of uranyl luminescence. The molecular orbitals were computed at the gas phase ground-state structure at the DFT/PBE0 level of theory.

The origin of the spectral envelope usually shifts along the energy scale as a function of the nature of the equatorial ligands, the stoichiometry and the complex structure. Several spectroscopic studies evidenced a luminescence blue shift of the carbonate complexes as compared to many other uranyl species such as phosphates, halides or hydrates!^[17, 20, 21, 205]. From previous studies on triscarbonatouranyl complexes [183, 206], the blue shift was estimated to 7, 15, and 25 nm (in approximately $300 - 1100 \text{ cm}^{-1}$) with respect to $\text{UO}_2(\text{H}_2\text{O})_5^{2+}$, $\text{UO}_2\text{Cl}_4^{2-}$ and $\text{UO}_2(\text{NO}_3)_2$ complexes, respectively. Wang et al. [17] inferred that ionic interactions between the uranyl ion and anions with stronger basicity lead to larger decrease of the symmetric O=U=O stretching frequency, along with a larger redshift of the luminescence spectra. This explanation holds for

carbonate ligands that are softer bases than chlorides, for instance [226].

Theoretically, the vertical emission energy, averaged by their nature $E_{1a,2a}$ and $E_{3a,4a}$ should explain the position of the “hot band.” The theoretical $E_{1a,2a}$ and $E_{3a,4a}$ values together with the experimental emission maxima are shown in Table 4.5. The experimental “hot band” values for the series of magnesium and calcium triscarbonatouranyl complexes agreed well with the previous spectroscopic studies [183, 206] and usually remain constant within 2 nm. In aqueous solution, Mg^{2+} exhibits a stronger polarizing effect than Ca^{2+} due to its higher charge density. When M^{2+} counterions interact with $\text{UO}_2(\text{CO}_3)_3^{4-}$, the global electron density of the negative ion group, especially of the equatorial oxygen atoms in carbonates, would be more distorted towards the Mg^{2+} than Ca^{2+} . The effect of distortion could change the bonding character from ionic to covalent if enough valence electrons are attracted to the positive ions [227]. The electronic redistribution occurred in $\text{Mg}-\text{UO}_2-\text{CO}_3$ complexes results in a less symmetric structure, which probably reasons out the weak shift of emission spectra to longer wavelengths. In a previous study, the effect of molecular symmetry on fluorescence results has been specially studied by comparing the experimental parameters of a set of organic molecules [228]. It was shown that the more symmetric molecules often give rise to larger quantum yield and longer decay time because of several transitions forbidden by symmetry. For the more symmetric $\text{Ca}-\text{UO}_2-\text{CO}_3$ complexes, the decrease in the number of non-radiative pathways theoretically contributes to less energy losses between excitation and emission, thus should cause the hypsochromic shift in emission spectra [229].

The comparison of the $E_{1a,2a}$ and $E_{3a,4a}$ theoretical energies showed that the $E_{3a,4a}$ values agree better with experimental “hot band” values than the $E_{1a,2a}$. However, the $E_{1a,2a}$ energies are in the range of the triscarbonatouranyl spectral envelope, thus they can contribute to the experimental spectra. For the Mg^{2+} and Ca^{2+} triscarbonatouranyl complexes our calculations showed a redshift from $\text{Na}_3\text{UO}_2(\text{CO}_3)_3^-$ to $\text{Na}_2\text{MUO}_2(\text{CO}_3)_3$ and $\text{NaM}_2\text{UO}_2(\text{CO}_3)_3^+$ as a result of negative and positive charges in our model structures used for calculations, while the complexes in solution are stabilized by counter-ions present in the working solution. It is worth noting that our calculations did not show any significant impact of the alkaline earth metal on the position of the emission

Table 4.5: Experimental and computed “hot band” energies (in nm and cm^{-1}) of $\text{Na}_m\text{M}_n\text{UO}_2(\text{CO}_3)_3^{(4-m-2n)-}$ ($\text{M} = \text{Mg}, \text{Ca}$; $m, n = 0-2$) complexes in water. Theoretical values were obtained at all-electron SOC CAM-B3LYP level of theory, modeling the water solvent with the COSMO model.

	Exp.		$E_{1a,2a}^a$		$E_{3a,4a}^a$	
	nm	cm^{-1}	nm	cm^{-1}	nm	cm^{-1}
$\text{Mg}-\text{UO}_2-\text{CO}_3$	464.7 ^b / 466 [183]	21552/ 21459				
$\text{Ca}-\text{UO}_2-\text{CO}_3$	466 ^b / 467 [206]	21459/ 21413				
$\text{Na}_3\text{UO}_2(\text{CO}_3)_3^-$			487	20543	467	21412
$\text{Na}_2\text{MgUO}_2(\text{CO}_3)_3$			492	20339	473	21131
$\text{NaMg}_2\text{UO}_2(\text{CO}_3)_3^+$			491	20372	474	21111
$\text{Na}_2\text{CaUO}_2(\text{CO}_3)_3$			491	20362	473	21421
$\text{NaCa}_2\text{UO}_2(\text{CO}_3)_3^+$			493	20268	476	21211
$\text{UO}_2(\text{H}_2\text{O})_5^{2+}$	471 [22]	21231				
$[\text{A336}]_2[\text{UO}_2\text{Cl}_4]^{c,d}$	479 [136]	20877	499	20044	485	20599
$\text{UO}_2(\text{NO}_3)_2 \cdot 2\text{H}_2\text{O}^d$	490 [230]	20408	494	20260	484	20651

^athe reported $E_{1a,2a}$ and $E_{3a,4a}$ values correspond to the average of the two first pairs of vertical emission energies (See Table B.7, Annex B) computed at the lowest triplet state geometries, with addition of the zero-point energy corrections of the ground and first excited states

^bthis work

^cin *n*-dodecane

^d $E_{1a,2a}$ and $E_{3a,4a}$ values were obtained at TD-DFT/PBE0 level of theory in the corresponding media

maxima. It is still difficult to predict emission energies of actinides with a high precision, but our method allowed to reproduce accurately the blue shift of the luminescence profile of triscarbonatouranyl complexes. As compared to similar calculations of the $E_{3a,4a}$ performed in our group at the same level of theory for the $[\text{A336}]_2[\text{UO}_2\text{Cl}_4]$ in *n*-dodecane and $\text{UO}_2(\text{NO}_3)_2 \cdot 2\text{H}_2\text{O}$ in water media, our method is qualified to reproduce experimental “hot band” position within ± 10 nm ($\approx 500 \text{ cm}^{-1}$) accuracy.

4.5.4 Vibronic progressions

The luminescence spectrum of U(VI) complexes typically shows well-spaced vibronic progressions that overlap with the pure electronic transition originates from the luminescent state to the ground state. The vibronic progression means that there is a coupling to symmetrical stretching mode of uranyl unit during the emission process. The theoretical and experimental luminescence spectra of Mg^{2+} and Ca^{2+} triscarbonatouranyl complexes are shown in Fig. 4.5. The theoretical spectra were all shifted to the position of the experimental “hot band” for the sake of spectra comparison. The calculated spectrum of $\text{Na}_3\text{UO}_2(\text{CO}_3)_3^-$ was not reported because it was considered not reliable due to the geometrical distortion of some electron configurations leading to a deficiency of degeneracy.

The intensity of luminescence depends on the quantum yield, which is basically a ratio of the rate of de-excitation by photons emission to the rate of de-excitation by both radiative and non-radiative processes. It is usually much lower than unity for uranyl species since non-radiative transitions are the major part of relaxation of the excited molecules [140]. This is why the prediction of real experimental intensities from quantum chemical model is necessarily incomplete, and only relative peak intensities and trends are relevant.

For all the triscarbonatouranyl complexes the vibronic part starts at the $10 \rightarrow 00$ transition with the band spacing equal to the ground state uranyl stretching frequency ν_s^{GS} , while the $11 \rightarrow 00$ “hot band” appears at higher energy from the $10 \rightarrow 00$ transition. The analysis of $E_{1a,2a}$ and $E_{3a,4a}$ theoretical emission energies has shown that the $E_{1a,2a}$ agreed well with the experimental $10 \rightarrow 00$ transition, while $E_{3a,4a}$ is much closer to the $11 \rightarrow 00$ value and spaced from $E_{1a,2a}$ by a ν value ranging from 729 to 798 cm^{-1} (See Table 4.6). Such observation is supporting the possibility of the simultaneous contributions of two excited states to the spectrum. Thus, it has been assumed that there are two vibronic progressions starting at $E_{1a,2a}$ and $E_{3a,4a}$ energies and contributing to the $10 \rightarrow 00$ and $11 \rightarrow 00$ transitions, respectively. To reconstruct theoretical spectra, two vibronic progressions, computed out of the first low-lying excited state, were superimposed on the same energy scale.

The analysis of computed spectra showed no other significant contributions

than uranyl symmetrical stretching mode, which means that the coupling scheme remains the same for Mg^{2+} and Ca^{2+} triscarbonatouranyl complexes. The detailed assignment of the peaks is provided in the Annex B. The experimental and theoretical spectral characteristics such as positions of the peaks and the band-spacing values are reported in Table 4.6.

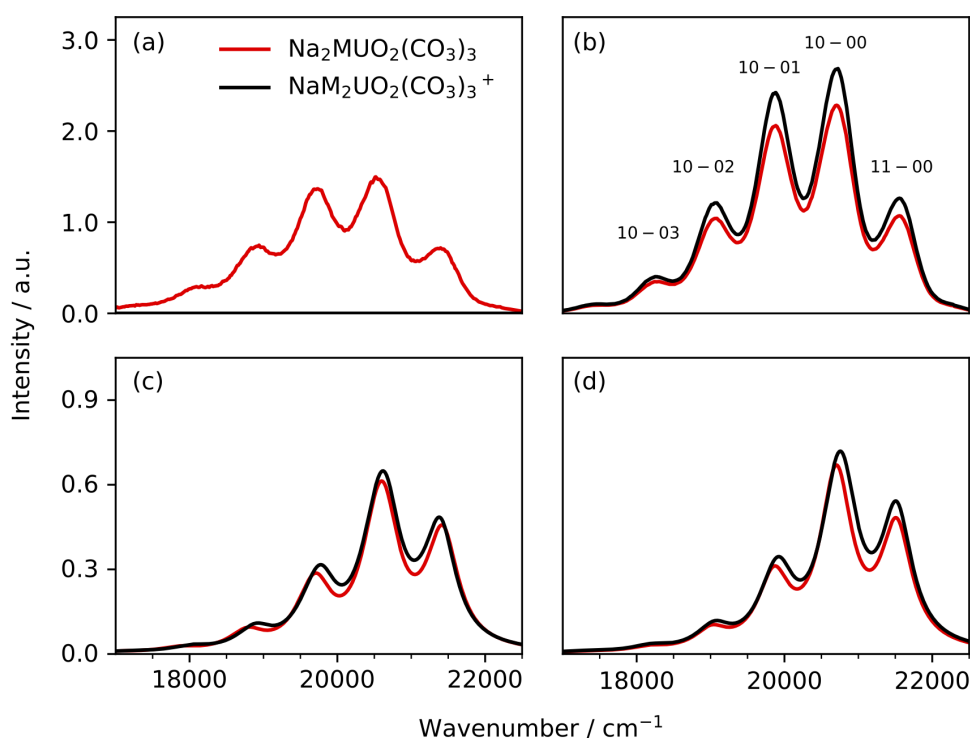


Figure 4.5: Deconvoluted experimental spectra of (a) $\text{MgUO}_2(\text{CO}_3)_3^{2-}$, and (b) $\text{CaUO}_2(\text{CO}_3)_3^{2-}$ and $\text{Ca}_2\text{UO}_2(\text{CO}_3)_3$ from TRLFS measurements. Theoretical luminescence spectra in water of (c) $\text{Na}_2\text{MgUO}_2(\text{CO}_3)_3$ (reconstructed as described in Annex B) and $\text{NaMg}_2\text{UO}_2(\text{CO}_3)_3^+$, and (d) $\text{Na}_2\text{CaUO}_2(\text{CO}_3)_3$ and $\text{NaCa}_2\text{UO}_2(\text{CO}_3)_3^+$.

The peak positions were predicted with the maximal deviation of about 224 cm^{-1} for Mg^{2+} and 131 cm^{-1} for Ca^{2+} complexes. Theoretical values of the band spacing are overestimated by maximum 48 and 30 cm^{-1} for Mg^{2+} and Ca^{2+} systems, respectively, compared to experimentally obtained values. The calculated ν values are found to be systematically lower by about 89 and 116

cm^{-1} for Mg^{2+} and Ca^{2+} correspondingly with respect to experimental data, what is deduced from the spacing between the $11 \rightarrow 00$ and $10 \rightarrow 00$ transitions, and they are very similar to the excited state symmetrical stretching mode. The higher values attributed to ν from experimental spectra could originate from small additional contributions to the vibronic coupling that are not accounted for. Indeed, our theoretical model does not account for explicit water molecules in the structure's calculations, and anharmonicity effects were not accounted for in the spectra computations. Although the model could be improved, but with additional calculation cost, we conclude that the agreement between the peak positions in the experimental and computed spectra is satisfactory for such modelling of luminescence peaks from the uranyl complexes.

It is worth analyzing the change of the theoretical and experimental luminescence intensities of the complexes not in absolute terms but relative ones for the two alkaline earth metal ions. First, the comparison of theoretical intensities of Mg^{2+} and Ca^{2+} complexes between each other is scientifically wrong because the used theoretical models do not account for many other experimental factors that have an influence on luminescence intensities (pH, ionic strength etc.). Moreover, experimental luminescence intensities of the whole spectral envelope depend on additional factors like the effective laser excitation of each species, influence of experimental apparatus such as slot width, or quenching effects, which are not included in the theoretical calculations.

The spectrum of the $\text{NaMg}_2\text{UO}_2(\text{CO}_3)_3^+$ complex was fully calculated whereas we were unsuccessful in calculating the vibronic progressions in $\text{Na}_2\text{MgUO}_2(\text{CO}_3)_3$ in the framework of the Franck-Condon harmonic approximation. Indeed, we observed a distortion of the $\text{UO}_2(\text{CO}_3)_3^{4-}$ moiety upon Mg^{2+} complexation in $\text{Na}_2\text{MgUO}_2(\text{CO}_3)_3$, that was reflected in the out-of-plane molecule distortion caused by increasing of a polarizing effect of Mg^{2+} in water. The full theoretical spectrum of $\text{Na}_2\text{MgUO}_2(\text{CO}_3)_3$ could be obtained using gas-phase geometries of $\text{Na}_2\text{MgUO}_2(\text{CO}_3)_3$ including water structures corrections, and then plotted in Fig. 4.5 (c). The detailed procedure of a spectrum prediction is available in the Annex B.

On Fig. 4.5 (c) the calculated intensity of the $10 \rightarrow 01$ peak in the magnesium complexes, decreases more than the experimental $\text{Mg}-\text{UO}_2-\text{CO}_3$ inten-

Table 4.6: Experimental and theoretical spectral characteristics of triscarbonatouranyl complexes. Experimental ν_s^{GS} and ν values were obtained by Lorentzian fitting procedure.

Complex	Spectral maxima (cm ⁻¹)				ν_s^{GSa}	ν^a
	11→00	10→00	10→01	10→02		
Experimental						
Mg-UO ₂ -CO ₃	21459	20631	19794	18986	18202	826 828
Ca-UO ₂ -CO ₃	21519	20674	19818	18986	18202	832 845
Theoretical						
Na ₂ MgUO ₂ (CO ₃) ₃	21459 ^b	20737	19822	18904	17978	857 792
Na ₁ Mg ₂ UO ₂ (CO ₃) ₃ ⁺	21459 ^b	20720	19847	18972	18099	874 739
Na ₂ CaUO ₂ (CO ₃) ₃	21519 ^b	20799	19949	19099	18249	850 798
NaCa ₂ UO ₂ (CO ₃) ₃ ⁺	21519 ^b	20790	19928	19066	18205	862 729

^aThe ν_s^{GS} corresponds to the averaged band-spacing values between vibronic transitions, the ν corresponds to spacing between the 11→00 and 10→00 transitions. The spectral characteristics in nm is available in the Tables B.8 and B.9 of Annex B

^bthe 11→00 was taken from experimental Mg-UO₂-CO₃ and Ca-UO₂-CO₃ emission spectra to match position of theoretical peaks with experimental ones

sity because the calculations might underestimate the theoretical U–O_{ax} bond length changes upon excitation. From Table B.1 in Annex B we observed that U–O_{ax} bond displacement from the ground to the luminescent state is identical and equal to 0.036 Å. Thus, our theoretical model showed that even if the Mg₂UO₂(CO₃)₃ could form in experimental conditions, its luminescence spectrum will be hardly distinguished by TRLFS from the one by MgUO₂(CO₃)₃, except if they have significantly different luminescence lifetimes. On the contrary, the addition of a second Ca²⁺ ion to the triscarbonatouranyl complexes induced an enhancement of the experimental luminescence intensities Fig. 4.5 (b), as shown otherwise [183, 194, 206]. This enhancement was well reproduced in the computed spectra comparing the Na₂CaUO₂(CO₃)₃ and NaCa₂UO₂(CO₃)₃⁺ model systems Fig. 4.5 (d). This result is consistent with the fact that the U–O_{ax} bond changes are slightly different and equal to 0.035 and 0.036 Å for complexes with one and two Ca²⁺, respectively.

The theoretical results confirmed that the luminescence intensities of the triscarbonatouranyl complexes depend on the structure of uranyl unit with a major contribution from the U–O_{ax} bond displacement, and only a minor one from equatorial ligands. The intensity trends of the 10→00 transition were correctly reproduced by the quantum chemical simulations without any fitting.

4.6 Conclusions

The interaction of the triscarbonatouranyl complex UO₂(CO₃)₃⁴⁻ with alkaline earth metal ions M²⁺ (Mg and Ca) in solution is known to induce stable complexes of stoichiometry M_nUO₂(CO₃)₃⁽⁴⁻²ⁿ⁾⁻ (n=1, 2), which has important implication on uranyl speciation in different environments. These species have specific luminescence features, as a result of the electronic configurations of the ground and excited states, the vibronic states and vibrational coupling. The luminescence of the complexes with Mg²⁺ (n=1) and Ca²⁺ (n=1, 2) were measured by TRLFS and compared for the first time with simulated spectra obtained using quantum mechanics applied to model structures Na_mM_nUO₂(CO₃)₃^{(4-m-2n)-} (M = Mg, Ca; m, n = 0-2). The ground and excited state geometries of each

structure were optimized by DFT/PBE0 and TD-DFT/PBE0 at the spin-free level including relativistic effects and water solvent effects (CPCM). The first low-lying excited states were successfully computed together with the vibrational harmonic frequencies for $\text{Na}_2\text{MgUO}_2(\text{CO}_3)_3$, $\text{NaMg}_2\text{UO}_2(\text{CO}_3)_3^+$, $\text{Na}_2\text{CaUO}_2(\text{CO}_3)_3$, and $\text{NaCa}_2\text{UO}_2(\text{CO}_3)_3^+$. The $11 \rightarrow 00$ “hot band” positions were determined by the more accurate TD-DFT/CAM-B3LYP with single-point calculations. This theoretical approach enabled to calculate the main luminescence emissions of the complexes with the corresponding assignment of the electronic transitions and vibronic modes involved. The resulting calculated spectra showed a very good agreement with experimental band positions and band spacing attributed to $\text{MgUO}_2(\text{CO}_3)_3^{2-}$, $\text{CaUO}_2(\text{CO}_3)_3^{2-}$, and $\text{Ca}_2\text{UO}_2(\text{CO}_3)_3$. Particularly, the calculations reproduce fairly well the blue shift of the triscarbonatouranyl complexes luminescence as compared with other uranyl complexes. The calculations also confirmed the similarities of the spectra for Mg^{2+} and Ca^{2+} complexes, and correctly reproduced the increase of the luminescence intensity upon addition of a second Ca^{2+} as a result of a slightly large increase of the $\text{U}-\text{O}_{\text{ax}}$ distance upon excitation and change of polarizing effect. In the case of Mg^{2+} complexes, the $\text{U}-\text{O}_{\text{ax}}$ bond change was found to be the same for both $\text{Na}_2\text{MgUO}_2(\text{CO}_3)_3$ and $\text{NaMg}_2\text{UO}_2(\text{CO}_3)_3^+$, the polarizing effect of magnesium is found to have more impact on the $\text{U}-\text{O}_{\text{yl}}$ unit, suggesting that the luminescence of these complexes would hardly be distinguished experimentally, unless they have very different decay times.

The QM method applied in this work offered an appropriate compromise between the calculation cost and the accuracy of the results in comparison with experimental data. Further works could improve the representativity of the model structures by adding explicit water molecules in the structures for instance that will affect the positions of the alkaline earth metal ions and vibronic coupling.

Bibliography of the current chapter

- (10) Pierloot, K.; van Besien, E. Electronic structure and spectrum of UO_2^{2+} and $\text{UO}_2\text{Cl}_4^{2-}$. *Journal of Chemical Physics* **2005**, *123*, 204309, DOI: 10.1063/1.2121608.
- (17) Wang, Z.; M. Zachara, J.; Liu, C.; Gassman, P.; R. Felmy, A.; B. Clark, S. A cryogenic fluorescence spectroscopic study of uranyl carbonate, phosphate and oxyhydroxide minerals. *Radiochimica Acta* **2008**, *96*, 591–598, DOI: 10.1021/es048448d.
- (18) Moulin, C.; Decambox, P.; Moulin, V.; Decaillon, J. G. Uranium Speciation in Solution by Time-Resolved Laser-Induced Fluorescence. *Analytical Chemistry* **1995**, *67*, 348–353, DOI: 10.1021/ac00098a019.
- (20) Geipel, G.; Amayri, S.; Bernhard, G. Mixed complexes of alkaline earth uranyl carbonates: A laser-induced time-resolved fluorescence spectroscopic study. *Spectrochimica Acta Part A: Molecular and Biomolecular Spectroscopy* **2008**, *71*, 53–58, DOI: 10.1016/j.saa.2007.11.007.
- (21) Bernhard, G.; Geipel, G.; Reich, T.; Brendler, V.; Amayri, S.; Nitsche, H. Uranyl(VI) carbonate complex formation: Validation of the $\text{Ca}_2\text{UO}_2(\text{CO}_3)_3(\text{aq.})$ species. *Radiochimica Acta* **2001**, *89*, 511–518, DOI: 10.1524/ract.2001.89.8.511.
- (22) Drobot, B.; Steudtner, R.; Raff, J.; Geipel, G.; Brendler, V.; Tsushima, S. Combining luminescence spectroscopy, parallel factor analysis and quantum chemistry to reveal metal speciation—a case study of uranyl (VI) hydrolysis. *Chemical Science* **2015**, *6*, 964–972, DOI: 10.1039/C4SC02022G.
- (26) Tecmer, P.; Gomes, A. S. P.; Ekström, U.; Visscher, L. Electronic spectroscopy of UO_2^{2+} , NUO^+ and NUN : an evaluation of time-dependent density functional theory for actinides. *Physical Chemistry Chemical Physics* **2011**, *13*, 6249–6259, DOI: 10.1039/C0CP02534H.
- (44) Réal, F.; Vallet, V.; Marian, C.; Wahlgren, U. Theoretical investigation of the energies and geometries of photoexcited uranyl(VI) ion: A comparison between wave-function theory and density functional theory. *The Journal of Chemical Physics* **2007**, *127*, 214302, DOI: 10.1063/1.2814157.
- (57) Moll, H.; Geipel, G.; Brendler, V.; Bernhard, G.; Nitsche, H. Interaction of uranium(VI) with silicic acid in aqueous solutions studied by time-resolved laser-induced fluorescence spectroscopy (TRLFS). *Journal of Alloys and Compounds* **1998**, *271*, 765–768, DOI: 10.1016/S0925-8388(98)00203-5.

- (86) Ernzerhof, M.; Scuseria, G. E. Assessment of the Perdew–Burke–Ernzerhof exchange–correlation functional. *Journal of Chemical Physics* **1999**, *110*, 5029–5036, DOI: 10.1063/1.478401.
- (87) Yanai, T.; Tew, D. P.; Handy, N. C. A new hybrid exchange–correlation functional using the Coulomb-attenuating method (CAM-B3LYP). *Chemical Physics Letters* **2004**, *393*, 51–57, DOI: 10.1016/j.cpllett.2004.06.011.
- (111) Van Lenthe, E.; Baerends, E.-J.; Snijders, J. G. Relativistic regular two-component Hamiltonians. *Journal of Chemical Physics* **1993**, *99*, 4597–4610, DOI: 10.1063/1.466059.
- (122) Weigend, F.; Ahlrichs, R. Balanced basis sets of split valence, triple zeta valence and quadruple zeta valence quality for H to Rn: Design and assessment of accuracy. *Physical Chemistry Chemical Physics* **2005**, *7*, 3297–3305, DOI: 10.1039/B508541A.
- (123) Weigend, F.; Häser, M.; Patzelt, H.; Ahlrichs, R. RI-MP2: optimized auxiliary basis sets and demonstration of efficiency. *Chemical Physics Letters* **1998**, *294*, 143–152, DOI: 10.1016/S0009-2614(98)00862-8.
- (124) Küchle, W.; Dolg, M.; Stoll, H.; Preuss, H. Energy-adjusted pseudopotentials for the actinides. Parameter sets and test calculations for thorium and thorium monoxide. *Journal of Chemical Physics* **1994**, *100*, 7535–7542, DOI: 10.1063/1.466847.
- (125) Baerends, E. J. et al. ADF2018, SCM, Theoretical Chemistry, Vrije Universiteit, Amsterdam, The Netherlands, <https://www.scm.com>.
- (126) Van Lenthe, E.; Baerends, E. J. Optimized Slater-type basis sets for the elements 1–118. *Journal of Computational Chemistry* **2003**, *24*, 1142–1156, DOI: 10.1002/jcc.10255.
- (131) Klamt, A.; Schüürmann, G. COSMO: a new approach to dielectric screening in solvents with explicit expressions for the screening energy and its gradient. *Journal of Chemical Society, Perkin Transactions 2* **1993**, *5*, 799–805, DOI: 10.1039/P29930000799.
- (132) Klamt, A. Conductor-like Screening Model for Real Solvents: A New Approach to the Quantitative Calculation of Solvation Phenomena. *Journal of Physical Chemistry* **1995**, *99*, 2224–2235, DOI: 10.1021/j100007a062.
- (133) Klamt, A.; Jonas, V. Treatment of the outlying charge in continuum solvation models. *Journal of Chemical Physics* **1996**, *105*, 9972–9981, DOI: 10.1063/1.472829.

- (136) Oher, H.; Réal, F.; Vercouter, T.; Vallet, V. Investigation of the Luminescence of $[\text{UO}_2\text{X}_4]^{2-}$ (X = Cl, Br) Complexes in the Organic Phase Using Time-Resolved Laser-Induced Fluorescence Spectroscopy and Quantum Chemical Simulations. *Inorganic Chemistry* **2020**, *59*, 5896–5906, DOI: 10.1021/acs.inorgchem.9b03614.
- (138) Su, J.; Wang, Y.-L.; Wei, F.; Schwarz, W.; Li, J. Theoretical Study of the Luminescent States and Electronic Spectra of UO_2Cl_2 in an Argon Matrix. *Journal of Chemical Theory and Computation* **2011**, *7*, 3293–3303, DOI: 10.1021/ct200419x.
- (139) Su, J.; Wang, Z.; Pan, D.; Li, J. Excited States and Luminescent Properties of UO_2F_2 and Its Solvated Complexes in Aqueous Solution. *Inorganic Chemistry* **2014**, *53*, 7340–7350, DOI: 10.1021/ic5006852.
- (140) Su, J.; Zhang, K.; Schwarz, W. E.; Li, J. Uranyl-glycine-water complexes in solution: Comprehensive computational modeling of coordination geometries, stabilization energies, and luminescence properties. *Inorganic Chemistry* **2011**, *50*, 2082–2093, DOI: 10.1021/ic200204p.
- (144) Watkin, D. J.; Denning, R. G.; Prout, K. Structure of dicaesium tetrachlorodioxouranium (VI). *Acta Crystallographica C* **1991**, *47*, 2517–2519, DOI: 10.1107/S0108270191006777.
- (150) Vercouter, T.; Vitorge, P.; Amekraz, B.; Moulin, C. Stoichiometries and Thermodynamic Stabilities for Aqueous Sulfate Complexes of U(VI). *Inorganic Chemistry* **2008**, *47*, 2180–2189, DOI: 10.1021/ic701379q.
- (151) Mozhayskiy, V.; Krylov, A. ezSpectrum, <http://iopshell.usc.edu/downloads>.
- (156) Frisch, M. J. et al. Gaussian 16 Revision B.01, Gaussian Inc. Wallingford CT, 2016.
- (157) Cao, X.; Dolg, M.; Stoll, H. Valence basis sets for relativistic energy-consistent small-core actinide pseudopotentials. *Journal of Chemical Physics* **2003**, *118*, 487–496, DOI: 10.1063/1.1521431.
- (158) Eichkorn, K.; Weigend, F.; Treutler, O.; Ahlrichs, R. Auxiliary basis sets for main row atoms and transition metals and their use to approximate Coulomb potentials. *Theoretical Chemistry Accounts* **1997**, *97*, 119–124, DOI: 10.1007/s002140050244.
- (163) Tecmer, P.; Bast, R.; Ruud, K.; Visscher, L. Charge-Transfer Excitations in Uranyl Tetrachloride ($[\text{UO}_2\text{Cl}_4]^{2-}$): How Reliable are Electronic Spectra from Relativistic Time-Dependent Density Functional Theory? *Journal of Physical Chemistry A* **2012**, *116*, 7397–7404, DOI: 10.1021/jp3011266.

- (164) Tecmer, P.; Govind, N.; Kowalski, K.; De Jong, W. A.; Visscher, L. Reliable modeling of the electronic spectra of realistic uranium complexes. *Journal of Chemical Physics* **2013**, *139*, 034301, DOI: 10.1063/1.4812360.
- (177) Oher, H.; Vercouter, T.; Réal, F.; Shang, C.; Reiller, P. E.; Vallet, V. Influence of alkaline earth metal ions on structures and luminescent properties of $\text{Na}_m\text{Me}_n\text{UO}_2(\text{CO}_3)_3^{(4-m-2n)-}$ (Me = Mg, Ca; m, n = 0-2): time-resolved fluorescence spectroscopy and ab initio studies. *Inorganic Chemistry* **2020**, *Submitted*.
- (178) Moulin, C.; Laszak, I.; Moulin, V.; Tondre, C. Time-resolved laser-induced fluorescence as a unique tool for low-level uranium speciation. *Applied Spectroscopy* **1998**, *52*, 528–535, DOI: 10.1366/0003702981944076.
- (179) Eliet, V.; Bidoglio, G.; Omenetto, N.; Parma, L.; Grenthe, I. Characterization of Hydroxide Complexes of Uranium(VI) by Time-Resolved Fluorescence Spectroscopy. *Journal of the Chemical Society-Faraday Transactions* **1995**, *91*, 2275–2285, DOI: 10.1039/FT9959102275.
- (180) Meinrath, G.; Lis, S.; Stryla, Z.; Noubactep, C. Lifetime and fluorescence quantum yield of uranium(VI) species in hydrolyzed solutions. *Journal of Alloys and Compounds* **2000**, *300*, 107–112, DOI: 10.1016/S0925-8388(99)00739-2.
- (181) Couston, L.; Pouyat, D.; Moulin, C.; Decambox, P. Speciation of Uranyl Species in Nitric-Acid Medium by Time-Resolved Laser-Induced Fluorescence. *Applied Spectroscopy* **1995**, *49*, 349–353, DOI: 10.1366/0003702953963553.
- (182) Geipel, G.; Brachmann, A.; Brendler, V.; Bernhard, G.; Nitsche, H. Uranium(VI) sulfate complexation studied by time-resolved laser-induced fluorescence spectroscopy (TRLFS). *Radiochimica Acta* **1996**, *75*, 199–204, DOI: 10.1524/ract.1996.75.4.199.
- (183) Lee, J. Y.; Yun, J. I. Formation of ternary $\text{CaUO}_2(\text{CO}_3)_3^2$ and $\text{Ca}_2\text{UO}_2(\text{CO}_3)_3(\text{aq})$ complexes under neutral to weakly alkaline conditions. *Journal of the Chemical Society. Dalton Transactions* **2013**, *42*, 9862–9869, DOI: 10.1039/c3dt50863c.
- (184) Geipel, G.; Bernhard, G.; Rutsch, M.; Brendler, V.; Nitsche, H. Spectroscopic properties of uranium(VI) minerals studied by time-resolved laser-induced fluorescence spectroscopy (TRLFS). *Radiochimica Acta* **2000**, *88*, 757–762, DOI: 10.1524/ract.2000.88.9-11.757.

- (185) Lehmann, S.; Geipel, G.; Foerstendorf, H.; Bernhard, G. Syntheses and spectroscopic characterization of uranium(VI) silicate minerals. *Journal of Radioanalytical and Nuclear Chemistry* **2008**, *275*, 633–642, DOI: 10.1007/s10967-007-7060-z.
- (186) Massuyeau, F.; Perry, D. L.; Kalashnyk, N.; Faulques, E. Spectroscopic markers for uranium(VI) phosphates. Part II: the use of time-resolved photoluminescence. *Rsc Advances* **2017**, *7*, 919–926, DOI: 10.1039/c6ra26157d.
- (187) Wang, G.; Su, Y.; Monts, D. L. Parametric investigation of laser-induced fluorescence of solid-state uranyl compounds. *J. Phys. Chem. A* **2008**, *112*, 10502–10508, DOI: 10.1021/jp802327f.
- (188) Amayri, S.; Arnold, T.; Reich, T.; Foerstendorf, H.; Geipel, G.; Bernhard, G.; Massanek, A. Spectroscopic characterization of the uranium carbonate andersonite $\text{Na}_2\text{Ca}[\text{UO}_2(\text{CO}_3)_3] \cdot 6\text{H}_2\text{O}$. *Environmental Science & Technology* **2004**, *38*, 6032–6036, DOI: 10.1021/es0494171.
- (189) Amayri, S.; Arnold, T.; Foerstendorf, H.; Geipel, G.; Bernhard, G. Spectroscopic characterization of synthetic becquerelite, $\text{Ca}[(\text{UO}_2)_6\text{O}_4(\text{OH})_6] \cdot 8\text{H}_2\text{O}$, and swartzite, $\text{CaMg}[\text{UO}_2(\text{CO}_3)_3] \cdot 12\text{H}_2\text{O}$. *Canadian Mineralogist* **2004**, *42*, 953–962, DOI: 10.2113/gscanmin.42.4.953.
- (190) Amayri, S.; Reich, T.; Arnold, T.; Geipel, G.; Bernhard, G. Spectroscopic characterization of alkaline earth uranyl carbonates. *Journal of Solid State Chemistry* **2005**, *178*, 567–577, DOI: 10.1016/j.jssc.2004.07.050.
- (191) Arnold, T.; Baumann, N. Boltwoodite $[\text{K}(\text{UO}_2)(\text{SiO}_3\text{OH})(\text{H}_2\text{O})_{1.5}]$ and compreignacite $\text{K}_2[(\text{UO}_2)_3\text{O}_2(\text{OH})_3]_2 \cdot 7\text{H}_2\text{O}$ characterized by laser fluorescence spectroscopy. *Spectrochimica Acta Part A: Molecular and Biomolecular Spectroscopy* **2009**, *71*, 1964–1968, DOI: 10.1016/j.saa.2008.07.029.
- (192) DeNeufville, J. P. Selective detection of uranium by laser-induced fluorescence: a potential remote-sensing technique. 1: Optical characteristics of uranyl geologic targets, Washington, D.C., 1981, DOI: 10.1364/AO.20.001279.
- (193) Prat, O.; Vercouter, T.; Ansoborlo, E.; Fichet, P.; Perret, P.; Kurttio, P.; Salonen, L. Uranium Speciation in Drinking Water from Drilled Wells in Southern Finland and Its Potential Links to Health Effects. *Environmental Science & Technology* **2009**, *43*, 3941–3946, DOI: 10.1021/es803658e.

- (194) Shang, C.; Reiller, P. E. Determination of formation constants and specific ion interaction coefficients for $\text{Ca}_n\text{UO}_2(\text{CO}_3)_3^{(4-2n)-}$ complexes in NaCl solution by time-resolved laser-induced luminescence spectroscopy. *Dalton Transactions* **2020**, *49*, 466–481, DOI: 10.1039/C9DT03543E.
- (195) Scanlan, J. P. Equilibria in uranyl carbonate systems-II. The overall stability constant of $\text{UO}_2(\text{CO}_3)_2^{2-}$ and the third formation constant of and the third formation constant of $\text{UO}_2(\text{CO}_3)_3^{4-}$. *Journal of Inorganic & Nuclear Chemistry* **1977**, *39*, 635–639, DOI: 10.1016/0022-1902(77)80578-2.
- (196) Meinrath, G.; Klenze, R.; Kim, J. I. Direct spectroscopic speciation of uranium(VI) in carbonate solutions. *Radiochimica Acta* **1996**, *74*, 81–86, DOI: 10.1524/ract.1996.74.special-issue.81.
- (197) Jung, E. C.; Cho, H.-R.; Baik, M. H.; Kim, H.; Cha, W. Time-resolved laser fluorescence spectroscopy of $\text{UO}_2(\text{CO}_3)_3^{4-}$. *Dalton Transactions* **2015**, *44*, 18831–18838, DOI: 10.1039/C5DT02873F.
- (198) Bernhard, G.; Geipel, G.; Brendler, V.; Nitsche, H. Speciation of Uranium in Seepage Waters of a Mine Tailing Pile Studied by Time-Resolved Laser-Induced Fluorescence Spectroscopy (TRLFS). *Radiochimica Acta* **1996**, *74*, 87–91, DOI: 10.1524/ract.1996.74.special-issue.87.
- (199) Jo, Y.; Kirishima, A.; Kimuro, S.; Kim, H. K.; Yun, J. I. Formation of $\text{CaUO}_2(\text{CO}_3)_3^{2-}$ and $\text{Ca}_2\text{UO}_2(\text{CO}_3)_3(\text{aq})$ complexes at variable temperatures (10–70 °C). *Dalton Transactions* **2019**, *48*, 6942–6950, DOI: 10.1039/c9dt01174a.
- (200) Endrizzi, F.; Rao, L. F. Chemical Speciation of Uranium(VI) in Marine Environments: Complexation of Calcium and Magnesium Ions with $\text{UO}_2(\text{CO}_3)_3^{4-}$ and the Effect on the Extraction of Uranium from Seawater. *Chemistry-a European Journal* **2014**, *20*, 14499–14506, DOI: 10.1002/chem.201403262.
- (201) Dong, W.; Brooks, S. C. Determination of the formation constants of ternary complexes of uranyl and carbonate with alkaline earth metals (Mg^{2+} , Ca^{2+} , Sr^{2+} , and Ba^{2+}) using anion exchange method. *Environmental Science & Technology* **2006**, *40*, 4689–4695, DOI: 10.1021/es0606327.
- (202) Kalmykov, S. N.; Choppin, G. R. Mixed $\text{Ca}^{2+}/\text{UO}_2^{2+}/\text{CO}_3^{2-}$ complex formation at different ionic strengths. *Radiochimica Acta* **2000**, *88*, 603–606, DOI: 10.1524/ract.2000.88.9-11.603.
- (203) Baik, M. H.; Jung, E. C.; Jeong, J. Determination of uranium concentration and speciation in natural granitic groundwater using TRLFS. *Journal of Radioanalytical and Nuclear Chemistry* **2015**, *305*, 589–598, DOI: 10.1007/s10967-015-3971-2.

- (204) Maloubier, M.; Solari, P. L.; Moisy, P.; Monfort, M.; Den Auwer, C.; Moulin, C. XAS and TRLIF spectroscopy of uranium and neptunium in seawater. *Dalton Transactions* **2015**, *44*, 5417–5427, DOI: 10.1039/c4dt03547j.
- (205) Wang, Z.; Zachara, J. M.; Yantasee, W.; Gassman, P. L.; Liu, C.; Joly, A. G. Cryogenic laser induced fluorescence characterization of U (VI) in Hanford vadose zone pore waters. *Environmental science & technology* **2004**, *38*, 5591–5597.
- (206) Lee, J. Y.; Vespa, M.; Gaona, X.; Dardenne, K.; Rothe, J.; Rabung, T.; Altmaier, M.; Yun, J. I. Formation, stability and structural characterization of ternary $\text{MgUO}_2(\text{CO}_3)_3^{2-}$ and $\text{Mg}_2\text{UO}_2(\text{CO}_3)_3(\text{aq})$ complexes. *Radiochimica Acta* **2017**, *105*, 171–185, DOI: 10.1515/ract-2016-2643.
- (207) Beccia, M. R.; Matara-Aho, M.; Reeves, B.; Roques, J.; Solari, P. L.; Monfort, M.; Moulin, C.; Den Auwer, C. New insight into the ternary complexes of uranyl carbonate in seawater. *Journal of environmental radioactivity* **2017**, *178*, 343–348, DOI: 10.1016/j.jenvrad.2017.08.008.
- (208) Kalashnyk, N.; Perry, D. L.; Ivanov, V. G.; Faulques, E. Combined experimental and first-principles studies of a hydrated uranyl carbonate: Insight into phonon spectra for a core environmental class of uranium materials. *Journal of Physics and Chemistry of Solids* **2020**, *138*, 109260, DOI: 10.1016/j.jpics.2019.109260.
- (209) Allen, P. G. et al. Multinuclear NMR, Raman, EXAFS, and X-ray diffraction studies of uranyl carbonate complexes in near-neutral aqueous solution. X-ray structure of $[\text{C}(\text{NH}_2)_3]_6[(\text{UO}_2)_3(\text{CO}_3)_6] \cdot 6.5\text{H}_2\text{O}$. *Inorganic Chemistry* **1995**, *34*, 4797–4807, DOI: 10.1021/ic00123a013.
- (210) Kelly, S. D.; Kemner, K. M.; Brooks, S. C. X-ray absorption spectroscopy identifies calcium-uranyl-carbonate complexes at environmental concentrations. *Geochimica Et Cosmochimica Acta* **2007**, *71*, 821–834, DOI: 10.1016/j.gca.2006.10.013.
- (211) Ikeda, A.; Hennig, C.; Tsushima, S.; Takao, K.; Ikeda, Y.; Scheinost, A. C.; Bernhard, G. Comparative study of uranyl(VI) and-(V) carbonate complexes in an aqueous solution. *Inorganic chemistry* **2007**, *46*, 4212–4219, DOI: 10.1021/ic070051y.
- (212) De Jong, W. A.; Apra, E.; Windus, T. L.; Nichols, J. A.; Harrison, R. J.; Gutowski, K. E.; Dixon, D. A. Complexation of the Carbonate, Nitrate, and Acetate Anions with the Uranyl Dication: Density Functional Studies with Relativistic Effective Core Potentials. *Journal of Physical Chemistry A* **2005**, *109*, 11568–11577, DOI: 10.1021/jp0541462.

- (213) Kalashnyk, N.; Perry, D. L.; Massuyeau, F.; Faulques, E. Exploring Optical and Vibrational Properties of the Uranium Carbonate Andersonite with Spectroscopy and First-Principles Calculations. *The Journal of Physical Chemistry C* **2018**, *122*, 7410–7420, DOI: 10.1021/acs.jpcc.8b00871.
- (214) Madic, C.; Hobart, D. E.; Begun, G. M. Raman spectrometric studies of actinide(V) and-(VI) complexes in aqueous sodium carbonate solution and of solid sodium actinide (V) carbonate compounds. *Inorganic Chemistry* **1983**, *22*, 1494–1503, DOI: 10.1021/ic00152a015.
- (215) Maya, L.; Begun, G. M. A Raman spectroscopy study of hydroxo and carbonato species of the uranyl(VI) ion. *Journal of Inorganic and Nuclear Chemistry* **1981**, *43*, 2827–2832, DOI: 10.1016/0022-1902(81)80625-2.
- (216) Doudou, S.; Arumugam, K.; Vaughan, D. J.; Livens, F. R.; Burton, N. A. Investigation of ligand exchange reactions in aqueous uranyl carbonate complexes using computational approaches. *Physical Chemistry Chemical Physics* **2011**, *13*, 11402–11411, DOI: 10.1039/c1cp20617f.
- (217) Kubicki, J. D.; Halada, G. P.; Jha, P.; Phillips, B. L. Quantum mechanical calculation of aqueous uranium complexes: carbonate, phosphate, organic and biomolecular species. *Chemistry Central Journal* **2009**, *3*, 10, DOI: 10.1186/1752-153X-3-10.
- (218) Tirler, A. O.; Hofer, T. S. Structure and dynamics of the uranyl tricarbonate complex in aqueous solution: Insights from quantum mechanical charge field molecular dynamics. *The Journal of Physical Chemistry B* **2014**, *118*, 12938–12951, DOI: 10.1021/jp503171g.
- (219) Li, B.; Zhou, J.; Priest, C.; Jiang, D.-e. Effect of Salt on the Uranyl Binding with Carbonate and Calcium Ions in Aqueous Solutions. *The Journal of Physical Chemistry B* **2017**, *121*, 8171–8178, DOI: 10.1021/acs.jpcc.7b04449.
- (220) Gorller-Walrand, C.; De Houwer, S.; Fluyt, L.; Binnemans, K. Spectroscopic properties of uranyl chloride complexes in non-aqueous solvents. *Physical Chemistry Chemical Physics* **2004**, *6*, 3292–3298, DOI: 10.1039/b317002k.
- (221) Docrat, T. I.; Mosselmans, J. F. W.; Charnock, J. M.; Whiteley, M. W.; Collison, D.; Livens, F. R.; Jones, C.; Edmiston, M. J. X-ray absorption spectroscopy of tricarbonatodioxouranate(V), $[\text{UO}_2(\text{CO}_3)_3]^{5-}$, in aqueous solution. *Inorganic Chemistry* **1999**, *38*, 1879–1882, DOI: 10.1021/ic9814423.

- (222) Parkhurst, D. L.; Appelo, C. A. J. *User's Guide to PHREEQC (Version 2) — A Computer Program for Speciation, Batch-Reaction, One-Dimensional Transport, and Inverse Geochemical Calculations*, Lakewood, Colorado, USA, 1999.
- (223) Guillaumont, R.; Fanghänel, T.; Fuger, J.; Grenthe, I.; Neck, V.; Palmer, D. A.; Rand, M. H., *Update on the Chemical Thermodynamics of Uranium, Neptunium, Plutonium, Americium and Technetium, Chemical Thermodynamics*, p 918.
- (224) Shannon, R. D. Effective ionic radii and systematic studies of interatomic distances in halides and chalcogenides. *Acta Crystallographica A* **1976**, *32*, 751–767, DOI: 10.1107/S0567739476001551.
- (225) Anderson, A.; Chieh, C.; Irish, D. E.; Tong, J. P. K. An X-ray crystallographic, Raman, and infrared spectral study of crystalline potassium uranyl carbonate, $K_4UO_2(CO_3)_3$. *Canadian Journal of Chemistry* **1980**, *58*, 1651–1658, DOI: 10.1139/v80-264.
- (226) Parr, R. G.; Pearson, R. G. Absolute hardness: companion parameter to absolute electronegativity. *Journal of the American Chemical Society* **1983**, *105*, 7512–7516, DOI: 10.1021/ja00364a005.
- (227) Clugston, M. J.; Flemming, R., *Advanced chemistry*; Oxford University Press: Oxford New York, 2000.
- (228) Nizhegorodov, N. I. Effect of molecule symmetry on fluorescence parameters and on the intercombination conversion constant. *Journal of Applied Spectroscopy* **1992**, *57*, 873–878, DOI: 10.1007/BF00663933.
- (229) Lakowicz, J. R., *Principles of fluorescence spectroscopy*, 3rd; Springer: New York, 2006, xxvi, 954 p.
- (230) Moulin, C.; Decambox, P.; Mauchien, P.; Pouyat, D.; Couston, L. Direct uranium (VI) and nitrate determinations in nuclear reprocessing by time-resolved laser-induced fluorescence. *Analytical Chemistry* **1996**, *68*, 3204–3209, DOI: 10.1021/ac9602579.

Influence of the first coordination of uranyl on its luminescence properties: study of uranyl binitrate with monoamide DEiBA and water

5.1 Introduction

The production of electricity from nuclear energy has been developed in several countries. Some countries among which the U.S.A., France, United Kingdom, chose to reprocess the spent nuclear fuel for an economic reuse of the uranium and plutonium, and a reduction of the radioactivity and volume of the wastes [231]. The recovery of uranium and plutonium, and effective separation from fission products and minor actinides has been achieved at both laboratory and industrial scales by solvent extraction techniques using an aqueous phase and an immiscible organic phase. The transfer of actinide metal cations occurs from an acidic aqueous phase resulting from the dissolution of the fuel in nitric acid into an organic phase by complexation with liposoluble extracting molecules [232, 233]. Nowadays, the main industrial solvent extraction process is Plutonium Uranium Refining by Extraction (PUREX) in which the tri-*n*-butyl phosphate (TBP) extracting agent is used to separate U(VI) and Pu(IV)

from minor actinides and fission products in highly concentrated nitric acid solution [234]. Though efficient the PUREX process requires a reduction of plutonium for the U/Pu partitioning by addition of U(IV) and anti-nitrous reagents. Moreover, the washing and recycling of the solvent has to account for the degradation of TBP by radiolysis [235]. Thus, several processes have been developed to modify or replace the PUREX process, and meet new requirements such as the development of a one-cycle process without redox chemistry. Following the principle of interaction of O- or N-donor organic molecules with uranium or plutonium [236, 237], new types of complexing agents have been studied.

In France, the GANEX process (Group ActiNide EXtraction) has been developed by CEA for the industrial reprocessing of spent nuclear fuel and the homogeneous recycling of actinides [238, 239]. In this process, the selective separation is operated by solvent extraction using a new group of the N,N-dialkyl amides (further monoamides) first appeared in the 1960s [240–242]. It has been demonstrated that monoamides have a strong affinity with both the uranyl or plutonium cations [243–246]. Their selectivity can be adjusted by varying either the length or the ramification of monoamide alkyl chain [240, 247, 248]. In the first cycle of the GANEX process, the use of N,N-di-(ethyl-2-hexyl)isobutyramide (DEHiBA) has been proposed, as it shows a good compromise between a quantitative extraction of uranium, its high loading capacity and a high U(VI)/Pu(IV) selectivity [249, 250]. The knowledge of the stoichiometries and coordination of the actinide cations in aqueous and organic media are of high importance not only to better understand the extraction mechanism but also to optimize the extraction efficiency and selectivity. In the case of uranyl extraction, it has been shown that the neutral complex $\text{UO}_2(\text{NO}_3)_2(\text{L})_2$ forms in the organic phase [251–253]. It has a hexagonal bipyramidal geometry corresponding to the uranyl center to which two nitrates and two amide groups are linked as it has been confirmed by X-ray Diffraction (XRD), Raman, and IR spectroscopies [243, 254]. One should point out that the nitrates can be located either in *cis* or *trans* positions. Although they are cases reported in the literature involving a *cis* conformation around the uranyl moiety [243, 244, 255], it is far less common than the *trans* conformation. As the two conformations exist in crystals, they might both be present in nitric acid solution and in organic phases.

The existence of different species could induce a change in the electronic structure of uranyl binitrate complexes. For example, the study of IR spectra would show that several modes of coordination of uranyl binitrates could exist in the organic phase after extraction [232]. In order to reveal a difference in the coordination sphere of uranyl in terms of position of the nitrates and monoamides, the organic phase after extraction can be characterized by UV-Vis or time-resolved laser-induced fluorescence spectroscopy (TRLFS). The latter method has some advantageous features allowing to measure luminescence spectra at low total uranium concentration and discriminate side emitting compounds by temporal resolution. Moreover, the positions of the luminescence bands, band spacings, bandwidths, and intensities are features that can be interpreted to determine the nature and the number of ligands in the first coordination layer of UO_2^{2+} , as well as the local symmetry of the complex. For this, the spectroscopic characteristics should be well analyzed and interpreted. However, the determination of an electronic structure information from the luminescence spectra is either still unresolved or it requires additional experimental data. For instance, to study an electronic structure of $\text{UO}_2\text{Cl}_4^{2-}$ complex, Görrler-Warland et al. [23] used UV-Vis and magnetic circular dichroism spectroscopies. Another way is based on the Franck-Condon principle, where the overlapped region between the absorption and luminescence spectra gives an idea about the position of the electronic transitions on the energy scale, but not the exact value, since several transitions may appear in that region.

As we already described in Chapters 3 and 4, to study the uranium-based complexes and interpret the experimental spectra, the quantum chemical modeling is an insightful tool as it provides an accurate description of the electronic structure. Using the methodology described earlier, the luminescence spectrum, as well as spectroscopic characteristics can be computed and used for the assignment of the experimental spectrum. In our previous studies, the methodology has been proven to give an accurate description of the uranyl complexes electronic structures allowing to elucidate and quantify the influence of the first and second coordination spheres on the luminescence features. The structural parameters, emission energies and simulated luminescence spectra were found to be in good accordance with experimental data giving a significant level of

confidence in the chosen theoretical methodology.

In this chapter, we aim at studying the uranyl binitrate complexes and the influence of water and monoamide molecules in the first coordination sphere using quantum chemical simulations and the comparison to available experimental data. Theoretical models were created based on previous studies on the uranyl binitrate compounds [173, 256] and will be described in detail further. The structural parameters of uranyl binitrate models will be discussed at the relativistic PBE0 level of theory in their *cis* and *trans* configurations. In the sake of guiding future experimental studies on uranyl binitrate compounds, the conformers stabilities and probabilities have been computed. As the spin-orbit CAM-B3LYP method has been found to accurately place electron transition energies of actinide complexes [26], it is used to determine the “hot band” position in experimental luminescence spectra, since it is not easily identified experimentally. Moreover, we expect that this study is not only useful in illustrating the broad applicability of quantum modeling, but may also guide scientists in spectral data processing, *i.e.*, identification of the bands and importance of their intensities.

5.2 Computational Details

The detailed theoretical methodology has been described in the Chapters 3 and 4. Since it is not exactly the same, there are some details which are different; thus we decided to keep the full description of computational details part to ease the reading.

For the computation of the theoretical luminescence spectra of uranium (VI) complexes, the ezSpectrum 3.0 [151] software was used. The spectral lines are basically the Franck-Condon factors (FCFs) which correspond to the overlaps between the excited and the ground-state vibrational wavefunctions and were computed analytically including Duschinsky transformations of the normal modes between the ground and excited states. The number of vibrational quanta in the luminescent and ground state were selected to be one and five, respectively, to match the recorded experimental vibronic transitions. All the vibronic progressions were computed at 300 K to include contributions from

the thermally active vibrational modes. As our quantum chemical methods cannot compute absolute intensities, we manually adjusted the intensity of the “hot band” peak to match the experimental intensity distributions. The spectral shapes were estimated by convoluting the discrete stick spectra with Lorentzian broadening functions adjusting the width to that of the experimental full widths at half-maxima. All the necessary data for the spectra computations were obtained with *ab initio* methods as detailed further in this section.

The choice of the used QM methods was justified in the previous Chapters 3 and 4 and the corresponding published works [136, 163]. The ground and excited-state molecular geometries were optimized with Gaussian 16 [156] software including scalar relativistic effects and using the PBE0 functional of the density [86]. For the $\text{UO}_2(\text{NO}_3)_2(\text{H}_2\text{O})$ and *cis-/trans*- $\text{UO}_2(\text{NO}_3)_2(\text{H}_2\text{O})_2$ complexes, the water solvent was accounted for using the continuum polarizable conductor model (CPCM) [127] ($\epsilon_r = 78.36$). The experimental luminescence spectrum of the $\text{UO}_2(\text{NO}_3)_2(\text{DEHiBA})_2$ complex was recorded in hydrogenated tetrapropylene (TPH) which is an industrial solvent that is often described as a branched dodecane; thus one can assume that it has similar properties to that of *n*-dodecane, namely a low polarity. Therefore, the structures of *cis-/trans*- $\text{UO}_2(\text{NO}_3)_2(\text{DEiBA})_2$ complexes were optimized in the gas phase, as the solvent is expected to not induced sizable changes of the complex geometries because of its low permittivity value ($\epsilon_r = 2.00$ taken for *n*-dodecane) [136]. The geometries of the luminescent states (first triplet excited states) were optimized using the time-dependent (TD)-DFT/PBE0 approach as implemented in Gaussian 16 code [156] with equilibrium solvation where it was necessary. The vibrational harmonic frequencies of the ground and luminescent states were computed analytically. All optimized geometries considered for the vibronic spectra calculations represent real minima as they have no imaginary frequencies. In these calculations, the def2-TZVP basis sets [122, 123] were used for the H, C, N and O elements. A small-core Relativistic Effective Core Potential (RECP), that accounts for scalar relativistic effects of the 60 core electrons [124, 157] was used for the uranium atom, while the valence electrons were described by the def-TZVP basis set [158]. To speed up the TD-DFT calculations within the Gaussian 16 package, the inner U(5*s*, 5*p*, 5*d*), O(1*s*), C(1*s*), N(1*s*) orbitals were

frozen.

In order to compute accurate absolute energies of the electronic transitions involved in the luminescence spectra of uranyl nitrate complexes, we have performed CAM-B3LYP [87] TD-DFT single-point calculations, at the spin-free excited-state structures, including spin-orbit coupling effects with the ZORA Hamiltonian [257], and modeling the environment effect (water solvent for *cis*- and *trans*- $\text{UO}_2(\text{NO}_3)_2(\text{H}_2\text{O})_n$ ($n=1,2$) and *n*-dodecane for $\text{UO}_2(\text{NO}_3)_2(\text{DEiBA})_2$) with the conductor-like screening model COSMO [131–133]. These calculations were carried out with the Amsterdam Density Functional package (ADF 2018.01) [125]. All atoms were described by TZ2P Slater-type basis sets [126] without freezing the atomic cores.

The free energy calculations were performed at DFT/PBE0 and MP2 levels of theory using the Turbomole 7.3 [155] and the Gaussian 16 [156].

5.3 Results

5.3.1 Choice of the model systems

In general, the coordination number of the uranyl unit varies from four to six depending on the ligands nature and media [258]. In nitric acid solutions the uranium(VI) speciation may be composed of several species like uranyl UO_2^{2+} and uranyl nitrate complexes $(\text{UO}_2(\text{NO}_3)_n)^{(2-n)}$, $n = 1, 2$) that can be detected by TRLS [230]. In organic media the uranyl nitrate complex is soluble as a neutral compound $\text{UO}_2(\text{NO}_3)_2(\text{L})_2$ [256]. As one of the main goals of this study is to elucidate the influence of organic ligands present in the first coordination sphere, the chemical model systems should have the same coordination number and molecular charge. In the present work, the majority of the model systems are sixfold coordinated and are neutral. The structures are shown in Figure 5.1. In the crystal phase, the uranyl nitrate complex hydration shell contains six water molecules, but there are at most two water molecules in the first coordination sphere, $[\text{UO}_2(\text{NO}_3)_2(\text{H}_2\text{O})_2] \cdot 4\text{H}_2\text{O}$ [259]. As the $\text{UO}_2(\text{NO}_3)_2$ molecule has a coordination of four, with the two bidentate nitrate groups coordinated to uranyl, we have added one or two water molecules in the uranyl equatorial plane 1) to

check the influence of the amount of water molecules on the $\text{UO}_2(\text{NO}_3)_2(\text{H}_2\text{O})_n$ ($n = 1, 2$) complexes spectra and emission energies, and 2) to quantify the relative stability of *cis-/trans*- $\text{UO}_2(\text{NO}_3)_2(\text{H}_2\text{O})_2$ conformers. Hereafter, the two water molecules were substituted by two N,N-dialkyl amides. However, in order to keep reasonable computational costs, the experimentally studied N,N-di(2-ethylhexyl)-*iso*-butanamide (DEHiBA) molecule was transformed to the N,N-diethyl-*iso*-butanamide (DEiBA) molecule with a shorter alkyl chain, as the original alkyl chain is located beyond the first coordination sphere of U(VI) and is expected not to affect the uranyl-core electronic structure [136].

Before we start the discussion on the ground and excited-state properties of the model systems, we have computed the relative free energies to get a global picture about the conformers stability. These quantities have been obtained both at the DFT/PBE0 and MP2 levels of theory in the gas phase for the $\text{UO}_2(\text{NO}_3)_2(\text{DEiBA})_2$ isomers, and in a CPCM water solvent for the $\text{UO}_2(\text{NO}_3)_2(\text{H}_2\text{O})_2$ ones. The results are shown in Table 5.1. For both the water and monoamide uranyl binitrate complexes, the *trans*-conformer is found to be the most stable conformer, but energy differences between the *trans*- and *cis*-conformations are small in the gas phase, about 14–17 kJ mol⁻¹. The *cis-trans* energetic difference is even smaller for $\text{UO}_2(\text{NO}_3)_2(\text{H}_2\text{O})_2$ in water, 3 kJ mol⁻¹. As the free energy difference between these two conformers is small, we have decided to compute the structural and spectroscopic properties of both conformers with the aim to give an estimation of the species discrimination by different experimental techniques, in particular by TRLFS.

5.3.2 Theoretical ground and excited-state structures

cis-/trans- $\text{UO}_2(\text{NO}_3)_2(\text{H}_2\text{O})_n$ ($n=1, 2$)

Uranyl nitrate is a water-soluble uranium salt. It exists in the form of the crystal uranyl binitrate hexahydrate $[\text{UO}_2(\text{NO}_3)_2] \cdot 6\text{H}_2\text{O}$. The structural studies performed on a crystal compound showed that there are two bidentate nitrates and two water molecules bounded to uranyl unit in a *trans*-configuration [260–262]. Unluckily, the speciation of uranyl nitrate compounds in aqueous phase is less documented as there are other solvated and nitrate species present [230,

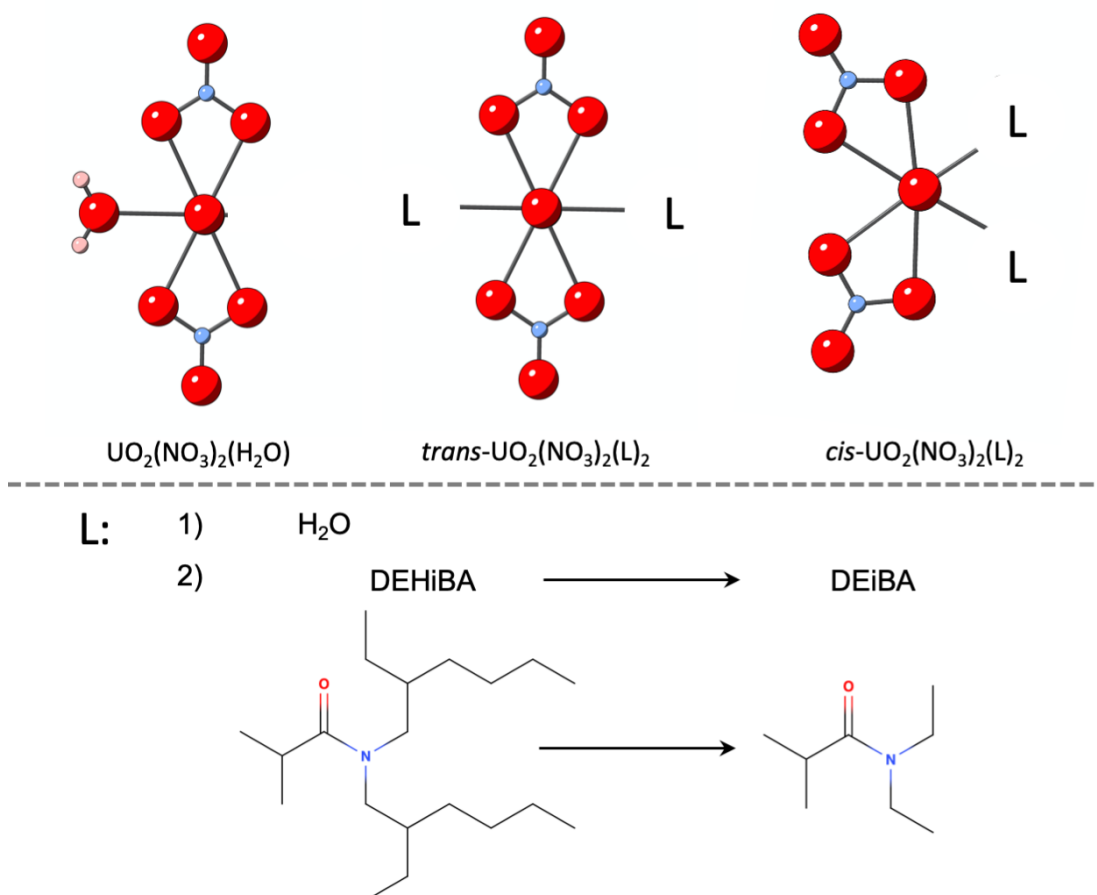


Figure 5.1: The structures of $\text{UO}_2(\text{NO}_3)_2(\text{H}_2\text{O})$ and $\text{UO}_2(\text{NO}_3)_2(\text{L})_2$ ($\text{L}=\text{H}_2\text{O}$, DEiBA) model systems in their *trans* (a) and *cis* (b) configurations.

263]. The dissolution of crystallohydrates in water may be accompanied by the destruction of the crystal lattice, as well as (de-)hydration process. Thus, we have made an assumption that either one or two water molecules may fill the $\text{UO}_2(\text{NO}_3)_2$ first coordination sphere.

All the distances for the $\text{UO}_2(\text{NO}_3)_2(\text{H}_2\text{O})$ and $\text{trans-UO}_2(\text{NO}_3)_2(\text{H}_2\text{O})_2$ complexes are reported in Table 5.2 along with experimental data available in the literature. The ground-state structures of these two complexes are found to be almost identical with a maximum deviation of 0.003 \AA for $\text{U}-\text{O}_{\text{ax}}$,

Table 5.1: DFT/PBE0 and MP2 free energies (relative to *trans* conformer) difference in kJ mol^{-1} and probability of *cis* conformer over the *trans* for GP and CPCM ground state structures of $\text{UO}_2(\text{NO}_3)_2(\text{H}_2\text{O})_2$ and GP structures of $\text{UO}_2(\text{NO}_3)_2(\text{DEiBA})_2$.

Media	Method	$\text{UO}_2(\text{NO}_3)_2(\text{H}_2\text{O})_2$		$\text{UO}_2(\text{NO}_3)_2(\text{DEiBA})_2$	
		$\Delta G [\text{kJ mol}^{-1}]$	$p_i [\%]$	$\Delta G [\text{kJ mol}^{-1}]$	$p_i [\%]$
GP	PBE0	16.6	0.1	22.9	0.0
	MP2	17.9	0.1	14.9	0.2
CPCM	PBE0	3.0	29.7		
	MP2	3.4	25.5		

$\text{U}-\text{O}_{\text{NO}_3}$ and $\text{U}-\text{N}_{\text{NO}_3}$ bond lengths. The $\text{U}-\text{O}_{\text{H}_2\text{O}}$ bond is 0.024 \AA longer in the *trans*- $\text{UO}_2(\text{NO}_3)_2(\text{H}_2\text{O})_2$ complex than in the $\text{UO}_2(\text{NO}_3)_2(\text{H}_2\text{O})$ complex, as there are more electrostatic repulsions in the former than in the latter. One interesting observation is that Taylor et al. [261] obtained non-equivalent $\text{U}-\text{O}_{\text{ax}}$ bond distances ($1.770(7)$ and $1.749(7) \text{ \AA}$), while in our calculations these distances are strictly equal (1.749 \AA). We suspect the experimental bond length difference to be related to the fit uncertainty, because most of the uranyl complexes have almost equivalent $\text{U}-\text{O}_{\text{ax}}$ bond length [144, 167]. The *trans*- $\text{UO}_2(\text{NO}_3)_2(\text{H}_2\text{O})_2$ complex structure has been studied previously by theoretical DFT/SVWN [264] and Car-Parrinello (CP/BLYP) calculations [265]. The results obtained by these two methods overestimate the bond lengths found in the crystal structures by neutron diffraction measurements [261], whereas our DFT/PBE0 ground-state structures are in better agreement with the experimental structural data. These compiled results indicate that the choices of both the functional and the basis sets have a significant impact on the accuracy of the computed U(VI)-based complexes structures, and since we are aiming at capturing the evolution between the ground state and excited state geometries, we can postulate that any functional should be benchmarked to be able to provide a reasonable picture. Comparing the computed geometries of *cis*- and *trans*- $\text{UO}_2(\text{NO}_3)_2(\text{H}_2\text{O})_2$ conformers, we did not observe any change in the structures except for the $\text{U}-\text{O}_{\text{H}_2\text{O}}$ bond which was found to be 0.014 \AA longer in the *cis* conformer than in the *trans*. This is probably related to the greater energetic stability of the *trans* complex as shown

in Table 5.1.

The geometrical parameters of the lowest triplet excited states are reported in Table 5.2. A detailed description of the luminescent state nature will be made in Section 5.3.3. As a result of the electronic excitation, we observe an elongation of the U–O_{ax} bond length by 0.038 Å for the uranyl binitrate complex with one water molecule and 0.037 Å for both *cis*- and *trans*-UO₂(NO₃)₂(H₂O)₂ conformers. For the equatorial ligands, the structural changes are found to be very minor; the greatest bond-length change is 0.006 Å, suggesting that there are no significant contributions of water ligands to the orbitals participating to the excitation.

Insofar as vibrational frequencies contribute to the luminescence spectra to some extent, it is of high importance to characterize them. There are three main vibrational modes that may appear in the vibronic progressions: uranyl bending ν_b , symmetrical stretching ν_s and asymmetrical stretching ν_a modes. The values of these frequencies are reported in Table 5.3 together with the experimental IR and Raman data obtained for solid [266] and liquid [173] uranyl binitrate. The experimental ν_s and ν_a are found to be almost identical for UO₂(NO₃)₂ in solid and in solution, the largest difference being 16 cm⁻¹ for the uranyl asymmetrical stretching mode. The analysis of the theoretical harmonic frequencies of UO₂(NO₃)₂(H₂O) and *cis*-/*trans*-UO₂(NO₃)₂(H₂O)₂ complexes shows that they are nearly the same, but they are found to be overestimated by at most 62 cm⁻¹ for the uranyl symmetrical stretching mode as compared to experimental data. In the series of the chemical models, the largest changes of the theoretical frequency values are found to be 9 cm⁻¹ and 11 cm⁻¹ for ν_s and ν_a modes, respectively, values that are in line with the magnitudes of the structural changes. Moreover, our calculations showed that the ν_b mode is coupled with the motions of ligands, an information that cannot be deduced from the IR spectra of UO₂(NO₃)₂ in solution [173]. It is thus inappropriate to describe this vibrational frequency as a pure uranyl bending mode. Experimentally, it was measured at 254 cm⁻¹, matching the range of our computed values 217–276 cm⁻¹.

As a result of the U–O_{ax} bond elongation from the ground to the luminescence state, the ν_s and ν_a vibrational frequencies are lowered by 101 cm⁻¹ and 133 cm⁻¹, respectively in the *trans*-UO₂(NO₃)₂(H₂O) complexe. A similar be-

Table 5.2: Ground and excited state geometries (in Å) of $\text{UO}_2(\text{NO}_3)_2(\text{H}_2\text{O})$ and *cis-/trans-* $\text{UO}_2(\text{NO}_3)_2(\text{L})_2$ (L= H_2O , DEiBA) compared to selected results from the literature.

	U-O _{ax}	U-O _{NO3}	U-N _{NO3}	U-O _L	Method	Ref.
					Ground State	
$\text{UO}_2(\text{NO}_3)_2(\text{H}_2\text{O})$	1.746	2.473	2.917	2.474	PBE0/CPCM	this study
<i>trans-</i> $\text{UO}_2(\text{NO}_3)_2(\text{H}_2\text{O})_2$	1.749	2.470	2.914	2.498	PBE0/CPCM	this study
<i>cis-</i> $\text{UO}_2(\text{NO}_3)_2(\text{H}_2\text{O})_2$	1.749	2.469	2.914	2.512	PBE0/CPCM	this study
<i>trans-</i> $\text{UO}_2(\text{NO}_3)_2(\text{DEiBA})_2$	1.756	2.496	2.945	2.390	PBE0/GP	this study
<i>cis-</i> $\text{UO}_2(\text{NO}_3)_2(\text{DEiBA})_2$	1.755	2.480	2.929	2.441	PBE0/GP	this study
<i>trans-</i> $\text{UO}_2(\text{NO}_3)_2(\text{H}_2\text{O})_2$	1.749(7)	2.504(5)		2.397(3)	neutrons	[261]
	1.770(7)	2.547(7)			diffraction	
	1.820	2.530		2.550	CP/ZORA(aq)	[265]
	1.800	2.490		2.590	CP/BLYP/ECP60	[265]
$\text{UO}_2(\text{NO}_3)_2(\text{DEHiBA})_2$	1.77(1)	2.53(1)	2.97(3)	2.38(2)	EXAFS	[256]
<i>cis-</i> $\text{UO}_2(\text{NO}_3)_2(\text{dam})_2$	1.760(3)	2.533(3)	-	2.362(3)	X-ray	[243]
<i>trans-</i> $\text{UO}_2(\text{NO}_3)_2(\text{eam})_2$	1.747(3)	2.526(4)	-	2.363(3)	X-Ray	[243]
					Excited state	
$\text{UO}_2(\text{NO}_3)_2(\text{H}_2\text{O})$	1.784	2.479	2.921	2.479	PBE0/CPCM	this study
<i>trans-</i> $\text{UO}_2(\text{NO}_3)_2(\text{H}_2\text{O})_2$	1.786	2.476	2.918	2.500	PBE0/CPCM	this study
<i>cis-</i> $\text{UO}_2(\text{NO}_3)_2(\text{H}_2\text{O})_2$	1.786	2.473	2.918	2.515	PBE0/CPCM	this study
<i>trans-</i> $\text{UO}_2(\text{NO}_3)_2(\text{DEiBA})_2$	1.792	2.515	2.963	2.375	PBE0/GP	this study
<i>cis-</i> $\text{UO}_2(\text{NO}_3)_2(\text{DEiBA})_2$	1.791	2.495	2.943	2.428	PBE0/GP	this study

Table 5.3: Ground and excited state vibrational frequencies (in cm^{-1}) of the $\text{UO}_2(\text{NO}_3)_2(\text{H}_2\text{O})$ and *cis-/trans*- $\text{UO}_2(\text{NO}_3)_2(\text{L})_2$ ($\text{L}=\text{H}_2\text{O}$, DEiBA) compared to selected results from the literature.

	ν_b	ν_s	ν_a	Method	Ref.
Ground state					
$\text{UO}_2(\text{NO}_3)_2(\text{H}_2\text{O})$	217-276	934	989	PBE0/CPCM	this study
<i>trans</i> - $\text{UO}_2(\text{NO}_3)_2(\text{H}_2\text{O})_2$	230-264	925	978	PBE0/CPCM	this study
<i>cis</i> - $\text{UO}_2(\text{NO}_3)_2(\text{H}_2\text{O})_2$	217-265	928	980	PBE0/CPCM	this study
<i>trans</i> - $\text{UO}_2(\text{NO}_3)_2(\text{DEiBA})_2$	280	911	987	PBE0/GP	this study
<i>cis</i> - $\text{UO}_2(\text{NO}_3)_2(\text{DEiBA})_2$	278	913	989	PBE0/GP	this study
$\text{UO}_2(\text{NO}_3)_2$	254	872	961	IR/Raman	[173]
$\text{UO}_2(\text{NO}_3)_2(\text{H}_2\text{O})_2$		875	945	IR/Raman	[266]
$\text{UO}_2(\text{NO}_3)_2(\text{DEiBA})_2$			935	IR	[245]
<i>cis</i> - $\text{UO}_2(\text{NO}_3)_2(\text{dam})_2$			923	IR	[243]
<i>trans</i> - $\text{UO}_2(\text{NO}_3)_2(\text{eam})_2$			932	IR	[243]
Excited state					
$\text{UO}_2(\text{NO}_3)_2(\text{H}_2\text{O})$	210-267	833	856	PBE0/CPCM	this study
<i>trans</i> - $\text{UO}_2(\text{NO}_3)_2(\text{H}_2\text{O})_2$	220-257	833	857	PBE0/CPCM	this study
<i>cis</i> - $\text{UO}_2(\text{NO}_3)_2(\text{H}_2\text{O})_2$	223-261	834	857	PBE0/CPCM	this study
<i>trans</i> - $\text{UO}_2(\text{NO}_3)_2(\text{DEiBA})_2$	275	822	850	PBE0/GP	this study
<i>cis</i> - $\text{UO}_2(\text{NO}_3)_2(\text{DEiBA})_2$	270	823	850	PBE0/GP	this study

havior, within 12 cm^{-1} difference, is observed for *cis-/trans*- $\text{UO}_2(\text{NO}_3)_2(\text{H}_2\text{O})_2$ complexes. One can, however, note that the coupled ν_b frequency range is not significantly affected by the excitation process.

cis-/trans- $\text{UO}_2(\text{NO}_3)_2(\text{DEiBA})_2$

To probe the electronic structure of U(VI) surrounded by inorganic and organic ligands, two molecules of the DEiBA monoamide were placed in the first coordination sphere instead of the water molecules forming $\text{UO}_2(\text{NO}_3)_2(\text{DEiBA})_2$ *cis*- and *trans*-conformers (Fig. 5.2). The optimized bond distances are shown in Table 5.2. The substitution of the water by the DEiBA monoamide induces a lengthening of the $\text{U}-\text{O}_{\text{ax}}$, $\text{U}-\text{O}_{\text{NO}_3}$ and $\text{U}-\text{N}_{\text{NO}_3}$ bonds in the range of 0.007 – 0.031 \AA for *trans*- and 0.006 – 0.015 \AA for *cis*-conformer, while the distance between uranium and the oxygen atom of the monoamide is shorter than that with

the oxygens of the water molecules, by 0.108 Å and 0.071 Å for the *trans* and *cis* configurations, respectively. This is simply a result of the larger electron donation to uranium of the DEiBA monoamide as compared to water [256].

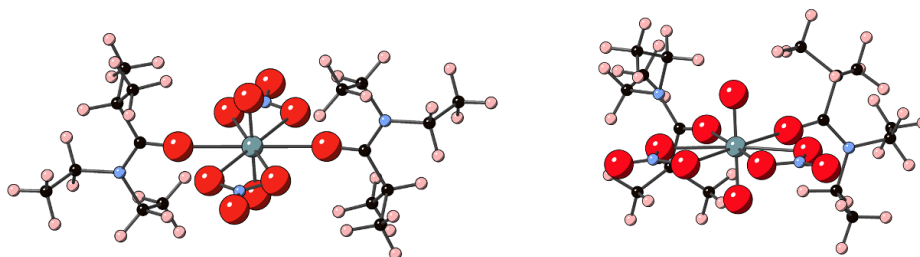


Figure 5.2: The optimized at R-ECP DFT/PBE0 ground state geometries of the *cis*- and *trans*- $\text{UO}_2(\text{NO}_3)_2(\text{DEiBA})_2$ conformers.

The ground-state geometries of the *cis*- and *trans*- $\text{UO}_2(\text{NO}_3)_2(\text{DEiBA})_2$ complexes have very similar distances in the equatorial plane, and the free energy difference of two conformers is small. Nevertheless, the *trans* conformer of this complex is found to be more stable as compared to *cis*, its energies being lower than the *cis* by about 23 kJ mol^{-1} and 15 kJ mol^{-1} at the DFT/PBE0 and MP2 level of theory, respectively (see Table 5.1). The computed geometry of *trans*- $\text{UO}_2(\text{NO}_3)_2(\text{DEiBA})_2$ complex agreed well with experimental EXAFS results obtained by Acher et al. [256]. In the same way, computed bond lengths within $\text{UO}_2(\text{NO}_3)_2(\text{DEiBA})_2$ conformers also agree with the single-crystal X-ray structures of similar amide compounds like *cis*- $\text{UO}_2(\text{NO}_3)_2(\text{dam})_2$ (dam - N',N'-diethylacetamide) and *trans*- $\text{UO}_2(\text{NO}_3)_2(\text{eam})_2$ (eam - N-ethylacetamide) [243].

The changes in the geometries when switching from the ground to the luminescent state in *cis*-/ *trans*- $\text{UO}_2(\text{NO}_3)_2(\text{DEiBA})_2$ complexes is of the same order as that reported for the *cis*- / *trans*- $\text{UO}_2(\text{NO}_3)_2(\text{H}_2\text{O})_2$ complexes. The minor differences are the variation of $\text{U}-\text{O}_{\text{NO}_3}$ and $\text{U}-\text{N}_{\text{NO}_3}$ bonds of monoamide complexes upon excitation which is a little larger than in complexes with water molecules, and the $\text{U}-\text{O}_{\text{L}}$ bonds are shortened by about 0.014 Å, while in case of the complexes with water, they remained almost unchanged. These structural changes will be reflected in the theoretical luminescence intensities distribution

as discussed further in the Section 5.4.

The theoretical vibrational frequencies of *cis*- and *trans*- $\text{UO}_2(\text{NO}_3)_2(\text{DEiBA})_2$ complexes are listed in the Table 5.3. As in the uranyl binitrate complex with water molecules, there is almost no difference for the ν_b , ν_s and ν_a frequencies values between the *cis* and *trans* conformers. Moreover, the ν_b frequency corresponds to a pure uranyl bending motion, uncoupled from the equatorial ligands, ν_s is smaller and ν_a remains almost unchanged. The changes are probably related to the weakening of the $\text{U}-\text{O}_{\text{ax}}$ bond and the decrease in stretching force constant. The calculated ν_a frequency can be compared with experimental data measured by IR spectroscopy for various crystals and liquid samples of *cis*-/ *trans*- $\text{UO}_2(\text{NO}_3)_2(\text{L})_2$ complexes [243, 256]. As observed for the $\text{UO}_2(\text{NO}_3)_2(\text{H}_2\text{O})_2$ complexes, our theoretical vibrational frequencies for the $\text{UO}_2(\text{NO}_3)_2(\text{DEiBA})_2$ complexes are overall larger than the experimental values by 65 cm^{-1} . Thus this systematic difference might be related to choice of the computational methodology (DFT functional, basis sets, and/or solvation model).

The changes between the ground and the luminescent states vibrational frequencies in the *cis*-/*trans*- $\text{UO}_2(\text{NO}_3)_2(\text{DEiBA})_2$ complexes are equal in average to 90 cm^{-1} and 138 cm^{-1} for the symmetrical and asymmetrical uranyl stretching modes, respectively, while the ν_b frequency is similar to that in the ground state.

5.3.3 Theoretical emission energies

For the uranyl-based complexes, the nature of the luminescent emission was previously discussed by several experimental [7, 16, 165] and theoretical [9, 10, 24] studies. It was deduced from the examples of uranyl tetrachloride $\text{UO}_2\text{Cl}_4^{2-}$ in the Chapter 3 [136] and uranyl triscarbonate $\text{UO}_2(\text{CO}_3)_3^{4-}$ (Chapter 4) [177] complexes that the luminescence state has a triplet character and that the emission occurs as a result of an electron transition from one of the four non-bonding $5f$ orbitals of uranium(VI) to an orbital that has a uranyl σ character possibly mixed with orbitals of the equatorial ligands. In the present $\text{UO}_2(\text{NO}_3)_3(\text{L})_2$ complexes, the plots of the molecular orbitals involved in the luminescent process

shown in Figure 5.3 reveal that the emission corresponds to a metal-to-ligand charge transfer de-excitation from non-bonding uranium(VI) orbitals to orbitals delocalized over the uranyl unit, the nitrate ligands and the monoamide linking groups.

Since the luminescence spectra of uranyl-based complexes have similar shapes (with some exceptions like $\text{UO}_2\text{Cl}_4^{2-}$), the nature of the equatorial ligands can be deduced from the position of the spectral envelope on the energy scale. In the luminescence spectra, the origin is usually defined by the position of the “hot band.” For instance, luminescence blue shifts of the uranyl triscarbonate complexes are observed as compared to most other uranyl species, while hydrated uranyl exhibits a red shift on the energy scale [17, 20, 21]. It has been proposed by Wang et al. [17] that position of the “hot band” depends on the basicity of the equatorial ligand. The ionic interactions between uranyl ion and ligands with stronger interacting ability lead to a larger decrease of the ν_s frequency, causing a larger red shift of the luminescence spectra.

To discuss Wang et al.’s hypothesis [17], we have used the SOC CAM-B3LYP calculations to predict the “hot band” positions by the averaging of first four vertical emission energies computed out of the first low-lying excited state geometry and corrected by the zero-point energies of the ground and luminescent states of the $\text{UO}_2(\text{NO}_3)_2(\text{H}_2\text{O})$ and *cis-/trans*- $\text{UO}_2(\text{NO}_3)_2(\text{L})_2$ ($\text{L}=\text{H}_2\text{O}$, DEiBA). The computed “hot band” energies E are listed in Table 5.4. The comparison of theoretical data with experimental results is not relevant at this stage, because the position of the “hot band” was never discussed before for the uranyl binitrate complexes.

The theoretical “hot band” energies of the $\text{UO}_2(\text{NO}_3)_2(\text{H}_2\text{O})$ and *cis-/trans*- $\text{UO}_2(\text{NO}_3)_2(\text{H}_2\text{O})_2$ complexes in water come out close, 413 cm^{-1} (10 nm), from each other. These differences are within the expected accuracy of our quantum chemical methodology. Notwithstanding, we restrict ourselves to making a comparison with the results obtained for compounds with different basicity of equatorial ligands. Within the uranyl binitrate water complexes with one or two coordinated water molecules, since the equatorial plane does not differ by the nature of the ligands (it means that basicity remains unchanged), we can take an average “hot band” value of $\text{UO}_2(\text{NO}_3)_2(\text{H}_2\text{O})$, *cis-/trans*- $\text{UO}_2(\text{NO}_3)_2(\text{H}_2\text{O})_2$ and com-

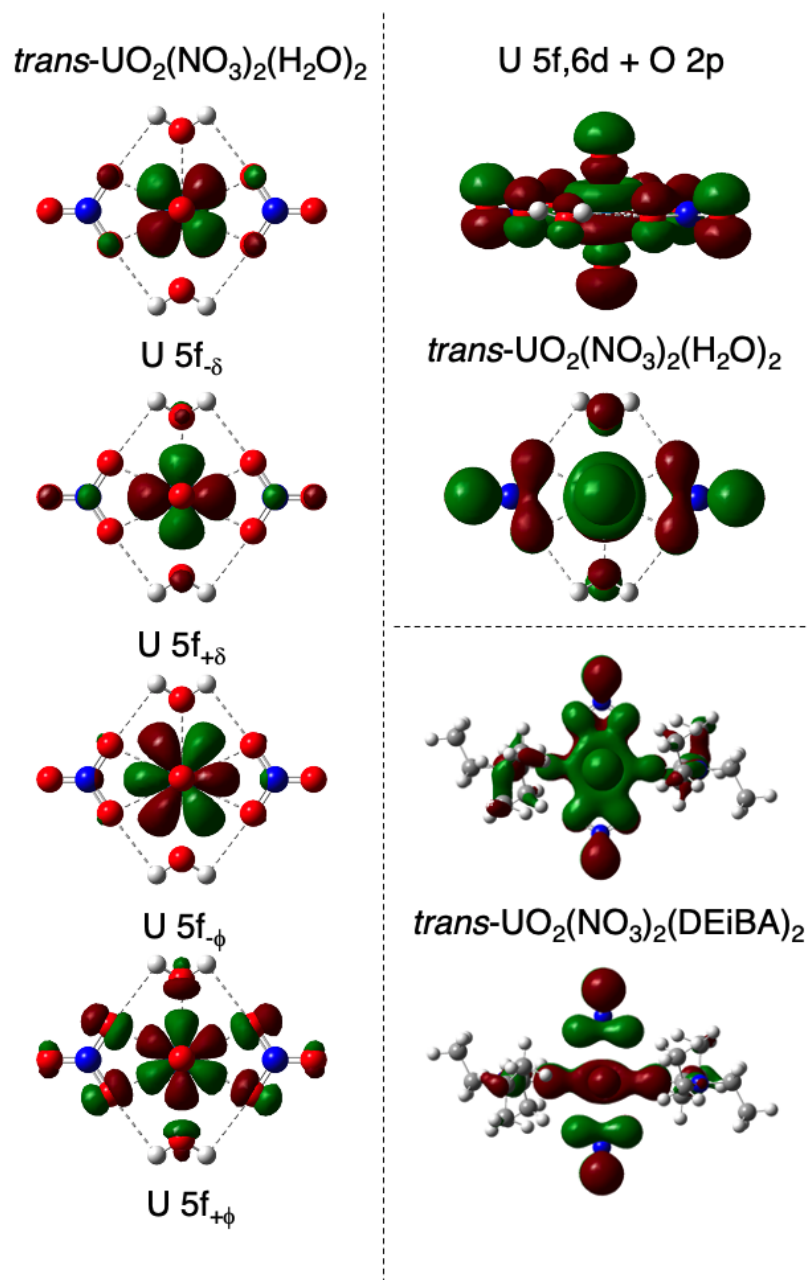


Figure 5.3: The highest occupied (right panel) and lowest unoccupied (left panel) molecular orbitals of *trans*-UO₂(NO₃)₂(L)₂ (L = H₂O, DEiBA) involved in the triplet-singlet electronic transitions, responsible of uranyl luminescence. The molecular orbitals were obtained at the RECP DFT/PBE0 level of theory.

Table 5.4: The “hot band” energies E of uranyl binitrate complexes (in cm^{-1} and nm) compared to $\text{Na}_3\text{UO}_2(\text{CO}_3)_3^-$ and $[\text{A336}]_2[\text{UO}_2\text{Cl}_4]$ results. The computed values are obtained at the all-electron SOC CAM-B3LYP level of theory, and corrected with the spin-free Zero-Point Energy correction of the ground and luminescent states.

	$E [\text{cm}^{-1}]$	$E [\text{nm}]$
Water COSMO		
$\text{UO}_2(\text{NO}_3)_2(\text{H}_2\text{O})$	20204	495
<i>trans</i> - $\text{UO}_2(\text{NO}_3)_2(\text{H}_2\text{O})_2$	20456	489
<i>cis</i> - $\text{UO}_2(\text{NO}_3)_2(\text{H}_2\text{O})_2$	20616	485
$\text{Na}_3\text{UO}_2(\text{CO}_3)_3^-$	20978	477
<i>n</i> -dodecane COSMO		
<i>trans</i> - $\text{UO}_2(\text{NO}_3)_2(\text{DEiBA})_2$	20116	497
<i>cis</i> - $\text{UO}_2(\text{NO}_3)_2(\text{DEiBA})_2$	20171	496
$[\text{A336}]_2[\text{UO}_2\text{Cl}_4]$	20001	500

pare it to the $\text{Na}_3\text{UO}_2(\text{CO}_3)_3^-$ complex value. It is known from Parr et al. [267] studies that nitrates and water molecules are less basic than the carbonate anions. From our calculations, the “hot band” of $\text{Na}_3\text{UO}_2(\text{CO}_3)_3^-$ is placed at $20\,978\text{ cm}^{-1}$ (477 nm), while the averaged value of the uranyl binitrate “hot band” is $20\,425\text{ cm}^{-1}$ (490 nm), showing 553 cm^{-1} (13 nm) red shift which is in consistency with Wang’s assumption.

For the *cis*- and *trans*- $\text{UO}_2(\text{NO}_3)_2(\text{DEiBA})_2$ (for which the basicity is not known) in *n*-dodecane, we have computed the “hot band” energies at $20\,116\text{ cm}^{-1}$ (497 nm) and $20\,171\text{ cm}^{-1}$ (496 nm), respectively. They are somewhat red shifted with respect to that of the water complexes of uranyl binitrate. As compared to the “hot band” value of the $[\text{A336}]_2[\text{UO}_2\text{Cl}_4]$ complex, $20\,001\text{ cm}^{-1}$ (500 nm), the uranyl binitrates with monoamides “hot band” energy exhibit a blue shift, probably because of the chloride ligands’ higher interaction ability.

One can conclude that the discrimination of the *cis*- and *trans*-conformers of uranyl binitrate complexes solely by the “hot band” energy is very unlikely, thus only uranyl complexes differing by the ligand’s nature can be distinguished experimentally.

5.3.4 Vibronic progressions

In the luminescent emission of U(VI) complexes, the principal vibronic progression is a result of an electronic transition coupled to the symmetrical stretching mode of the uranyl unit. Secondary progressions may also appear in the spectrum because of the coupling to other symmetrical motions of the molecular complex. The quantum chemical simulations of the vibronic spectra allow to quantify the contributions of the vibronic modes. To guide the discussion and the comparison to experimental data, the computed stick spectra of all binitrate uranyl complexes are convoluted and drawn on Figure 5.4.

The structural and vibrational parameters directly reflect in the shape of the luminescence spectra. The most evident and easily detectable fingerprint is the ground state symmetrical stretching mode of the uranyl moiety, as it is equal to the spacing between the main peaks of the vibronically resolved envelope. Some other vibrational frequencies (symmetrical mostly) appear in the vibronic progression to a smaller extent and might be hardly detectable in the broad spectral envelope. The vibrational frequencies contributions, their natures and intensities are listed in Table 5.5 for the $\text{UO}_2(\text{NO}_3)_2(\text{H}_2\text{O})$ and *cis-/ trans*- $\text{UO}_2(\text{NO}_3)_2(\text{L})_2$ ($\text{L} = \text{H}_2\text{O}$, DEiBA) complexes. One can note that the excited state uranyl symmetrical stretching mode can be detected in these luminescence spectra as discussed later in Section 5.4.

The ground-state symmetrical stretching uranyl frequency has been discussed previously. From the comparison of the spectra displayed in Figure 5.4 and the symmetric stretching frequencies listed in Table 5.5, we can infer that the vibronic band spacings are very similar, thus the spectra of aqueous and organic uranyl binitrate complexes are difficult to separate solely by the main vibronic band spacings. The detailed analysis of the vibronic bands (See Table 5.5) reveals that some other modes build up a secondary vibronic progression. In the case of the $\text{UO}_2(\text{NO}_3)_2(\text{H}_2\text{O})$ complex, the uranyl rocking appears at 156 cm^{-1} after the $0 \rightarrow 0$ band. In the *cis*- and *trans*- $\text{UO}_2(\text{NO}_3)_2(\text{H}_2\text{O})_2$ spectra, we observe contributions from the U–H₂O stretching mode coupled with uranyl bending motions at 249 cm^{-1} and 315 cm^{-1} for the *cis*- and *trans*-conformers, respectively. A symmetrical U–NO₃ stretching mode coupled with the weak uranyl bend-

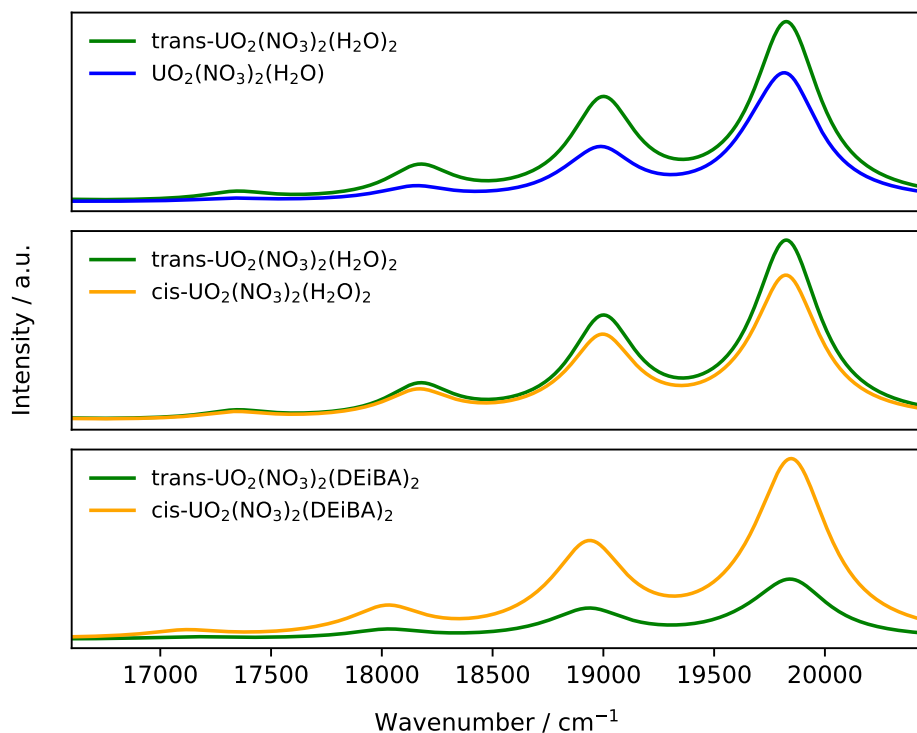


Figure 5.4: Theoretical vibronic progressions of the $\text{UO}_2(\text{NO}_3)_2(\text{H}_2\text{O})$ and *cis-/trans*- $\text{UO}_2(\text{NO}_3)_2(\text{L})_2$ ($\text{L} = \text{H}_2\text{O}, \text{DEiBA}$) complexes. The position of the first peak is adjusted to the “hot band” value of the *trans*-complexes and corrected by the ν_s of the excited state. The spectral shapes were estimated by convoluting the stick spectra with Lorentzian functions with a FWHM of 400 cm^{-1} .

ing motion contributes to the spectra of the *cis*- and *trans*- $\text{UO}_2(\text{NO}_3)_2(\text{DEiBA})_2$ complexes at 234 cm^{-1} and 212 cm^{-1} , respectively.

The theoretical luminescence intensities distributions are mainly linked to the $\text{U}-\text{O}_{\text{ax}}$ bond elongations between the ground to the luminescent state [140], but this relation is not defined yet. We have performed a comparison of the vibronic progressions to elucidate the influence of the nature of the ligands and of their orientations on theoretical intensities. On the top panel of Figure 5.4 we observe that the absolute intensity of the *trans*- $\text{UO}_2(\text{NO}_3)_2(\text{H}_2\text{O})_2$ complex is higher than that of $\text{UO}_2(\text{NO}_3)_2(\text{H}_2\text{O})$ by 0.184 au for the $0 \rightarrow 0$ band. The middle panel of Figure 5.4 reveals that the *trans*-conformer of uranyl

Table 5.5: Assignments of the $\text{UO}_2(\text{NO}_3)_2(\text{H}_2\text{O})$ and *cis-/trans*- $\text{UO}_2(\text{NO}_3)_2(\text{L})_2$ ($\text{L} = \text{H}_2\text{O}, \text{DEiBA}$) theoretical luminescence spectra computed in the gas phase and in the CPCM water solvent for complexes with organic and inorganic ligands respectively. The energy of the spectrum was adjusted to the theoretical “hot band” value and corrected by ν_s of the excited state.

E, cm^{-1}	$\Delta E, \text{cm}^{-1}$	I, a.u.	E, cm^{-1}	$\Delta E, \text{cm}^{-1}$	I, a.u.	Identification
$\text{UO}_2(\text{NO}_3)_2(\text{H}_2\text{O})$						
19831		0.347				$0(0) \rightarrow 1(0)$
19675	156	0.061				$0(0) \rightarrow 1(1\nu_1)$
18897	934	0.138				$0(0) \rightarrow 1(1\nu_s)$
18741	156	0.018				$0(0) \rightarrow 1(1\nu_1, 1\nu_s)$
17963	934	0.037				$0(0) \rightarrow 1(2\nu_s)$
17807	156	0.004				$0(0) \rightarrow 1(1\nu_1, 2\nu_s)$
17028	935	0.008				$0(0) \rightarrow 1(3\nu_s)$
16094	934	0.001				$0(0) \rightarrow 1(4\nu_s)$
<i>trans</i> - $\text{UO}_2(\text{NO}_3)_2(\text{H}_2\text{O})_2$			<i>cis</i> - $\text{UO}_2(\text{NO}_3)_2(\text{H}_2\text{O})_2$			
20104		0.531	20344		0.424	$0(0) \rightarrow 1(0)$
19789	315	0.005	20095	249	0.014	$0(0) \rightarrow 1(1\nu_2)$
19179	925	0.291	19417	927	0.236	$0(0) \rightarrow 1(1\nu_s)$
18864	315	0.003	19167	249	0.008	$0(0) \rightarrow 1(1\nu_2, 1\nu_s)$
18255	924	0.096	18489	927	0.080	$0(0) \rightarrow 1(2\nu_s)$
17645	315	0.000	18240	249	0.003	$0(0) \rightarrow 1(1\nu_2, 2\nu_s)$
17330	925	0.024	17562	927	0.021	$0(0) \rightarrow 1(3\nu_s)$
16405	925	0.005	16634	927	0.005	$0(0) \rightarrow 1(4\nu_s)$
<i>trans</i> - $\text{UO}_2(\text{NO}_3)_2(\text{DEiBA})_2$			<i>cis</i> - $\text{UO}_2(\text{NO}_3)_2(\text{DEiBA})_2$			
19674		0.097	19850		0.313	$0(0) \rightarrow 1(0)$
19462	212	0.007	19616	234	0.011	$0(0) \rightarrow 1(1\nu_3)$
18763	911	0.047	18937	913	0.158	$0(0) \rightarrow 1(1\nu_s)$
18551	212	0.003	18703	234	0.007	$0(0) \rightarrow 1(1\nu_3, 1\nu_s)$
17852	911	0.014	18024	913	0.049	$0(0) \rightarrow 1(2\nu_s)$
17640	212	0.000	17790	234	0.002	$0(0) \rightarrow 1(1\nu_3, 2\nu_s)$
16942	911	0.003	17111	913	0.012	$0(0) \rightarrow 1(3\nu_s)$
ν_1 is uranyl rocking, ν_2 is U-H ₂ O stretching + weak ν_b , ν_3 is U-NO ₃ stretching + weak ν_b						

binitrate with two water molecules exhibits higher intensities than the *cis* conformer by 0.107 au. In the bottom panel of Figure 5.4, the spectra of *cis*- and *trans*- $\text{UO}_2(\text{NO}_3)_2(\text{DEiBA})_2$ have been compared and, unlike in the uranyl bini-

trate water complexes, the spectrum of the *cis* conformer is more intense by 0.216 au than the *trans*-one. From the analysis of the geometries and their shift from the ground to the luminescent state, we did not find any significant difference, especially in the U–O_{ax} bond. It means that intensities change is not related here to the geometrical changes discussed earlier, but rather to some other factors. As the vibronic intensities arise from the Franck-Condon overlaps between the ground and excited-state normal modes, if they are not parallel, Duschinsky rotations need to be accounted for.

5.4 Discussions

As for most of the U(VI) compounds, the luminescence spectra of the uranyl nitrate complexes show well-resolved vibronic progressions that overlap with the pure electronic transition originates from the luminescent state to the ground state. In this chapter, we have not performed new TRLFs experimental measurements as there were data available in the literature, for UO₂(NO₃)₂ in nitric acid (plain line) [230], UO₂(NO₃)₂(DEHiBA)₂ in TPH solvent (dotted line) [232] and UO₂(NO₃)₂(TBP)₂ in supercritical CO₂ (dashed line, shown for comparison) [268]. The normalized experimental time-resolved luminescence spectra are shown in Figure 5.5.

The different complexes of uranium(VI) in nitric acid solution induce several luminescence components with similar monoexponential luminescent decay. The individual components are thus difficult to separate by using the time resolution of the detection. It has been assumed that in uranium(VI) sample with 0.2–4.0 M nitric acid concentration, three species are present: UO₂²⁺(aq), UO₂(NO₃)⁺(aq) and UO₂(NO₃)₂(aq). First, the UO₂²⁺(aq) species was measured in a highly acidic conditions. Then, using the assumption of a bathochromic shift upon nitrate complexation, stepwise least square fittings were applied iteratively to a set of experimental and numerical data gathered over the nitric acid concentration range. Accordingly, the spectrum of UO₂(NO₃) in nitric acid was extracted by the deconvolution procedure detailed in the paper by Couston et al. [263]. The spectral shape and characteristics compare well with the ones measured earlier in similar conditions [269] and in the solid state [30]. A

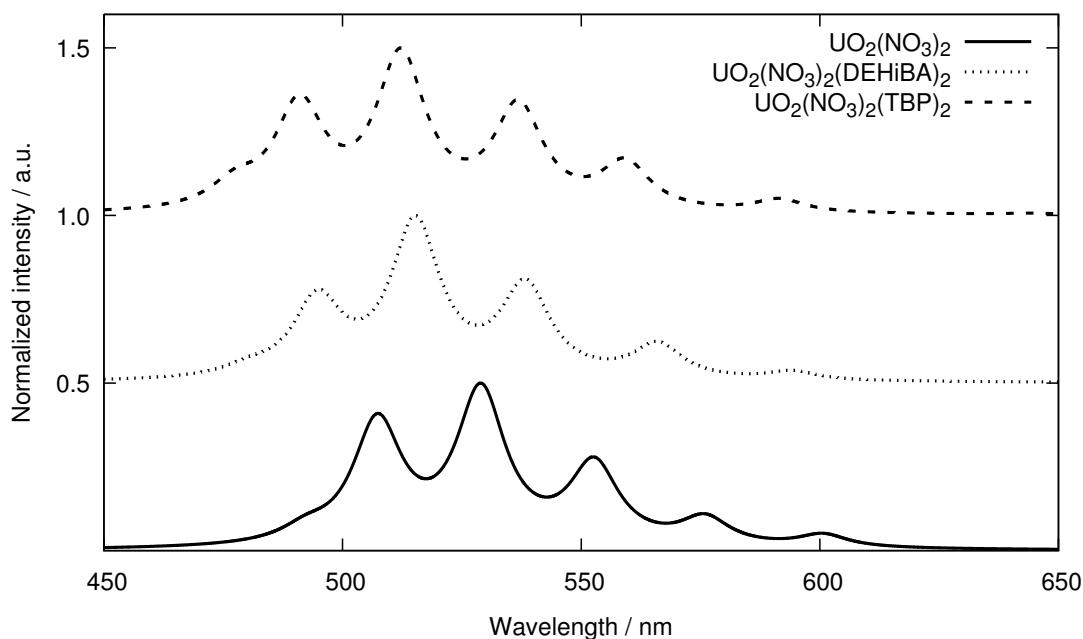


Figure 5.5: Experimental time-resolved luminescence spectra of $\text{UO}_2(\text{NO}_3)_2$ in nitric acid [230] (plain lines), $\text{UO}_2(\text{NO}_3)_2(\text{DEHiBA})_2$ in TPH solvent, $\epsilon=2.0$ [232] (dotted line) and $\text{UO}_2(\text{NO}_3)_2(\text{TBP})_2$ in a supercritical (CO_2), $\epsilon=1.6$ [268] (dashed line). The spectra were rebuilt from the data of the quoted references.

measurement sample of $\text{UO}_2(\text{NO}_3)_2(\text{DEHiBA})_2$ in TPH was prepared by liquid-liquid extraction [232]. The $\text{UO}_2(\text{NO}_3)_2(\text{TBP})_2$ complex was prepared by mixing $\text{UO}_2(\text{NO}_3)_2 \cdot 6\text{H}_2\text{O}$ with an excess of TBP solvent in supercritical CO_2 [268, 270]. The total concentration of uranium(VI) in all the samples was not exceeding 1 m.

To the best of our knowledge, there is no information in the literature about the nature of observed transitions in the uranyl binitrate complexes. The general observation that the vibronic progression overlaps with the electronic transition can be interpreted in different ways. In the example of the emission spectrum of the $\text{UO}_2(\text{NO}_3)_2(\text{DEHiBA})_2$ complex (Fig. 5.5 and Fig. 5.6) we observed two peaks in the low energy region at 480–495 nm with different intensities. It is known that the intensity of luminescence depends on the quantum yield - the ratio of the rate of de-excitation by photons emission and the rate of de-excitation by both radiative and non-radiative processes [140]. For this particular case, it is difficult not only to determine the origin of the relaxation but also to

predict the temporal evolution of the electronic intensity; thus both transitions could correspond to the electronic one. From another viewpoint, in most of the uranium(VI)-based complexes the absorption spectrum is a mirror image of the emission spectrum [23]. This phenomenon is known as the mirror image rule and is related to the Franck–Condon principle which states that electronic transitions are vertical, that is the energy changes without any geometry change. This means that the vibration levels of the excited state resemble the vibration levels of the ground state. Usually, when the absorption and emission spectra are built on the same energy scale, they overlap at the electronic transition region as shown on Figure 5.6. Here we notice the overlay of the same two peaks around 480 and 495 nm. Using the analogy adverted by Görller-Warland et al. [23] on the example of uranyl chloride complexes, the first small peak at 480 nm could be assigned to a “hot band,” while the second at 495 nm should correspond to the $0 \rightarrow 0$ band (dashed line on Figure 5.6).

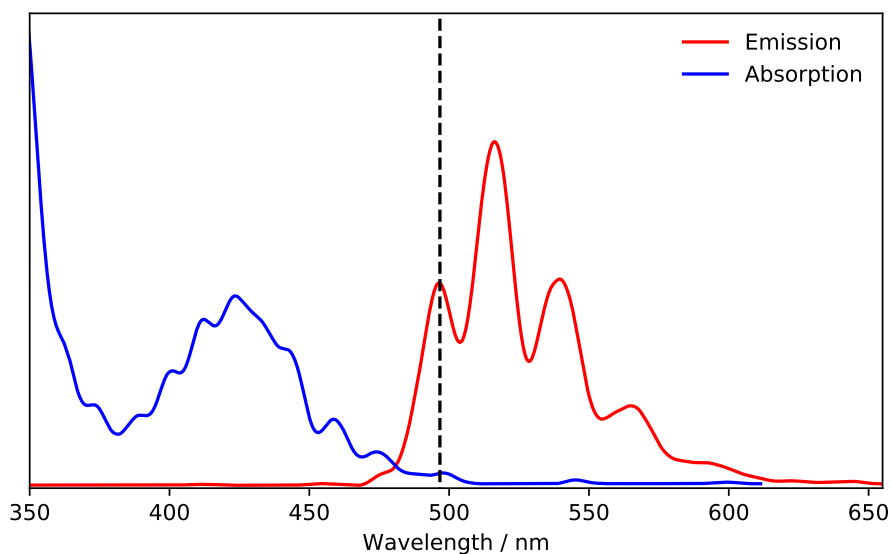


Figure 5.6: Superposition of the emission (TRLFS) and absorption (UV-vis) spectra of $\text{UO}_2(\text{NO}_3)_2(\text{DEHiBA})_2$ in TPH solvent of the same sample [232]. The spectra were rebuilt from corresponding literature sources.

Another way to attribute the position of the “hot band” in $\text{UO}_2(\text{NO}_3)_2(\text{L})_2$

is to use the band spacing value and results obtained by the *ab initio* calculations. In the luminescence spectrum, the vibronic progression starts at the $0 \rightarrow 0$ transition with a spacing equal to the ground state uranyl stretching frequency ν_s^{gs} . The “hot band” appears at an energy shifted by the excited state uranyl stretching frequency ν_s^{es} above the $0 \rightarrow 0$ transition. A multi-peaks Lorentzian fitting was applied to the experimental spectra to determine the band spacing values. The results of this fitting and the ν_s^{gs} , ν_s^{es} frequencies computed by (TD)-DFT/PBE0 methods are shown in Table 5.6. Insofar as the experimental data for $\text{UO}_2(\text{NO}_3)_2(\text{L})_2$ were extracted from the plots, they likely deviate from the raw acquisition data which are crucial to reveal the low-intensity peaks. Furthermore, the fitting process increases the degree of uncertainty. Notwithstanding, we restrict ourselves to compare the results of this fitting procedure with our theoretical data.

It has been observed that for $\text{UO}_2(\text{NO}_3)_2(\text{L})_2$ complexes, the experimental ground and excited-state symmetrical stretching frequencies of the uranyl reproduced the theoretical trend that the ν_s^{gs} frequency is larger than the ν_s^{es} . Moreover, the ν_s^{gs} extracted from the luminescence spectra agreed within 11 cm^{-1} with Raman data for $\text{UO}_2(\text{NO}_3)_2(\text{H}_2\text{O})_2$ in liquid [173]. The shifts between the ground and excited state stretching frequencies $\Delta\nu_s$ are 65 and 49 cm^{-1} for the $\text{UO}_2(\text{NO}_3)_2$ and $\text{UO}_2(\text{NO}_3)_2(\text{DEHiBA})_2$, respectively, while the theoretical shifts equal to 90 cm^{-1} in average. As it has been explained in Section 5.3.2, our theoretical methodology tends to overestimate the vibrational frequencies values; thus we can consider that the agreement between theoretical and experimental data is satisfactory. Moreover, it is difficult to estimate the degree of anharmonicity effects in experimental spectra, which might obviously decrease the band spacings in the higher energy region.

Based on the discussions above we have tried to attribute the electronic and vibronic transitions of experimental spectra being guided by the theoretical results. The direct comparisons of our theoretical spectra with the experimental ones can be visualized on Figure 5.7, the spectral characteristics and attribution of bands are listed in Table 5.6. To simplify the discussion, we have shifted the theoretical spectra to match the experimental energy range and normalized the intensities of both sets to the maximum value. First of all, the difference between

Table 5.6: Experimental and theoretical spectral characteristics of uranyl binitrate complexes. The peak maxima are reported in nm. Experimental ν_s^{gs} and ν_s^{es} values were obtained by a Lorentzian fitting procedure. The ν_s^{gs} corresponds to the averaged band-spacing values between the vibronic transitions, the ν_s^{es} corresponds to spacing between the $1 \rightarrow 0$ and $0 \rightarrow 0$ transitions. ν_s^{gs} and ν_s^{es} are given in cm^{-1} .

UO ₂ (NO ₃) ₂ (L) ₂ L	Spectral maxima (nm)					ν_s^{gs}	ν_s^{es}
	1 \rightarrow 0	0 \rightarrow 0	0 \rightarrow 1	0 \rightarrow 2	0 \rightarrow 3	[cm ⁻¹]	[cm ⁻¹]
Experimental							
H ₂ O [230]	507	529	554			864	799
DEHiBA [232]	495	516	540	566	593	844	795
Theoretical							
<i>trans</i> -H ₂ O ^a	507	529	557	587	621	925	833
<i>cis</i> -H ₂ O ^a	507	529	557	587	621	928	834
<i>trans</i> -DEiBA ^b	495	516	542	570	601	911	822
<i>cis</i> -DEiBA ^b	495	516	542	570	601	913	823

^{a, b} the 1 \rightarrow 0 was taken from experimental UO₂(NO₃)₂(L)₂ (L = H₂O, DEHiBA) emission spectra to match position of theoretical peaks with experimental ones

the ν_s^{gs} and ν_s^{es} experimental values lead us to propose that the $1 \rightarrow 0$ band pops up at 507 nm and 495 nm for UO₂(NO₃)₂(H₂O)₂ and UO₂(NO₃)₂(DEHiBA)₂, respectively. Another remarkable result is that the theoretical vibronic progression intensities distributions beautifully match the experimental ones when placing them next to the proposed “hot band.” Moreover, it has been confirmed previously that the $0 \rightarrow 0$ bands in uranium(VI)-based complexes are usually more intense compared to the “hot band” intensity at room temperature [17, 136, 140]. The nature of the bands at 495 and 480 nm in UO₂(NO₃)₂(H₂O)₂ and UO₂(NO₃)₂(DEHiBA)₂, respectively, remains an open question. Thus we can just suggest that these bands are related to the sample reabsorption, since the luminescence intensity of the band at 480 nm changes depending on the uranium(VI) concentration ([232, p. 150]). Also this band could correspond to an emission from another excited state.

One last point that was not yet discussed in detail is the probability of detection of the *cis*- and *trans*-conformers of uranyl binitrate complexes to confirm it from the experimental luminescence data. When we discussed the

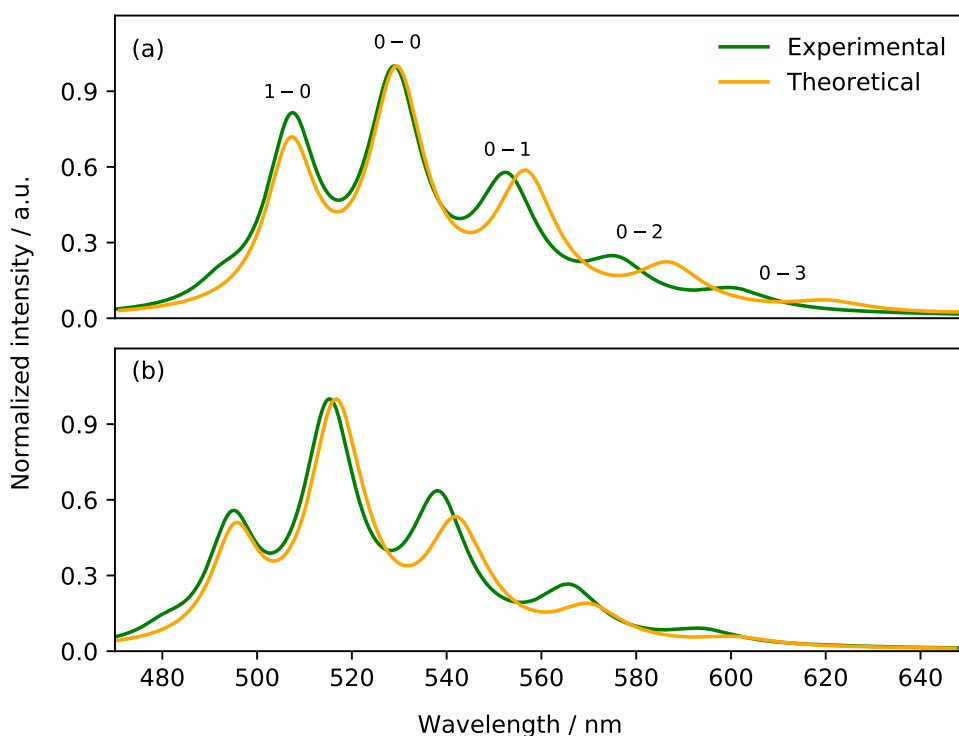


Figure 5.7: Comparison of experimental emission spectra (TRLFS) with theoretical spectra of (a) $\text{UO}_2(\text{NO}_3)_2(\text{H}_2\text{O})_2$ and (b) $\text{UO}_2(\text{NO}_3)_2(\text{DEiBA})_2$.

differences in the structures (Table 5.2) and harmonic frequencies (Table 5.3) of both conformers, the same as predicted luminescence spectra (Table 5.6), it was difficult to distinguish the more probable configuration of the $\text{UO}_2(\text{NO}_3)_2(\text{H}_2\text{O})_2$ and $\text{UO}_2(\text{NO}_3)_2(\text{DEiBA})_2$. The same as the relative free energies (see Table 5.1) computed for both types of the complexes are found to be very small to give an exact picture. Nevertheless, the *cis-trans* energetic difference data predicted the *cis*- and *trans*-isomers to be probable by about 30 % and 70% respectively for the uranyl binitrate complexes with water, and *trans*- $\text{UO}_2(\text{NO}_3)_2(\text{DEiBA})_2$ complex to be 100% probable. This kind of analysis represents a static picture only, while in experimental conditions the dynamic properties are valuable and may change a probability ratio.

5.5 Conclusions

The speciation of uranyl in solution can be investigated by TRLFS to determine the species that may dominate or coexist. This requires an accurate decomposition scheme and experimental data of high quality. In the context of spent fuel reprocessing, monoamide molecules are developed to selectively extract uranium(VI) from the aqueous to the organic phase. The present work by *ab initio* based methodology shows that no significant change is to be expected in the electronic structure of the uranium binitrate moiety. PBE0 (TD)-DFT approach accurately captured the ground and excited state structures with minor discrepancies which can probably be attributed to the choice of the functional of the density, the basis set and the solvation model. The proposed theoretical methodology allowed to calculate the main vibronic progression of the complexes with the corresponding assignment of the electronic transitions and vibrational modes involved, showing that PBE0 (TD)-DFT is an effective tool for prediction and assignment of luminescent spectra of U(VI)-based complexes.

In this work, we have used a stepwise growth of the chemical models to assess the sensitivity to the amount of water molecules in the coordination sphere of uranyl, and by substituting the water molecules with monoamide DEiBA. Using the chemical models in a form of $\text{UO}_2(\text{NO}_3)_2(\text{H}_2\text{O})$ and *cis/trans*- $\text{UO}_2(\text{NO}_3)_2(\text{L})_2$ ($\text{L} = \text{H}_2\text{O}$, DEiBA) it has been confirmed that the structural and spectroscopic parameters exhibit similar and hardly distinguishable features. Structural isomers for a given stoichiometry are indeed energetically very close and have almost identical TRLFS spectra. Calculations of luminescence bands intensities were found to be in excellent agreement with experimental TRLFS spectra, giving confidence in the validity of our methodology. This approach could be emphasized for a deeper interpretation of the data from time-resolved laser-induced fluorescent spectroscopy which is often efficiently used to track changes in the first coordination sphere of uranyl unit.

Bibliography of the current chapter

- (7) Denning, R.; Snellgrove, T.; Woodwark, D. The electronic structure of the uranyl ion: Part I. The electronic spectrum of $\text{Cs}_2\text{UO}_2\text{Cl}_4$. *Molecular Physics* **1976**, *32*, 419–442, DOI: 10.1080/00268977600103211.
- (9) Matsika, S.; Zhang, Z.; Brozell, S.; Blaudeau, J.-P.; Wang, Q.; Pitzer, R. Electronic structure and spectra of actinyl ions. *Journal of Physical Chemistry A* **2001**, *105*, 3825–3828, DOI: 10.1021/jp003085z.
- (10) Pierloot, K.; van Besien, E. Electronic structure and spectrum of UO_2^{2+} and $\text{UO}_2\text{Cl}_4^{2-}$. *Journal of Chemical Physics* **2005**, *123*, 204309, DOI: 10.1063/1.2121608.
- (16) Flint, C. D.; Tanner, P. A. Luminescence spectrum of $\text{Cs}_2\text{UO}_2\text{Cl}_4$. *Journal of the Chemical Society, Faraday Transactions 2: Molecular and Chemical Physics* **1978**, *74*, 2210–2217, DOI: 10.1039/F29787402210.
- (17) Wang, Z.; M. Zachara, J.; Liu, C.; Gassman, P.; R. Felmy, A.; B. Clark, S. A cryogenic fluorescence spectroscopic study of uranyl carbonate, phosphate and oxyhydroxide minerals. *Radiochimica Acta* **2008**, *96*, 591–598, DOI: 10.1021/es048448d.
- (20) Geipel, G.; Amayri, S.; Bernhard, G. Mixed complexes of alkaline earth uranyl carbonates: A laser-induced time-resolved fluorescence spectroscopic study. *Spectrochimica Acta Part A: Molecular and Biomolecular Spectroscopy* **2008**, *71*, 53–58, DOI: 10.1016/j.saa.2007.11.007.
- (21) Bernhard, G.; Geipel, G.; Reich, T.; Brendler, V.; Amayri, S.; Nitsche, H. Uranyl(VI) carbonate complex formation: Validation of the $\text{Ca}_2\text{UO}_2(\text{CO}_3)_3(\text{aq.})$ species. *Radiochimica Acta* **2001**, *89*, 511–518, DOI: 10.1524/ract.2001.89.8.511.
- (23) Görller-Walrand, C.; De Houwer, S.; Fluyt, L.; Binnemans, K. Spectroscopic properties of uranyl chloride complexes in non-aqueous solvents. *Physical Chemistry Chemical Physics* **2004**, *6*, 3292–3298, DOI: 10.1039/B317002K.
- (24) Van Besien, E.; Pierloot, K.; Görller-Walrand, C. Electronic spectra of uranyl chloride complexes in acetone: a CASSCF/CASPT2 investigation. *Physical Chemistry Chemical Physics* **2006**, *8*, 4311–4319, DOI: 10.1039/B607026D.
- (26) Tecmer, P.; Gomes, A. S. P.; Ekström, U.; Visscher, L. Electronic spectroscopy of UO_2^{2+} , NUO^+ and NUN : an evaluation of time-dependent density functional theory for actinides. *Physical Chemistry Chemical Physics* **2011**, *13*, 6249–6259, DOI: 10.1039/C0CP02534H.

- (30) Nichols, E. L.; Howes, H. L.; Merritt, E.; Wilber, D. T.; Wick, F. G., *Fluorescence of the uranyl salts*; 298; Carnegie institution of Washington: 1919.
- (86) Ernzerhof, M.; Scuseria, G. E. Assessment of the Perdew–Burke–Ernzerhof exchange–correlation functional. *Journal of Chemical Physics* **1999**, *110*, 5029–5036, DOI: 10.1063/1.478401.
- (87) Yanai, T.; Tew, D. P.; Handy, N. C. A new hybrid exchange–correlation functional using the Coulomb-attenuating method (CAM-B3LYP). *Chemical Physics Letters* **2004**, *393*, 51–57, DOI: 10.1016/j.cpllett.2004.06.011.
- (122) Weigend, F.; Ahlrichs, R. Balanced basis sets of split valence, triple zeta valence and quadruple zeta valence quality for H to Rn: Design and assessment of accuracy. *Physical Chemistry Chemical Physics* **2005**, *7*, 3297–3305, DOI: 10.1039/B508541A.
- (123) Weigend, F.; Häser, M.; Patzelt, H.; Ahlrichs, R. RI-MP2: optimized auxiliary basis sets and demonstration of efficiency. *Chemical Physics Letters* **1998**, *294*, 143–152, DOI: 10.1016/S0009-2614(98)00862-8.
- (124) Küchle, W.; Dolg, M.; Stoll, H.; Preuss, H. Energy-adjusted pseudopotentials for the actinides. Parameter sets and test calculations for thorium and thorium monoxide. *Journal of Chemical Physics* **1994**, *100*, 7535–7542, DOI: 10.1063/1.466847.
- (125) Baerends, E. J. et al. ADF2018, SCM, Theoretical Chemistry, Vrije Universiteit, Amsterdam, The Netherlands, <https://www.scm.com>.
- (126) Van Lenthe, E.; Baerends, E. J. Optimized Slater-type basis sets for the elements 1–118. *Journal of Computational Chemistry* **2003**, *24*, 1142–1156, DOI: 10.1002/jcc.10255.
- (127) Tomasi, J.; Mennucci, B.; Cammi, R. Quantum mechanical continuum solvation models. *Chemical Reviews* **2005**, *105*, 2999–3094, DOI: 10.1021/cr9904009.
- (131) Klamt, A.; Schüürmann, G. COSMO: a new approach to dielectric screening in solvents with explicit expressions for the screening energy and its gradient. *Journal of Chemical Society, Perkin Transactions 2* **1993**, *5*, 799–805, DOI: 10.1039/P29930000799.
- (132) Klamt, A. Conductor-like Screening Model for Real Solvents: A New Approach to the Quantitative Calculation of Solvation Phenomena. *Journal of Physical Chemistry* **1995**, *99*, 2224–2235, DOI: 10.1021/j100007a062.

- (133) Klamt, A.; Jonas, V. Treatment of the outlying charge in continuum solvation models. *Journal of Chemical Physics* **1996**, *105*, 9972–9981, DOI: 10.1063/1.472829.
- (136) Oher, H.; Réal, F.; Vercouter, T.; Vallet, V. Investigation of the Luminescence of $[\text{UO}_2\text{X}_4]^{2-}$ (X = Cl, Br) Complexes in the Organic Phase Using Time-Resolved Laser-Induced Fluorescence Spectroscopy and Quantum Chemical Simulations. *Inorganic Chemistry* **2020**, *59*, 5896–5906, DOI: 10.1021/acs.inorgchem.9b03614.
- (140) Su, J.; Zhang, K.; Schwarz, W. E.; Li, J. Uranyl-glycine-water complexes in solution: Comprehensive computational modeling of coordination geometries, stabilization energies, and luminescence properties. *Inorganic Chemistry* **2011**, *50*, 2082–2093, DOI: 10.1021/ic200204p.
- (144) Watkin, D. J.; Denning, R. G.; Prout, K. Structure of dicaesium tetrachlorodioxouranium (VI). *Acta Crystallographica C* **1991**, *47*, 2517–2519, DOI: 10.1107/S0108270191006777.
- (151) Mozhayskiy, V.; Krylov, A. ezSpectrum, <http://iopenshell.usc.edu/downloads>.
- (155) TURBOMOLE V7.3 2018, a development of University of Karlsruhe and Forschungszentrum Karlsruhe GmbH, TURBOMOLE GmbH, since 2007; available from <http://www.turbomole.com>. 1989-2007.
- (156) Frisch, M. J. et al. Gaussian 16 Revision B.01, Gaussian Inc. Wallingford CT, 2016.
- (157) Cao, X.; Dolg, M.; Stoll, H. Valence basis sets for relativistic energy-consistent small-core actinide pseudopotentials. *Journal of Chemical Physics* **2003**, *118*, 487–496, DOI: 10.1063/1.1521431.
- (158) Eichkorn, K.; Weigend, F.; Treutler, O.; Ahlrichs, R. Auxiliary basis sets for main row atoms and transition metals and their use to approximate Coulomb potentials. *Theoretical Chemistry Accounts* **1997**, *97*, 119–124, DOI: 10.1007/s002140050244.
- (163) Tecmer, P.; Bast, R.; Ruud, K.; Visscher, L. Charge-Transfer Excitations in Uranyl Tetrachloride ($[\text{UO}_2\text{Cl}_4]^{2-}$): How Reliable are Electronic Spectra from Relativistic Time-Dependent Density Functional Theory? *Journal of Physical Chemistry A* **2012**, *116*, 7397–7404, DOI: 10.1021/jp3011266.
- (165) Dau, P.; Su, J.; Liu, H.-T.; Huang, D.-L.; Li, J.; Wang, L.-S. Photoelectron spectroscopy and the electronic structure of the uranyl tetrachloride dianion: $\text{UO}_2\text{Cl}_4^{2-}$. *Journal of Chemical Physics* **2012**, *137*, 064315, DOI: 10.1063/1.4742062.

- (167) Wilson, R. E.; Skanthakumar, S.; Cahill, C.; Soderholm, L. Structural studies coupling X-ray diffraction and high-energy X-ray scattering in the $\text{UO}_2^{2+} - \text{HBr}_{\text{aq}}$ system. *Inorganic Chemistry* **2011**, *50*, 10748–10754, DOI: 10.1021/ic201265s.
- (173) Gal, M.; Goggin, P.; Mink, J. Mid-, far-infrared and raman spectra of uranyl complexes in aqueous solutions. *Journal of Molecular Spectroscopy* **1984**, *114*, 459–462, DOI: 10.1016/0022-2860(84)87186-0.
- (177) Oher, H.; Vercouter, T.; Réal, F.; Shang, C.; Reiller, P. E.; Vallet, V. Influence of alkaline earth metal ions on structures and luminescent properties of $\text{Na}_m\text{Me}_n\text{UO}_2(\text{CO}_3)_3^{(4-m-2n)-}$ (Me = Mg, Ca; m, n = 0-2): time-resolved fluorescence spectroscopy and ab initio studies. *Inorganic Chemistry* **2020**, *Submitted*.
- (230) Moulin, C.; Decambox, P.; Mauchien, P.; Pouyat, D.; Couston, L. Direct uranium (VI) and nitrate determinations in nuclear reprocessing by time-resolved laser-induced fluorescence. *Analytical Chemistry* **1996**, *68*, 3204–3209, DOI: 10.1021/ac9602579.
- (231) Taylor, R., *Reprocessing and recycling of spent nuclear fuel*; Elsevier: 2015.
- (232) Ferru, G. Spéciation moléculaire et supramoléculaire des systèmes extractants à base de monoamides, Ph.D. Thesis, Paris 6, 2012.
- (233) *Ion Exchange and Solvent Extraction: A Series of Advances*; Moyer, B. A., Ed.; CRC Press: 2009; Vol. 19.
- (234) Baron, P.; Boullis, B. *Modeling of uranium / plutonium splitting in PUREX process*; tech. rep. CEA-CONF-9089; CEA Centre d'Etudes Nucleaires de Fontenay-aux-Roses, 92 (France). Dept. de Genie Radioactif, 1987, p 323.
- (235) Saab, M.; Réal, F.; Šulka, M.; Cantrel, L.; Viro, F.; Vallet, V. Facing the challenge of predicting the standard formation enthalpies of *n*-butyl-phosphate species with ab initio methods. *The Journal of Chemical Physics* **2017**, *146*, 244312, DOI: 10.1063/1.4986953.
- (236) Madic, C.; Lecomte, M.; Baron, P.; Boullis, B. Separation of long-lived radionuclides from high active nuclear waste. *Comptes Rendus Physique* **2002**, *3*, 797–811, DOI: 10.1016/S1631-0705(02)01370-1.
- (237) Dinh, B.; Baron, P.; Duhamet, J. In *Monographies DEN CEA, Le traitement - recyclage du combustible nucléaire usé*, CEA Saclay et Groupe Moniteur: 2008.
- (238) Adnet, J.-M.; Miguiritchian, M.; Hill, C.; Heres, X.; Lecomte, M.; Masson, M.; Brossard, P.; Baron, P. In *Proceedings of GLOBAL*, 2005, pp 2562–2566.

- (239) Miguirditchian, M.; Sorel, C.; Camès, B.; Bisel, I.; Baron, P.; Espinoux, D.; Calor, J.; Viallesoubranne, C.; Lorrain, B.; Masson, M. In *Proceedings of GLOBAL*, 2009, pp 1032–1035.
- (240) Siddall III, T. Effects of structure of N, N-disubstituted amides on their extraction of actinide and zirconium nitrates and of nitric acid. *The Journal of Physical Chemistry* **1960**, *64*, 1863–1866, DOI: 10.1021/j100841a014.
- (241) Fritz, J. S.; Orf, G. M. Extraction of metal ions with N, N-disubstituted amides. *Analytical Chemistry* **1975**, *47*, 2043–2045, DOI: 10.1021/ac60362a008.
- (242) Gasparini, G. M.; Grossi, G. Review article long chain disubstituted aliphatic amides as extracting agents in industrial applications of solvent extraction. *Solvent Extraction and Ion Exchange* **1986**, *4*, 1233–1271, DOI: 10.1080/07366298608917921.
- (243) Loubert, G.; Volkringer, C.; Henry, N.; Arab-Chapelet, B.; Delahaye, T.; Loiseau, T. Structural studies of a series of uranyl alkylacetamides and piracetam complexes obtained in nitric acid aqueous solution. *Polyhedron* **2017**, *138*, 7–12, DOI: 10.1016/j.poly.2017.09.006.
- (244) Deb, S.; Gamare, J.; Kannan, S.; Drew, M. Uranyl(VI) and lanthanum(III) thio-diglycolamides complexes: Synthesis and structural studies involving nitrate complexation. *Polyhedron* **2009**, *28*, 2673–2678, DOI: 10.1016/j.poly.2009.06.001.
- (245) Moeyaert, P.; Dumas, T.; Guillaumont, D.; Kvashnina, K.; Sorel, C.; Miguirditchian, M.; Moisy, P.; Dufrêche, J.-F. Modeling and speciation study of uranium(VI) and technetium(VII) coextraction with DEHiBA. *Inorganic Chemistry* **2016**, *55*, 6511–6519, DOI: 10.1021/acs.inorgchem.6b00595.
- (246) Pathak, P.; Kumbhare, L.; Manchanda, V. Structural effects in N, N-dialkyl amides on their extraction behavior toward uranium and thorium. *Solvent Extraction and Ion Exchange* **2001**, *19*, 105–126, DOI: 10.1081/SEI-100001377.
- (247) Nair, G.; Prabhu, D.; Mahajan, G. Extraction of uranium (VI) and plutonium (IV) with dihexylbutyramide and dihexylisobutyramide from nitric acid medium. *Journal of Radioanalytical and Nuclear Chemistry* **1994**, *182*, 393–399, DOI: 10.1007/bf02037516.
- (248) Prabhu, D.; Mahajan, G.; Nair, G. Di (2-ethyl hexyl) butyramide and di (2-ethyl hexyl) isobutyramide as extractants for uranium (VI) and plutonium(IV). *Journal of Radioanalytical and Nuclear Chemistry* **1997**, *224*, 113–117, DOI: 10.1007/bf02034622.

- (249) Suzuki, S.; Sasaki, Y.; Yaita, T.; Kimura, T. *Study on selective separation of uranium by N,N-dialkyl-amide in ARTIST process*; tech. rep.; Department of Materials Science, 2004.
- (250) Pathak, P.; Prabhu, D.; Ruikar, P.; Mancha, V. Evaluation of di (2-ethylhexyl) isobutyramide (D2EHIBA) as a process extractant for the recovery of ^{233}U from irradiated Th. *Solvent Extraction and Ion Exchange* **2002**, *20*, 293–311, DOI: 10.1081/SEI-120004806.
- (251) Condamines, N.; Musikas, C. The extraction by NN-dialkylamides. II. Extraction of actinide cations. *Solvent Extraction and Ion Exchange* **1992**, *10*, 69–100, DOI: 10.1080/07366299208918093.
- (252) Vasudevan, T.; Murali, M.; Nagar, M.; Mathur, J. Extraction of U(VI) from nitrate and thiocyanate media with monoamides. *Solvent Extraction and Ion Exchange* **2002**, *20*, 665–686, DOI: 10.1081/SEI-120016072.
- (253) Rodrigues, F.; Ferru, G.; Berthon, L.; Boubals, N.; Guilbaud, P.; Sorel, C.; Diat, O.; Bauduin, P.; Simonin, J.; Morel, J.-P., et al. New insights into the extraction of uranium(VI) by an N,N-dialkylamide. *Molecular Physics* **2014**, *112*, 1362–1374, DOI: 10.1080/00268976.2014.902139.
- (254) Wahu, S.; Berthet, J.-C.; Thuéry, P.; Guillaumont, D.; Ephritikhine, M.; Guillot, R.; Cote, G.; Bresson, C. Structural versatility of uranyl(VI) nitrate complexes that involve the diamide ligand $\text{Et}_2\text{N}(\text{C}=\text{O})(\text{CH}_2)_n(\text{C}=\text{O})\text{NEt}_2$ ($0 \leq n \leq 6$). *European Journal of Inorganic Chemistry* **2012**, *2012*, 3747–3763, DOI: 10.1002/ejic.201200243.
- (255) Kannan, S.; Deb, S. B.; Drew, M. G. Synthesis, structural and emission studies of a bis (carbamoyl methyl) sulfone complex of uranyl nitrate. *Inorganic Chemistry Communications* **2011**, *14*, 225–227, DOI: 10.1016/j.inoche.2010.10.028.
- (256) Acher, E.; Hacene Cherkaski, Y.; Dumas, T.; Tamain, C.; Guillaumont, D.; Boubals, N.; Javierre, G.; Hennig, C.; Solari, P. L.; Charbonnel, M.-C. Structures of plutonium(IV) and uranium(VI) with N,N-dialkyl amides from crystallography, X-ray absorption spectra, and theoretical calculations. *Inorganic chemistry* **2016**, *55*, 5558–5569, DOI: 10.1021/acs.inorgchem.6b00592.
- (257) Deetlefs, M.; Hussey, C. L.; Mohammed, T. J.; Seddon, K. R.; van den Berg, J.-A.; Zora, J. A. Uranium halide complexes in ionic liquids: an electrochemical and structural study. *Dalton Trans.* **2006**, 2334–2341, DOI: 10.1039/B512212K.

- (258) Grenthe, I.; Drożdżyński, J.; Fujino, T.; Buck, E. C.; Albrecht-Schmitt, T. E.; Wolf, S. F. In *The Chemistry of the Actinide and Transactinide Elements*, Morss, L. R., Edelstein, N. M., Fuger, J., Eds., 4th; Springer: Dordrecht, The Netherlands, 2010; Chapter 5, pp 253–698, DOI: 10.1007/978-94-007-0211-0_5.
- (259) Field, B.; Hardy, C. Inorganic nitrates and nitrate-compounds. *Quarterly Reviews, Chemical Society* **1964**, *18*, 361–388, DOI: 10.1039/QR9641800361.
- (260) Pauling, L.; Dickinson, R. G. The crystal structure of uranyl nitrate hexahydrate. *Journal of the American Chemical Society* **1924**, *46*, 1615–1622, DOI: 10.1021/ja01672a009.
- (261) Taylor, J.; Mueller, M. A neutron diffraction study of uranyl nitrate hexahydrate. *Acta Crystallographica* **1965**, *19*, 536–543, DOI: 10.1107/S0365110X65003857.
- (262) Hall, D.; Rae, A.; Waters, T. The crystal structure of bisnitratodiaquodioxo-uranium(VI) tetrahydrate (uranyl nitrate hexahydrate). *Acta Crystallographica* **1965**, *19*, 389–395, DOI: 10.1107/S0365110X6500350X.
- (263) Couston, L.; Pouyat, D.; Moulin, C.; Decambox, P. Speciation of uranyl species in nitric acid medium by time-resolved laser-induced fluorescence. *Applied Spectroscopy* **1995**, *49*, 349–353, DOI: 10.1366/0003702953963553.
- (264) De Jong, W. A.; Aprà, E.; Windus, T. L.; Nichols, J. A.; Harrison, R. J.; Gutowski, K. E.; Dixon, D. A. Complexation of the carbonate, nitrate, and acetate anions with the uranyl dication: density functional studies with relativistic effective core potentials. *The Journal of Physical Chemistry A* **2005**, *109*, 11568–11577, DOI: 10.1021/jp0541462.
- (265) Bühl, M.; Kabrede, H.; Diss, R.; Wipff, G. Effect of hydration on coordination properties of uranyl(VI) complexes. A first-principles molecular dynamics study. *Journal of the American Chemical Society* **2006**, *128*, 6357–6368, DOI: 10.1021/ja057301z.
- (266) McGlynn, S.; Smith, J.; Neely, W. Electronic structure, spectra, and magnetic properties of oxycations. III. Ligation effects on the infrared spectrum of the uranyl ion. *The Journal of Chemical Physics* **1961**, *35*, 105–116, DOI: 10.1063/1.1731876.
- (267) Parr, R. G.; Pearson, R. G. Absolute hardness: companion parameter to absolute electronegativity. *Journal of the American chemical society* **1983**, *105*, 7512–7516, DOI: 10.1021/ja00364a005.

- (268) Addleman, R. S.; Wai, C. M. Luminescence quenching of $\text{UO}_2(\text{NO}_3)_2 \cdot 2\text{TBP}$ in supercritical fluid CO_2 . *Physical Chemistry Chemical Physics* **1999**, *1*, 783–790, DOI: 10.1039/A807753C.
- (269) Pant, D.; Khandelwal, D. In *Proceedings of the Indian Academy of Sciences-Section A*, 1959; Vol. 50, pp 323–335.
- (270) Addleman, R. S.; Wai, C. M. On-Line Time-Resolved Laser-Induced Fluorescence of $\text{UO}_2(\text{NO}_3)_2 \cdot 2\text{TBP}$ in Supercritical Fluid CO_2 . *Analytical Chemistry* **2000**, *72*, 2109–2116, DOI: 10.1021/ac991135u.

General conclusions and perspectives

The interpretation of the luminescence spectra of uranium(VI) compounds, such as those measured by TRLFS, is often a difficult task since a spectrum itself gives just "locked" information about electronic structure. In this thesis work, the use of *ab initio* quantum chemistry has been proposed to model and explain experimental spectra of U(VI) complexes. The prediction of the luminescence spectra of uranyl-containing complexes remains quite a challenge for quantum chemistry since it requires an accurate treatment of both correlation and relativistic effects at the same time. The U(VI) complexes are closed-shell systems of various molecular sizes, which implies that only the use of DFT and TD-DFT approaches is computationally affordable. It has been previously shown and also confirmed by the present study, that the hybrid and range-separated functionals perform well for the prediction of structural and spectroscopic properties, respectively, with an accuracy close to that of WFT-based methods. In this thesis, the use of experimental TRLFS and theoretical *ab initio* techniques opened the possibility to explain the uranium(VI) electronic structure of different complexes, and estimate the capabilities of both techniques. A methodology has been developed to better understand the behavior of uranyl during electronic relaxation in the presence of ligands of different nature and properties. By following *in silico* the experimental excitation-emission process we succeeded to obtain the vibronic progressions and emission energies for further theoretical reconstruction of luminescence spectra which can be compared to experimental data. The obtained intermediate data such as optimized geometries and harmonic frequencies of both ground and luminescent states turned out to play a key role in this study allowing to understand the experimental observations like the shape of the spectrum, the relative intensities of the luminescence peaks, the band spacings

and positions of the whole spectra on the energy scale.

As it has been mentioned, the theoretical methodology has been first assessed. In Chapter 3, we have made use of a large set of available experimental data for the $\text{UO}_2\text{Cl}_4^{2-}$ complex to carry out a detailed step-by-step validation of the proposed methodology. The theoretical approach showed the capability to decompose the effect of the first and second coordination spheres, the solvent influence and the impact of the complex's symmetry. From this study, we have established that the major influence on the electronic structure of uranium(VI) originates from the inorganic ligands present in the first coordination sphere, as they change the $\text{U}-\text{O}_{\text{yl}}$ geometry, symmetrical stretching frequency and, as a result, the emission energy out of the luminescence state. When we have further considered the presence of the long-range components in our model systems such as the organic counter-ion Aliquate 336 and a solvent with low polarity, we did not observe any significant changes in the geometrical characteristics, but their presence was more reflected in the emission energies. Moreover, it has been deduced that the uranyl(VI) complexes with a high symmetry can exhibit a non-standard shape of the luminescence spectrum as observed with the complexes $\text{UO}_2\text{X}_4^{2-}$ ($\text{X} = \text{Cl}, \text{Br}$) that have D_{4h} symmetry. This is the result of coupling of additional vibrational modes to the main progression. The good agreement between theoretical and experimental data gave us enough confidence in the use of this quantum chemical approach to explain some phenomena observed in the luminescence spectra of uranium(VI) complexes.

In a subsequent study described in Chapter 4, we were aiming at explaining the phenomena of the experimental luminescence intensity change of the $\text{UO}_2(\text{CO}_3)_3^{4-}$ complexes as a function of the alkaline earth counter cations such as Mg^{2+} and Ca^{2+} in aqueous phase. This is a second key example of the efficiency and accuracy of the quantum chemical approach, we devised. It was deduced, that the U-O bond length of uranyl as well as its symmetrical stretching frequency are sensitive to the ligand's basicity, causing also a change in the emission energy from the first low-lying states (stronger basicity leads to the red-shift of luminescence). We reproduced theoretically the "hot band" position and, moreover, the relative intensities of triscarbonatouranyl complexes with different stoichiometries of Mg and Ca, showing that the inorganic counter-

ions have higher impact on the uranium(VI) electronic structure. Additional calculations revealed the importance of the long-range high polar solvent like water included into our theoretical models. We have succeeded to reproduce the main luminescence emissions of model complexes and have provided a complete assignment of the electronic transitions and the vibrational modes involved in the coupling. This part of the study also suggested that proposed theoretical models could be improved by adding explicit water molecules that might affect the position of the counter ions, for instance.

In the last Chapter 5, we studied the effect of monamide DEHiBA ligands placed in the first coordination sphere of $\text{UO}_2(\text{NO}_3)_2$ complex. Our objective was to determine whether one can distinguish the *cis* and *trans* conformers experimentally using luminescence measurements, as the investigation of U(VI) speciation in presence of extracting molecules is of high interest in separation chemistry. This lead us to predict the spectra of these two conformers and to propose assignments of the luminescence bands. In addition we checked their relative thermodynamic stability, and our calculations suggest that the *trans* conformer is more probable than the *cis* one, but the conformational equilibrium could be shifted in real experimental conditions. It has also been shown that the "hot band" maxima and the vibronic progression shapes are almost identical for these two complexes, making it very difficult to distinguish them with luminescence measurements.

After completing these studies I would like to write a little more about the luminescence spectra assignment. Unfortunately, there is no unique scheme to provide a correct information about the band - nature correspondence. Some small bands can contain information on both electronic structure changes, and physico-chemical phenomena (additional emissions, reabsorption processes, specific quenching effects). Usually, it is difficult to distinguish the different origins, thus possibly making the assignment inaccurate. For instance, in the case of the triscarbonatouranyl complexes we observed that the lower part of electronic spectrum is different with respect to energy gaps between the vibronic bands as compared to uranyl tetrahalides or uranyl binitrates systems. Hence, for this particular case, there are two progressions overlapping to produce one luminescence spectrum. In case of $\text{UO}_2(\text{NO}_3)_2\text{L}_2$ complexes, the experimental spectrum

showed several small contributions in the lower energy part. A thorough analysis of the experimental data revealed that these small peaks are coming from sample reabsorption and have nothing to do with the electronic structure of the uranyl complex. Thus, there are really many aspects that should be carefully taken into account while doing the luminescence spectrum assignment.

For many researchers working with time-resolved spectroscopic techniques, there is an interest in kinetics. In this work, the reader did not find much information about the decay times of uranium(VI) luminescence with the further quenching effects studies, or about chemical kinetics from which the evolution of reactants and products can be followed. In the frame of this thesis we have shown that the TRLFS technique is also efficient to study the electronic structure of the uranium(VI) complexes, as it is sensitive to its closest chemical environment. Unfortunately, as we worked on this topic, we have realized that the experimental data available in the literature did not always report a detailed processing of the luminescence data. We are not talking about the studies addressed to determination of the complexation constants, for instance, but about the literature where the purpose was to perform an electronic structure investigation. This sadly reveals that one should pay much attention to the information hidden in luminescence spectra, since new phenomena can be discovered by the multi-peak fitting, or by simple analysis of vibronic intensities ratio.

All the results presented in this thesis showed that the proposed quantum chemical methodology works well for uranium(VI) complexes with different types of ligands in organic and aqueous media. The combination of experimental TRLFS and theoretical *ab initio* quantum modeling appears to be a powerful tool to explain the luminescence properties of uranium(VI)-based complexes and to decompose the effect of solvent, counter-ions or extracting agents present in a sample. But, there are many properties of uranium(VI) which are just combined right. The closed-shell configuration of uranyl(VI), the type of excitation and the ability to exhibit luminescence. One should say, that the proposed methodology probably will not work the same way if one of these properties is different (such as another luminescent actinide, *e.g.* Cm(III) with open-shell configuration, charge-transfer transitions, etc.). Nevertheless, sometimes it is worth to develop a methodology, which may not be universal, but efficient for one particular class

of systems and probably may serve as an inspiration for the further works on compounds with different from U(VI) properties.

As a perspective, the theoretical methodology could be extended in several ways. For instance, the explicit inclusion of solvent molecules into the chemical model could improve not only the emission energies but also the band spacing in the vibronic progression part. The addition of anharmonic contributions to the Franck-Condon vibronic calculations could improve the high energy part of the spectra. From my own experience, to obtain theoretical luminescence spectra of the uranium(VI) complexes with a high symmetry is troublesome because a spontaneous symmetry breaking occurs during the excitation that cannot be caught by the TD-DFT method. Thus, for small-size highly symmetrical uranium(VI) complexes, the proposed methodology could be extended with restricted-active-space wave function calculations as proposed by Heit et al. [271]. Furthermore, an approximate mathematical methodology combined with *ab initio* approach for the computations of a radiative lifetime is available and can be adapted to be applied to the case of uranium(VI) complexes [272, 273].

A short to mid-term extension of my thesis work could focus on uranyl hydrolyzed monomeric, dimeric and trimeric species. Indeed, it is of high relevance to explore the sensitivity of theoretical methodology to the deprotonation of water molecules in the first coordination sphere. Moreover, the uranyl hydrolysis is very complex as many species can coexist in solution depending on pH and uranium concentration as it has been extensively confirmed by TRLFS technique [18, 22, 59]. The few preliminary calculations I have performed on $\text{UO}_2(\text{H}_2\text{O})_5^{2+}$, $\text{UO}_2(\text{H}_2\text{O})_4(\text{OH})^+$ and $(\text{UO}_2)_2(\text{OH})_2(\text{H}_2\text{O})_6^{2+}$ species show promising results and discoveries. We expect to compute the emission energies and vibronic progressions together with relative intensities for further decomposition of experimental spectra, since the luminescence spectra of some of the hydrolyzed species of uranyl was never observed by TRLFS, probably because of their low signal or because they lose an ability to emit light as a result of specific structure formation.

Bibliography of the current chapter

- (18) Moulin, C.; Decambox, P.; Moulin, V.; Decaillon, J. G. Uranium Speciation in Solution by Time-Resolved Laser-Induced Fluorescence. *Analytical Chemistry* **1995**, *67*, 348–353, DOI: 10.1021/ac00098a019.
- (22) Drobot, B.; Steudtner, R.; Raff, J.; Geipel, G.; Brendler, V.; Tsushima, S. Combining luminescence spectroscopy, parallel factor analysis and quantum chemistry to reveal metal speciation—a case study of uranyl (VI) hydrolysis. *Chemical Science* **2015**, *6*, 964–972, DOI: 10.1039/C4SC02022G.
- (59) Kirishima, A.; Kimura, T.; Tochiyama, O.; Yoshida, Z. Speciation study on uranium (VI) hydrolysis at high temperatures and pressures. *Journal of Alloys and Compounds* **2004**, *374*, 277–282, DOI: 10.1016/j.jallcom.2003.11.105.
- (271) Heit, Y. N.; Gendron, F.; Autschbach, J. Calculation of dipole-forbidden $5f$ absorption spectra of uranium(V) hexa-halide complexes. *The Journal of Physical Chemistry Letters* **2018**, *9*, 887–894, DOI: 10.1021/acs.jpcllett.7b03441.
- (272) Sahoo, B. K.; Majumder, S.; Chaudhuri, R. K.; Das, B.; Mukherjee, D. Ab initio determination of the lifetime of the $6^2P_{3/2}$ state for $^{207}\text{Pb}^+$ by relativistic many-body theory. *Journal of Physics B: Atomic, Molecular and Optical Physics* **2004**, *37*, 3409–3418, DOI: 10.1088/0953-4075/37/17/002.
- (273) Flick, J.; Welakuh, D. M.; Ruggenthaler, M.; Appel, H.; Rubio, A. Light-Matter Response in Non-Relativistic Quantum Electrodynamics: Quantum Modifications of Maxwell's Equations. *ACS Photonics* **2019**, *6*, 2757–2778, DOI: 10.1021/acsp Photonics.9b00768..

Supplementary information for Chapter 3

A.1 Selection of the delay time

To select a correct delay time for recording of time-resolved spectrum of $[A336]_2[UO_2Cl_4]$ in *n*-dodecane, we have performed measurements at several delay time, 20, 50, 100 and 200 ns. The corresponding recorded spectra are shown in Figure A.1.

By inspecting the normalized spectra at different delay times, we have found that positions of maxima remain the same, along with the vibronic features. However, at short delay times (20 and 50 ns), a background luminescence contribution appears in the short wavelength range (around 430 nm), which, by comparison to the spectra of the reference media (solution without uranium), might be attributed to the luminescence of the solvent or the A336 molecule (Figure A.2), with its own exponential decay.

This background emission vanished for larger delay times (100, up to 200 ns), and as the recorded spectra are essentially the same for these two-time values, we chose the 100 ns delay time.

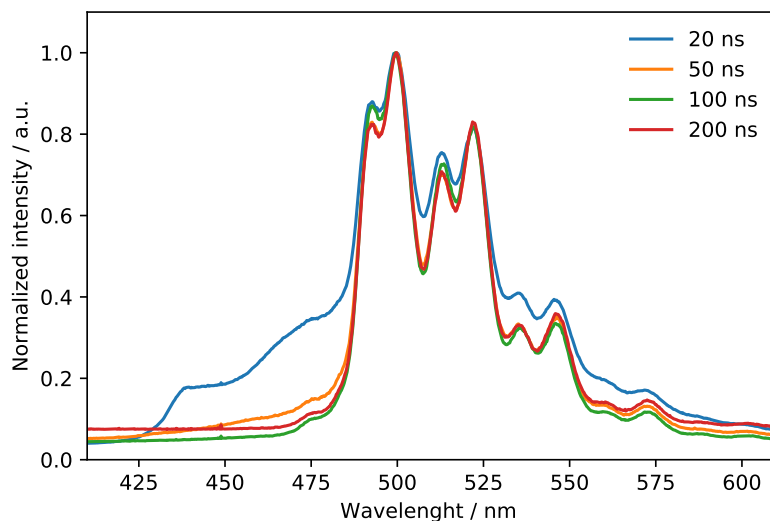


Figure A.1: Normalized time-resolved luminescence spectra of $[A336]_2[UO_2Cl_4]$ in *n*-dodecane measured at different delay time.

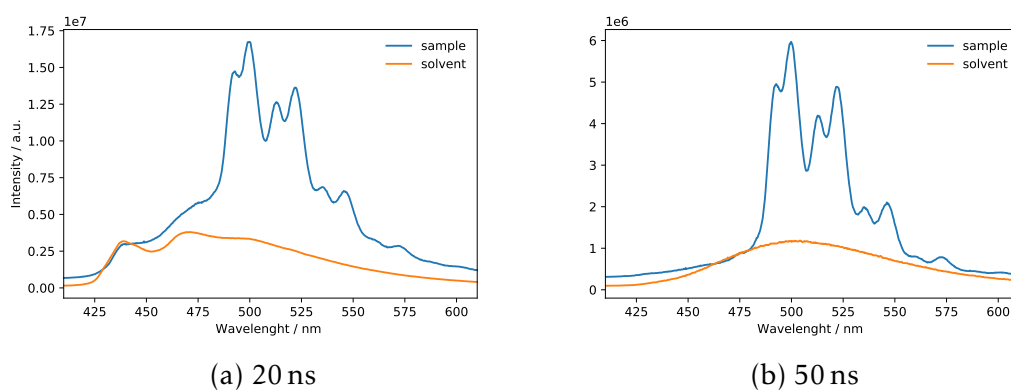


Figure A.2: Comparison of reference sample (without U) with the sample of $[A336]_2[UO_2Cl_4]$ in *n*-dodecane measured at different delay time.

A.2 Supplemental Tables

Table A.1: Experimental luminescence data of the $[\text{R}_4\text{N}]_2[\text{UO}_2\text{Cl}_4]$ complexes at room temperature. The ν corresponds to the position of the band, the $\Delta\nu$ is a difference between the bands position in a region, the $\Delta\nu_n$ is a difference between the peaks of the same nature located in different regions. All data are in cm^{-1} . The luminescence spectra are shown on Figure 3.2.

		$[\text{A336}]_2[\text{UO}_2\text{Cl}_4]$ in <i>n</i> -dodecane				$[\text{Bu}_4\text{N}]_2[\text{UO}_2\text{Cl}_4]$ in acetone			
		ν/cm^{-1}	$\Delta\nu$	$\Delta\nu_n$	Intensity	ν/cm^{-1}	$\Delta\nu$	$\Delta\nu_n$	Intensity
Region		21025			0.06				
1	I_1	20295	730		0.84	20325	-		0.74
	I'_1	20015	280		1.00	20032	293		0.95
	I_1^*					19944	88		0.91
						19763	181		0.40
2	I_2	19488	527	807	0.70	19501	262	824	0.84
	I'_2	19155	333	860	0.81	19238	263	794	0.83
	I_2^*					19113	125	831	1.00
						18925	188	838	0.34
3	I_3	18651	504	837	0.28	18664	261	837	0.39
	I'_3	18305	346	850	0.30	18403	261	836	0.36
	I_3^*					18282	121	832	0.51
						18103	179	822	0.16
4	I_4	17839	466	812	0.08	17825	278	838	0.11
	I'_4	17454	385	851	0.08	17593	232	810	0.09
	I_4^*					17452	141	830	0.16
						17289	163	814	0.05
5	I_5	16996	458	843	0.02	17013	277	813	0.03
	I'_5	16625	371	829	0.02	16795	217	798	0.02
	I_5^*					16628	168	824	0.03
						16442	186	847	0.01

Table A.2: Ground and excited state harmonic and anharmonic frequencies (in cm^{-1}) of the $[\text{UO}_2\text{Cl}_4]^{2-}$ complex in a gas phase computed by G16 at R-ECP DFT/PBE0 and TD-DFT/PBE0 level of theory for the ground and first excited states respectively.

ν	Ground state		Excited state		Nature of the band
	E_{harm}	E_{anharm}	E_{harm}	E_{anharm}	
1	75.7	76.4	71.3	72.4	out-of-plane asymmetrical Cl-U-Cl bending
2	76.6	76.6	77.2	77.2	in plane Cl-U-Cl bending
3	76.6	76.6	77.2	77.2	
4	97.3	98.0	98.7	99.8	U-Cl scissoring
5	110.0	110.3	104.1	105.0	out-of-plane symmetrical Cl-U-Cl bending
6	197.2	193.7	170.5	166.7	$\text{O}_{\text{yl}}-\text{U}-\text{O}_{\text{yl}}$ rocking
7	197.2	193.7	170.5	166.7	
8	202.3	202.5	199.2	199.0	asymmetrical Cl-U-Cl stretching
9	219.1	219.2	214.5	214.6	asymmetrical Cl-U-Cl stretching
10	219.1	219.2	214.5	214.6	
11	237.3	237.0	232.6	231.6	symmetrical Cl-U-Cl stretching
12	274.5	271.4	271.8	268.5	$\text{O}_{\text{yl}}-\text{U}-\text{O}_{\text{yl}}$ bending
13	274.5	271.4	271.8	268.5	
14	894.5	889.4	813.7	810.9	symmetrical $\text{O}_{\text{yl}}-\text{U}-\text{O}_{\text{yl}}$ stretching
15	974.2	966.9	858.9	854.3	asymmetrical $\text{O}_{\text{yl}}-\text{U}-\text{O}_{\text{yl}}$ stretching

Table A.3: The chloride-hydrogen bond lengths (in Å) in $[\text{R}_4\text{N}]_2[\text{UO}_2\text{Cl}_4]$ complexes computed at the R-ECP DFT/PBE0 and TD-DFT/PBE0 levels of theory for the ground and first excited states, respectively. Atom labeling corresponds to the one shown on Figure A.3.

	$[\text{Bu}_4\text{N}]_2[\text{UO}_2\text{Cl}_4]$		$[\text{A336}]_2[\text{UO}_2\text{Cl}_4]$		
	GS	ES	GS	ES	
Cl33-H83	2.534	2.524	Cl25-H57	2.427	2.411
Cl36-H53	2.642	2.606	Cl28-H48	2.557	2.535
Cl33-H97	2.646	2.632	Cl28-H37	2.656	2.626
Cl36-H71	2.789	2.744	Cl28-H151	2.672	2.685
Cl36-H66	2.893	2.885	Cl27-H71	2.851	2.901

Table A.4: Assignment of the $[\text{UO}_2\text{Cl}_4]^{2-}$ (gas-phase) theoretical luminescence spectrum. The energy of the spectrum was adjusted to experimental band-origin value of $[\text{UO}_2\text{Cl}_4]^{2-}$ in acetone. The nature of bands is explained in Table A.2.

Region	E, cm^{-1}	$\Delta\nu$, cm^{-1}	I, a.u.	Identification
0	20325.0		6.50E-01	0(0)->1(0)
	20087.9	237.1	1.43E-02	0(0)->1(1 ν_{11})
	19930.6	394.4	1.72E-03	0(0)->1(2 ν_7)
	19850.8	474.2	3.29E-04	0(0)->1(2 ν_{11})
1	19430.6	894.4	2.46E-01	0(0)->1(1 ν_{14})
	19193.5	237.1	7.21E-03	0(0)->1(1 ν_{11} , 1 ν_{14})
	19036.2	394.4	6.52E-04	0(0)->1(2 ν_7 , 1 ν_{14})
	18955.6	475.0	1.84E-04	0(0)->1(2 ν_{11} , 1 ν_{14})
2	18536.2	894.4	5.91E-02	0(0)->1(2 ν_{14})
	18299.1	237.1	2.11E-03	0(0)->1(1 ν_{11} , 2 ν_{14})
	18141.8	394.4	1.56E-04	0(0)->1(2 ν_7 , 2 ν_{14})
	18061.2	475.0	5.94E-05	0(0)->1(2 ν_{11} , 2 ν_{14})
3	17641.8	894.4	1.11E-02	0(0)->1(3 ν_{14})
	17404.7	237.1	4.66E-04	0(0)->1(1 ν_{11} , 3 ν_{14})
	17247.4	394.4	2.95E-05	0(0)->1(2 ν_7 , 3 ν_{14})
	17166.7	475.0	1.44E-05	0(0)->1(2 ν_{11} , 3 ν_{14})
4	16747.4	894.4	1.80E-03	0(0)->1(4 ν_{14})
	16510.3	237.1	8.61E-05	0(0)->1(1 ν_{11} , 4 ν_{14})
5	15853.0	894.4	2.62E-04	0(0)->1(5 ν_{14})

Table A.5: Assignment of the $[\text{UO}_2\text{Cl}_4]^{2-}$ (dodecane) theoretical luminescence spectrum. The energy of the spectrum was adjusted to experimental band-origin value of $[\text{UO}_2\text{Cl}_4]^{2-}$ in acetone. The nature of bands is explained in Table A.2.

Region	E, cm^{-1}	$\Delta\nu$, cm^{-1}	I, a.u.	Identification
0	20325.0		6.59E-01	0(0)->1(0)
	20116.9	208.1	1.48E-04	0(0)->1(2 ν_5)
	20085.5	239.5	2.42E-02	0(0)->1(1 ν_{11})
	19926.6	398.4	1.79E-03	0(0)->1(2 ν_7)
	19845.9	479.1	6.63E-04	0(0)->1(2 ν_{11})
1	19435.4	889.6	2.34E-01	0(0)->1(1 ν_{14})
	19227.4	208.1	5.26E-05	0(0)->1(2 ν_5 , 1 ν_{14})
	19195.9	239.5	8.19E-03	0(0)->1(1 ν_{11} , 1 ν_{14})
	19037.0	398.4	6.34E-04	0(0)->1(2 ν_7 , 1 ν_{14})
	18956.4	479.1	2.17E-04	0(0)->1(2 ν_{11} , 1 ν_{14})
2	18545.9	889.6	5.30E-02	0(0)->1(2 ν_{14})
	18337.8	208.1	1.19E-05	0(0)->1(2 ν_5 , 2 ν_{14})
	18306.3	239.5	1.79E-03	0(0)->1(1 ν_{11} , 2 ν_{14})
	18147.5	398.4	1.44E-04	0(0)->1(2 ν_7 , 2 ν_{14})
	18066.8	479.1	4.62E-05	0(0)->1(2 ν_{11} , 2 ν_{14})
3	17656.3	889.6	9.47E-03	0(0)->1(3 ν_{14})
	17416.8	239.5	3.09E-04	0(0)->1(1 ν_{11} , 3 ν_{14})
	17257.9	398.4	2.57E-05	0(0)->1(2 ν_7 , 3 ν_{14})
4	16766.7	889.6	1.46E-03	0(0)->1(4 ν_{14})
	16527.2	239.5	4.60E-05	0(0)->1(1 ν_{11} , 4 ν_{14})
5	15877.2	889.6	2.01E-04	0(0)->1(5 ν_{14})

Table A.6: Assignment of the $[\text{UO}_2\text{Cl}_4]^{2-}$ (acetone) theoretical luminescence spectrum. The energy of the spectrum was adjusted to experimental band-origin value of $[\text{UO}_2\text{Cl}_4]^{2-}$ in acetone. The nature of bands is explained in Table A.2.

Region	E, cm^{-1}	$\Delta\nu$, cm^{-1}	I, a.u.	Identification
0	20325.0		5.30E-01	0(0)->1(0)
	20081.4	243.6	1.45E-01	0(0)->1(1 ν_{11})
	19929.0	396.0	1.56E-03	0(0)->1(2 ν_7)
	19838.7	486.3	2.08E-02	0(0)->1(2 ν_{11})
	19595.1	729.9	2.10E-03	0(0)->1(3 ν_{11})
1	19441.9	883.1	1.79E-01	0(0)->1(1 ν_{14})
	19198.3	243.6	4.82E-02	0(0)->1(1 ν_{11} , 1 ν_{14})
	19045.9	396.0	5.28E-04	0(0)->1(2 ν_7 , 1 ν_{14})
	18955.6	486.3	6.82E-03	0(0)->1(2 ν_{11} , 1 ν_{14})
2	18558.8	883.1	3.89E-02	0(0)->1(1 ν_{14})
	18316.0	242.8	1.03E-02	0(0)->1(1 ν_{11} , 2 ν_{14})
	18162.8	396.0	1.14E-04	0(0)->1(2 ν_7 , 2 ν_{14})
	18072.4	486.3	1.44E-03	0(0)->1(2 ν_{11} , 2 ν_{14})
3	17675.6	883.1	6.66E-03	0(0)->1(3 ν_{14})
	17432.9	242.8	1.74E-03	0(0)->1(1 ν_{11} , 3 ν_{14})
	17280.5	395.2	1.96E-05	0(0)->1(2 ν_7 , 3 ν_{14})
	17189.3	486.3	2.40E-04	0(0)->1(2 ν_{11} , 3 ν_{14})
4	16793.3	882.3	9.80E-04	0(0)->1(4 ν_{14})
	16549.8	243.6	2.54E-04	0(0)->1(1 ν_{11} , 4 ν_{14})
5	15910.2	883.1	1.30E-04	0(0)->1(5 ν_{14})

Table A.7: Assignment of the $[\text{UO}_2\text{Br}_4]^{2-}$ theoretical luminescence spectrum. The energy of the spectrum was adjusted to experimental band-origin value of $[\text{UO}_2\text{Cl}_4]^{2-}$ in acetone. The bands representation is taken from the $[\text{UO}_2\text{Cl}_4]^{2-}$ frequencies, the nature of bands is explained in Table A.2.

Region	E, cm^{-1}	$\Delta\nu$, cm^{-1}	I, a.u.	Identification
0	20325.0		4.70E-01	0(0)->1(0)
	20229.0	96.0	1.63E-02	0(0)->1(2 ν_3)
	20181.4	143.6	4.06E-02	0(0)->1(1 ν_{11})
	20081.4	243.6	7.03E-03	0(0)->1(2 ν_8)
	19971.8	353.2	2.07E-03	0(0)->1(2 ν_7)
1	19418.5	906.5	1.53E-01	0(0)->1(1 ν_{14})
	19274.1	144.4	1.54E-02	0(0)->1(1 ν_{11} , 1 ν_{14})
	19174.9	243.6	2.29E-03	0(0)->1(2 ν_8 , 1 ν_{14})
2	18511.2	907.3	2.76E-02	0(0)->1(2 ν_{14})
	18367.6	143.6	3.16E-03	0(0)->1(1 ν_{11} , 2 ν_{14})
	18268.4	242.8	4.13E-04	0(0)->1(2 ν_8 , 2 ν_{14})
3	17604.7	906.5	3.63E-03	0(0)->1(3 ν_{14})
	17461.1	143.6	4.66E-04	0(0)->1(1 ν_{11} , 3 ν_{14})
4	16697.4	907.3	3.88E-04	0(0)->1(4 ν_{14})
	16553.8	143.6	5.49E-05	0(0)->1(1 ν_{11} , 4 ν_{14})
5	15790.9	906.5	3.56E-05	0(0)->1(5 ν_{14})

Table A.8: Assignment of the $[\text{Bu}_4\text{N}]_2[\text{UO}_2\text{Cl}_4]$ (gas-phase) theoretical luminescence spectrum. The energy of the spectrum was adjusted to experimental band-origin value of $[\text{UO}_2\text{Cl}_4]^{2-}$ in acetone. The nature of bands is shown in Table A.2.

Region	E, cm^{-1}	$\Delta\nu$, cm^{-1}	I, a.u.	Identification
0	20325		1.73E-01	0(0)->1(0)
	20114	211	1.24E-04	0(0)->1(1 ν_7)
	20092	233	2.29E-03	0(0)->1(1 ν_8)
	20056	269	1.32E-03	0(0)->1(1 ν_{11})
	19902	423	4.00E-04	0(0)->1(2 ν_7)
1	19456	869	5.26E-02	0(0)->1(1 ν_{14})
	19245	211	1.47E-05	0(0)->1(1 ν_7 ,1 ν_{14})
	19223	233	7.05E-04	0(0)->1(1 ν_8 ,1 ν_{14})
	19187	269	3.53E-04	0(0)->1(1 ν_{11} ,1 ν_{14})
	19034	423	1.19E-04	0(0)->1(2 ν_7 ,1 ν_{14})
2	18588	869	1.03E-02	0(0)->1(2 ν_{14})
	18356	232	1.40E-04	0(0)->1(1 ν_8 ,2 ν_{14})
	18318	269	6.24E-05	0(0)->1(1 ν_{11} ,2 ν_{14})
	18165	423	2.32E-05	0(0)->1(2 ν_7 ,2 ν_{14})
3	17719	869	1.60E-03	0(0)->1(3 ν_{14})
	17487	232	2.19E-05	0(0)->1(1 ν_8 ,3 ν_{14})
4	16851	869	2.14E-04	0(0)->1(4 ν_{14})
5	15982	869	2.57E-05	0(0)->1(5 ν_{14})

Table A.9: Assignment of the $[A336]_2[UO_2Cl_4]$ gas-phase theoretical luminescence spectrum. The energy of the spectrum was adjusted to experimental band-origin value of $[A336]_2[UO_2Cl_4]$ in *n*-dodecane. The bands representation is taken from the $[UO_2Cl_4]^{2-}$ frequencies, with details found in Table A.2.

Region	E, cm ⁻¹	$\Delta\nu$, cm ⁻¹	I, a.u.	Identification
0	21025.0		7.55E-01	0(0)->1(0)
	20786.3	238.7	2.59E-03	0(0)->1(1 ν_8 , 1 ν_{12})
	20758.9	266.1	1.25E-02	0(0)->1(1 ν_{11})
	20492.7	532.3	2.54E-04	0(0)->1(2 ν_{11})
1	20149.1	875.9	8.88E-02	0(0)->1(1 ν_{14})
	19910.4	238.7	2.93E-04	0(0)->1(1 ν_8 , 1 ν_{12} , 1 ν_{14})
	19883.0	266.1	1.32E-03	0(0)->1(1 ν_{11} , 1 ν_{14})
2	19274.1	875.1	6.75E-03	0(0)->1(2 ν_{14})
	19032.9	241.1	3.44E-05	0(0)->1(1 ν_9 , 1 ν_{12} , 2 ν_{14})
	19007.1	267.0	9.21E-05	0(0)->1(1 ν_{11} , 2 ν_{14})
3	18398.2	875.9	4.07E-04	0(0)->1(3 ν_{14})
	18159.5	238.7	1.26E-06	0(0)->1(1 ν_8 , 1 ν_{12} , 3 ν_{14})
	18132.1	266.1	5.13E-06	0(0)->1(1 ν_{11} , 3 ν_{14})
4	17522.4	875.9	2.11E-05	0(0)->1(4 ν_{14})
	17256.2	266.1	2.48E-07	0(0)->1(1 ν_{11} , 4 ν_{14})

Table A.10: Theoretical displacements of geometries ΔR , and absolute frequency shifts $\Delta\nu$ from the ground to the first excited state.

		ΔR , Å		$\Delta\nu$, cm ⁻¹			
		R _{U-O}	R _{U-X}	ν_{U-X}	ν_b	ν_s	ν_a
$[UO_2Cl_4]^{2-}$	gas phase	0.031	0.007	-4	-4	-80	-115
	dodecane	0.031	0.007	1	-1	-78	-106
	acetone	0.03	0.009	-1	-2	-81	-101
$[UO_2Br_4]^{2-}$	gas phase	0.028	0.012	7	2	-31	-53
$[Bu_4N]_2[UO_2Cl_4]$	gas phase	0.026	0.003-0.027	-4	-5	-70	-100
$[A336]_2[UO_2Cl_4]$	gas phase	0.029	0.005-0.021	-5	-4	-74	-103

A.3 Supplemental Figures

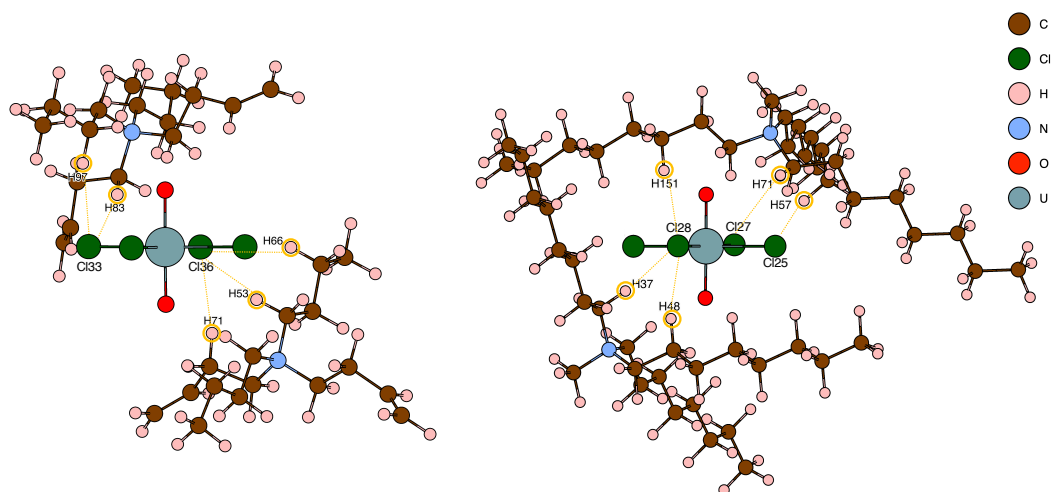


Figure A.3: Illustrations of hydrogen bonds between the first and second coordination spheres of uranyl in $[\text{R}_4\text{N}]_2[\text{UO}_2\text{Cl}_4]$ complexes. Left panel is representing interactions in $[\text{Bu}_4\text{N}]_2[\text{UO}_2\text{Cl}_4]$ and right in $[\text{A336}]_2[\text{UO}_2\text{Cl}_4]$.

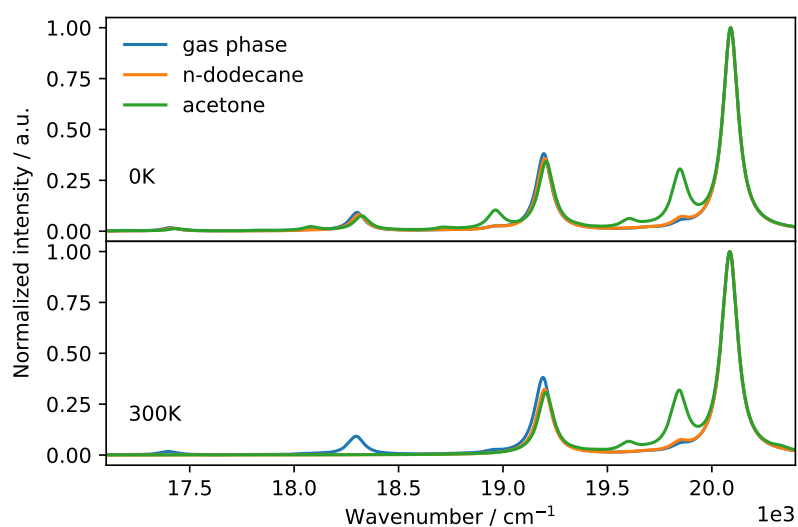


Figure A.4: Influence of solvent effects on the theoretical spectrum of $[\text{UO}_2\text{Cl}_4]^{2-}$ at 0 K (upper panel) and 300 K (lower panel). The spectral shapes were obtained by a Lorentzian convolution; the assignments are provided in Tables A.4, A.5 and A.6 for the $[\text{UO}_2\text{Cl}_4]^{2-}$ in gas-phase, *n*-dodecane and acetone, respectively.

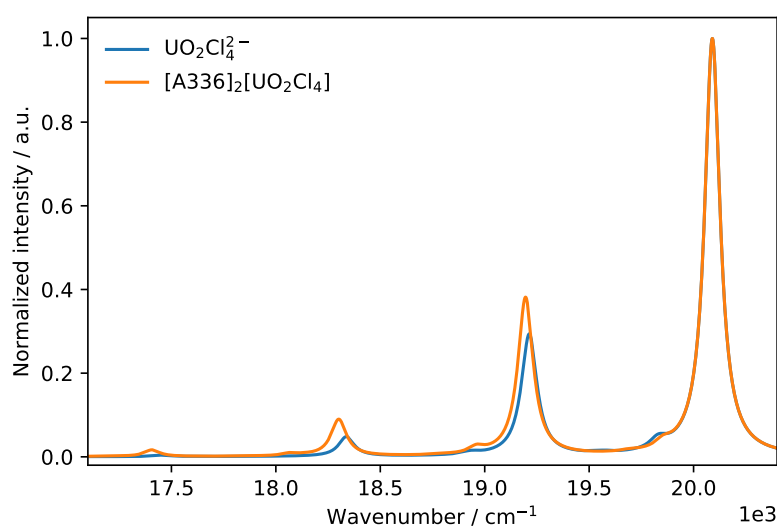


Figure A.5: Effect of a $[\text{A336}]^+$ counter ion on the theoretical $[\text{UO}_2\text{Cl}_4]^{2-}$ spectrum in gas-phase at 300 K. The spectral shapes were obtained by a Lorentzian convolution; the assignments are provided in Tables A.4 and A.9 for the $[\text{UO}_2\text{Cl}_4]^{2-}$ and $[\text{A336}]_2[\text{UO}_2\text{Cl}_4]$, respectively.

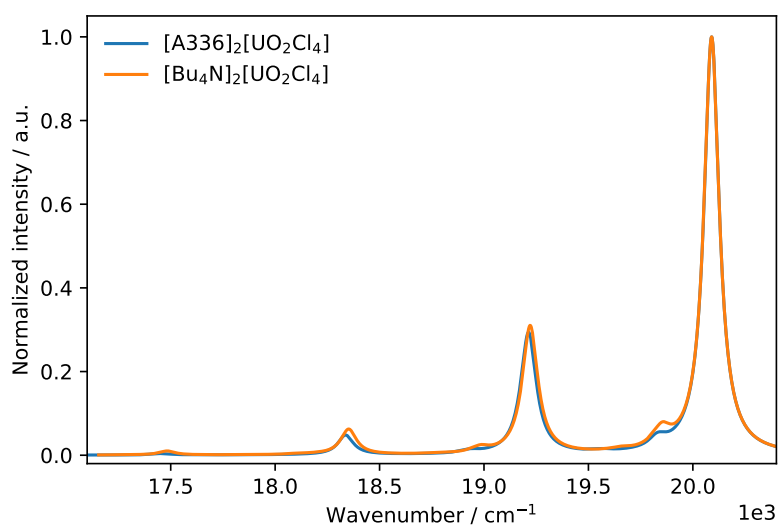


Figure A.6: Comparison of the theoretical spectra of $[\text{Bu}_4\text{N}]_2[\text{UO}_2\text{Cl}_4]$ and $[\text{A336}]_2[\text{UO}_2\text{Cl}_4]$ complexes in a gas-phase at 300 K. The spectral shapes were obtained by a Lorentzian convolution; the assignments are provided in Tables A.8 and A.9 for the $[\text{Bu}_4\text{N}]_2[\text{UO}_2\text{Cl}_4]$ and $[\text{A336}]_2[\text{UO}_2\text{Cl}_4]$, respectively.

Supplementary information for Chapter 4

B.1 Extraction of the pure spectra of the (Mg/Ca–) UO₂–CO₃) species from the raw TRLFS data

The assumption that the experimentally measured fluorescence intensity is the sum of individual contributions of existing aqueous species constitutes the basic prerequisite in deducing the pure spectra of known fluorescent complexes. The total fluorescence intensity is expressed as a linear combination of independent fluorescence intensities of predetermined U(VI) components in solution. In the present study, the three main species are (UO₂(CO₃)₃)^{4–}, CaUO₂(CO₃)₃^{2–}, Ca₂UO₂(CO₃)₃ for the case of calcium and the two (UO₂(CO₃)₃)^{4–}, MgUO₂(CO₃)₃^{2–}) complexes for magnesium:

$$FI = FI_{Ca_0} + FI_{Ca_1} + FI_{Ca_2} \quad (\text{B.1})$$

$$FI = FI_{Mg_0} + FI_{Mg_1} \quad (\text{B.2})$$

where *FI* represents the fluorescence intensity acquired using identical acquisition parameters of TRLFS. The *FI* terms noted *FI*_{Ca_{*n*}} (*n* = 0, 1, 2) and *FI*_{Mg_{*n*}} (*n* = 0, 1) respectively refer to the actual fluorescence intensities of Ca_{*n*}UO₂(CO₃)₃^{4–2*n*–} (*n* = 0, 1, 2) and Mg_{*n*}UO₂(CO₃)₃^{4–2*n*–} (*n* = 0, 1).

For the sake of simplicity, the process of obtaining the individual spectra for Ca_{*n*}UO₂(CO₃)₃^{4–2*n*–} (*n* = 0, 1, 2) presented in the text will be detailed here, and it also applies to the Mg_{*n*}UO₂(CO₃)₃^{4–2*n*–} (*n* = 0, 1) complexes.

In experiments, 22 samples were prepared at 0.1 M NaCl for the series

of $\text{Ca-}\text{UO}_2\text{-CO}_3$, where the concentrations of the three different species $\text{Ca}_n\text{UO}_2(\text{CO}_3)_3^{4-2n-}$ ($n = 0, 1, 2$) are evolving as a function of the aqueous calcium concentration. With the published stability constants of U(VI) carbonate complexes,[194, 200] the chemical speciation as well as the relative concentration ratio C_{Ca_n} ($n = 0, 1, 2$) were determined for the analyzed samples. The emission spectra were then acquired using identical configuration parameters of the TRLFS instrument. The implemented CCD array detector with 1024 pixels enables to cover an extended range of wavelengths 401.9906–614.5806 nm when applying the 300 lines/mm grating.

As described in Eq.B.1, the fluorescence intensities FI_{Ca_n} ($n = 0, 1, 2$) can be further developed into the sum of products of the relative concentration ratio C_{Ca_n} ($n = 0, 1, 2$) and the fluorescence intensities $FI_{Ca_n}^\circ$ ($n = 0, 1, 2$) of the pure chemical species:

$$FI = C_{Ca_0} \times FI_{Ca_0}^\circ + C_{Ca_1} \times FI_{Ca_1}^\circ + C_{Ca_2} \times FI_{Ca_2}^\circ \quad (\text{B.3})$$

According to the physical meaning of data structures, the idea behind the processing method is to introduce data matrices which correspond to the relationship between the relative concentration ratios and the fluorescence intensities FI and allow to extract the desirable information $FI_{Ca_n}^\circ$ ($n = 0, 1, 2$) from matrix operations. To this aim, we define three matrices, respectively $A \in R^{m \times n}$ containing the chemical speciation information of 22 samples with $m = 22$ and $n = 3$, $x \in R^{p \times q}$ representing the unknown matrix with $p = 3$ and $q = 1024$, and $B \in R^{i \times j}$ containing the spectra intensity data at each pixel for the 22 samples with $i = 22$ and $j = 1024$. The following equivalent equations are therefore proposed to deduce the unknown x matrix:

$$A \times x = B \iff x = A^{-1} \times B$$

$$\text{with } A = \begin{bmatrix} a_{11} & a_{12} & a_{13} \\ \vdots & \vdots & \vdots \\ a_{22,1} & a_{22,2} & a_{22,3} \end{bmatrix}; x = \begin{bmatrix} x_{11} & \dots & x_{1,1024} \\ x_{21} & \dots & x_{2,1024} \\ x_{31} & \dots & x_{3,1024} \end{bmatrix}; B = \begin{bmatrix} b_{11} & \dots & b_{1,1024} \\ \vdots & \ddots & \vdots \\ b_{22,1} & \dots & b_{22,1024} \end{bmatrix}$$

where (i) the m th row $A(m, :) = [a_{m,1} \ a_{m,2} \ a_{m,3}]$ listing the calculated concentration ratio of $\text{Ca}_x\text{UO}_2(\text{CO}_3)_3^{4-2x-}$ ($x = 0, 1, 2$) species in the m th sample solution, the n th column $A(:, n)$ corresponding to C_{Ca_n} ($n = 1, 2, 3$); (ii) the p th row $x(p, :) = [x_{p,1} \ \dots \ x_{p,1024}]$ representing the determined fluorescence intensity of pure U(VI) species at investigated pixel numbers, i.e. $FI_{Ca_0}^\circ$ ($\text{UO}_2(\text{CO}_3)_3^{4-}$) for $p = 1$, $FI_{Ca_1}^\circ$ ($\text{CaUO}_2(\text{CO}_3)_3^{2-}$) for $p = 2$, $FI_{Ca_2}^\circ$ ($\text{Ca}_2\text{UO}_2(\text{CO}_3)_3$) for $p = 3$; (iii) the i th row $B(i, :) = [b_{i,1} \ \dots \ b_{i,1024}]$ contains the fluorescence intensity measured at each pixel for the i th sample solution. Finally, the graphical representations

of $\text{Ca}_x\text{UO}_2(\text{CO}_3)_3^{4-2x-}$ ($x = 0, 1, 2$) pure spectra were plotted by associating the wavelength with the pixel number, as shown in the manuscript.

B.2 Procedure to estimate the spectrum of the $\text{Na}_2\text{MgUO}_2(\text{CO}_3)_3$ complex in water

In this section, first we explain why we have a problem to construct the theoretical spectrum of $\text{Na}_2\text{MgUO}_2(\text{CO}_3)_3$ complex in water, and explain how we have rebuilt it from the gas-phase data after small justifications.

In a polar solvent like water, Mg^{2+} exhibits a stronger polarizing effect than Ca^{2+} due to its higher charge density. When Mg^{2+} interacts with $\text{UO}_2(\text{CO}_3)_3^{4-}$, the global electron density of the negative ion group, especially of the equatorial oxygen atoms in carbonates, would be more distorted towards the Mg^{2+} than Ca^{2+} . It has been observed from our calculations of $\text{Na}_2\text{MgUO}_2(\text{CO}_3)_3$ complex in water media, that the Mg^{2+} cation do not only distort the equatorial oxygen atoms belonging to the carbonate groups but also moves out of the equatorial plane to approach one of the axial uranyl oxygen atoms. This induces a bending of the uranyl moiety, thus making the computed vibronic spectrum silent. On the contrary, in the $\text{NaMg}_2\text{UO}_2(\text{CO}_3)_3^+$ complex, Mg^{2+} lies in the equatorial plane, probably because the short U–Na bond stabilizes the equatorial ligands. In experimental conditions, the Mg^{2+} counter-cation is most probably surrounded by some water molecules from the solvent, thus since our chemical model does not include implicit water molecules, the complex structure is free to undergo out-of-plane distortions that are energetically costless (0.38 kJ mol^{-1}). Working with a more detailed solvation model in which the outer solvation shell are described explicitly brings in computational difficulties in part because of the many possible locations and conformations of the explicit solvent molecules but also because of the significant increase of the computational costs for the calculations of the vibronically resolved spectra.

With the objective to propose a reasonable spectrum of $\text{Na}_2\text{MgUO}_2(\text{CO}_3)_3$ in water, we suggest to use the results obtained from quantum chemical calculations of $\text{Na}_2\text{CaUO}_2(\text{CO}_3)_3$, $\text{NaCa}_2\text{UO}_2(\text{CO}_3)_3^+$, and $\text{NaMg}_2\text{UO}_2(\text{CO}_3)_3^+$ complexes in terms of intensity and vibronic-progression evolutions when going from the gas phase to the solvent. In Table B.9, we have reported the intensities ratio of the five main bands, that correspond to the I_i/I_1 for the two complexes, computed in GP ($(I_i/I_1)_{GP}$) and in water ($(I_i/I_1)_w$). One can see that the ratio for a given band does not evolve strongly from GP to water and that it is almost independent of the number of countercations and their nature. In addition

to these quantities we have estimated the gamma factor (γ) defined as the ratio of $(I_i/I_1)_w$ by $(I_i/I_1)_{GP}$. Plotting the evolution of gamma as a function of $(i-1)$, i.e with an origin set to 1, one can observe a linear decrease of the gamma value with a slop of -0.089 in the case of $\text{Na}_2\text{CaUO}_2(\text{CO}_3)_3$, -0.086 for $\text{NaCa}_2\text{UO}_2(\text{CO}_3)_3^+$, and -0.068 in the $\text{NaMg}_2\text{UO}_2(\text{CO}_3)_3^+$ complex. One can see that the values and the trends estimated in the Ca^{2+} case are similar for one or two calcium ions. Thus, we have used the $\text{NaMg}_2\text{UO}_2(\text{CO}_3)_3^+$ complex's gamma factors to reconstruct the evolution of the main five-bands($0(0)\rightarrow 1(i\nu_3)$) transition intensities $\text{Na}_2\text{MgUO}_2(\text{CO}_3)_3$ in water. The "extrapolated" intensities are reported in Table B.10. For the other less intense bands, we decide to keep the gas-phase values. Thus, in Table B.10, for $\text{Na}_2\text{MgUO}_2(\text{CO}_3)_3$ the first intensity is identical to the one computed in GP. This prevents us to really estimate the absolute change induces by the solvent effect. However, since Figure fig:Ca-0kspectra shows that solvent effects reduce the difference between systems with either one or two calciums, one can expect the situation to be the same in the Mg^{2+} case.

B.3 Supplemental Tables

Table B.1: The ground and excited-state displacements in $\text{Na}_2\text{MgUO}_2(\text{CO}_3)_3$ and $\text{NaMg}_2\text{UO}_2(\text{CO}_3)_3^+$ complexes between the structures obtained in the gas phase and in the CPCM water solvent, at the DFT/PBE0 and TD-DFT/PBE0 levels of theory.

	U-O _{ax}	U-O _{eq}	U-C	U-O _{dist}	U-Na	U-Mg
			Displacement			
			<i>Ground state</i>			
$\text{Na}_2\text{MgUO}_2(\text{CO}_3)_3$	0.018/ 0.017	0.031($\times 2$)/-0.027/ -0.028/-0.132($\times 2$)	0.002/ -0.108($\times 2$)	0.024/ -0.090($\times 2$)	0.194($\times 2$)	0.197
$\text{NaMg}_2\text{UO}_2(\text{CO}_3)_3^+$	0.019/ 0.018	0.030/0.031/-0.040($\times 2$)/ -0.107/-0.108	-0.04/-0.041/ -0.141	-0.013($\times 2$)/ -0.118	0.135	0.177($\times 2$)
			<i>Excited state</i>			
$\text{Na}_2\text{MgUO}_2(\text{CO}_3)_3$	0.017/ 0.016	0.025/0.061/-0.043/ -0.032/-0.147/-0.124	0.016/-0.119/ -0.114	0.038/-0.101/ -0.095	0.181/ 0.208	0.199
$\text{NaMg}_2\text{UO}_2(\text{CO}_3)_3^+$	0.017/ 0.018	0.038/0.039/-0.044/ -0.032/-0.147/-0.124	-0.036($\times 2$)/ -0.146	-0.009/ -0.123	0.134	0.175/ 0.176

Table B.2: Ground and excited-state bond distances (in Å) in the $\text{Na}_2\text{MgUO}_2(\text{CO}_3)_3$ and $\text{NaMg}_2\text{UO}_2(\text{CO}_3)_3^+$ complexes optimized in the gas phase and in the CPCM water solvent, at the DFT/PBE0 and TD-DFT/PBE0 levels of theory.

	U-O _{ax}	U-O _{eq}	U-C	U-O _{dist}	U-Na	U-Mg
$\text{Na}_2\text{MgUO}_2(\text{CO}_3)_3$	1.764/	2.356(×2)/2.466/	2.855/	4.065/	3.607(×2)	3.318
	1.765	2.467/2.609(×2)	3.056(×2)	4.262(×2)		
$\text{NaMg}_2\text{UO}_2(\text{CO}_3)_3^+$	1.755/	2.360(×2)/2.469(×2)/	2.939(×2)/	4.132(×2)/	3.605	3.334(×2)
	1.756	2.577/2.578	3.121	4.311		
$\text{Na}_2\text{MgUO}_2(\text{CO}_3)_3$	1.800/	2.349(×2)/2.478(×2)/	2.842/	4.052/	3.602(×2)	3.323
	1.801	2.629(×2)	3.071(×2)	4.278(×2)		
$\text{NaMg}_2\text{UO}_2(\text{CO}_3)_3^+$	1.792(×2)	2.340/2.341/2.498(×2)/	2.939(×2)/	4.132(×2)/	3.583	3.344(×2)
		2.591/2.592	3.134	4.326		
$\text{Na}_2\text{MgUO}_2(\text{CO}_3)_3$	1.782(×2)	2.387(×2)/2.439(×2)/	2.857/	4.089/	3.801(×2)	3.515
		2.477(×2)	2.948(×2)	4.172(×2)		
$\text{NaMg}_2\text{UO}_2(\text{CO}_3)_3^+$	1.774(×2)	2.390/2.391/	2.899/2.900/	4.119(×2)/	3.74	3.511(×2)
		2.429(×2)/2.470(×2)	2.980	4.193		
$\text{Na}_2\text{MgUO}_2(\text{CO}_3)_3$	1.817(×2)	2.374/2.410/2.436/	2.858/2.952/	4.090/4.177/	3.783/	3.521
		2.447/2.482/2.505	2.958	4.183	3.809	
$\text{NaMg}_2\text{UO}_2(\text{CO}_3)_3^+$	1.809/	2.379/2.380/2.454/	2.903(×2)/	4.123/4.124/	3.717	3.518/
	1.810	2.455/2.479/2.480	2.988	4.202		3.519

Ground state, Water, $\epsilon_r = 78$

Excited state, Water, $\epsilon_r = 78$

Ground state, Gas phase, $\epsilon_r = 0$

Excited state, Gas phase, $\epsilon_r = 0$

Table B.3: The ground and excited-state displacements in $\text{Na}_2\text{CaUO}_2(\text{CO}_3)_3$ and $\text{NaCa}_2\text{UO}_2(\text{CO}_3)_3^+$ complexes between the structures obtained in the gas phase and in the CPCM water solvent, at the DFT/PBE0 and TD-DFT/PBE0 levels of theory.

	U-O _{ax}	U-O _{eq}	U-C	U-O _{dist}	U-Na	U-Ca
$\text{Na}_2\text{CaUO}_2(\text{CO}_3)_3$	0.018(x2)	0.032(x2)/-0.035(x2)/ -0.103(x2)	Displacement <i>Ground state</i> 0.003/ -0.094(x2)	0.025/ -0.075(x2)	0.192(x2)	0.242
$\text{NaCa}_2\text{UO}_2(\text{CO}_3)_3^+$	0.020(x2)	0.026(x2)/-0.034(x2)/ -0.084/-0.085	-0.036(x2)/ -0.112 <i>Excited state</i>	-0.009(2x)/ -0.089	0.142	0.215(x2)
$\text{Na}_2\text{CaUO}_2(\text{CO}_3)_3$	0.017(x2)	0.040/-0.060/0.060/ -0.053/-0.104/-0.086	0.023/-0.101/ -0.106	0.046/-0.087/ -0.082	0.194/ 0.182	0.248
$\text{NaCa}_2\text{UO}_2(\text{CO}_3)_3^+$	0.019/ 0.018	0.035(x2)/-0.039(x2)/ -0.087(x2)	-0.032/-0.033/ -0.116	-0.005/-0.006/ -0.092	0.144	0.212(x2)

Table B.4: Ground and excited-state bond distances (in Å) in the $\text{Na}_2\text{CaUO}_2(\text{CO}_3)_3$ and $\text{NaCa}_2\text{UO}_2(\text{CO}_3)_3^+$ complexes optimized in the gas phase and in the CPCM water solvent, at the DFT/PBE0 and TD-DFT/PBE0 levels of theory.

	U-O _{ax}	U-O _{eq}	U-C	U-O _{dist}	U-Na	U-Ca
$\text{Na}_2\text{CaUO}_2(\text{CO}_3)_3$	1.767(×2)	2.372(×2)/2.468(×2)/ 2.572(×2)	2.871/ 3.026(×2)	4.083/ 4.237(×2)	3.626(×2)	3.623
		<i>Ground state, Gas phase, $\epsilon_r = 0$</i>				
$\text{NaCa}_2\text{UO}_2(\text{CO}_3)_3^+$	1.759(×2)	2.380(×2)/2.471(×2)/ 2.545/2.547	2.938(×2)/ 3.065	4.138(×2)/ 4.264	3.654	3.649(×2)
		<i>Excited state, Gas phase, $\epsilon_r = 0$</i>				
$\text{Na}_2\text{CaUO}_2(\text{CO}_3)_3$	1.803(×2)	2.364/2.367/2.481/ 2.482/2.584/2.586	2.859/3.038/ 3.039	4.072/ 4.250(×2)	3.623/ 3.625	3.627
$\text{NaCa}_2\text{UO}_2(\text{CO}_3)_3^+$	1.796(×2)	2.363(×2)/2.500/ 2.501/2.544(×2)	2.940/2.941/ 3.072	4.140/4.141/ 4.272	3.633	3.659(×2)
		<i>Ground state, Water, $\epsilon_r = 78$</i>				
$\text{Na}_2\text{CaUO}_2(\text{CO}_3)_3$	1.785(×2)	2.404(×2)/2.433(×2)/ 2.469(×2)	2.874/2.931/ 2.932	4.108/ 4.162(×2)	3.818(×2)	3.865
$\text{NaCa}_2\text{UO}_2(\text{CO}_3)_3^+$	1.779(×2)	2.406(×2)/2.437(×2)/ 2.462(×2)	2.902(×2)/ 2.953	4.129(×2)/ 4.176	3.796	3.864(×2)
		<i>Excited state, Water, $\epsilon_r = 78$</i>				
$\text{Na}_2\text{CaUO}_2(\text{CO}_3)_3$	1.820(×2)	2.406/2.422/2.425/ 2.428/2.482/2.497	2.882/2.933/ 2.927	4.118/4.164/ 4.168	3.817/ 3.806	3.875
$\text{NaCa}_2\text{UO}_2(\text{CO}_3)_3^+$	1.814/ 1.815	2.398(×2)/2.462(×2)/ 2.467(×2)	2.908(×2)/ 2.956	4.135(×2)/ 4.135	3.778	3.871(×2)

Table B.5: Absolute frequency shifts $\Delta\nu$ (in cm^{-1}) from the ground to the first excited state geometries.

$\Delta\nu, \text{cm}^{-1}$	Gas phase		Water	
	ν_s	ν_a	ν_s	ν_a
$\text{Na}_3\text{UO}_2(\text{CO}_3)_3^-$	-83	-137	-125	-100
$\text{Na}_2\text{MgUO}_2(\text{CO}_3)_3$	-84	-142	-135	-102
$\text{NaMg}_2\text{UO}_2(\text{CO}_3)_3^+$	-90	-140	-135	-106
$\text{Na}_2\text{CaUO}_2(\text{CO}_3)_3$	-84	-139	-130	-100
$\text{NaCa}_2\text{UO}_2(\text{CO}_3)_3^+$	-89	-136	-134	-104

Table B.6: First four vertical emission energies in cm^{-1} computed at the SF and SOC CAM-B3LYP level of theory with the COSMO water solvent model.

	$\text{Na}_3\text{UO}_2(\text{CO}_3)_3^-$	$\text{Na}_2\text{MgUO}_2(\text{CO}_3)_3$	$\text{NaMg}_2\text{UO}_2(\text{CO}_3)_3^+$	$\text{Na}_2\text{CaUO}_2(\text{CO}_3)_3$	$\text{NaCa}_2\text{UO}_2(\text{CO}_3)_3^+$
	Spin-free emission energies				
1a	23801	23540	23341	23572	23310
2a	23887	23674	23597	23618	23482
3a	25618	25240	24975	25217	24839
4a	31148	30471	30168	30565	30220
	Spin-orbit coupling emission energies				
1a	20803	20629	20547	20622	20480
2a	20809	20634	20560	20624	20484
3a	21633	21387	21182	21393	21137
4a	21717	21450	21403	21448	21284

Table B.7: First four vertical emission energies in cm^{-1} computed at the SOC CAM-B3LYP level of theory with the COSMO water solvent model and corrected with the spin-free zero-point energy corrections, ΔZPE , of the ground and luminescent states.

	$\text{Na}_3 - \text{U} - \text{CO}_3$	$\text{Na}_2\text{Mg} - \text{U} - \text{CO}_3$	$\text{NaMg}_2 - \text{U} - \text{CO}_3$	$\text{Na}_2\text{Ca} - \text{U} - \text{CO}_3$	$\text{NaCa}_2 - \text{U} - \text{CO}_3$
$1a$	20803	20629	20547	20622	20480
$2a$	20809	20634	20560	20624	20484
$3a$	21633	21387	21182	21393	21137
$4a$	21717	21450	21403	21448	21284
$\bar{E}_{1a,2a}, \text{cm}^{-1}$	20806	20641	20554	20623	20482
$\bar{E}_{3a,4a}, \text{cm}^{-1}$	21675	21433	21293	21421	21211
$\text{ZPE}_{\text{GS}}, E_{\text{h}}$	-0.0582	-0.0594	-0.0598	-0.0583	-0.0590
$\text{ZPE}_{\text{ES,H}} E_{\text{h}}$	-0.0570	-0.0580	-0.0590	-0.0571	-0.0580
$\Delta\text{ZPE}, \text{cm}^{-1}$	-262.72	-301.34	-181.95	-261.40	-213.77
$\bar{E}_{1a,2a} + \Delta\text{ZPE}, \text{cm}^{-1}$	20543	20339	20372	20362	20268
$\bar{E}_{3a,4a} + \Delta\text{ZPE}, \text{cm}^{-1}$	21412	21131	21111	21159	20997

Table B.8: Experimental and theoretical spectral characteristics of triscarbonatouranyl complexes. The peak maxima are reported in nm. Experimental ν_s^{gs} and ν values were obtained by a Lorentzian fitting procedure. The ν_s^{gs} corresponds to the averaged band-spacing values between the vibronic transitions, the ν corresponds to spacing between the $11 \rightarrow 00$ and $10 \rightarrow 00$ transitions. ν_s^{gs} and ν are given in cm^{-1} .

Complex	Spectral maxima (nm)					ν_s^{gs} (cm^{-1})	ν (cm^{-1})
	$11 \rightarrow 00$	$10 \rightarrow 00$	$10 \rightarrow 01$	$10 \rightarrow 02$	$10 \rightarrow 03$		
Mg-U(VI)-CO ₃	466.0	484.7	505.2	526.7	549.4	826	828
	464.7	483.7	504.6	526.7	549.4	832	845
Ca-U(VI)-CO ₃	Experimental						
	466.0	482.2	504.5	529.0	556.2	857	722
NaMg ₂ UO ₂ (CO ₃) ₃ ⁺	466.0	482.6	503.9	527.0	552.2	874	739
	464.7	481.0	501.5	523.8	548.2	850	720
Na ₂ CaUO ₂ (CO ₃) ₃	464.7	481.0	501.5	523.8	548.2	850	720
	464.7	481.0	501.8	524.5	549.3	862	728
NaCa ₂ UO ₂ (CO ₃) ₃ ⁺	Theoretical						
	466.0	482.2	504.5	529.0	556.2	857	722
NaMg ₂ UO ₂ (CO ₃) ₃ ⁺	466.0	482.6	503.9	527.0	552.2	874	739
	464.7	481.0	501.5	523.8	548.2	850	720
NaCa ₂ UO ₂ (CO ₃) ₃ ⁺	464.7	481.0	501.8	524.5	549.3	862	728
	464.7	481.0	501.8	524.5	549.3	862	728

Table B.9: Computed intensity ratios of the five main bands of the uranyl complexes in a gas phase ($(I_i/I_1)_{GP}$) and in CPCM water ($(I_i/I_1)_w$). Gamma factor γ is defined as the ratio evolution of the ratio between the two media.

	$\text{Na}_2\text{CaUO}_2(\text{CO}_3)_3$	$\text{NaCa}_2\text{UO}_2(\text{CO}_3)_3^+$	$\text{NaMg}_2\text{UO}_2(\text{CO}_3)_3^+$	$\text{Na}_2\text{MgUO}_2(\text{CO}_3)_3$
$(I_2/I_1)_{GP}$	0.502	0.521	0.516	0.499
$(I_2/I_1)_w$	0.456	0.467	0.477	
γ	0.907	0.897	0.925	
$(I_3/I_1)_{GP}$	0.154	0.165	0.162	0.152
$(I_3/I_1)_w$	0.126	0.134	0.139	
γ	0.816	0.811	0.857	
$(I_4/I_1)_{GP}$	0.037	0.040	0.039	0.036
$(I_4/I_1)_w$	0.027	0.030	0.031	
γ	0.730	0.736	0.794	
$(I_5/I_1)_{GP}$	0.007	0.008	0.008	0.007
$(I_5/I_1)_w$	0.005	0.006	0.006	
γ	0.652	0.670	0.736	

Table B.10: Assignment of the $\text{Na}_2\text{MgUO}_2(\text{CO}_3)_3$ and $\text{NaMg}_2\text{UO}_2(\text{CO}_3)_3^+$ theoretical vibronic progressions computed in the gas phase and in the CPCM water solvent. The energy of the spectrum was adjusted to the experimental "hot band" value of $\text{Mg}-\text{UO}_2-\text{CO}_3$ in water.

$\text{Na}_2\text{MgUO}_2(\text{CO}_3)_3$			$\text{NaMg}_2\text{UO}_2(\text{CO}_3)_3^+$			Identification
E, cm^{-1}	$\Delta\nu$, cm^{-1}	I, a.u.	E, cm^{-1}	$\Delta\nu$, cm^{-1}	I, a.u.	
Gas phase, $\epsilon_r = 0$						
21459		0.462	21459		0.443	0(0)->1(0)
21300	159	0.016	21247	212	0.044	0(0)->1(1 ν_1)
21249	210	0.018	21202	257	0.034	0(0)->1(1 ν_2)
20562	897	0.231	20541	918	0.228	0(0)->1(1 ν_3)
20404	158	0.008	20329	233	0.023	0(0)->1(1 $\nu_1, 1\nu_3$)
20352	210	0.007	20283	279	0.016	0(0)->1(1 $\nu_2, 1\nu_3$)
19666	896	0.070	19623	939	0.072	0(0)->1(2 ν_3)
19507	159	0.003	19410	256	0.007	0(0)->1(1 $\nu_1, 2\nu_3$)
19456	210	0.002	19365	301	0.005	0(0)->1(1 $\nu_2, 2\nu_3$)
18769	897	0.017	18705	961	0.017	0(0)->1(3 ν_3)
17873	896	0.003	17787	982	0.004	0(0)->1(4 ν_3)
Water, $\epsilon_r = 78$						
21459		0.462	21459		0.484	0(0)->1(0)
21295	146	0.016	21235	224	0.025	0(0)->1(1 ν_1)
21264	246	0.018	21198	261	0.016	0(0)->1(1 ν_2)
20544	856	0.213	20586	873	0.231	0(0)->1(1 ν_3)
20381	146	0.008	20361	202	0.012	0(0)->1(1 $\nu_1, 1\nu_3$)
20351	246	0.007	20323	239	0.006	0(0)->1(1 $\nu_2, 1\nu_3$)
19626	856	0.060	19711	851	0.067	0(0)->1(2 ν_3)
19460	146	0.003	19487	179	0.003	0(0)->1(1 $\nu_1, 2\nu_3$)
19432	246	0.002	19450	216	0.002	0(0)->1(1 $\nu_2, 2\nu_3$)
18700	856	0.013	18838	828	0.015	0(0)->1(3 ν_3)
17768	856	0.002	17964	805	0.003	0(0)->1(4 ν_3)
ν_1 - CO_3 asym. motions, ν_2 - CO_3 sym. motions + U-O-U bend., ν_3 - U-O-U sym. str.						

Table B.11: Assignment of the $\text{Na}_2\text{CaUO}_2(\text{CO}_3)_3$ and $\text{NaCa}_2\text{UO}_2(\text{CO}_3)_3^+$ theoretical vibronic progressions computed in the gas phase and in the CPCM water solvent. The energy of the spectrum was adjusted to the experimental "hot band" value of $\text{Ca}-\text{UO}_2-\text{CO}_3$ in water.

$\text{Na}_2\text{CaUO}_2(\text{CO}_3)_3$			$\text{NaCa}_2\text{UO}_2(\text{CO}_3)_3^+$			Identification
E, cm^{-1}	$\Delta\nu$, cm^{-1}	I, a.u.	E, cm^{-1}	$\Delta\nu$, cm^{-1}	I, a.u.	
Gas phase, $\epsilon_r = 0$						
21519		0.263	21519		0.452	0(0)->1(0)
21317	202	0.013	21325	194	0.063	0(0)->1(1 ν_1)
20628	891	0.132	20609	910	0.236	0(0)->1(1 ν_2)
20426	202	0.006	20415	194	0.033	0(0)->1(1 ν_1 ,1 ν_2)
19737	891	0.041	19700	909	0.075	0(0)->1(2 ν_2)
19535	202	0.002	19506	194	0.010	0(0)->1(1 ν_1 ,2 ν_2)
18845	891	0.010	18791	910	0.018	0(0)->1(3 ν_2)
17954	891	0.002	17881	910	0.004	0(0)->1(4 ν_2)
Water, $\epsilon_r = 78$						
21519		0.476	21519		0.530	0(0)->1(0)
21336	183	0.016	21314	205	0.013	0(0)->1(1 ν_1)
20669	850	0.217	20657	862	0.248	0(0)->1(1 ν_2)
20486	183	0.009	20452	205	0.006	0(0)->1(1 ν_1 ,1 ν_2)
19819	850	0.060	19795	862	0.071	0(0)->1(2 ν_2)
19636	183	0.003	19590	205	0.001	0(0)->1(1 ν_1 ,2 ν_2)
18969	850	0.013	18933	862	0.016	0(0)->1(3 ν_2)
18119	850	0.002	18070	863	0.003	0(0)->1(4 ν_2)
ν_1 - Na, Ca, CO_3 motions, ν_2 - U-O-U sym. str.						

B.4 Supplemental Figures

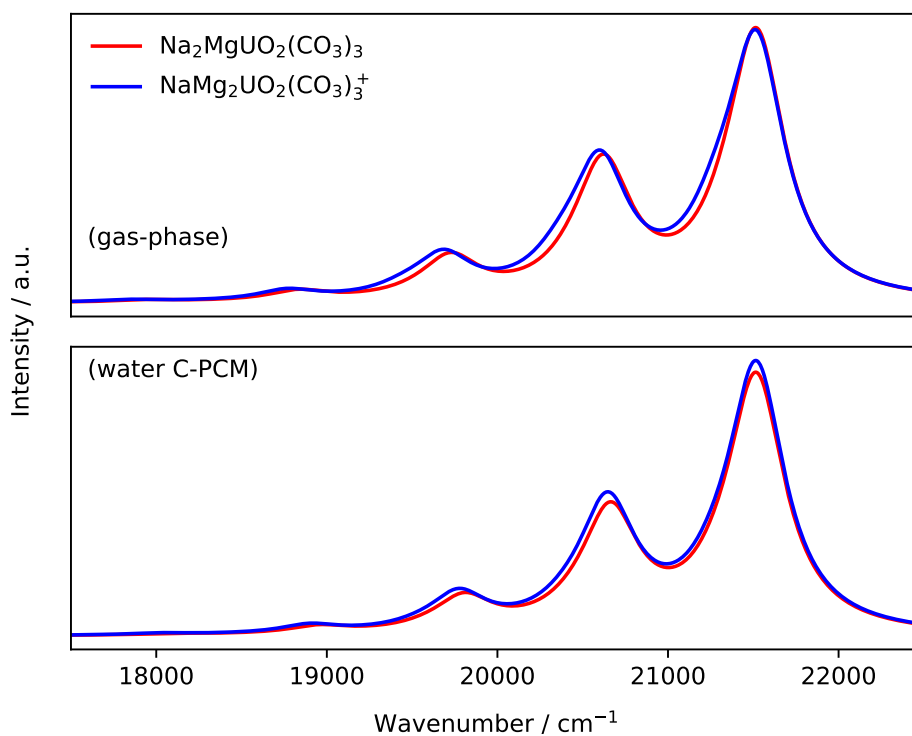


Figure B.1: Theoretical vibronic progressions of $\text{Na}_2\text{MgUO}_2(\text{CO}_3)_3$ and $\text{NaMg}_2\text{UO}_2(\text{CO}_3)_3^+$ complexes computed from the structural parameters obtained in the gas phase and the CPCM water solvent. The spectral shapes were obtained by Lorentzian convolution using experimental value of the FWHM (400 cm^{-1}). All the bands were considered for the shapes prediction, the identification of bands is shown in Table B.10.

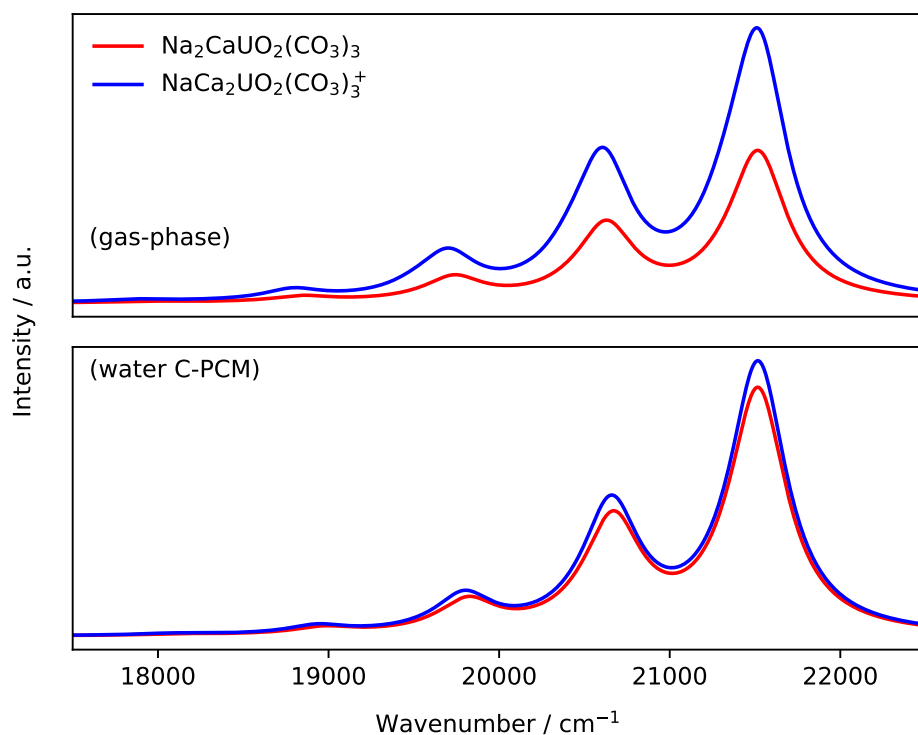


Figure B.2: Theoretical vibronic progressions of $\text{Na}_2\text{CaUO}_2(\text{CO}_3)_3$ and $\text{NaCa}_2\text{UO}_2(\text{CO}_3)_3^+$ complexes computed from the structural parameters obtained in the gas phase and in the CPCM water solvent. The spectral shapes were obtained by Lorentzian convolutions using the experimental value of the FWHM (400 cm^{-1}). All the bands were considered for the shapes prediction, the identification of bands is shown in Table B.11.

Bibliography of the current chapter

- (194) Shang, C.; Reiller, P. E. Determination of formation constants and specific ion interaction coefficients for $\text{Ca}_n\text{UO}_2(\text{CO}_3)_3^{(4-2n)-}$ complexes in NaCl solution by time-resolved laser-induced luminescence spectroscopy. *Dalton Transactions* **2020**, 49, 466–481, DOI: 10.1039/C9DT03543E.
- (200) Endrizzi, F.; Rao, L. F. Chemical Speciation of Uranium(VI) in Marine Environments: Complexation of Calcium and Magnesium Ions with $\text{UO}_2(\text{CO}_3)_3^{4-}$ and the Effect on the Extraction of Uranium from Seawater. *Chemistry-a European Journal* **2014**, 20, 14499–14506, DOI: 10.1002/chem.201403262.

Scientific contributions

Conferences

- 1 Poster at 4th International Workshop in Advanced Techniques in Actinides Spectroscopy, November 2018, Nice, France
- 2 Oral presentation at 49th Journée des Actinides 2019, April 2019, Erice, Italy
- 3 Oral presentation at International Workshop on Theory Frontiers in Actinide Sciences: Chemistry and Materials, February 2020, Santa Fe, USA
- 4 Poster at GDR SciNEE: "Matériaux de nucléaire et transfert: approches expérimentales et théoriques", March 2020, Villeneuve D'Ascq, France

Publications

- 1 H. Oher, F. Réal, T. Vercouter, V. Vallet "Investigation of the luminescence of $[\text{UO}_2\text{X}_4]^{2-}$ (X=Cl, Br) complexes in organic phase using time-resolved laser-induced fluorescence spectroscopy and quantum chemical simulations" *Inorganic Chemistry* **2020**, 59, 9, 5896-5906,
- 2 H. Oher, T. Vercouter, F. Réal, C. Shang, P.E. Reiller, V. Vallet "Influence of alkaline earth metal ion on structures and luminescent properties of $\text{Na}_m\text{M}_n\text{UO}_2(\text{CO}_3)_3^{(4-m-2n)-}$ (M = Mg, Ca; m, n = 0-2): time-resolved fluorescence spectroscopy and *ab initio* studies", *Inorganic Chemistry* **2020**, *In Press*,

List of Tables

3.1	Ground and excited state geometries of the $[\text{UO}_2\text{X}_4]^{2-}$, $\text{X} = \text{Cl}, \text{Br}$ compared to selected previous results.	90
3.2	Ground and excited state vibrational frequencies (in cm^{-1}) of the $[\text{R}_4\text{N}]_2[\text{UO}_2\text{X}_4]$, ($[\text{R}_4\text{N}] = [\text{Bu}_4\text{N}], [\text{A336}]$) compounds.	92
3.3	Ground and excited state geometries of the $[\text{R}_4\text{N}]_2[\text{UO}_2\text{Cl}_4]$ compounds compared to selected experimental results.	95
3.4	Experimental and computed vertical absorption (E_{VA}) and vertical emission (E_{VE}) energies of uranyl tetrahalide complexes (in cm^{-1}). The computed values are obtained at the all-electron SOC CAM-B3LYP level of theory, and corrected with the spin-free Zero-Point Energy correction of the ground and luminescent states.	97
4.1	The aqueous compositions of prepared sample solutions calculated with published thermodynamic data from Shang et al. [194], Lee et al. [206] and Dong et al. [201]	120
4.2	Ground state geometries (in Å) of $\text{Na}_m\text{M}_n\text{UO}_2(\text{CO}_3)_3^{(4-m-2n)-}$ ($\text{M}=\text{Mg}, \text{Ca}$; $m, n = 0-2$) complexes computed with the PBE0 functional in the CPCM water solvent, and compared to selected literature data. The experimental uncertainties are given in parentheses.	124
4.3	Excited state geometries (in Å) of $\text{Na}_m\text{M}_n\text{UO}_2(\text{CO}_3)_3^{(4-m-2n)-}$ ($\text{M}=\text{Mg}, \text{Ca}$; $m, n = 0-2$) complexes computed with the PBE0 functional in the CPCM water solvent.	125
4.4	Ground and excited-state vibrational frequencies (in cm^{-1}) of $\text{Na}_m\text{M}_n\text{UO}_2(\text{CO}_3)_3^{(4-m-2n)-}$ ($\text{M} = \text{Mg}, \text{Ca}$; $m, n = 0-2$) complexes computed with the PBE0 functional in the CPCM water solvent.	128
4.5	Experimental and computed “hot band” energies (in nm and cm^{-1}) of $\text{Na}_m\text{M}_n\text{UO}_2(\text{CO}_3)_3^{(4-m-2n)-}$ ($\text{M} = \text{Mg}, \text{Ca}$; $m, n = 0-2$) complexes in water. Theoretical values were obtained at all-electron SOC CAM-B3LYP level of theory, modeling the water solvent with the COSMO model.	131

4.6	Experimental and theoretical spectral characteristics of triscarbonatouranyl complexes. Experimental ν_s^{GS} and ν values were obtained by Lorentzian fitting procedure.	135
5.1	DFT/PBE0 and MP2 free energies (relative to <i>trans</i> conformer) difference in kJ mol^{-1} and probability of <i>cis</i> conformer over the <i>trans</i> for GP and CPCM ground state structures of $\text{UO}_2(\text{NO}_3)_2(\text{H}_2\text{O})_2$ and GP structures of $\text{UO}_2(\text{NO}_3)_2(\text{DEiBA})_2$	155
5.2	Ground and excited state geometries (in Å) of $\text{UO}_2(\text{NO}_3)_2(\text{H}_2\text{O})$ and <i>cis-/trans</i> - $\text{UO}_2(\text{NO}_3)_2(\text{L})_2$ (L= H_2O , DEiBA) compared to selected results from the literature.	157
5.3	Ground and excited state vibrational frequencies (in cm^{-1}) of the $\text{UO}_2(\text{NO}_3)_2(\text{H}_2\text{O})$ and <i>cis-/trans</i> - $\text{UO}_2(\text{NO}_3)_2(\text{L})_2$ (L= H_2O , DEiBA) compared to selected results from the literature.	158
5.4	The “hot band” energies E of uranyl binitrate complexes (in cm^{-1} and nm) compared to $\text{Na}_3\text{UO}_2(\text{CO}_3)_3^-$ and $[\text{A}336]_2[\text{UO}_2\text{Cl}_4]$ results. The computed values are obtained at the all-electron SOC CAM-B3LYP level of theory, and corrected with the spin-free Zero-Point Energy correction of the ground and luminescent states.	163
5.5	Assignments of the $\text{UO}_2(\text{NO}_3)_2(\text{H}_2\text{O})$ and <i>cis-/trans</i> - $\text{UO}_2(\text{NO}_3)_2(\text{L})_2$ (L = H_2O , DEiBA) theoretical luminescence spectra computed in the gas phase and in the CPCM water solvent for complexes with organic and inorganic ligands respectively. The energy of the spectrum was adjusted to the theoretical “hot band” value and corrected by ν_s of the excited state.	166
5.6	Experimental and theoretical spectral characteristics of uranyl binitrate complexes. The peak maxima are reported in nm. Experimental ν_s^{GS} and ν_s^{ES} values were obtained by a Lorentzian fitting procedure. The ν_s^{GS} corresponds to the averaged band-spacing values between the vibronic transitions, the ν_s^{ES} corresponds to spacing between the $1 \rightarrow 0$ and $0 \rightarrow 0$ transitions. ν_s^{GS} and ν_s^{ES} are given in cm^{-1}	171
A.1	Experimental luminescence data of the $[\text{R}_4\text{N}]_2[\text{UO}_2\text{Cl}_4]$ complexes at room temperature. The ν corresponds to the position of the band, the $\Delta\nu$ is a difference between the bands position in a region, the $\Delta\nu_n$ is a difference between the peaks of the same nature located in different regions. All data are in cm^{-1} . The luminescence spectra are shown on Figure 3.2.	191

A.2	Ground and excited state harmonic and anharmonic frequencies (in cm^{-1}) of the $[\text{UO}_2\text{Cl}_4]^{2-}$ complex in a gas phase computed by G16 at R-ECP DFT/PBE0 and TD-DFT/PBE0 level of theory for the ground and first excited states respectively.	192
A.3	The chloride-hydrogen bond lengths (in Å) in $[\text{R}_4\text{N}]_2[\text{UO}_2\text{Cl}_4]$ complexes computed at the R-ECP DFT/PBE0 and TD-DFT/PBE0 levels of theory for the ground and first excited states, respectively. Atom labeling corresponds to the one shown on Figure A.3. . .	192
A.4	Assignment of the $[\text{UO}_2\text{Cl}_4]^{2-}$ (gas-phase) theoretical luminescence spectrum. The energy of the spectrum was adjusted to experimental band-origin value of $[\text{UO}_2\text{Cl}_4]^{2-}$ in acetone. The nature of bands is explained in Table A.2.	193
A.5	Assignment of the $[\text{UO}_2\text{Cl}_4]^{2-}$ (dodecane) theoretical luminescence spectrum. The energy of the spectrum was adjusted to experimental band-origin value of $[\text{UO}_2\text{Cl}_4]^{2-}$ in acetone. The nature of bands is explained in Table A.2.	194
A.6	Assignment of the $[\text{UO}_2\text{Cl}_4]^{2-}$ (acetone) theoretical luminescence spectrum. The energy of the spectrum was adjusted to experimental band-origin value of $[\text{UO}_2\text{Cl}_4]^{2-}$ in acetone. The nature of bands is explained in Table A.2.	195
A.7	Assignment of the $[\text{UO}_2\text{Br}_4]^{2-}$ theoretical luminescence spectrum. The energy of the spectrum was adjusted to experimental band-origin value of $[\text{UO}_2\text{Cl}_4]^{2-}$ in acetone. The bands representation is taken from the $[\text{UO}_2\text{Cl}_4]^{2-}$ frequencies, the nature of bands is explained in Table A.2.	196
A.8	Assignment of the $[\text{Bu}_4\text{N}]_2[\text{UO}_2\text{Cl}_4]$ (gas-phase) theoretical luminescence spectrum. The energy of the spectrum was adjusted to experimental band-origin value of $[\text{UO}_2\text{Cl}_4]^{2-}$ in acetone. The nature of bands is shown in Table A.2.	197
A.9	Assignment of the $[\text{A336}]_2[\text{UO}_2\text{Cl}_4]$ gas-phase theoretical luminescence spectrum. The energy of the spectrum was adjusted to experimental band-origin value of $[\text{A336}]_2[\text{UO}_2\text{Cl}_4]$ in <i>n</i> -dodecane. The bands representation is taken from the $[\text{UO}_2\text{Cl}_4]^{2-}$ frequencies, with details found in Table A.2.	198
A.10	Theoretical displacements of geometries ΔR , and absolute frequency shifts $\Delta\nu$ from the ground to the first excited state. . .	198
B.1	The ground and excited-state displacements in $\text{Na}_2\text{MgUO}_2(\text{CO}_3)_3$ and $\text{NaMg}_2\text{UO}_2(\text{CO}_3)_3^+$ complexes between the structures obtained in the gas phase and in the CPCM water solvent, at the DFT/PBE0 and TD-DFT/PBE0 levels of theory.	207

B.2	Ground and excited-state bond distances (in Å) in the $\text{Na}_2\text{MgUO}_2(\text{CO}_3)_3$ and $\text{NaMg}_2\text{UO}_2(\text{CO}_3)_3^+$ complexes optimized in the gas phase and in the CPCM water solvent, at the DFT/PBE0 and TD-DFT/PBE0 levels of theory.	208
B.3	The ground and excited-state displacements in $\text{Na}_2\text{CaUO}_2(\text{CO}_3)_3$ and $\text{NaCa}_2\text{UO}_2(\text{CO}_3)_3^+$ complexes between the structures obtained in the gas phase and in the CPCM water solvent, at the DFT/PBE0 and TD-DFT/PBE0 levels of theory.	209
B.4	Ground and excited-state bond distances (in Å) in the $\text{Na}_2\text{CaUO}_2(\text{CO}_3)_3$ and $\text{NaCa}_2\text{UO}_2(\text{CO}_3)_3^+$ complexes optimized in the gas phase and in the CPCM water solvent, at the DFT/PBE0 and TD-DFT/PBE0 levels of theory.	210
B.5	Absolute frequency shifts $\Delta\nu$ (in cm^{-1}) from the ground to the first excited state geometries.	211
B.6	First four vertical emission energies in cm^{-1} computed at the SF and SOC CAM-B3LYP level of theory with the COSMO water solvent model.	212
B.7	First four vertical emission energies in cm^{-1} computed at the SOC CAM-B3LYP level of theory with the COSMO water solvent model and corrected with the spin-free zero-point energy corrections, ΔZPE , of the ground and luminescent states.	213
B.8	Experimental and theoretical spectral characteristics of triscarbonatouranyl complexes. The peak maxima are reported in nm. Experimental ν_s^{gs} and ν values were obtained by a Lorentzian fitting procedure. The ν_s^{gs} corresponds to the averaged band-spacing values between the vibronic transitions, the ν corresponds to spacing between the $11 \rightarrow 00$ and $10 \rightarrow 00$ transitions. ν_s^{gs} and ν are given in cm^{-1}	214
B.9	Computed intensity ratios of the five main bands of the uranyl complexes in a gas phase ($(I_i/I_1)_{\text{GP}}$) and in CPCM water ($(I_i/I_1)_w$). Gamma factor γ is defined as the ratio evolution of the ratio between the two media.	215
B.10	Assignment of the $\text{Na}_2\text{MgUO}_2(\text{CO}_3)_3$ and $\text{NaMg}_2\text{UO}_2(\text{CO}_3)_3^+$ theoretical vibronic progressions computed in the gas phase and in the CPCM water solvent. The energy of the spectrum was adjusted to the experimental "hot band" value of $\text{Mg}-\text{UO}_2-\text{CO}_3$ in water.	216

B.11 Assignment of the $\text{Na}_2\text{CaUO}_2(\text{CO}_3)_3$ and $\text{NaCa}_2\text{UO}_2(\text{CO}_3)_3^+$ theoretical vibronic progressions computed in a the gas phase and in the CPCM water solvent. The energy of the spectrum was adjusted to the experimental "hot band" value of $\text{Ca-UO}_2\text{-CO}_3$ in water.	217
--	-----

List of Figures

1	Location of the actinides in the periodic table of elements. . . .	2
1.1	General Jablonski diagram representing the electronic transitions in a diatomic molecule.	14
1.2	The uranyl(VI) di-cation structure.	16
1.3	The effect of the spin-orbit coupling on the bare UO_2^{2+} . The schematic diagram is obtained at the spin free at spin-orbit CAM-B3LYP/DFT level of theory.	17
1.4	Energy levels [5] and characteristic Kohn-Sham molecular orbitals of uranyl.	18
1.5	Pentaaquauranyl $\text{UO}_2(\text{H}_2\text{O})_5^{2+}$ structure.	19
1.6	A simplified Franck-Condon principle diagram applied to U(VI) luminescence [41](left) and the time-resolved luminescence spectrum of uranyl in aqueous acidic media (pH = 1) with corresponding transition lines (right).	20
1.7	A temporal resolution principle used for the time-resolved laser-induced fluorescence spectroscopy measurements.	24
1.8	The scheme of the used TRLFS technique.	26
2.1	Franck-Condon principle energy diagram. The S_0 corresponds to the ground state potential energy curve, while S_1 and T_1 represent first singlet and triplet states, respectively.	34
2.2	Schematic two-dimensional description of Duschinsky rotation potential energy surface.	36
2.3	Construction of the Slater type function by $n\text{GTO}$ ($n=1-3$).	59
2.4	C-PCM solute cavity for uranyl binitrate complex.	63
2.5	The structures of the studied model systems.	76
3.1	The complexes structures of $[\text{R}_4\text{N}]_2[\text{UO}_2\text{X}_4]$ ($[\text{R}_4\text{N}] = [\text{Bu}_4\text{N}]$, [A336] and $\text{X}=\text{Cl}, \text{Br}$) in gas phase optimized at the DFT/PBE0 level of theory.	84

3.2	Recorded time-resolved luminescence spectra of $[\text{Bu}_4\text{N}]_2[\text{UO}_2\text{Cl}_4]$ in acetone (the maxima taken from Görrler-Walrand et al. [[23]], the Lorentzian shape computed) and $[\text{A336}]_2[\text{UO}_2\text{Cl}_4]$ in <i>n</i> -dodecane (this work). Vertical dashed red line shows the “hot band” position and R_n , ($n = 1 - 5$) corresponds to vibronic progression region. Details on the spectral data are available in Table A.1 of the Annex A.	87
3.3	The highest occupied (HOMO) and lowest unoccupied molecular orbitals (LUMO) of $[\text{Bu}_4\text{N}]_2[\text{UO}_2\text{Cl}_4]$ in gas phase obtained at RECP DFT/PBE0 level of theory.	98
3.4	Theoretical luminescence spectra of $[\text{UO}_2\text{Cl}_4]^{2-}$ and $[\text{UO}_2\text{Br}_4]^{2-}$ in gas phase computed at 300 K.	100
3.5	Experimental and theoretical luminescence spectra of $[\text{A336}]_2[\text{UO}_2\text{Cl}_4]$ in <i>n</i> -dodecane and a gas-phase respectively at 300 K.	101
4.1	The structures of uranyl bidentate tri-carbonate complexes $\text{Na}_m\text{M}_n\text{UO}_2(\text{CO}_3)_3^{(4-m-2n)-}$ ($\text{M} = \text{Mg}, \text{Ca}$; $m, n = 0-2$) in water with different composition of the second coordination sphere optimized at the DFT/PBE0 level of theory. In red - O, brown - C, dark blue - U, gray - Na, light blue - Ca, Mg.	116
4.2	Measured luminescence spectra of U(VI) at various concentration ratios $[\text{Mg}^{2+}]/([\text{Mg}^{2+}] + [\text{Ca}^{2+}])$ using (a) the 300 lines /mm grating, and (b)-(f) using the 1800 lines /mm grating for each characteristic peak, normalized to the area of the spectrum in the working wavelength range.	119
4.3	Schematic notation of U-CO ₃ bonds in a) $\text{Na}_2\text{MUO}_2(\text{CO}_3)_3$ and b) $\text{NaM}_2\text{UO}_2(\text{CO}_3)_3^+$ ($\text{M} = \text{Mg}, \text{Ca}$) complexes depending on the position of the alkaline earth metals in the second coordination sphere. Notation r_1, r_2 and r_3 correspond to different U-O _{eq} bonds, while the dashed lines r_A and r_B correspond to different U-C and U-O _{dist} bonds. In red - O, brown - C, dark blue - U, gray - Na, light blue - Ca, Mg.	126
4.4	The highest occupied and lowest unoccupied molecular orbitals of $\text{Na}_3\text{UO}_2(\text{CO}_3)_3^-$ involved in the triplet-singlet electronic transitions, responsible of uranyl luminescence. The molecular orbitals were computed at the gas phase ground-state structure at the DFT/PBE0 level of theory.	129

4.5	Deconvoluted experimental spectra of (a) $\text{MgUO}_2(\text{CO}_3)_3^{2-}$, and (b) $\text{CaUO}_2(\text{CO}_3)_3^{2-}$ and $\text{Ca}_2\text{UO}_2(\text{CO}_3)_3$ from TRLFS measurements. Theoretical luminescence spectra in water of (c) $\text{Na}_2\text{MgUO}_2(\text{CO}_3)_3$ (reconstructed as described in Annex B) and $\text{NaMg}_2\text{UO}_2(\text{CO}_3)_3^+$, and (d) $\text{Na}_2\text{CaUO}_2(\text{CO}_3)_3$ and $\text{NaCa}_2\text{UO}_2(\text{CO}_3)_3^+$	133
5.1	The structures of $\text{UO}_2(\text{NO}_3)_2(\text{H}_2\text{O})$ and $\text{UO}_2(\text{NO}_3)_2(\text{L})_2$ ($\text{L}=\text{H}_2\text{O}$, DEiBA) model systems in their <i>trans</i> (a) and <i>cis</i> (b) configurations.	154
5.2	The optimized at R-ECP DFT/PBE0 ground state geometries of the <i>cis</i> - and <i>trans</i> - $\text{UO}_2(\text{NO}_3)_2(\text{DEiBA})_2$ conformers.	159
5.3	The highest occupied (right panel) and lowest unoccupied (left panel) molecular orbitals of <i>trans</i> - $\text{UO}_2(\text{NO}_3)_2(\text{L})_2$ ($\text{L} = \text{H}_2\text{O}$, DEiBA) involved in the triplet-singlet electronic transitions, responsible of uranyl luminescence. The molecular orbitals were obtained at the RECP DFT/PBE0 level of theory.	162
5.4	Theoretical vibronic progressions of the $\text{UO}_2(\text{NO}_3)_2(\text{H}_2\text{O})$ and <i>cis</i> -/ <i>trans</i> - $\text{UO}_2(\text{NO}_3)_2(\text{L})_2$ ($\text{L} = \text{H}_2\text{O}$, DEiBA) complexes. The position of the first peak is adjusted to the “hot band” value of the <i>trans</i> -complexes and corrected by the ν_s of the excited state. The spectral shapes were estimated by convoluting the stick spectra with Lorentzian functions with a FWHM of 400 cm^{-1}	165
5.5	Experimental time-resolved luminescence spectra of $\text{UO}_2(\text{NO}_3)_2$ in nitric acid [230] (plain lines), $\text{UO}_2(\text{NO}_3)_2(\text{DEHiBA})_2$ in TPH solvent, $\epsilon=2.0$ [232] (dotted line) and $\text{UO}_2(\text{NO}_3)_2(\text{TBP})_2$ in a supercritical (CO_2), $\epsilon=1.6$ [268] (dashed line). The spectra were rebuilt from the data of the quoted references.	168
5.6	Superposition of the emission (TRLFS) and absorption (UV-vis) spectra of $\text{UO}_2(\text{NO}_3)_2(\text{DEHiBA})_2$ in TPH solvent of the same sample [232]. The spectra were rebuilt from corresponding literature sources.	169
5.7	Comparison of experimental emission spectra (TRLFS) with theoretical spectra of (a) $\text{UO}_2(\text{NO}_3)_2(\text{H}_2\text{O})_2$ and (b) $\text{UO}_2(\text{NO}_3)_2(\text{DEiBA})_2$	172
A.1	Normalized time-resolved luminescence spectra of $[\text{A336}]_2[\text{UO}_2\text{Cl}_4]$ in <i>n</i> -dodecane measured at different delay time.	190
A.2	Comparison of reference sample (without U) with the sample of $[\text{A336}]_2[\text{UO}_2\text{Cl}_4]$ in <i>n</i> -dodecane measured at different delay time.	190

A.3	Illustrations of hydrogen bondings between the first and second coordination spheres of uranyl in $[R_4N]_2[UO_2Cl_4]$ complexes. Left panel is representing interactions in $[Bu_4N]_2[UO_2Cl_4]$ and right in $[A336]_2[UO_2Cl_4]$	199
A.4	Influence of solvent effects on the theoretical spectrum of $[UO_2Cl_4]^{2-}$ at 0 K (upper panel) and 300 K (lower panel). The spectral shapes were obtained by a Lorentzian convolution; the assignments are provided in Tables A.4, A.5 and A.6 for the $[UO_2Cl_4]^{2-}$ in gas-phase, <i>n</i> -dodecane and acetone, respectively.	200
A.5	Effect of a $[A336]^+$ counter ion on the theoretical $[UO_2Cl_4]^{2-}$ spectrum in gas-phase at 300 K. The spectral shapes were obtained by a Lorentzian convolution; the assignments are provided in Tables A.4 and A.9 for the $[UO_2Cl_4]^{2-}$ and $[A336]_2[UO_2Cl_4]$, respectively.	201
A.6	Comparison of the theoretical spectra of $[Bu_4N]_2[UO_2Cl_4]$ and $[A336]_2[UO_2Cl_4]$ complexes in a gas-phase at 300 K. The spectral shapes were obtained by a Lorentzian convolution; the assignments are provided in Tables A.8 and A.9 for the $[Bu_4N]_2[UO_2Cl_4]$ and $[A336]_2[UO_2Cl_4]$, respectively.	202
B.1	Theoretical vibronic progressions of $Na_2MgUO_2(CO_3)_3$ and $NaMg_2UO_2(CO_3)_3^+$ complexes computed from the structural parameters obtained in the gas phase and the CPCM water solvent. The spectral shapes were obtained by Lorentzian convolution using experimental value of the FWHM (400 cm^{-1}). All the bands were considered for the shapes prediction, the identification of bands is shown in Table B.10.	218
B.2	Theoretical vibronic progressions of $Na_2CaUO_2(CO_3)_3$ and $NaCa_2UO_2(CO_3)_3^+$ complexes computed from the structural parameters obtained in the gas phase and in the CPCM water solvent. The spectral shapes were obtained by Lorentzian convolutions using the experimental value of the FWHM (400 cm^{-1}). All the bands were considered for the shapes prediction, the identification of bands is shown in Table B.11.	219

A COMBINED AB INITIO AND TIME-RESOLVED LASER-INDUCED FLUORESCENCE STUDY OF URANIUM-LIGAND INTERACTIONS

Abstract

Uranyl complexes have been the subject of many research works for fundamental chemistry of actinides, environmental issues, or nuclear fuel cycle processes. The formation of various uranium(VI) complexes, with ligands in solution must be characterized for a better understanding of U(VI) speciation. Uranyl-ligand interactions and symmetry of the complexes both affect the electronic structure of U(VI), and thus its luminescence properties. Time-resolved laser induced fluorescence spectroscopy (TRLFS) is one of the widely used techniques to get insights on the closest chemical environment of the uranyl ion in samples, owing to its high sensitivity and selectivity. However, the luminescence spectra fingerprints hold information within and beyond the first-coordination sphere of uranyl(VI), that needs to be more deeply investigated by supplementary techniques. A promising route for data interpretation consists in creating a synergy between TRLFS and ab initio-based interpretations. Luminescence spectra of uranyl complexes in solution typically show well-spaced vibronic progressions that overlap with the pure electronic transition from the excited state to the ground state. This has driven the theoretical methodology implementation. In the frame of this thesis, time-dependent density functional theory (TD-DFT) with hybrid and range-separated functionals is used to model the electronic structure of uranium(VI) complexes. This represents an effective theoretical approach with a reasonable computational cost and accuracy, compared with computationally expensive wave-function based methods, in a relativistic context. It enabled to characterize the main spectral parameters and the first low-lying excited state of uranyl compounds with different ligands and counterions after the photo-excitation, and to compute with a high accuracy the vibronic progression in order to guide the interpretation of experimental results.

In particular we focused our efforts on characterizing the influence of the organic or inorganic closest chemical environment of the uranium(VI)-based complexes. We studied 1) the influence of the extracting agent such as Aliquate 336 and solvent effect on uranyl tetrahalides; 2) inorganic Ca^{2+} and Mg^{2+} counterions on uranyl triscarbonates; and 3) monoamide ligands (di-2-ethylhexyl-isobutyramide) on uranyl binitrate complexes. Their electronic structures and main spectroscopic properties have been estimated by both TRLFS and ab initio techniques. The theoretical approach enabled to calculate the main luminescence emissions of the complexes with the corresponding assignment of the electronic transitions and vibronic modes involved. For all the studied complexes, a good agreement between theory and experiment was found, allowing to build a full picture about the capabilities of the methods.

Keywords: *ab initio*, photochemistry, uranium, trlfs

Laboratoire PhLAM

Laboratoire PhLAM – CNRS UMR 8523 – Université Lille Nord de France –
Bâtiment P5 – 59655 Villeneuve d'Ascq – France

Résumé

Les complexes d'uranyle ont fait l'objet de nombreux travaux de recherche pour la chimie fondamentale des actinides, les enjeux environnementaux ou les procédés du cycle du combustible nucléaire. La formation de divers complexes d'uranium(VI), avec des ligands en solution doit être caractérisée pour une meilleure compréhension de la spéciation de U(VI). Les interactions uranyl-ligand et la symétrie des complexes modifient la structure électronique de U(VI) et donc ses propriétés de luminescence. La spectrofluorimétrie laser résolue en temps (SLRT) est l'une des techniques largement utilisées pour obtenir des informations sur l'environnement chimique proche de l'ion uranyle dans les échantillons, en raison de sa sensibilité et de sa sélectivité élevées. Cependant, les signatures des spectres de luminescence contiennent des informations liées à la première sphère de coordination de l'uranyle et au-delà, et méritent d'être étudiées de manière plus approfondie par des techniques adaptées.

Une voie prometteuse pour l'interprétation des données consiste à créer une synergie entre SLRT et les interprétations *ab initio*. Les spectres de luminescence des complexes d'uranyle en solution montrent généralement des progressions vibroniques bien espacées qui se chevauchent avec la transition électronique pure provenant de l'état excité à l'état fondamental. Ceci a conduit la mise en œuvre de notre méthodologie théorique. Dans le cadre de cette thèse, la théorie de la fonctionnelle de la densité dépendante du temps (TD-DFT) avec des fonctionnelles hybrides et séparées par une plage est utilisée pour modéliser la structure électronique de complexes d'uranium(VI) dans un contexte relativiste. Cela a permis de caractériser les principaux paramètres spectraux et le premier état excité de plusieurs composés d'uranyle avec différents ligands et contre-ions, et de calculer avec une grande précision la progression vibronique afin de guider l'interprétation des résultats expérimentaux.

En particulier, nous avons concentré nos efforts sur la caractérisation de l'influence de l'environnement chimique le plus proche des complexes à base d'uranium(VI). Nous avons étudié 1) l'influence d'un agent d'extraction tel que l'Aliquate 336 et l'effet du solvant sur les tétrahalogénures d'uranyle; 2) les contre-ions inorganiques Ca^{2+} et Mg^{2+} sur les triscarbonates d'uranyle; et 3) les ligands monoamide (di-2-éthylhexylisobutyramide) sur les complexes de binitrate d'uranyle. Leurs structures électroniques et leurs principales propriétés spectroscopiques ont été estimées par les deux techniques SLRT et *ab initio*. L'approche théorique a permis de calculer les principales émissions de luminescence des complexes avec l'affectation correspondante des transitions électroniques et des modes vibroniques impliqués. Pour tous les complexes étudiés, un bon accord entre la théorie et l'expérience a été obtenu, permettant de construire une image plus complète des capacités des méthodes.

Mots clés : *ab initio*, photochimie, uranium, slrt
